

# **STRUCTURAL BEHAVIOUR OF ELEMENTS COMBINING ULTRA-HIGH PERFORMANCE FIBRE REINFORCED CONCRETES (UHPFRC) AND REINFORCED CONCRETE**

THÈSE N° 3036 (2004)

PRÉSENTÉE À LA FACULTÉ ENVIRONNEMENT NATUREL, ARCHITECTURAL ET CONSTRUIT

Institut de structures

SECTION DE GÉNIE CIVIL

ÉCOLE POLYTECHNIQUE FÉDÉRALE DE LAUSANNE

POUR L'OBTENTION DU GRADE DE DOCTEUR ÈS SCIENCES TECHNIQUES

PAR

**Katrin HABEL**

Dipl.-Bauing., Universität Karlsruhe, Allemagne  
et de nationalité allemande

acceptée sur proposition du jury:

Prof. E. Brühwiler, directeur de thèse  
Dr E. Denarié, rapporteur  
Prof. P. Marti, rapporteur  
Dr P. Rossi, rapporteur  
Prof. K. Scrivener, rapporteur

Lausanne, EPFL  
2004



*The important thing is not to stop questioning. Curiosity has its own reason for existing. One cannot help but be in awe when he contemplates the mysteries of eternity, of life, of the marvellous structure of reality. It is enough if one tries merely to comprehend a little of this mystery every day. Never lose a holy curiosity.*

***Albert Einstein (1879 - 1955)***





# Table of Contents

Table of Contents .....	I
Foreword .....	VII
Summary .....	IX
Version abrégée .....	X
Zusammenfassung .....	XI
Acknowledgements .....	XIII
Glossary .....	XV
Symbols .....	XIX
<b>1 Introduction .....</b>	<b>1</b>
1.1 Context and motivation .....	1
1.2 Concepts for composite elements consisting of reinforced cementitious materials .....	3
1.3 Objectives .....	4
1.4 Thesis structure .....	5
<b>2 State of the art .....</b>	<b>9</b>
2.1 Scales to describe the behaviour of reinforced cementitious materials .....	9
2.2 Cementitious materials .....	10
2.2.1 Early age behaviour .....	10
2.2.1.1 Hydration .....	10
2.2.1.2 Heat of hydration .....	13
2.2.1.3 Self-desiccation .....	13
2.2.1.4 Chemical shrinkage .....	13
2.2.1.5 Evolution of mechanical properties .....	13
2.2.2 Tensile behaviour .....	14
2.2.3 Time-dependent macroscopic deformations .....	16
2.2.3.1 Free deformations .....	16
2.2.3.2 Viscoelastic behaviour .....	18
2.3 Ultra-High Performance Fibre-Reinforced Concretes (UHPFRC) .....	19
2.3.1 General .....	19
2.3.2 Principles of UHPFRC .....	20
2.3.3 Constituents of UHPFRC .....	20
2.3.4 Material properties .....	21
2.3.4.1 Hydration .....	21
2.3.4.2 Mechanical properties .....	21
2.3.4.3 Time-dependent deformations .....	23
2.3.4.4 Other physical properties .....	25
2.3.5 Applications .....	27
2.4 Cementitious material-to-rebar behaviour .....	27
2.5 Deformation capacity .....	29

2.6	Composite structural elements of reinforced cementitious materials	30
2.6.1	Degree of restraint	31
2.6.2	Composite RC elements	33
2.6.2.1	<i>Processing</i>	33
2.6.2.2	<i>Time-dependent behaviour</i>	33
2.6.2.3	<i>Failure modes</i>	35
2.6.3	Composite “ACM-concrete” elements	36
2.6.3.1	<i>Composite “HPFRCC-concrete” beams</i>	36
2.6.3.2	<i>Composite “UHPFRC-concrete” beams</i>	36
<b>3</b>	<b>Experimental investigation</b>	<b>39</b>
3.1	Introduction	39
3.2	Characterization of the UHPFRC	39
3.2.1	UHPFRC composition	39
3.2.2	Heat of hydration and evolution of the relative humidity	40
3.2.3	Compression properties	41
3.2.4	Tensile properties	41
3.2.4.1	<i>General</i>	41
3.2.4.2	<i>Development of a uniaxial tensile test</i>	41
3.2.4.3	<i>Results and discussion</i>	42
3.2.4.4	<i>Domains of cracking</i>	43
3.2.5	Free shrinkage	44
3.2.5.1	<i>Free autogenous shrinkage at early age</i>	44
3.2.5.2	<i>Free shrinkage tests on cylinders</i>	45
3.2.6	Viscoelastic behaviour	46
3.2.6.1	<i>Restrained autogenous shrinkage at early age</i>	46
3.2.6.2	<i>Compression creep</i>	47
3.2.7	Air permeability	48
3.3	Concrete properties	48
3.4	Composite “UHPFRC-concrete” beams	49
3.4.1	Experimental program	49
3.4.2	Early age and long-term behaviour	52
3.4.2.1	<i>General behaviour</i>	52
3.4.2.2	<i>Early age behaviour</i>	52
3.4.2.3	<i>Influence of the static system</i>	53
3.4.2.4	<i>Influence of the thickness of the UHPFRC layer</i>	54
3.4.2.5	<i>Influence of reinforcement in the UHPFRC layer</i>	54
3.4.2.6	<i>Bending creep</i>	55
3.4.2.7	<i>Cracking</i>	55
3.4.3	Structural response under bending	56
3.4.3.1	<i>Beams without reinforcement in the UHPFRC layer (beams NR)</i>	56
3.4.3.2	<i>Beams with reinforcement in the UHPFRC layer (beams R)</i>	56
3.5	Synthesis of the test results	58
<b>4</b>	<b>Time-dependent behaviour of composite “UHPFRC-concrete” elements</b>	<b>61</b>
4.1	Importance of the time-dependent behaviour	61
4.2	Description of the numerical model	61

4.3	Modelling of UHPFRC properties	62
4.3.1	Self-desiccation	62
4.3.2	Thermal deformation	63
4.3.3	Autogenous shrinkage	63
4.3.4	Drying shrinkage due to external drying	64
4.3.5	Viscoelastic behaviour	64
4.3.6	Mechanical properties	69
4.4	Composite “UHPFRC-concrete” elements	69
4.4.1	Introduction	69
4.4.2	General description of the time-dependent behaviour of the beam tests	71
4.4.3	Early age behaviour	73
4.4.4	Static system	76
4.4.5	Thickness of the UHPFRC layer	78
4.4.6	Reinforcement in the UHPFRC layer	79
4.4.7	Tensile strain-hardening of UHPFRC	80
4.4.8	Magnitude of autogenous shrinkage	82
4.4.9	Interface cracks and debonding at free ends	84
4.4.10	Extrapolation to higher ages	87
4.4.11	Composite “UHPFRC-concrete” elements with a new substrate	87
4.5	Conclusions	88
<b>5</b>	<b>Structural response</b>	<b>91</b>
5.1	Analytical model for bending	91
5.1.1	General	91
5.1.2	Hypotheses	91
5.1.3	Description	91
5.1.3.1	<i>Material laws</i>	91
5.1.3.2	<i>Kinematics</i>	93
5.1.3.3	<i>Equilibrium of internal forces and moment</i>	93
5.1.3.4	<i>Moment-curvature diagram</i>	94
5.1.4	Validation	94
5.1.4.1	<i>Composite 3-point bending beams with UHPFRC [Denarie01]</i>	94
5.1.4.2	<i>Composite “SIMCON-concrete” beams</i>	96
5.1.4.3	<i>Conclusion</i>	97
5.2	Structural response of composite “UHPFRC-concrete” beams	98
5.2.1	General	98
5.2.2	Beams without reinforcement in the UHPFRC layer (beams NR)	98
5.2.2.1	<i>Discussion of experimental results</i>	98
5.2.2.2	<i>Structural response</i>	105
5.2.2.3	<i>Potential application</i>	106
5.2.3	Beams with reinforcement in the UHPFRC layer (R)	106
5.2.3.1	<i>Discussion of experimental results</i>	106
5.2.3.2	<i>Structural response</i>	109
5.2.3.3	<i>Potential application</i>	111
5.2.4	Macrocrack formation and deformation capacity	111
5.3	Reference length	113
5.3.1	General	113
5.3.2	Reference length values	113
5.3.3	Determination of the reference length	114
5.3.4	Prospects	115

5.4	Conclusions	116
5.4.1	Structural response of composite “UHPFRC-concrete” beams	116
5.4.2	Modelling	117
<b>6</b>	<b>Design of composite “UHPFRC-concrete” elements</b>	<b>119</b>
6.1	Conceptual idea	119
6.2	Verification of composite “UHPFRC-concrete” structural elements	120
6.2.1	General	120
6.2.2	Material properties of UHPFRC	120
6.2.3	Durability	121
6.2.3.1	General	121
6.2.3.2	Hazard scenarios	121
6.2.3.3	Permeability	121
6.2.3.4	Limitation of crack widths	122
6.2.4	Serviceability limit state (SLS)	122
6.2.4.1	General	122
6.2.4.2	Stiffness	122
6.2.4.3	Water tightness	123
6.2.5	Ultimate limit state (ULS)	123
6.2.5.1	General	123
6.2.5.2	Failure modes	123
6.2.5.3	Discussion of partial safety factors	124
6.2.5.4	Verification of the negative bending moment	125
6.2.5.5	Verification of the positive bending moment	126
6.2.5.6	Shear	127
6.2.6	Example	128
6.2.6.1	Description	128
6.2.6.2	Results and discussion	129
6.2.6.3	Conclusion	132
6.3	Parametric study	133
6.3.1	Scope	133
6.3.2	Basic parameters	133
6.3.3	Curve description	134
6.3.4	Configuration of the cross-section	136
6.3.5	Influence of the cross-section geometry	137
6.3.6	Influence of the tensile properties of the UHPFRC	139
6.3.6.1	Contribution of the UHPFRC	139
6.3.6.2	Influence of UHPFRC tensile properties	139
6.3.7	Influence of the concrete strength	142
6.3.8	Influence of the type of reinforcement in the UHPFRC layer	144
6.4	Rules for efficient design of composite “UHPFRC-concrete” elements	146
6.4.1	Design criteria	146
6.4.2	Selection of materials	147
6.4.3	Selection of element configuration	147
6.4.3.1	Conservation projects	147
6.4.3.2	New construction projects	148
6.4.4	Efficient configurations	149
6.4.4.1	Configuration P	149
6.4.4.2	Configuration PR	149
6.4.4.3	Configuration R	150

---

<b>7</b>	<b>Conclusions and future work</b>	<b>153</b>
7.1	Conclusions	153
7.1.1	Composite “UHPFRC-concrete” elements	153
7.1.2	UHPFRC	155
7.1.3	Modelling	156
7.2	Future work	156
<b>8</b>	<b>References</b>	<b>159</b>
	<b>Appendices</b>	<b>171</b>
	Appendix A: Description of the numerical model (MLS)	171
	Appendix B: Material input of the numerical model (MLS)	179
	Appendix C: Parameters of the generalized age-dependent Maxwell chain model for UHPFRC	181
	Appendix D: Simulation of the composite beams with the numerical model (MLS)	183
	Appendix E: Analytical model for the composite “UHPFRC-concrete” beams	187
	Curriculum vitae	195



## Foreword

Ultra-High Performance Fibre-Reinforced Concretes (UHPRFC) have until now only been used for new structures. Surprisingly, the extraordinary properties of UHPRFC have not yet been exploited for application to improve and rehabilitate existing concrete structures although maintenance of structures is today the main structural engineering topic in developed countries.

The thesis of Katrin Habel deals with the question whether UHPRFC provide radically different solutions in terms of efficiency (i.e. rapid construction, lean interventions) when compared to currently applied methods and materials for the maintenance of structures. This thesis topic is extremely challenging since it may open completely new ways towards more efficient interventions on existing concrete structures.

In her thesis, Katrin Habel investigates ways to determine and improve the performance and structural behaviour of composite elements consisting of UHPRFC and conventional reinforced concrete. These composite elements are the result of the original basic conceptual idea developed at the Laboratory of Maintenance and Safety of Structures (MCS) of EPFL, i.e. to use the UHPRFC in zones of the concrete structure that are subjected to the most severe environmental and mechanical actions.

The present thesis contains an impressive amount of novel information on the mechanical properties of UHPRFC and the structural behaviour of composite UHPRFC-concrete elements, and provides thus advanced state-of-the-art knowledge. Also, the necessary basis is laid for the application on real structures of a novel technology with a very promising potential. I hope the reader will appreciate the very high quality of this research work.

Katrin Habel provides the proof of her capabilities to conduct a scientific study and to solve a complex problem independently. In the name of the whole team of MCS, I thank her for her thorough and constant investment to the thesis topic as well as for her professional skills and personal qualities.

Lausanne, 11 July 2004

Professor Eugen Brühwiler





## Summary

*Ultra-High Performance Fibre-Reinforced Concretes (UHPFRC)* have high mechanical strengths ( $f_{U,c} > 150$  MPa,  $f_{U,t} > 6$  MPa) and exhibit quasi-strain hardening in tension. Their very low permeability prevents the ingress of detrimental substances. In composite structural elements formed of normal strength reinforced concrete and Advanced Cementitious Materials (ACM), UHPFRC offer a high potential in view of the load carrying and protection function of the ACM layer.

The *objectives* of the study described in this thesis are to determine the performance and structural behaviour of composite “UHPFRC-concrete” elements in bending. Towards this end, the current knowledge of UHPFRC properties is to be extended and modelling tools are to be developed in order to predict the structural behaviour of such composite elements and to make recommendations for their design.

The *experimental program* is performed in order to characterize the UHPFRC and determine the structural behaviour of composite “UHPFRC-concrete” elements through 15 full-scale beam bending tests. The material tests focus on UHPFRC early age behaviour and on the determination of its outstanding tensile properties with an original uniaxial tensile test. They show that the *UHPFRC properties become virtually constant after 90 days*. The time-dependent behaviour of the composite beams is investigated during 11 weeks starting from the casting of the UHPFRC layer. After these long-term tests, the beams are subjected to bending until failure with the UHPFRC layer in tension. The parameters are the thickness of the UHPFRC layer, the presence of rebar in the UHPFRC and the static system.

The *time-dependent behaviour* of composite “UHPFRC-concrete” members is investigated focusing on early age by means of test results and an existing numerical model. Using the results of the material tests as input, the numerical model is able to predict the behaviour of composite “UHPFRC-concrete” elements with the exception of self-desiccation of the UHPFRC. However, the deformations of composite “UHPFRC-concrete” members are correctly modelled by introducing autogenous shrinkage directly as volumetric deformation in the model.

The *structural response* of the composite members under bending with the UHPFRC layer in tension is investigated with an original analytical model, which is an extension of the classical bending model for reinforced concrete. The influences of cross-section geometry, the UHPFRC tensile properties, the compressive strength of the substrate and the type of reinforcement are studied.

This study demonstrates that the use of *UHPFRC enhances the performance of composite “UHPFRC-concrete” elements in terms of resistance and stiffness*. Furthermore, *durability* is extended due to the low permeability and tensile strain hardening properties of UHPFRC. The *incorporation of rebar in the UHPFRC layer* leads to a further increase in resistance and stiffness of the composite element and to a higher apparent magnitude of hardening in the UHPFRC. The investigated composite elements show *monolithic behaviour* under service conditions. The time-dependent behaviour is mainly controlled by *autogenous shrinkage* of the UHPFRC, which may induce a few evenly distributed small-width macrocracks in the case of statically indeterminate systems, thin UHPFRC layers ( $\leq 1$  cm) or high magnitudes of autogenous shrinkage ( $\geq 750$   $\mu\text{m/m}$  at 28 days). The results show that the magnitude of autogenous shrinkage should not exceed 1000  $\mu\text{m/m}$  (at 28 days) in order to avoid debonding and extensive formation of distributed macrocracks.

Finally, three *basic composite “UHPFRC-concrete” element configurations* are proposed: *Configuration P* is designed for the protection function and consists of a thin UHPFRC layer. *Configuration PR* is proposed for existing elements with strongly deteriorated rebar and for new construction. It consists of an UHPFRC layer with reinforcement, and assumes no reinforcement in the concrete layer near the interface zone. *Configuration R* is proposed for existing structures requiring an enhancement of the structural behaviour. It is made of an UHPFRC layer with reinforcement, and assumes that there is reinforcement in the concrete layer near the interface zone.

## Version abrégée

Les *bétons fibrés ultra-performants (BFUP)* ont des résistances mécaniques élevées ( $f_{U,c} > 150$  MPa,  $f_{U,t} > 6$  MPa), un comportement ductile en traction uniaxiale ainsi qu'une très faible perméabilité qui leur permet de réduire la pénétration des substances agressives. Dans les éléments composés de béton armé ordinaire et de matériaux cimentaires avancés (MCA), les BFUP présentent un grand potentiel du point de vue de la capacité portante et de la protection des armatures des structures existantes.

L'*objectif* de cette étude est la détermination du comportement structural des éléments composés formés de béton armé ordinaire et de BFUP soumis à la flexion. Pour cela, les connaissances des propriétés des BFUP sont élargies et des modèles sont développés pour prédire le comportement structural des éléments composés. Finalement, des recommandations sont élaborées pour leur conception.

Des *essais* ont été effectués pour caractériser le BFUP et pour déterminer le comportement structural de 15 poutres composées soumises à la flexion. Les essais de caractérisation de matériau permettent de déterminer le comportement au jeune âge d'un BFUP et son comportement en traction avec un essai de traction uniaxiale original. Ils démontrent que *les propriétés de BFUP deviennent pratiquement constantes après 90 jours*. L'évolution du comportement des éléments composés est mesurée pendant 11 semaines, à partir du bétonnage de la couche supplémentaire de BFUP. Les poutres sont ensuite sollicitées en flexion jusqu'à leur rupture avec la couche de BFUP en traction. Les différents paramètres de l'étude sont l'épaisseur de la couche de BFUP, la présence des barres d'armature dans le BFUP et le système statique.

Le *comportement au jeune âge et à long terme* des éléments composés est étudié avec les résultats d'essais et un modèle numérique existant. Alimenté par les résultats d'essais sur les matériaux, le modèle est capable de prédire correctement le comportement des éléments composés en considérant le retrait endogène du BFUP, les déformations thermiques et le comportement viscoélastique.

La *réponse structurale des éléments composés* en flexion, pour laquelle la couche de BFUP est soumise à la traction, est étudiée avec un modèle analytique original, qui est une extension du modèle classique en flexion pour le béton armé. Les influences de la géométrie de la section, des propriétés en traction du BFUP, de la résistance à la compression du support et du type d'armature y sont présentées.

Les *résultats* de l'étude montrent que l'utilisation des BFUP *améliore la performance des éléments composés à l'égard de la résistance et de la rigidité*. En plus, leur *durabilité* est prolongée grâce à leur faible perméabilité et au comportement ductile en traction des BFUP. *L'incorporation des barres d'armature* conduit à une augmentation supplémentaire de la résistance et de la rigidité des éléments composés et à l'allongement apparent de la phase d'écroutissage du BFUP. Par ailleurs, les éléments composés étudiés montrent un *comportement monolithique* en conditions de service. Le comportement des éléments composés dans le temps est surtout contrôlé par le *retrait endogène* des BFUP et peut conduire à la formation de quelques microfissures distribuées avec des faibles ouvertures dans le cas où on a un système hyperstatique, des couches minces de BFUP ( $\leq 1$  cm) ou des valeurs élevées du retrait endogène ( $\geq 750$   $\mu\text{m/m}$  à 28 jours). Les résultats montrent que le retrait endogène ne devrait pas dépasser 1000  $\mu\text{m/m}$  (à 28 jours) afin d'éviter la délamination et une formation prononcée des microfissures distribuées.

Finalement, l'analyse du comportement structural des éléments composés de béton ordinaire et de BFUP a permis de déterminer *trois configurations de base* qui remplissent différentes fonctions: La *configuration P* est conçue pour la fonction de protection et est composée d'une couche mince en BFUP. La *configuration PR* est proposée pour des éléments existants avec des barres d'armature fortement détériorées ou pour de nouvelles constructions ; la section est formée d'une couche en BFUP renforcée avec des barres d'armature et aucune armature est située dans le support proche de la zone d'interface. La *configuration R* est proposée pour des structures existantes qui nécessitent une amélioration du comportement structural ; la section est constituée d'une couche en BFUP renforcée avec des barres d'armature et une armature localisée dans le support proche de la zone d'interface.

## Zusammenfassung

*Ultra-hochleistungsfähige Faserbetone (UHLFB)* haben hohe mechanische Festigkeiten ( $f_{U,c} > 150$  MPa,  $f_{U,t} > 6$  MPa) und zeigen verfestigendes Verhalten unter Zugbeanspruchung. Die sehr geringe Permeabilität begrenzt oder verhindert sogar das Eindringen schädlicher Substanzen. In Verbundbauteilen, bestehend aus traditionellem Stahlbeton und hochleistungsfähigen zementösen Werkstoffen (HZW) bieten UHLFB ein großes Potential im Bezug auf die Trag- und Schutzfunktion der HZW-Schicht.

Das generelle *Ziel* dieser Arbeit ist, die Leistungsfähigkeit und das Tragverhalten von “UHLFB-Beton” Verbundbauteilen unter Biegebelastung zu bestimmen. Dazu muss der Kenntnisstand über UHLFB erweitert werden, und Modelle müssen zur Verfügung gestellt werden, mit denen das Tragverhalten derartiger Verbundbauteile vorhergesagt werden kann. Die Untersuchungen münden in Empfehlungen zum Entwurf von “UHLFB-Beton” Verbundbauteilen.

Die Werkstoffeigenschaften von UHLFB und das Tragverhalten von 15 großen “UHLFB-Beton” Verbund-Biegebalken werden *experimentell* untersucht. Die Schwerpunkte der Werkstoffversuche liegen in der Bestimmung der UHLFB-Eigenschaften in jungem Alter und des UHLFB-Zugverhaltens mit einem neuartigen einachsigen Zugversuch. Die Versuche zeigen, dass die *UHLFB-Eigenschaften nach 90 Tagen praktisch konstant bleiben*. Das zeitabhängige Verhalten der Verbundbalken wird während 11 Wochen untersucht, beginnend mit dem Betonieren der UHLFB-Schicht. Anschließend werden die Balken unter Biegung bis zum Bruch belastet. Dabei befindet sich die UHLFB-Schicht unter Zug. Parameter der Bauteilversuche sind die Dicke der UHLFB-Schicht, das Vorhandensein von Bewehrung in der UHLFB-Schicht und das statische System.

Das *zeitabhängige Verhalten* von “UHLFB-Beton” Verbundbauteilen wird anhand der Versuche und eines bestehenden numerischen Modells untersucht. Die Betrachtungen konzentrieren sich auf das junge Alter. Das Modell verwendet die Versuchsergebnisse aus den Werkstoffversuchen als Eingabewerte und ist in der Lage, das Verhalten von “UHLFB-Beton” Verbundbauteilen vorherzusagen mit Ausnahme der Selbstaustrocknung des UHLFB. Die Verformungen der “UHLFB-Beton” Verbundbauteile werden jedoch zutreffend modelliert, wenn autogenes Schwinden als volumetrische Verformung eingegeben wird.

Die *Tragwerksantwort* von Verbundbauteilen unter Biegebeanspruchung mit der UHLFB-Schicht unter Zug wird mit einem analytischen Modell bestimmt, welches eine Erweiterung des klassischen Biegemodells für Stahlbeton ist. Die Einflüsse der Querschnittsgeometrie, der Zugeigenschaften der UHLFB, der Druckfestigkeit des Betons des Untergrunds und die Art der Bewehrung werden untersucht.

Diese Arbeit zeigt, dass die *Leistungsfähigkeit von “UHLFB-Beton” Verbundbauteilen im Hinblick auf die Steifigkeit und das Tragvermögen durch die Verwendung von UHLFB gesteigert* wird. Zusätzlich wird die *Dauerhaftigkeit* verlängert infolge der geringen Permeabilität und des verfestigenden Zugverhaltens der UHLFB. *Bewehrungsstäbe in der UHLFB-Schicht* führen zu einer weiteren deutlichen Steigerung des Tragvermögens und der Steifigkeit und zu einem scheinbar größeren verfestigenden Bereich. Die untersuchten Verbundbauteile zeigen *monolithisches Verhalten* unter Gebrauchslasten. Das zeitabhängige Verhalten wird hauptsächlich von *autogenem Schwinden* des UHLFB bestimmt. Einige wenige verteilte Makrorisse mit kleinen Rissöffnungen können in der UHLFB-Schicht entstehen im Fall von statisch unbestimmten Systemen, in dünnen ( $\leq 1$  cm) UHLFB-Schichten oder bei hohem autogenem Schwinden ( $\geq 750$   $\mu\text{m/m}$  nach 28 Tagen). Letzteres sollte 1000  $\mu\text{m/m}$  (nach 28 Tagen) nicht überschreiten.

Schließlich werden *drei grundlegenden Konfigurationen* für “UHLFB-Beton” Verbundbauteile vorgeschlagen: *Konfiguration P* ist für die Schutzfunktion konzipiert und besteht aus einer dünnen UHLFB-Schicht. *Konfiguration PR* wird für bestehende Bauteile mit stark beschädigter Bewehrung und für Neubauten vorgeschlagen. Der Querschnitt besteht aus einer UHLFB-Schicht mit Bewehrung und es befindet sich keine Bewehrung im Untergrund nahe der Grenzschicht. *Konfiguration R* setzt sich aus einer bewehrten UHLFB und einem bewehrten Untergrund zusammen und sollte in bestehenden Bauteilen angewendet werden, wenn eine Steigerung des Tragverhaltens gefordert ist.



## Acknowledgements

This research project was carried out at the Laboratory for Maintenance and Safety of Structures (MCS) in the School of Architecture, Civil and Environmental Engineering at the Swiss Federal Institute of Technology in Lausanne (EPFL). It was funded by the Swiss Federal Office of Education and Science within the scope of the European Research Project: Sustainable and Advanced Materials for Road InfraStructure (SAMARIS)

First of all, I would like to thank my thesis director Prof. Dr. Eugen Brühwiler for having given me the opportunity to work on this research project, for the freedom he gave me to realize my ideas, for the rich discussions, for his guidance and for creating an excellent work environment at MCS. I would also like to thank Dr. Emmanuel Denarié for following this research project, for his suggestions and advice and for sharing with me his detailed knowledge in concrete science. This research project is a continuation of the work of Dr. Olivier Bernard on composite normal strength concrete elements. I would like to thank him for our discussions, which helped me to define my subject, and for his help with the experimental program.

I wish to express my thanks to the thesis defence committee for the time and effort which they put into reading and judging the thesis and for their valuable comments: Prof. Dr. Karen Scrivener (LMC, EPFL), Dr. Emmanuel Denarié (MCS, EPFL), Prof. Dr. Peter Marti (IBK, ETHZ), Dr. Pierre Rossi (LCPC, France) and the president of the jury: Prof. Dr. Manfred Hirt (ICOM, EPFL). I would also like to thank Dr. Pierre Rossi for his guidance and his help with UHPFRC and UHPFRC technology. I also thank Prof. Dr. Bruno Massicotte (Ecole Polytechnique de Montréal, Canada) for his advice and Dr. Pierino Lestuzzi (IMAC, EPFL) for his help with the example in Chapter 6.

Much of the experimental program of this thesis could not have been conducted without the help of the technicians and engineers of our laboratory: First of all, I would like to express my sincere gratitude to Roland Gysler who helped me enormously with all the experimental work. He made much of the experimental program possible with his great experience, availability and patience. I would also like to thank Sylvain Demierre for his advice and help with the measuring devices and Gilbert Pidoux, Hansjakob Reist and François Perrin for their help. In this context, I would also express my thanks to Philippe Simonin, Philippe Vulliemin, Minh Dai Vuong, Michel Dizerens and Dr. Yves Houst from the institute of materials at the EPFL for their advice and help with the materials testing. Early age restrained and free shrinkage tests were conducted on UHPFRC at the university LAVAL in Québec, Canada, by the team of Prof. Jacques Marchand, in particular by Dr. Bruno Zuber, Fabien Perez and Mohamed Bouh-lel. Thanks to you and all the team for the opportunity to do this testing, for the execution of the tests and for the warm welcome during my two-week stay. Moreover, I would also like to thank Prof. Dr. Benoit Bissonnette for the discussions and advice about composite elements and creep.

I would like to thank my colleagues at MCS and IS for their friendship, their help and their cooperation. First of all, I would like to mention David Conciatori with whom I have been sharing an office for the past three years. Many thanks for your help during the last years at work, for all the discussions we had and for all the time we have spent together in the mountains, in Lausanne, in Munich... By the way, I greatly appreciated learning Valaisan French to refine my “German” French. I would also like to thank our postdoc: Prof. Dr. Jean-Philippe Charron for his advice and our discussions with respect to my research project, Christine Benoit-Roulin for all the small things she did for me that made life better and much easier, Marco Viviani for his help with SOFO and the discussions about early age concrete and Scott Walbridge for his last minute English corrections and Dr. Yvan Robert-Nicoud for the French summary. Finally, several persons casted the specimens with me - thanks to John Wuest, Michael Maître and Damien Metry. I greatly appreciated the last years not only for the good work environment, but also for all the spare time activities... Thanks to all the present and former employees of MCS in particular to the above mentioned and to Dr. Bryan Adey, Dr. Hannes Ludescher and Sacha Antille for the great times we had.

Life has not only consisted of work these last few years. I wish to express my sincerest thanks to all my friends within and outside the EPFL for your support and all the time we spent together. Special thanks go to my handball and field hockey teams. Finally, I would like to thank my family for their unconditional support, encouragement and help.



## Glossary

### *Actions (Einwirkungen, actions)*

Mechanical (loads, forces), other physical (temperature, humidity), chemical (salts, acids and alkaline substances, organic compounds) and biological (bacteria, insects, fungi, algae) actions on the structure resulting from the execution and use as well as from environmental influences [SIA260].

### *Composite structural member (Verbundbauteil, élément de structure composé)*

Structural member that consists of several materials which are mechanically connected over an extensive part of their contact surface.

### *Conservation (Erhaltung, conservation)*

All the activities and measures undertaken to ensure the continued existence of a construction works, including its material and non material values [SIA260]

### *Debonding (Ablösung, délamination)*

Crack in the interface zone of a composite element in direction of the interface that alters the structural response.

### *Deformation capacity (Verformungsvermögen, capacité de déformation)*

Ability of a structure and its members to be deformed up to failure, elastically and in general also plastically [SIA260].

### *Design service life (geplante Nutzungsdauer, durée de service prévue)*

Planned period of use [SIA260].

### *Discrete crack (Einzelriss, fissure discrète)*

Crack that is defined by two planes in models.

### *Distributed macrocracks (verteilte Makrorisse, macrofissures réparties)*

Macrocracks of small widths ( $< 0.1$  mm) in the UHPFRC that form during the hardening domain.

### *Ductility (Duktilität, ductilité)*

(Plastic) deformation capacity characterised by irreversible deformations and energy dissipation, usually related to the limit of the elastic behaviour [SIA 260].

### *Durability (Dauerhaftigkeit, durabilité)*

Structures are durable when they meet the requirements of serviceability and structural safety throughout their design service life according to the planned use without unforeseen maintenance (adapted from [SIA260]).

### *Failure (Versagen, défaillance)*

Exceeding of limit states as a result of fracture or due to time-dependent actions (adapted from [SIA260]).

### *First cracking strength (Festigkeit bei Erstrissbildung, résistance de première fissuration)*

Tensile strength of the material characterizing the end of the quasi-linear domain and the beginning of the hardening domain in UHPFRC [Naaman02].

### *Fracture (Bruch, rupture)*

Breaking of the material structure [Sigrist95].

*Hardening (Verfestigung, écrouissage)*

Property of a material, structural member or a structure to have an increasing resistance with increasing deformations beyond the elastic domain [Pfy103].

*Improvement (Veränderung, modification)*

Intervention into a structure in order to adapt it to modified new requirements [SIA469].

*Interface crack (Riss in der Grenzschicht, fissure d'interface)*

Crack in the interface zone of a composite element in direction of the interface that does not alter the structural response.

*Interface zone (Grenzschicht, zone d'interface)*

Zone of the substrate in the composite element that may be partly microcracked due to surface preparation and the roughness of the interface.

*Length of the plastic hinge (Länge des plastischen Gelenks, longueur de la rotule plastique)*

Length over which the concentrated deformations of a plastic hinge are distributed.

*Localized macrocrack (lokalisierter Makroriss, macrofissure localisée)*

Macrocrack in the UHPFRC that forms at the end of the hardening domain.

*Macrocrack (Makroriss, macrofissure)*

Crack in a cementitious material ( $> 40$  to  $50 \mu\text{m}$ ) that is visible with the naked eye.

*Magnitude of hardening (Größe des verfestigenden Bereichs, étendue du domaine écrouissant)*

Deformation characterizing the hardening domain of UHPFRC ( $\epsilon_{U,\text{hard}} = \epsilon_{U_t,\text{max}} - \epsilon_{U_t,1\text{st}}$ ).

*Microcrack (Mikroriss, microfissure)*

Fine crack in a cementitious material ( $< 40$  to  $50 \mu\text{m}$ ).

*Normal strength concrete (NSC) (normalfester Beton, béton ordinaire)*

Conventional concrete with a compressive strength lower than 60 MPa and a fracture energy of approximately  $G_F = 150 \text{ J/m}^2$ .

*Plastic hinge (plastisches Gelenk, rotule plastique)*

Zone of the structural member in which plastic deformations occur.

*Preexisting microcrack (bereits existierender Mikroriss, microfissure préexistante)*

Microcracks that are formed prior to fracture tests of the material.

*Real crack (wirklicher Riss, fissure réelle)*

Crack through which no tensile stresses are transferred [Hillerborg83].

*Rehabilitation (Instandsetzung, remise en état)*

Re-establishment of the safety and the serviceability during a defined time span [SIA469].

*Reinforcement in the UHPFRC layer (Bewehrung in der UHLFB-Schicht, armature dans la couche en BFUP)*

Rebars or other additional reinforcement that is placed in the UHPFRC. The fibres of the UHPFRC are seen as part of the UHPFRC and are not included in the term “reinforcement”.



*Reliability (Zuverlässigkeit, fiabilité)*

Ability of a structure or a structural member to fulfil the specified requirements, including the design service life. Reliability is usually expressed in probabilistic terms [EC01].

In general, a probabilistically formulated measure for fulfilling the requirements of structural safety and serviceability [SIA260].

*Resistance (Tragfähigkeit, résistance)*

Capacity of a member or component, or a cross-section of a member or component of a structure to withstand actions without mechanical failure e.g. bending resistance, buckling resistance, tension resistance [EC01].

Ability of a structure and its members to withstand actions during execution and use [SIA260].

*Serviceability (Gebrauchstauglichkeit, aptitude au service)*

Ability of a structure and its members to ensure functionality and appearance of the construction works as well as the user comfort, in accordance with serviceability limits [SIA260].

*Serviceability limit (Gebrauchsgrenze, limite de service)*

Specified limit of serviceability [SIA260].

*Serviceability limit state (SLS) (Grenzzustand der Gebrauchstauglichkeit, état limite de service)*

States that correspond to conditions beyond which specified service requirements for a structure of structural member are no longer met [EC01].

State when a serviceability limit is reached [SIA260].

*Softening (Entfestigung, adoucissement)*

Fracture process that is characterized by the reduction of resistance and localization of deformations in the fracture zone under imposed deformations [Pfy103].

*Structural response (Tragwerksantwort, réponse structural)*

Deformations and stresses in a structural member that is submitted to actions.

*Structural safety (Tragsicherheit, sécurité structurale)*

Ability of a structure and its members to guarantee the overall stability as well as an adequate ultimate resistance (including fatigue resistance), corresponding to the assumed actions and the required reliability [SIA260].

*Substrate (Untergrund, support)*

Reinforced concrete layer of composite “UHPRFC-concrete” elements.

*Transverse crack (Trennriss, fissure traversante)*

Crack that crosses the entire (UHPRFC) layer.

*Ultimate limit state (ULS) (Grenzzustand der Tragsicherheit, état limite ultime)*

State associated with collapse or with other similar form of structural failure [EC01].

State at which the limit of structural safety is reached [SIA260].

*Tensile strength (Zugfestigkeit, résistance à la traction)*

Maximum strength in uniaxial tension, i.e. for UHPFRC the strength at the end of the hardening domain.

*Ultimate resistance (Tragwiderstand, résistance ultime)*

Limit of resistance [SIA260].

*Ultra-high performance fibre-reinforced concrete (UHPFRC) (béton fibré ultra--performant (BFUP), ultra-hochleistungsfähiger Faserbeton (UHLFB))*

Cementitious fibre-reinforced material that is characterized by a strain hardening domain in uniaxial tension and by very low permeability.

# Symbols

## Latin lower case symbols

$a$	parameter of the SCM model
$a_1$	parameter of the model of Mensi
$a_2$	parameter of the model of Mensi
$a_c$	parameter of the maturity model
$a_{cc}$	lever arm of the concrete in compression
$a_{ct}$	lever arm of the concrete in tension
$a_d$	parameter of the Danish model
$a_h$	parameter of the model of Bazant
$a_T$	parameter of the model for non-linear viscoelasticity
$a_U$	lever arm of the UHPFRC
$b$	width
$b_c$	parameter of the maturity model
$b_d$	parameter of the Danish model
$c$	cover of rebar in the UHPFRC layer
$c_T$	parameter of the model for non-linear viscoelasticity
$c_T$	thermal capacity
$d$	parameter of the SCM model
$d_{s,cc}$	distance form extreme compression fibre to the centroid of the reinforcement in the concrete in compression
$d_{s,ct}$	distance form extreme compression fibre to the centroid of the reinforcement in the concrete in tension
$d_{s,U}$	distance form extreme compression fibre to the centroid of the reinforcement in the UHPFRC in tension
$f_{cc}$	strength of concrete in compression
$f_{ct}$	strength of concrete in tension
$f_{su}$	maximum strength of reinforcement
$f_{sy}$	yield strength of reinforcement
$f_{Uc}$	strength of UHPFRC in compression
$f_{Ut}$	strength of UHPFRC in tension
$f_{Ut,1st}$	first cracking strength of UHPFRC
$f_{Ut,max}$	tensile strength of UHPFRC
$h$	relative humidity
$h_c$	transition point of the relative humidity between moisture transport in liquid and gas phase in the model of Bazant
$h_c$	thickness of the concrete layer
$h_e$	external relative humidity
$h_{hydr}$	reduction of the relative humidity due to self-desiccation
$h_{tot}$	thickness of the composite element
$h_U$	thickness of the UHPFRC layer
$h_{U,thr}$	threshold of thickness for an increase in resistance in composite elements of type P

$k_T$	coefficient of air permeability
$l$	length
$l_f$	fibre length
$l_i$	length of the interface crack
$n$	parameter of the softening model of concrete
$n_{sec}$	parameter of the model of concrete in compression
$q$	temperature flux, moisture flux
$r_{\sigma T}$	parameter of the model of thermal transitional creep
$t$	time
$t_0$	initial time
$w^*$	crack width before unloading (definition of damage in the numerical model)
$w_i$	width of the interface crack
$w_{res}$	residual crack width (definition of damage in the numerical model)
$w_{Ut}$	width of a crack in the UHPFRC
$w_{Ut,1}$	parameter of the softening model of UHPFRC
$w_{Ut,2}$	parameter of the softening model of UHPFRC
$x$	depth of the compression zone

### Latin upper case symbols

$A_{s,cc}$	section of the reinforcement in the UHPFRC layer in compression
$A_{s,ct}$	section of the reinforcement in the concrete layer in tension
$A_{s,U}$	section of the reinforcement in the UHPFRC layer in tension
$D$	diffusion coefficient; damage as defined in the numerical model
$D_0$	diffusion coefficient in saturated state (model of Bazant)
$E_{c,sec}$	secant modulus of concrete in compression
$E_s$	modulus of elasticity of the rebars
$E_{s,c}$	modulus of elasticity of the rebars in the concrete layer
$E_{s,hard}$	hardening modulus of the rebars
$E_{s,U}$	modulus of elasticity of the rebars in the UHPFRC layer
$E_{U,hard}$	hardening modulus of the UHPFRC
$E_{Uc}$	modulus of elasticity of the UHPFRC in compression
$E_{Ut}$	modulus of elasticity of the UHPFRC in tension
$F_{cc}$	force of concrete in compression
$F_{ct}$	force of concrete in tension
$F_{s,cc}$	force of the reinforcement in the concrete layer in compression
$F_{s,ct}$	force of the reinforcement in the concrete layer in tension
$F_{s,U}$	force of the reinforcement in the UHPFRC layer in tension
$F_{Ut}$	force of UHPFRC in tension
$G_F$	fracture energy
$H_{hydr}$	liberated heat of hydration (at time $t$ )
$H_T$	total amount of heat of hydration
$J$	creep compliance

$L_{hi}$	length of the plastic hinge
$L_R$	reference length
$L_{R\text{“hi”}}$	reference length referred to a hinge
$L_{R\text{“span”}}$	reference length referred to a span
$M$	bending moment; maturity
$M_{cc}$	moment of concrete in compression
$M_{ct}$	moment of concrete in tension
$M_{pl}$	plastic moment
$M_{s,cc}$	moment of the reinforcement in concrete in compression
$M_{s,ct}$	moment of the reinforcement in concrete in tension
$M_{s,U}$	moment of the reinforcement in UHPFRC in tension
$M_{Ut}$	moment of UHPFRC in tension
$N$	normal force
$Q$	activation energy
$R$	universal gas constant
$T$	temperature
$T_e$	external temperature
$T_{ref}$	reference temperature

### Greek symbols

$\alpha$	factor defining the residual crack width $w^*$
$\alpha_h$	hygral dilation coefficient
$\alpha_T$	thermal dilation coefficient
$\epsilon$	deformation
$\epsilon_{c,upp}$	deformation in the extreme fibre of the concrete in compression
$\epsilon_{cc}$	deformation of the concrete in compression
$\epsilon_{ct}$	deformation of the concrete in tension
$\epsilon_h$	hygral deformation
$\epsilon_{int}$	deformation at the interface
$\epsilon_{limit}$	limit of deformation
$\epsilon_s$	deformation in the reinforcement
$\epsilon_{s,cc}$	deformation of the reinforcement in the concrete in compression
$\epsilon_{s,ct}$	deformation of the reinforcement in the concrete in tension
$\epsilon_{s,U}$	deformation of the reinforcement in the UHPFRC
$\epsilon_{su}$	deformation at the maximum force in the reinforcement
$\epsilon_{sy}$	deformation at yielding of the reinforcement
$\epsilon_T$	thermal deformation
$\epsilon_{U,hard}$	magnitude of hardening of the UHPFRC
$\epsilon_{U,l}$	deformation in the extreme fibre of the UHPFRC in tension
$\epsilon_{Uc}$	deformation of the UHPFRC in compression
$\epsilon_{Uc,u}$	deformation of the UHPFRC in compression at the maximum force
$\epsilon_{Uc,y}$	deformation of the UHPFRC in compression at the limit of elasticity
$\epsilon_{Ut}$	deformation of the UHPFRC in tension

$\varepsilon_{Ut,1st}$	deformation at the first cracking strength of UHPFRC
$\varepsilon_{Ut,max}$	deformation at the tensile strength of UHPFRC
$\kappa$	curvature
$\kappa_{pl}$	curvature in a plastic hinge
$\lambda_T$	thermal diffusivity
$\nu$	Poisson's ratio
$\pi_h$	hygral transfer coefficient
$\pi_T$	thermal transfer coefficient
$\rho_{s,cc}$	ratio of the reinforcement in the concrete layer in compression
$\rho_{s,ct}$	ratio of the reinforcement in the concrete layer in tension
$\rho_{s,U}$	ratio of the reinforcement in the UHPFRC layer in tension
$\sigma$	stress
$\sigma_1$	parameter of the softening diagram of UHPFRC
$\sigma_{c,upp}$	stress in the upper fibre of the concrete in compression
$\sigma_{cc}$	stress of the concrete in compression
$\sigma_{ct}$	stress of the concrete in tension
$\sigma^i$	stress in the i-th Maxwell chain (Maxwell chain model)
$\sigma_{int}$	stress at the interface
$\sigma_s$	stress in reinforcement
$\sigma_{s,cc}$	stress in the reinforcement in the concrete in compression
$\sigma_{s,ct}$	stress in the reinforcement in the concrete in tension
$\sigma_{s,U}$	stress in the reinforcement in the UHPFRC
$\sigma_{U,l}$	stress in the extreme fibre of the UHPFRC in tension
$\sigma_{Uc}$	stress of the UHPFRC in compression
$\sigma_{Ut}$	stress of the UHPFRC in tension
$\tau$	retardation time (Maxwell chain model)
$\emptyset$	rebar diameter

### Abbreviations

AS	autogenous shrinkage
CMOD	crack mouth opening displacement
EMH	exploitation of the magnitude of hardening
f1...f7	beam deflections
ODS	optical deformation sensor
RC	reinforced concrete
RH	relative humidity
TC	thermocouple
UHPFRC	ultra-high performance fibre reinforced concrete

# 1 Introduction

## 1.1 Context and motivation

*Composite structures* consist of several building materials that work together in a monolithic way. They are widely used in constructions as for example in bridges. The most common composite structures are “steel-reinforced concrete” structures, but nearly all combinations of building materials exist in modern constructions such as “glass-steel”, “composites-steel” or “timber-reinforced concrete”. This study deals with composite structures of two types of reinforced cementitious materials, in particular of composite materials consisting of Advanced Cementitious Materials (ACM) and reinforced normal strength concrete (NSC).

*Composite “ACM-NSC” elements* are appropriate for new constructions and conservation of existing structures. Advanced cementitious materials are generally used in parts of the structures that are exposed to detrimental substances or that have to transfer high mechanical loads, for example at points of concentrated load introduction or when an existing structure has to be strengthened without increasing the dead load.

The *goals of conservation projects* are either rehabilitation or improvement of existing structures. Rehabilitation is the re-establishment of the structural performance; improvement means that the structural response in terms of resistance and stiffness is enhanced for example to sustain higher traffic loads or to widen bridges for the addition of traffic lanes. In both cases, sufficient durability<sup>1</sup> should be guaranteed. Durability may be reduced by deterioration processes such as corrosion due to chloride ingress. Consequently, the structural elements need a sufficient resistance against these processes.

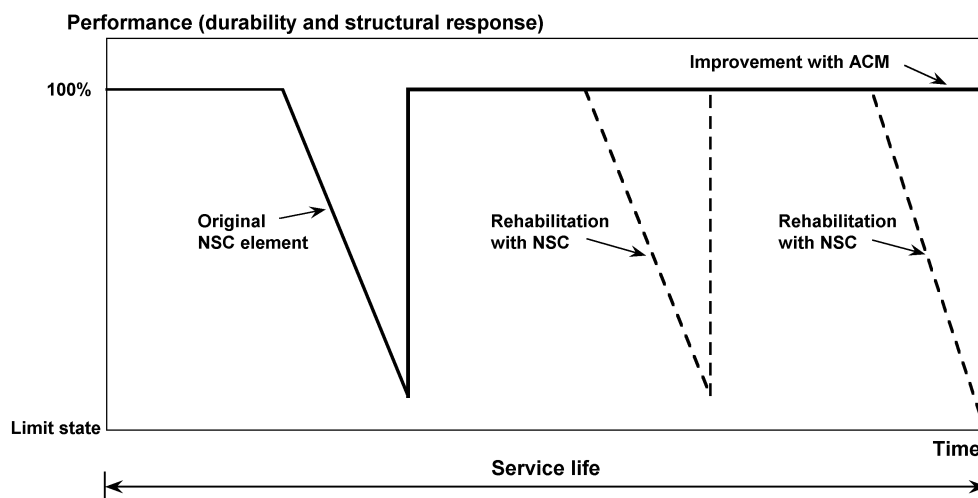


FIGURE 1.1: Conceptual illustration of the improvement of the performance of structural elements containing ACM, compared to rehabilitation with NSC

The *performance of a structure* during service life is schematically described in Figure 1.1 for the case of rehabilitation with advanced cementitious materials and for rehabilitation with normal strength concrete in comparison. The performance of the structure remains at 100% over a certain time period (initiation phase), i.e. the structural behaviour is as aimed during design. Then, deterioration processes start to significantly reduce the performance (propagation phase). When the performance approaches a limit state during service life, the structure must be modified either by rehabilitation or by improvement

1. Durability is defined to be the time span during which the requirements of serviceability and structural safety are met without unplanned maintenance.

if necessary. In some cases, the initial performance may be reduced in terms of stiffness and permeability due to residual stress development at early age which may induce microcracks [Bernard00].

The targeted use of high performance materials like ACM in new structures or conservation projects leads to enhanced performance and durability. Advanced cementitious materials such as *Ultra-High Performance Fibre Reinforced Concretes* (UHPFRC) are promising in structures. UHPFRC belong to the group of High Performance Fibre Reinforced Cement Composites (HPFRCC) (Figure 1.2). HPFRCC are Fibre Reinforced Concretes (FRC) that exhibit strain-hardening under uniaxial tension. In addition, UHPFRC are characterized by a dense matrix and have consequently a very low permeability when compared to HPFRCC and normal strength concretes.

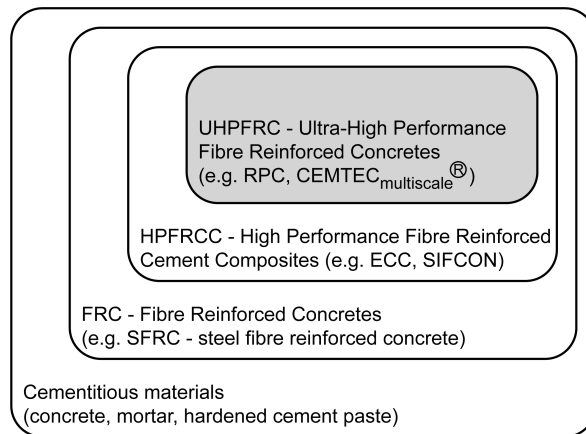


FIGURE 1.2: Definition of UHPFRC

UHPFRC have exceptional material properties, however, their material costs are significantly higher than those of normal strength concretes. Therefore, it is proposed to combine normal strength concrete and UHPFRC in composite structures in order to exploit the advantages of the two materials in an optimal way: UHPFRC is used in the parts of the structure subjected to the attack of detrimental substances and/or where high strengths or stiffness are required; the other parts are made of normal strength reinforced concrete. This concept of composite “UHPFRC-concrete” structures can be applied to new structures and to conservation projects as mentioned before.

*Composite “UHPFRC-concrete” structures* are enhanced reinforced concrete structures. Their field of application is illustrated by the example of a road bridge deck (Figure 1.3): crash barrier and deck overlay are made of UHPFRC (without water proofing membrane), while the rest is built of normal strength reinforced concrete. Crash barrier and deck overlay are exposed to detrimental substances (e.g. de-icing salts containing chlorides) and require a high resistance against the ingress of these substances in order to guarantee sufficient durability. Moreover, the crash barrier is a massive element with a high cracking risk at early age. The dimensions of the crash barrier and early age cracking risk are reduced due to the outstanding mechanical properties of UHPFRC in terms of resistance and energy dissipation.

The behaviour of *composite Reinforced Concrete (RC) members*, i.e. structural members consisting of two layers of normal strength reinforced concrete has been extensively studied and conditions have been defined to avoid transverse cracking and debonding (e.g. [Bernard00, Granju01, Saucier90]). However, the relatively high permeability of normal strength concrete when compared to UHPFRC leads to ingress of detrimental substances in shorter time spans. Moreover, the strengths of normal strength concrete may not be sufficient at points of concentrated load introduction or when the resistance of the structural element must be increased without increasing its dead load. Therefore, it has to be investigated whether the outstanding properties of UHPFRC are used in a beneficial way in composite “UHPFRC-concrete” elements in terms of durability and structural response.

Until now, *UHPFRC have only been used for new pre-cast structures*, for example for footbridges and prestressed beams for a nuclear power plant [Cheyreyzy97, Behloul03]. The high material cost of



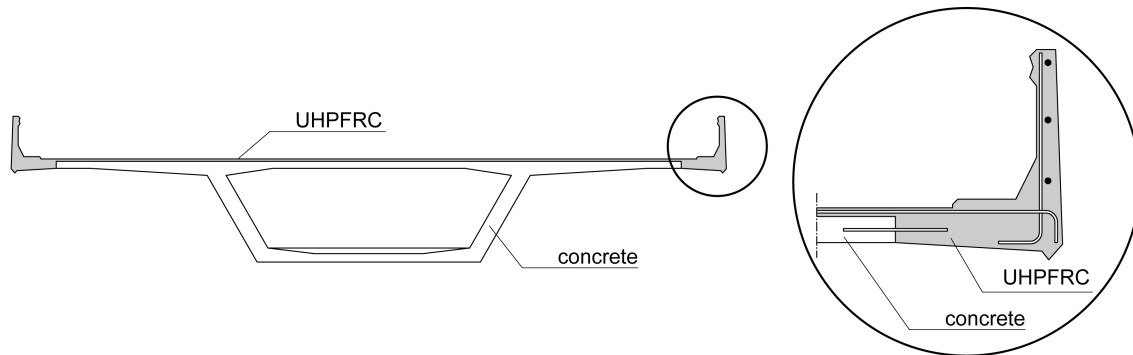


FIGURE 1.3: Composite “UHPFRC-concrete” bridge deck

UHPFRC leads to the question whether structures that are entirely made of UHPFRC are economic or whether it is better to use UHPFRC only in the parts of the structure where their advantageous material properties are exploited. In any case, the enhanced material properties of UHPFRC - mainly their very low permeability and the strain-hardening tensile behaviour - lead to the conclusion that the use of these materials in composite “UHPFRC-concrete” elements is promising.

The *design of composite “UHPFRC-concrete” elements requires research* in the following points: The material properties of UHPFRC, mainly the time-dependent behaviour and the tensile properties in structural members, have to be further studied in order to predict deformations, stresses and the structural response of the elements. Also the transport properties in sound and cracked UHPFRC have to be investigated. Furthermore, modelling of UHPFRC needs to be validated and improved. Composite “UHPFRC-concrete” elements are a new type of construction and their feasibility and structural response have to be investigated.

## 1.2 Concepts for composite elements consisting of reinforced cementitious materials

**Terminology.** Typical composite slabs or beams consisting of reinforced cementitious materials are composed of a reinforced old concrete layer (*substrate*) and a *new layer* (Figure 1.4). The new layer is either thin (< 5 cm) for rehabilitation or thicker ( $\approx$  5 to 15 cm) for improvement (increase in resistance). Rebar may be incorporated in the new layer in order to increase resistance and control cracking.

In general, the *contact surface* of the substrate is treated with a surface preparation method to obtain a rough contact surface. Damage may be induced in form of microcracking into the substrate during surface preparation. In this study, the *interface zone* is defined as the zone of the substrate that may be microcracked due to the surface preparation method and the roughness of the interface. In case of a rebar layer in the substrate close to the interface, the interface zone comprises the rebar. The interface zone has often a smaller tensile strength than the substrate and the new layer.

In this study, horizontal cracks in the interface zone that do not alter the structural response of the composite member (*monolithic behaviour*) are called *interface cracks*. If the cracks alter the structural response, they are called *debonding*.

**Actions and failure modes.** Composite elements are subjected to internal deformations and to external actions. For composite members with an existing substrate (i.e. in rehabilitation projects), the internal deformations are mainly due to shrinkage and thermal effects caused by heat of hydration in the new layer. External actions are due to climatic variations and imposed loads or deformations.

*Residual stress* state and associated failure modes due to uniform shrinkage in the new layer are described in Figure 1.5. The substrate partially restrains the shrinkage deformations of the new layer and generates a residual stress state. At the free ends of the composite element, the stresses perpendicu-

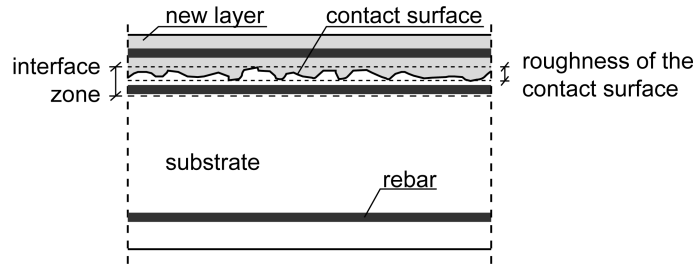


FIGURE 1.4: Definition of a composite member consisting of two different cementitious materials with reinforcement

lar to the interface ( $\sigma_y$ ) are high and may lead to debonding (Figure 1.5b, case 1) either at the contact surface (i) or in the interface zone in the substrate (ii). Debonding at the contact surface occurs when the adherence at the interface is low, debonding in the interface zone (in the substrate) occurs when the adherence between new layer and substrate is good. In case of transverse cracking, the elements show either monolithic behaviour with the cracks propagating straight into the substrate (case 2i) or there is debonding when the cracks penetrate to the interface (case 2ii). A two-dimensional stress state forms at crack tips and the stresses perpendicular to the interface may provoke debonding when the vertical cracks reach the interface zone [Bernard00].

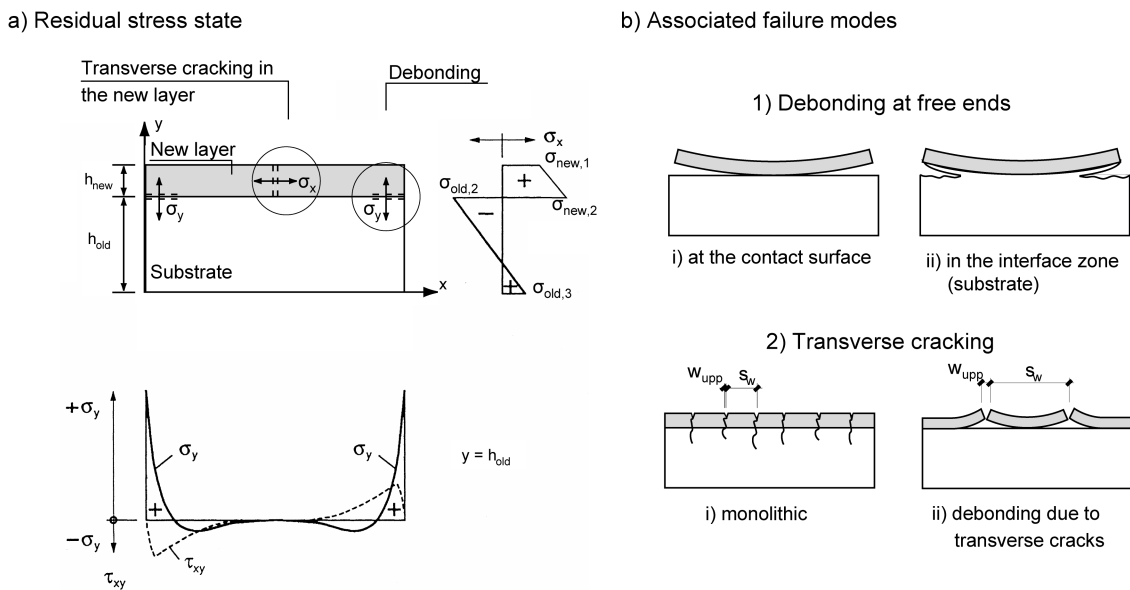


FIGURE 1.5: a) Residual stress state in a composite element after [Haardt91] and b) associated failure modes (from [Bernard00])

External actions induce additional stresses into the composite element. This additional stresses are superimposed to the stress state due to internal deformations.

### 1.3 Objectives

The present study aims to investigate performance and structural behaviour of composite “UHP-FRC-concrete” members and to provide a better knowledge of UHPFRC properties. More precisely, the following points are explored:

- A better knowledge of the structural behaviour of composite “UHPFRC-concrete” beams under bending is necessary under service conditions and at ultimate limit state in order to answer the following questions:
  - Is it possible to build composite “UHPFRC-concrete” elements with monolithic behaviour, and how can the advantageous UHPFRC properties be exploited in such composite elements?
  - How do deformations, stresses and cracking evolve in the composite members at early age and in the long-term?
  - What resistance and failure modes do the composite “UHPFRC-concrete” elements show under bending?
- UHPFRC properties must be better known and understood. Thus, the material properties are determined for the used UHPFRC with a focus on early age behaviour and tensile properties.
- Modelling tools are evaluated and developed in order to predict the behaviour of composite “UHPFRC-concrete” elements:
  - Are existing numerical models appropriate to simulate time-dependent UHPFRC behaviour and the structural response of composite “UHPFRC-concrete” elements?
  - What resistance and deformation capacity do composite “UHPFRC-concrete” elements have?

On the basis of the results, guidelines are developed for the design of composite “UHPFRC-concrete” members. Finally, configurations of efficient composite “UHPFRC-concrete” members are proposed.

## 1.4 Thesis structure

The thesis document consists of seven chapters as illustrated in Figure 1.6. Chapter 1 is the introduction. In Chapter 2, the state of the art is presented. Chapters 3 to 6 discuss the results of the experimental campaign, time-dependent behaviour, structural response and design of composite “UHPFRC-concrete” elements. The conclusions are presented in Chapter 7.

**Chapter 2.** In Chapter 2, the fundamentals for this thesis are presented. The focus is drawn to the early age behaviour of cementitious materials, to material properties of UHPFRC and to composite elements made of cementitious materials. Furthermore, the different scales of modelling and the structural response of concrete elements are discussed.

**Chapter 3.** In Chapter 3, the results of the experimental campaign are presented: tests are conducted to characterize the material properties of UHPFRC and to determine early age and long-term behaviour as well as the structural response of composite “UHPFRC-concrete” beams.

The material tests focus on early age behaviour and mechanical properties. An original uniaxial tensile test for UHPFRC is developed. On the basis of the tensile properties, different domains of UHPFRC cracking are defined. During the material characterization, all the determinant parameters for UHPFRC are determined in order to evaluate its structural behaviour in terms of deformation, i.e. the mechanical properties (tensile and compression behaviour) and time-dependent deformations. The concrete used in the composite “UHPFRC-concrete” members is also characterized.

The structural tests are conducted on full-size beams and are divided into two phases: In a first step, early age and long-term behaviour is investigated during 11 weeks under controlled climatic conditions; in a second step, the beams are subjected to 4-point-bending tests until their fracture. This allows to determine the structural performance of composite “UHPFRC-concrete” beams in terms of deformations due to internal deformations and externally imposed deformations.

**Chapter 4.** The time-dependent behaviour of composite “UHPFRC-concrete” members is investigated in Chapter 4. For this, a numerical model is used that considers couplings between thermal, hygral, chemical and mechanical properties for cementitious materials. Moreover, the modelling of UHPFRC on the basis of test results from Chapter 3 and the literature is discussed. It is shown that the existing

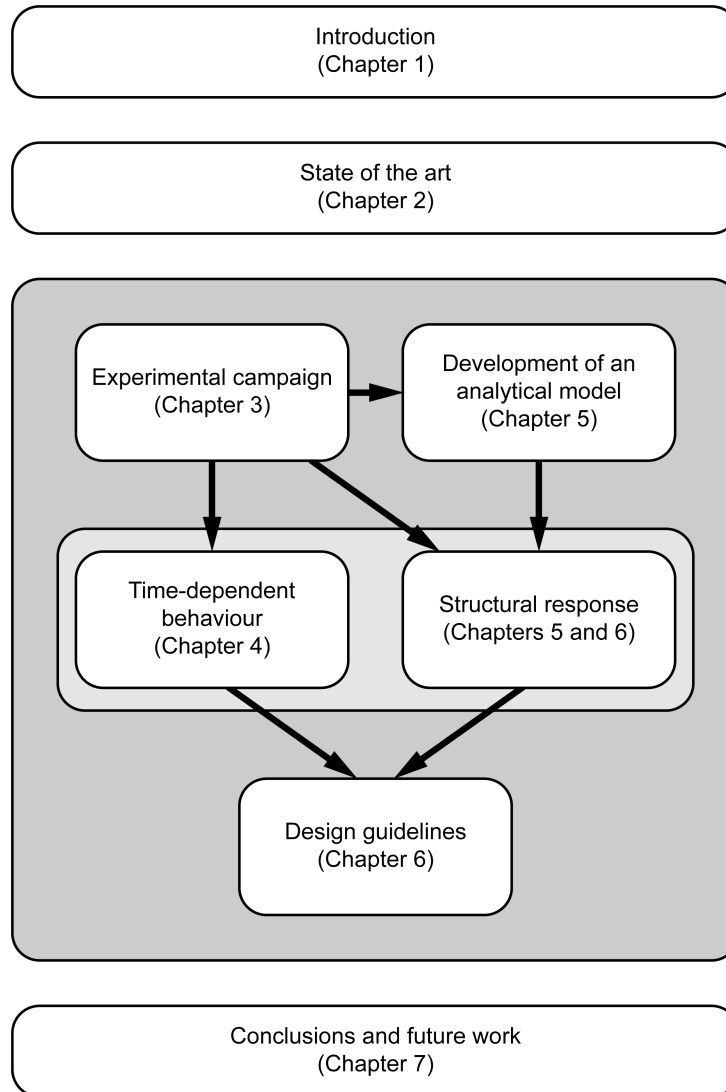


FIGURE 1.6: Thesis structure

numerical model is able to describe the time-dependent behaviour of UHPFRC. Viscoelasticity of UHPFRC is modelled at early age and long-term with an age-dependent generalized Maxwell chain model. Only self-desiccation is not modelled correctly. Also the mechanical model has to be adapted for UHPFRC tensile behaviour. The numerical model is validated by means of the results of the beam tests (Chapter 3). The time-dependent behaviour of composite “UHPFRC-concrete” members is investigated by means of the analysis of the beam tests and by a parametric study in order to evaluate the influence of structural parameters such as static system and beam geometry and UHPFRC properties such as autogenous shrinkage as well as tensile behaviour. The parameter EMH is introduced to characterize the exploitation of the magnitude of hardening in the UHPFRC.

**Chapter 5.** In Chapter 5, the structural response of composite “UHPFRC-concrete” members is determined with regard to resistance, stiffness and crack formation. For this, an analytical model and the experiments described in Chapter 3 are used. The original analytical model, developed in this chapter, is an extension of the cross-sectional bending model for reinforced concrete and considers the tensile behaviour of UHPFRC. It is validated with results from the literature. The structural response of composite “UHPFRC-concrete” beams is analysed by means of the model. Finally, the reference length  $L_R$ , necessary to transform crack width into equivalent deformation, and the length of plastic hinges  $L_{hi}$  are discussed.

**Chapter 6.** The design of composite “UHPRC-concrete” members is discussed in Chapter 6. The necessary verifications at SLS, ULS and to guarantee sufficient durability are presented. The determination of the ultimate load of a composite “UHPRC-concrete” beam in a statically determinate system is demonstrated in an example. Three basic configurations of composite “UHPRC-concrete” elements are proposed on the basis of the results of the previous chapters. They are designed as a function of the requirements on the structural member, i.e. it is distinguished between new construction and conservation projects (interventions for rehabilitation or improvement). The influence of structural and material parameters on the structural response is investigated in a parametric study with the analytical model from Chapter 5. On the basis of the results from Chapters 3 to 6, efficient geometries for the three basic configurations are determined.

**Chapter 7.** The thesis document ends with the conclusions and the recommendations for future work in Chapter 7.



## 2 State of the art

This chapter is limited to some aspects that are fundamental for the structural behaviour of composite “UHPFRC-concrete” members. It is not exhaustive and it focuses on UHPFRC properties and on composite “ACM-concrete” members.

In Section 2.1, the scales of concrete modelling are described. Sections 2.2 to 2.6 treat aspects of material and structural behaviour by going from material to structural level:

In Sections 2.2 and 2.3, the properties of cementitious materials in general and of UHPFRC on the material level are described. In Section 2.2, hydration and its effects, tensile behaviour and cracking, macroscopic deformations and viscoelasticity are discussed for cementitious materials. UHPFRC are discussed in detail in Section 2.3

The effects of rebar in cementitious materials are presented in Section 2.4 with a special regard to rebar in fibre reinforced materials and HPFRCC.

Sections 2.5 and 2.6 deal with the behaviour of structural elements: The deformation capacity of reinforced elements consisting of cementitious materials is important to evaluate the ULS and is treated in Section 2.5. Finally, findings of composite members made of cementitious materials are discussed in Section 2.6. Here, the focus is drawn to the notion of the degree of restraint and to composite “UHP-FRC-concrete” members.

### 2.1 Scales to describe the behaviour of reinforced cementitious materials

The behaviour of reinforced concrete can be described at three material and one structural level as shown in Figure 2.1.

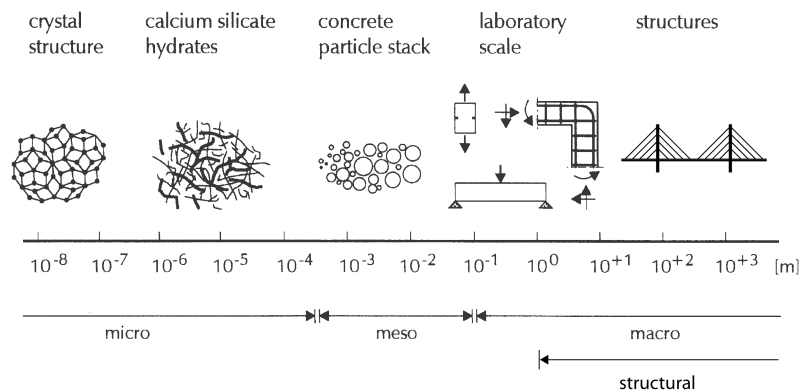


FIGURE 2.1: Scales for modelling of concrete (adapted from [VanMier97])

The three material levels are proposed by [Wittmann83]:

- The *micro-level* describes the structure of the hardened cement paste and is explained by material science models. Examples are chemical hydration reactions and their heat release.
- At the *meso-level*, concrete is seen as a heterogeneous material consisting of cement gel, aggregates, pores and free water. Material engineering, numerical and mechanical models are developed at this level such as moisture transport and mechanisms of self-desiccation shrinkage.
- The *macro-level* considers concrete as homogenous material. Material laws are deduced on this level. Bulk shrinkage measurements or the evolution of mechanical properties such as compressive strength are determined on the macro-level.

Schl fli [Schl fli99] defined as forth level the *structural level*, i.e. structural reinforced concrete members or structures that consider the system cementitious material and reinforcement. An example is the determination of the structural response of reinforced concrete beams and plates.

*In the present study, experimental investigations and modelling are entirely conducted on the macro- and structural level; micro- and meso-level approaches are only used for the explanation of time-dependent UHPRC behaviour in Chapters 3 and 4.*

## 2.2 Cementitious materials

*In this section, the properties of cementitious materials in general are described on the material level. The focus is drawn to time-dependent phenomena at early age and tensile behaviour.*

### 2.2.1 Early age behaviour

#### 2.2.1.1 Hydration

Hydration is the exothermal chemical reaction of Portland cement with water and the pozzolanic reaction of additives such as silica fume<sup>2</sup> (SF) that leads to the hardening of the cementitious material. Portland cement consists of four main phases ( $C_2S$ ,  $C_3S$ ,  $C_3A$ ,  $C_4AF$ ) that react with water mostly to CSH-gel and CH-crystals [Neville95]. Silica fume reacts with lime to CSH. A detailed overview over the chemical reactions can for example be found in [Waller00].

**Hydration reaction.** The *hydration reaction* for normal strength concrete can be described in five stages [Gartner89] (Figure 2.2). In parallel, the formation of the reaction products and the development of the structure of the cement paste are shown in Figure 2.3.

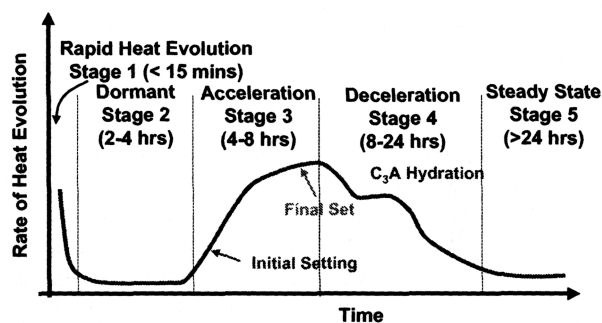


FIGURE 2.2: Conceptual illustration of the rate of heat evolution for a cement paste (adapted from [Gartner89] in [Weiss02])

- I. *Initial reaction:* This phase of several minutes is characterized by the formation of metastable CSH at the cement grain surface which acts as a protection layer and slows down significantly the hydration reaction.
- II. *Induction or dormant period:* During the dormant period, the hydration is nearly stopped and the material is still workable. This stage takes usually some hours, however, it can be significantly increased by the use of high amounts of superplasticizers [Morin01].
- III. *Acceleratory period:* The protection layer (formed during stage I) breaks open and the cement starts to hydrate at a high rate, which can be detected by the heat release. The hydration products increase

---

2. Silica Fume is a by-product of the smelting process used to produce silicon metal and ferrosilicon alloys. It is characterized by a high silica content (85 to 98%) and a mean particle size of 0.1 to 0.2  $\mu\text{m}$ . Silica Fume is both a reactive pozzolan and a very effective filler



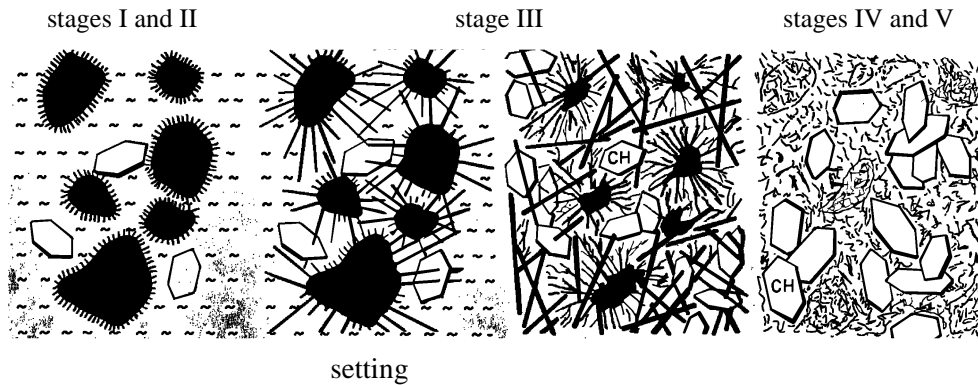


FIGURE 2.3: Formation of reaction products and build-up of structure (after [Locher76], from [VanBreugel92])

in volume and start to create bonds between each other. The mineral percolation threshold<sup>3</sup> is attained, when the first solid linear paths are created in the material, i.e. setting of the material occurs. This stage lasts for several hours.

IV. *Deceleratory period*: Hydrate layers form around the cement grains and diminish the rate of hydration during several days. This can be observed on the decreasing rate of heat release.

V. *Final slow reaction (steady state)*: This last stage takes several years. It finishes either with complete hydration of the cement or when no more water is available for the hydration reaction.

The *degree of hydration*  $\alpha$  is defined as the relation between the amount of hydrated cement and the initial amount of cement (EQ. 2.1) [VanBreugel92]. When there are also pozzolans such as silica fume in the mix, it may be defined as the reacted binder to the initial amount of binder.

$$\alpha(t) = \frac{\text{amount of hydrated cement at time } t}{\text{initial amount of cement}}, \quad \alpha \in [0, 1] \quad (\text{EQ 2.1})$$

Full hydration of the initial amount of cement can only occur in sealed systems for normal strength concrete for a water/cement-ratio superior to 0.42 [Hansen86]. For lower w/c-ratios, anhydrous cement remains in the material. The hydration process can therefore be described with a *degree of reaction* as defined in EQ. 2.2.

$$r(t) = \frac{\alpha(t)}{\alpha(t \rightarrow \infty)}, \quad r \in [0, 1] \quad (\text{EQ 2.2})$$

**Hardened cement paste models.** Hardened cement paste consists of CSH-gel, CH-crystals, minor components, anhydrous cement, pores and water. Powers and Brownyard developed a model that describes the CSH-particles as colloids that are called cement gel. Pores are divided in gel and capillary pores. The gel pores are within the cement gel and have a characteristic size of 2 to 4 nm; the capillary pores are 10 to 100 times bigger and are voids between the CSH-particles. Three kinds of water are distinguished in hardened cement paste: chemically bound water, physically bound water and free water. Chemically bound water is bound in the CSH-particles and is also called non-evaporable water. Physically bound water is tied by surface forces to the hydration products. Free water is found in the capillary pores and is also called capillary water. This water is available for hydration reaction. It governs the internal relative humidity (RH) and is at the origin of self-desiccation. The Powers model is still widely

3. first the 1D and soon afterwards the 3D mineral percolation threshold

used to determine the proportions of the anhydrous and the hydrated cement and the quantity of pores, however, it cannot explain all phenomena of cement paste [Powers48, Hansen86].

Cement pastes containing silica fume have a dense amorphous microstructure [Scrivener89]. Jensen extended the Powers model to systems containing silica fume [Jensen01]. Figure 2.4 illustrates the relative volume of the cement paste components in function of the degree of hydration of a normal strength concrete and an UHPFRC with 26%<sup>4</sup> of silica fume (SF) for a closed system, i.e. a system without water exchange with the surroundings. There is enough water in the normal strength concrete for full hydration (Figure 2.4a), while the degree of hydration is limited in the UHPFRC (Figure 2.4b) to 0.31 due to the low water content. The same degree of hydration is also determined by using the approach of [Waller00].

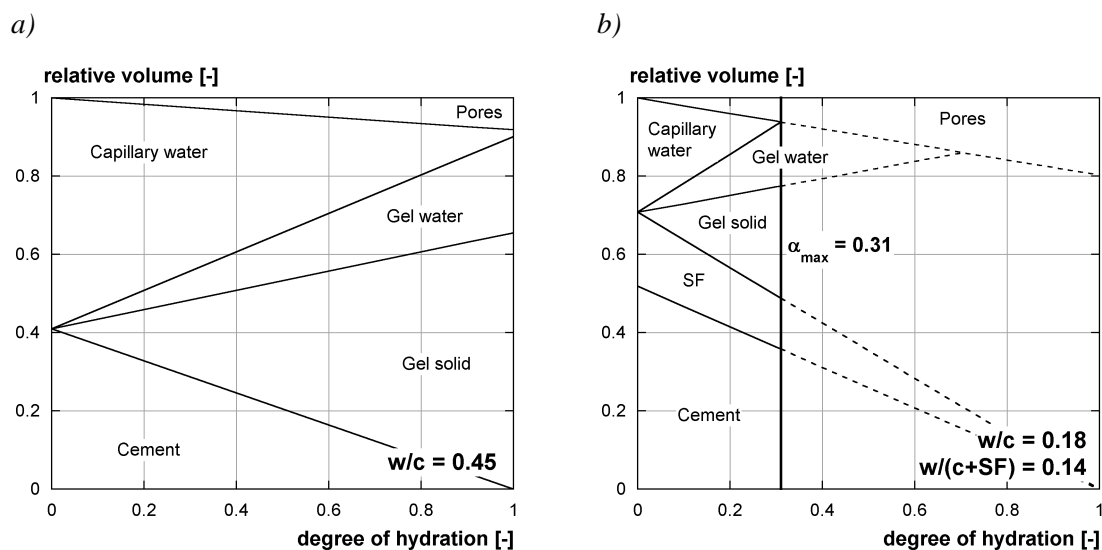


FIGURE 2.4: Composition of the cement paste in function of the degree of hydration: a) complete cement hydration, b) partial cement hydration with 26% of silica fume (SF) (after Powers model from [Hansen86] and [Jensen01])

Feldmann and Sereda proposed a model that describes CSH as a “layer structure of no definite number and of irregular configuration or arrangement” [Feldmann68] (Figure 2.5). They suggest that there is irreversible water that crosslinks the layers and that there is reversible water that can move reversibly in and out of the interlayer space and that adsorption of water molecules within the interlayer region distorts the measurements of water vapour [Hansen86]. This model is believed to come closer to reality than the Powers model, however, it describes cement paste only qualitatively, while the phases in the hardened cement paste can be quantified on the basis of the Powers model.

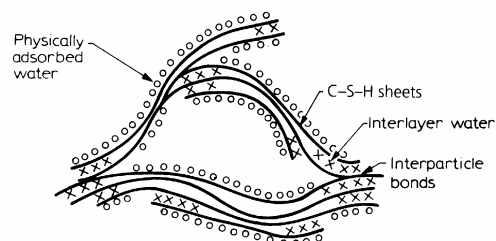


FIGURE 2.5: Simplified model for hydrated cement (after [Feldmann68])

4. of the cement mass

Recently, Jennings and co-workers proposed a colloid model in order to explain a wide range of experimental results with a single model [Jennings00]. They suggest that CSH has two different configurations: low density (LD) and high density (HD) CSH. The low density CSH forms at a high rate in the beginning of hydration and undergoes a slow maturation process at higher ages; high density CSH starts to form after approximately one day of hydration in the remaining pores. Mechanisms for drying, creep and shrinkage are also proposed on the basis of this model [Jennings04].

### 2.2.1.2 Heat of hydration

Heat is released during the exothermal hydration reaction. The rate of hydration corresponds to the rate of heat release. Its kinetics and magnitude are dependent on the binder composition. Table 2.1 gives mean values for the heat of hydration of the clinker phases and silica fume. The heat of hydration of silica fume is high, however, its activation energy is more than two times higher than that of Portland cement, thus, the hydration rate of silica fume is reduced in slender elements with their relatively low temperature rise during hydration [Waller00, DeLarrard99].

TABLE 2.1: Heat of hydration of the clinker phases and silica fume (from [Waller00])

Component	Heat of hydration [kJ/kg]
C <sub>3</sub> S	510
C <sub>2</sub> S	260
C <sub>3</sub> A	1100
C <sub>4</sub> AF	410
silica fume	870

### 2.2.1.3 Self-desiccation

“Self-desiccation is the reduction in the internal relative humidity of a sealed system when empty pores are generated.” [Bentur02] Water is consumed during the hydration reaction. When the cement paste is still fluid, the paste contracts and no internal voids are created. When the percolation threshold is attained and the formation of a rigid skeleton begins, the deformations of the cement paste are partially restrained and voids develop in the material. Vapour pressure builds up in the voids and the relative humidity in the material decreases. The smaller are the empty pores, the lower is the relative humidity (see e.g. [RILEM02]).

### 2.2.1.4 Chemical shrinkage

“Chemical shrinkage is the internal-microscopic volume reduction which is the result of the fact that the absolute volume of the hydration products is smaller than that of the reacting constituents.” [Bentur02] The volume decrease is between 7 and 10% [Barcelo02]. Chemical shrinkage leads directly to bulk deformation before the formation of a rigid skeleton, when the cement paste is still fluid. At setting, when a rigid skeleton forms, chemical shrinkage is higher than the externally observed volume reduction (autogenous shrinkage).

The chemical shrinkage caused by the pozzolanic reaction of silica fume is higher than that of pure cement paste. It is estimated to be 12 to 20 cm<sup>3</sup>/100 g silica fume [Jensen96], compared to a value of about 6 cm<sup>3</sup>/100 g cement [Powers48]. As a result, concretes with silica fume have a higher degree of self-desiccation and a lower internal relative water vapour pressure.

### 2.2.1.5 Evolution of mechanical properties

The evolution of the mechanical properties in function of the degree of reaction is shown in Figure 2.6a for a CEM I 52.5 De Schutter and Taerwe found the beginning of the evolution of the mechanical properties at a degree of reaction  $r_0 = 0.25$ ; the initial values in the literature vary between 0.15 and 0.4 [DeSchutter96]. Figure 2.6 shows the evolution of compressive strength, tensile strength

and Young’s modulus. The evolution of the compressive strength is the slowest. The tensile strength increase is faster, however, the modulus is the property that increases the fastest. This tendency was also observed by other authors [Laube90, Byfors82]. In case of restraint, the fast evolution of the modulus causes high stresses. At the same time, the strength evolution is slower and the risk of cracking increases.

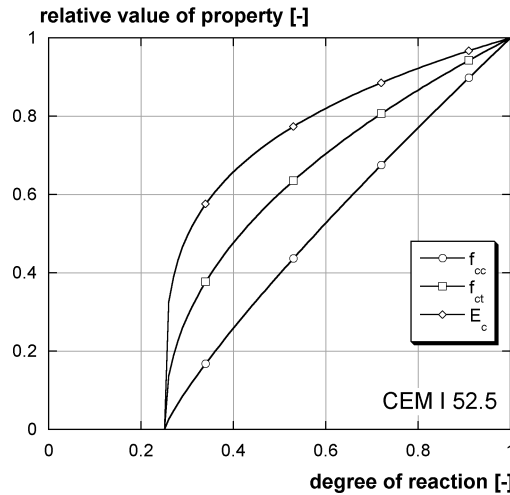


FIGURE 2.6: Evolution of the mechanical properties (adapted from data of [DeSchutter96])

The Poisson’s ratio is estimated to be 0.5 for concrete before setting, since the material can be seen as a fluid. It decreases to values of approximately 0.2 in hardened concrete. [DeSchutter02]

2.2.2 Tensile behaviour

In this section, the quasi-static behaviour of concrete under tension is discussed. A more detailed description can be found in [Denarie00] and [Bernard00]. Figure 2.7 shows macroscopic behaviour and cracking under uniaxial tension.

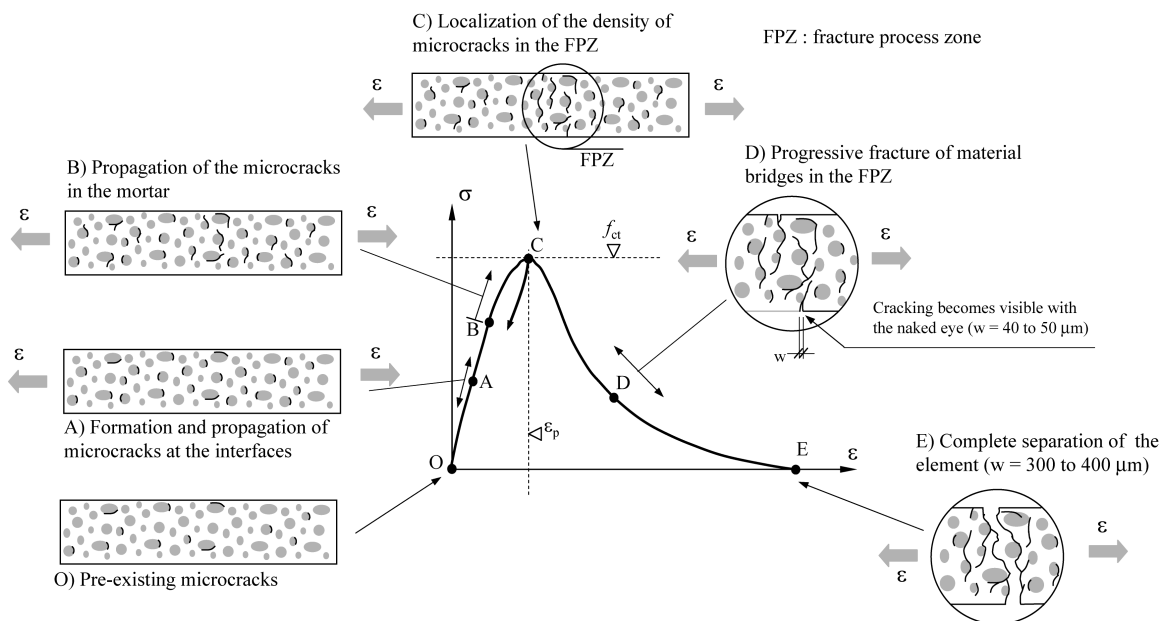


FIGURE 2.7: Conceptual illustration of the quasi-static concrete behaviour under tension and of crack formation and propagation (from [Bernard00])

**Pre-peak behaviour.** Prior to the fracture tests, pre-existing microcracks exist in concrete due to internal restraint of shrinkage by aggregates or fibres (point O). When the concrete is subjected to tensile strains, its behaviour is described by a stress-strain ( $\sigma$ - $\epsilon$ )-curve. Three mechanisms of crack propagation are distinguished:

- The formation and propagation of microcracks at the interfaces between hardened cement paste and aggregates is activated at approximately point A, i.e. at a stress level of 20 to 40% of the tensile strength  $f_{ct}$  [Alkubaisy75].
- Submicrocracking in the hardened cement paste accounts for 20 to 90% of the non-linear response of mortar [Attiogbe88].
- The propagation of interaggregate microcracking in the mortar. It becomes predominant beyond B at a stress level of 70 to 90% of the tensile strength.

When the tensile strength is reached (point C), a network of interconnected microcracks forms, localizing in the fracture process zone (FPZ) [Hillerborg83]. The size of the FPZ is governed by the concrete type and the size of aggregates and concrete type [Brühwiler88] and of specimen geometry and loading mode [Denarie00].

**Post-peak behaviour.** The post-peak behaviour of concrete in the FPZ is characterized by softening. The additional deformations localize in the FPZ and lead to the formation of larger cracks. Since the stresses are transferred through crack face bridges [VanMier97] and the size of these bridges decreases with increasing deformation, the stresses decrease. Outside the fracture zone, the deformations decrease with the stress decrease in the specimen.

At point D, the crack width in the FPZ is 40 to 50  $\mu\text{m}$  and the cracks become visible to the naked eye. At point E, the specimen is completely cracked and no more stresses can be transferred for a crack width between 300 and 400  $\mu\text{m}$  for normal strength concrete, depending on the maximum aggregate size.

**Crack types.** Four crack types are distinguished in Table 2.1: submicrocracks, microcracks, macrocracks and real cracks. The definition of Bernard is adapted to characterize micro- and macrocracks [Bernard00]: microcracks are small when compared to the diameter of the biggest aggregates and important when compared to the dimensions of CSH-sheets; macrocracks are visible with the naked eye. Finally, real cracks are macrocracks across which no more stress can be transferred [Hillerborg83].

TABLE 2.1: Definition of crack types (adapted from [Bernard00])

Type	Width	Nature	Reference
Submicrocracks	$w < 1 \mu\text{m}$	in the hardened cement paste	[Attiogbe88]
Microcracks	$1 \mu\text{m} \leq w < 40 \text{ to } 50 \mu\text{m}$	at interfaces mortar - aggregates	[Bernard00]
Macrocracks	$w \geq 40 \text{ to } 50 \mu\text{m}$	propagation in the mortar	[Hillerborg83]
Real cracks	$w \geq 300 \text{ to } 400 \mu\text{m}^a$	no stress transfer across the crack	[Hillerborg83]

a. for normal strength concrete

**Crack models.** Cracking in cementitious materials is modelled by discrete crack models such as the fictitious crack model [Hillerborg83] or smeared crack models such as the crack band model [Bazant83]. In the fictitious crack model, the crack is concentrated on one line, i.e. in FE-simulations, the crack propagates at the element borders. In the crack band model, the crack is smeared over a certain width which would be the element width in FE-simulations. Both models are commonly used in analytical models and numerical simulations (Figure 2.8).

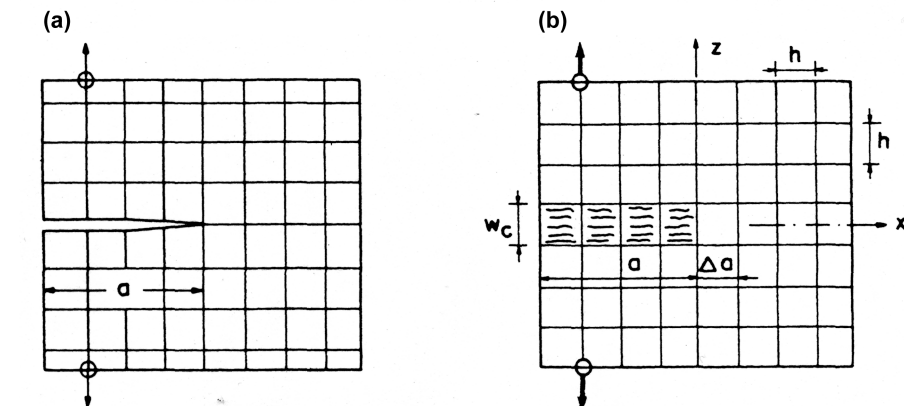


FIGURE 2.8: Conceptual illustration of a) a discrete crack model and b) a smeared crack model (from [Bazant83])

## 2.2.3 Time-dependent macroscopic deformations

### 2.2.3.1 Free deformations

**Thermal deformation.** “Thermal deformation is external-macroscopical (bulk) linear and volume change induced by thermal effects.” [Bentur02] It is dependent on the coefficient of thermal expansion  $\alpha_T$ . In general, the coefficient of thermal expansion is high before setting ( $\alpha_T \approx 70 \cdot 10^{-6} \text{ }^\circ\text{C}^{-1}$ ) and drops to approximately  $10 \cdot 10^{-6} \text{ }^\circ\text{C}^{-1}$  during the temperature rise due to the heat of hydration, i.e. during setting. The high initial values can be explained by the dominance of water before setting, while after setting, the solid cement paste is predominant [Laplante94, Kada02]. After setting the coefficient of thermal expansion is approximately constant with values between  $8$  to  $12 \cdot 10^{-6} \text{ }^\circ\text{C}^{-1}$ .

The thermal conductivity  $\lambda_T$  of concrete and mortar lies between  $0.6$  and  $3.8 \text{ W/(m K)}$  with average values between  $2.1$  and  $2.5 \text{ W/(m K)}$  [Gibbon98, Kim03]. Steel fibres increase and silica fume reduces the thermal conductivity. The thermal capacity can be estimated by considering the thermal capacity of the components of the cementitious material. The thermal capacity decreases of approximately  $10$  to  $15\%$  during hydration [Waller00].

**Autogenous swelling.** “Autogenous swelling is the external-macroscopical (bulk) dimensional expansion (volume or linear) of the cementitious system which occurs under isothermal conditions, without exchange of moisture or any other substance with the surrounding.” [Bentur02] It can be attributed to a variety of mechanisms associated with hydration such as swelling pressure and ettringite formation. Autogenous swelling typically occurs during the early age when the hydration rate is high and the rigid skeleton is built.

Several mechanisms are proposed for autogenous swelling [Barcelo01, RILEM02]:

- re-absorption of bleeding water,
- crystallization pressure of growing hydration products such as ettringite or portlandite and
- a topochemical reaction of anhydrous products or “crystallization” of inner CSH.

**Autogenous shrinkage.** “Autogenous shrinkage is the external-macroscopical (bulk) dimensional reduction (volume or linear) of the cementitious system which occurs under isothermal conditions without exchange of moisture or any other substance with the surrounding.” [Bentur02] The driving force of autogenous shrinkage is chemical shrinkage (Figure 2.9). Chemical and autogenous shrinkage are equal when the cementitious system is still fluid (before setting). After the percolation threshold is attained, autogenous shrinkage is smaller than chemical shrinkage [RILEM02]. In the following, autogenous shrinkage is debated after the percolation threshold, i.e. when the material is solid-like. There is general agreement that a major part of autogenous shrinkage, the self-desiccation shrinkage, is related to RH

changes in the pores during hydration. Self-desiccation is limited to a RH of approximately 75% [Jensen95], however, self-desiccation does not entirely explain autogenous shrinkage.

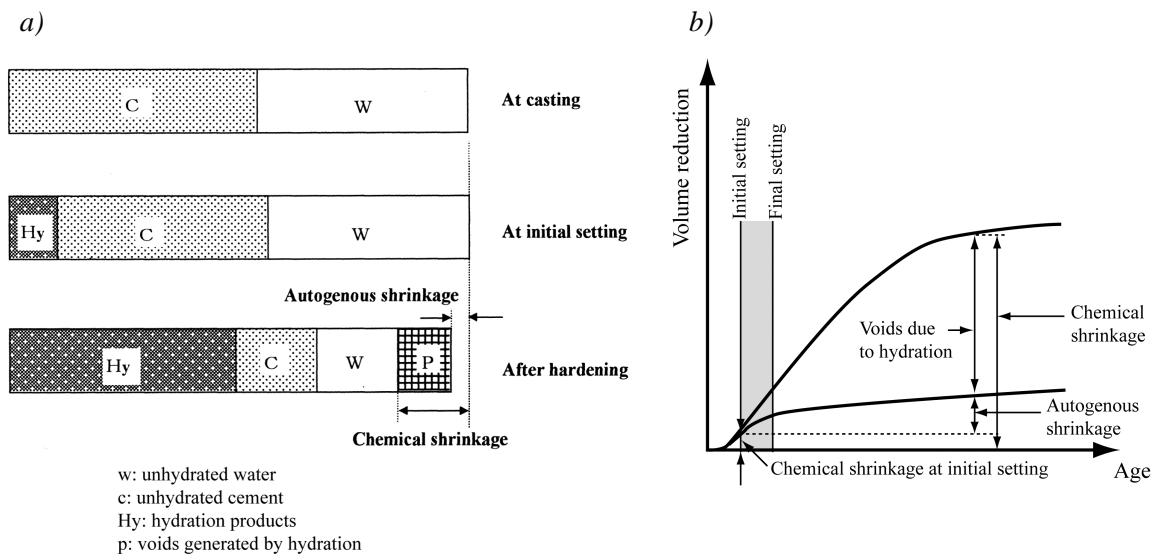


FIGURE 2.9: Chemical and autogenous shrinkage: a) phase distribution for different degrees of hydration, b) evolution in time (from [Tazawa98])

Silica fume increases autogenous shrinkage. Jensen observed that no RH change was linked to the silica fume pozzolanic reaction during which CH-crystals were consumed and explained the additional shrinkage as chemical shrinkage that was approximately 4 times higher than for Portland cement. The finer pore structure of the cement paste due to silica fume addition increases self-desiccation and thus shrinkage [Jensen96].

**Drying shrinkage.** Drying shrinkage occurs when the RH of the surrounding is lower than in the cementitious material. Diffusion occurs in the material, leading to a decrease of relative humidity and shrinkage. The main difference between autogenous shrinkage and drying shrinkage is that self-desiccation is internal and evenly distributed over the material, while drying leads to moisture gradients in the specimen resulting in shrinkage gradients (Figure 2.10).

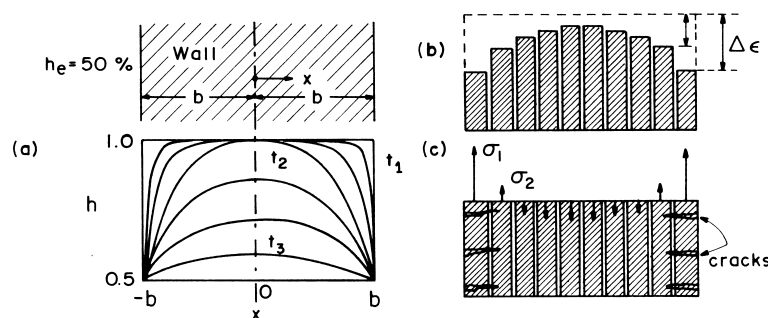


FIGURE 2.10: Schematic representation of the effect of drying creep (from [Wittmann82]): a) distribution of relative humidity, b) free shrinkage deformations, c) stress state and crack formation due to the gradient of relative humidity

**Mechanisms for self-desiccation and drying shrinkage.** Shrinkage mechanisms are divided into real and apparent mechanisms. Real mechanisms are related to material behaviour, apparent to structural effects. Three *real mechanisms* are debated for drying and self-desiccation shrinkage: capillary tension, disjoining pressure and surface tension. Only a short overview is given here, a detailed discussion can be found e.g. in [Charron03].

- *Capillary tension* in the pore fluid builds up when voids develop in the cement paste and water-air menisci form. It can be quantified by the Kelvin and Laplace laws. The capillary pores are emptied from big to small pores. With decreasing pore size, the menisci become smaller and the vapour pressure decreases leading to a contraction in the material. This mechanism explains drying shrinkage for high relative humidity (> 80%) and is assumed to be the major driving force of autogenous shrinkage [Hua95]. The relative humidity may be reduced by dissolved salts in the pore solution of 1 to 3% [Jensen01a].
- The mechanism of *disjoining pressure* is related to the interaction of two solid surfaces in presence of adsorbed water molecules. When the water adsorption on the CSH-particles is hindered because the solid particles are too close, disjoining pressures develop. When the relative humidity decreases, the disjoining pressure is reduced and shrinkage occurs. The disjoining pressure is nearly constant for relative humidities between 80 and 100% and becomes important for relative humidities between 40 and 80% [Ferraris87].
- Shrinkage is partially due to changes in the *surface tension* of the solid gel particles (Gibbs-Bangham-effect) [Bangham37]. This effect occurs mainly for low relative humidities (< 40%) [Ferraris87]. It may influence drying shrinkage, but is not determinant for autogenous shrinkage, since the hydration stops at a relative humidity of approximately 75%.

The formation of microcracks is an *apparent mechanism*. When the cementitious material is subjected to drying creep, moisture gradients occur leading to deformations gradients as shown in Figure 2.10. The deformation gradients induce stresses and cracks in the element. *Microcracking* may also occur due to internal restraint of shrinkage by aggregates or fibres.

### 2.2.3.2 Viscoelastic behaviour

Only the most important characteristics of viscoelasticity are discussed in this section. Comprehensive overviews of creep and its mechanisms are given for example in [Neville70, Wittmann82].

**Definitions.** *Viscoelasticity* is the superposition of elasticity and viscosity, i.e. of the behaviour of a solid and a fluid respectively. Cementitious materials exhibit viscoelastic behaviour when subjected to loads or to imposed deformations. Viscoelasticity is observed in cementitious material in form of creep or relaxation. *Creep* is the time-dependent component of deformations due to imposed loads, i.e. creep strain is defined as the total strain minus the initial elastic strain and shrinkage. *Relaxation* is the viscoelastic response of the material under imposed deformations. The viscoelasticity of cementitious materials is discussed in the following for creep.

**Concrete creep.** For concrete, it is generally distinguished between basic and drying creep. *Basic creep* is defined as creep in a sealed system when no water exchange with the surroundings occurs. *Drying creep*, also called Pickett-effect [Pickett42], involves an additional creep component due to drying of the cementitious material. Temperature rise also increases creep [Gamble78], the additional creep deformation is called transient thermal creep.

Three *phases of creep* are distinguished: primary, secondary and tertiary creep [Neville70]:

- The rate of *primary creep* decreases with time. It is mainly important during the first days of creep loading.
- *Secondary creep* is steady state creep, i.e. a long-term component that describes increase of deformation at a continuously decreasing rate.
- *Tertiary creep* exists only for high load levels and leads to an increase of the creep rate in time due to microcracking and finally to fracture of the specimen, the static fatigue failure. It was first observed by Rüsçh [Rüsçh60]. Under compression, the stress limit is estimated to be 70 to 90% of the quasi-static tensile strength  $f_{ct}$ , under tension [Neville70], it is estimated to be 60 to 76% [Denarie00].

Most creep studies concentrate on compression creep. Bissonnette studied the influence of several material parameters on tensile creep. He concluded that tensile creep is of the same magnitude as com-



pression creep and can significantly reduce stresses in case of restraint [Bissonnette00]. Viscoelasticity under tension was also investigated by [Bernard00] and [Denarie00].

At early age, the decrease of the creep rate is important with time. Early age creep is found to be directly related to the degree of hydration. It exposes the same non-linearity due to microcracking as observed for quasi-static loading [DeSchutter00].

**Mechanisms.** Concrete creep mechanisms are still not entirely understood. There is general agreement that basic creep of cementitious materials can be explained by the interaction of real and apparent mechanisms. It is distinguished between two major real and one apparent mechanisms [Guenot-Delahaie97, Acker01a]:

- a *real short-time* creep mechanism due to the *microdiffusion* of water from hindered zones to capillary pores (seepage of gel water),
- a *real long-term* creep mechanism that is mainly explained by *viscous flow*, i.e. dislocations occur within CSH-sheets of the hydrated cement paste.
- an *apparent* mechanism that attributes creep to the formation of *microcracks*.

In general, it is admitted that the excess deformation of drying creep is the combination of an intrinsic real mechanism in form of movement of water through gel pores [Bazant85] and an apparent mechanism in form of microcracking [Wittmann82]. Transient thermal creep is explained by thermodynamic activation [Hauggaard99].

For *tensile creep*, viscous flow is the predominant mechanism for stress levels below 50 to 60% of the quasi-static tensile strength; for higher stress levels, microcracks form in the concrete, mainly at the interfaces concrete-aggregate or concrete-fibres [Bissonnette00, Denarie00]. The two components were separated by Altoubat and Lange [Altoubat02].

## 2.3 Ultra-High Performance Fibre-Reinforced Concretes (UHPFRC)

*This section deals with UHPFRC. It concentrates on the principles and on the material properties of UHPFRC. Typical constituents of UHPFRC and a short historical overview are also discussed.*

### 2.3.1 General

**Definition.** UHPFRC are Advanced Cementitious Materials (ACM) with specifically tailored properties. They are characterized by an ultra-compact matrix with *very low permeability* and by *tensile strain-hardening*. They are part of the group of HPFRCC as described in Figure 1.2.

**Historical overview.** UHPFRC development found its origin in the studies of Odler, Brunauer and Yudenfreund in the beginning of the 1970s [Yudenfreund72,72a,72b, Odler72,72a, Brunauer73,73a]. They investigated high strength pastes with low w/c-ratios ( $w/c = 0.2$  to  $0.3$ ) whose main characteristic was the low porosity leading to high compressive strengths (up to 200 MPa) and to low dimensional changes. Strength enhancement by hot pressing techniques was first applied by Roy and resulted in very high strength cement pastes with compressive strengths up to 680 MPa [Roy72, 73].

With the development of superplasticizers and pozzolanic admixtures such as silica fume, two kinds of materials emerged in the 1980s: Birchall et al. developed polymer modified cementitious materials called Macro-Defect-Free (MDF) cements. The pores are filled by polymerization leading to a compact matrix. However, these concretes are susceptible to water and have high creep [Kendall83, Alford85]. Bache developed the DSP (Densified Small Particles) which use the interaction of superplasticizers and silica fume to decrease the porosity of the material and to increase the strengths. That way, he prepared the ground for modern UHPFRC development [Bache87]. The compacity of the matrix of these mixes was theoretically investigated and optimized e.g. by de Larrard and Sedran [DeLarrard94, Sedran94].

However, these high strength cement pastes and mortars are very brittle. Consequently, the addition of fibres is necessary to enhance ductility (increase of  $G_F$ ). Three tendencies are distinguished by [Rossi02]:

- DSP with an addition of 5 to 10% short steel fibres ( $l_f = 6$  mm), commercialized under the name CRC [Bache87, Aarup04].
- the so-called Reactive Powder Concrete (RPC) with 2.5% of short slender steel fibres ( $l_f = 13$  mm), developed by Bouygues, Lafarge and Rhodia and commercialized under the name Ductal<sup>®</sup> [Richard95, Orange00],
- and the Multi-Scale Cement Composite (MSCC) using a mixture of short and long steel fibres. MSCC are developed at the LCPC in France and are known under the name CEMTEC<sub>multiscale</sub><sup>®</sup> [Rossi97, Rossi02].

The development of UHPFRC and the tailoring of their specifically properties is still not entirely known and presents a research topic at several universities.

### 2.3.2 Principles of UHPFRC

The main principles for UHPFRC design are [Richard95]:

- *Homogeneity enhancement*: The homogeneity of the material is improved by eliminating coarse aggregates,
- *Compacity enhancement*: The density of the matrix is increased by optimizing the packing density. The different particle size classes are silica fume (mean size: 0.1 to 0.2  $\mu\text{m}$ ), cement (mean size: 15  $\mu\text{m}$ ) and fine sand (mean size: 0.2 mm). The optimum packing density can be determined with granular packing models by calculating the optimum ratio of the different aggregate classes [Sedran94, DeLarrard99, Jones02].
- *Ductility by fibres*: As the matrix of DSP is very brittle, steel or organic (e.g. carbon or glass) fibres have to be added to obtain strain-hardening behaviour in tension.

UHPFRC may be subjected to heat and / or pressure treatment. Pressure treatment of the fresh material increases the density by reducing the entrapped air, by removing excess water and by accelerating chemical shrinkage. Post-set heat treatment of 90 °C accelerates the pozzolanic reaction and modifies the microstructure of the hydrates.

*These two treatments are difficult to apply in case of composite “UHPFRC-concrete” elements and in-situ applications and would present major drawbacks. UHPFRC without heat and pressure treatment are proposed and used in the present study.*

### 2.3.3 Constituents of UHPFRC

UHPFRC consists of cement, silica fume, sand, fibres, water and superplasticizer. Typical water/cement-ratios are 0.15 to 0.20 with 20 to 30% of silica fume.

**Cement.** The cement content ( $\geq 700$  kg/m<sup>3</sup>) is more than two times higher than for normal strength concrete. There is general agreement that the cement should have a low alkali content, low to medium fineness and a low  $C_3A$ -content, thus, reducing water need, ettringite formation and heat of hydration. In most cases, CEM I 52.5 is used, however, there are also promising tentatives with other cement types such as CEM III/B. [Richard95, Siebel03]

**Silica fume.** Silica fume fulfils three functions in UHPFRC: it fills voids between cement grains, it enhances the rheological characteristics and it forms hydration products by pozzolanic activity. Thus, the mechanical strengths are increased and microstructure and compacity of the UHPFRC are enhanced. Best results are reported for silica fume from the zirconium industry having few impurities and a Blaine fineness of 14 m<sup>2</sup>/g. The optimum filling performance of silica fume in cement is reached for silica fume-contents of 25% of cement content [Richard95, Parant03].

**Sand.** UHPFRC aggregates are sand. Quartz sand is proposed, since it has a high hardness and provides good paste-aggregate interfaces. The mean particle size is often smaller than 1 mm, but also UHPFRC with maximum particle sizes of 8 to 16 mm are produced. [Holschemacher03, Richard95] It must be noted that the grain size distributions of cement, silica fume and sand have to be optimized in order to obtain high compacity and thus, a dense matrix with a very low permeability.

**Superplasticizer.** Superplasticizers are essential for the processing (workability) of UHPFRC with their low water-content. In general, superplasticizers of the third generation - polycarboxylates and polycarboxylateethers - are used, since they are highly efficient and have no efficiency threshold for low w/c-ratios [Holschemacher03].

**Fibres.** Steel and organic fibres are used in UHPFRC. Naaman defined the demands on fibres as “short, stiff and strong” [Naaman02]. Thus, steel fibres seem to be the most adapted. Steel fibres are generally pulled out; therefore, fibre ductility is less important than their strength. Naaman developed limit curves for hardening under bending and uniaxial tension as a function of the fibre properties [Naaman02]. Rossi developed UHPFRC on the basis of the multiscale concept with several kinds of steel fibres - going from steel wool ( $l_f \approx 1$  mm) to small steel fibres (5 to 15 mm) to long ones ( $> 15$  mm). The different fibres work on the material scale to increase the tensile strength and on the structural scale to increase resistance and deformation capacity. [Rossi87, Rossi02] Typically, UHPFRC have fibre contents of more than 2 Vol.-%. The maximum fibre content in function of the aspect ratio of the fibres is limited by processing factors such as workability.

## 2.3.4 Material properties

### 2.3.4.1 Hydration

The low water-content of UHPFRC hinders full hydration, e.g. an UHPFRC with a w/c-ratio of 0.18 and with 26% of SF has a final degree of hydration of approximately 31% (see Section 2.2.1.1). The hydration rate of UHPFRC at early age is shown in Figure 2.11. It is characterized by a long dormant period (typically 24 hours or longer) which is explained by the high amount of superplasticizer in the material, delaying the setting of the material [Morin01]. Then, a strong hydration reaction starts which can be observed on the heat release and the material starts to harden. The degree of hydration shows a high rate between 30 and 57 hours for the UHPFRC used by Morin et al., attaining a degree of hydration of 18% at 70 hours [Morin02].

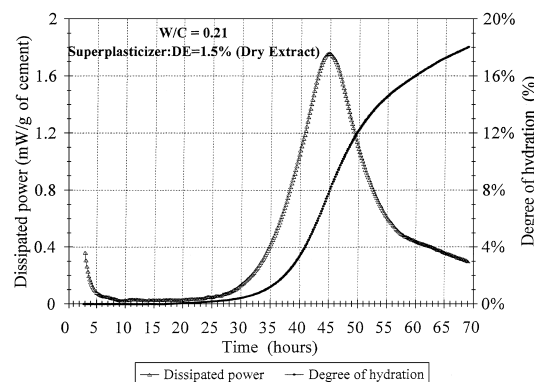


FIGURE 2.11: Heat release due to hydration and evolution of the degree of hydration of RPC (from [Morin02])

### 2.3.4.2 Mechanical properties

**Compression.** UHPFRC are characterized by high compressive strengths - typical values are 150 to 250 MPa at 28 days for UHPFRC without heat treatment. The secant modulus is also increased, but not

to the same extent as the compressive strengths:  $E = 45$  to  $65$  GPa at 28 days. The Poisson’s ratio for RPC was determined to be 0.22 to 0.24 [Dugat96] and for CEMTEC<sub>multiscale</sub><sup>®</sup> to be 0.21 at 28 days [Parant03].

**Tension.** One of the two main characteristics of UHPFRC is tensile strain-hardening. The comparison between strain hardening UHPFRC and conventional fibre reinforced concrete (FRC) is shown in Figure 2.12.

- *Domain I:* In the first part of the curves until point A, the stress rise is *quasi linear-elastic* until the cracking strength  $\sigma_{cc}$ .
- *Domain II:* It is followed by *strain-hardening* until point B with a post-cracking strength  $\sigma_{pc}$  for UHPFRC. The post-cracking strength of UHPFRC is higher than the cracking strength. Multiple cracks form during the strain-hardening, however, the macroscopic deformation is still uniform<sup>5</sup> and can be expressed by the strain  $\epsilon$ .
- *Domain III:* At point B, *crack localization* occurs and softening behaviour is observed (domain III), expressed by a  $\sigma$ - $w$ -curve.

Domain II barely exists for conventional FRC. Typical maximum strengths of UHPFRC are 6 to 20 MPa with fracture energies of  $G_F = 10$  to  $40$  kJ/m<sup>2</sup>, mainly dependent on the compacity of the matrix and fibre composition [Dugat96, Parant03]. Real cracks form (i.e. the stress becomes zero) for a crack width of approximately half the fibre length ( $\frac{1}{2} l_f$ ).

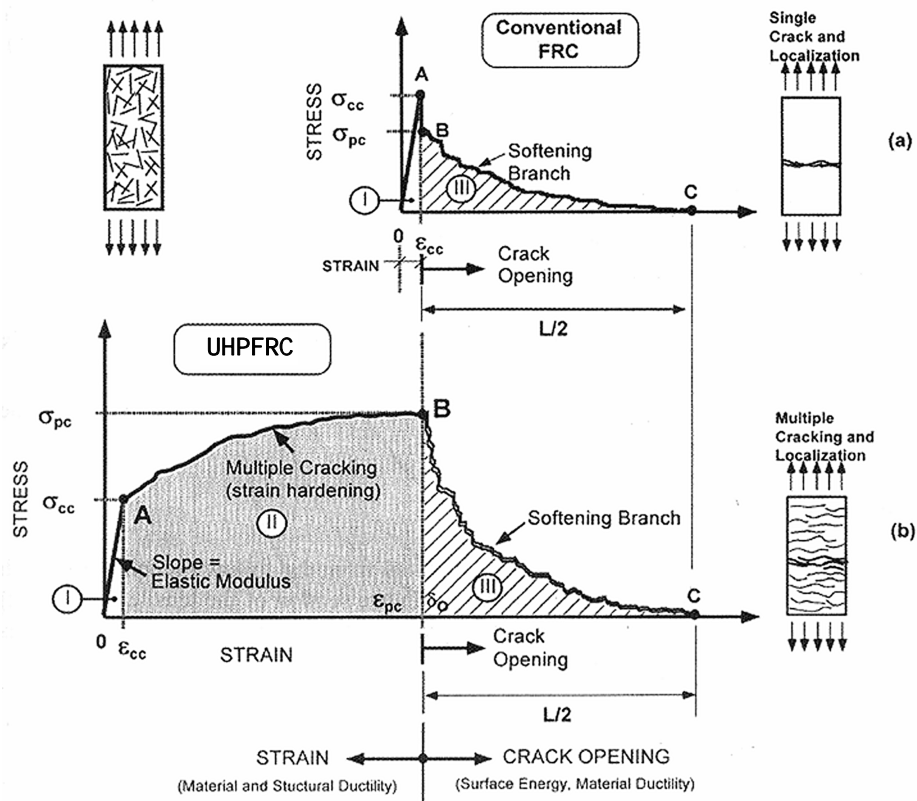


FIGURE 2.12: Comparison of typical stress-strain response of UHPFRC with SFRC (after [Naaman02])

**Determination of tensile properties.** Uniaxial tensile test for UHPFRC demand a stiff test set-up in order to avoid bending effects and an appropriate testing machine. A uniaxial tensile test was developed

5. macroscopic with respect to structural elements

by Boulay [Boulay03]. The execution of uniaxial tensile tests is time intensive. So, the tensile behaviour of UHPFRC is often determined by bending tests (see e.g. [Parant03]). However, bending test results have to be carefully interpreted: the bending strength is often expressed by the modulus of rupture (MOR), which is the flexural strength calculated for a linear-elastic stress distribution. UHPFRC do not have linear-elastic stress distribution under bending beyond point A in Figure 2.12.

Tensile properties depend significantly on the fibre distribution. This distribution is influenced by the way of casting and the specimen geometry as for FRC. Furthermore, fibre segregation may occur leading to an inhomogenous distribution of the tensile properties over the depth of the element.

### 2.3.4.3 Time-dependent deformations

**Influence of stress rate.** The effect of the stress rate on the resistance of UHPFRC specimens in bending was investigated by Parant for rates from 0.1 MPa/s to 100 GPa/s (Figure 2.13). Two domains are distinguished: domain I for quasi-static loading, where the increase of resistance (expressed by the MOR) is small, and domain II for dynamic loading where the stress rate increases significantly the resistance. The increase of resistance is reported to be more important for UHPFRC than for conventional FRC which is attributed to the high fibre content of UHPFRC [Parant03].

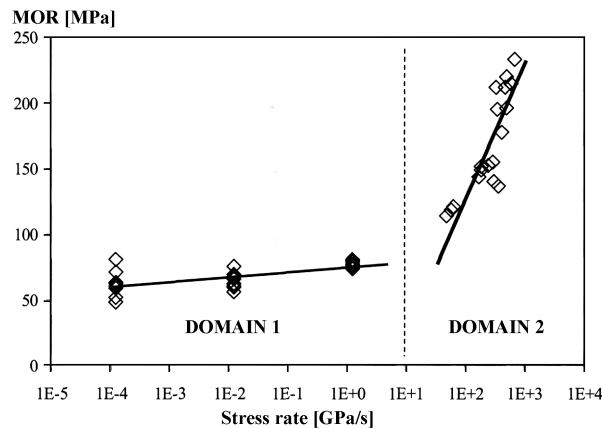


FIGURE 2.13: Influence of stress rate on the apparent MOR for the UHPFRC CEMTEC<sub>multiscale</sub><sup>®</sup> (adapted from [Parant03])

**Shrinkage.** Shrinkage on UHPFRC was measured for CRC, RPC and CEMTEC<sub>multiscale</sub><sup>®</sup>. The measurements started after setting of the material, i.e. the early age deformations were not considered. The shrinkage of heat-treated UHPFRC is zero after the application of the treatment, since all the shrinkage occurs during the heat treatment.

Autogenous and drying shrinkage was measured for CRC and RPC on cylindrical specimens ( $\varnothing$  9 cm,  $l$  = 60 cm), starting 24 hours after water addition. The autogenous shrinkage of CRC was approximately 450  $\mu$ m/m after 8 days and remained virtually constant until the end of the tests at 160 days. The evolution of autogenous shrinkage for RPC is shown in Figure 2.14. The high autogenous shrinkage (420  $\mu$ m/m after 140 days) is mainly explained by the high self-desiccation of the RPC. Drying shrinkage evolution was strong during the first 10 days and stabilized at a value of 180  $\mu$ m/m at higher ages. Furthermore, the results showed that autogenous and drying shrinkage decrease for decreasing w/b-ratio for RPC having w/b-ratio between 0.09 and 0.20, which is explained by the low hydration rate of UHPFRC. Additional weight loss measurements showed that microcracking occurred in the RPC during the first 10 days. The addition of steel fibres reduces shrinkage deformations by 10 to 20% [Loukili96, Cheyrezy01]. Acker explained that the major part of shrinkage is due to viscous response of CSH to hygral stresses provoked by capillary tension in the pores and disjoining pressure, since CSH is

the only viscous component in UHPFRC. He determined the saturated pore size to be 3 nm at a relative humidity of 75% [Acker01].

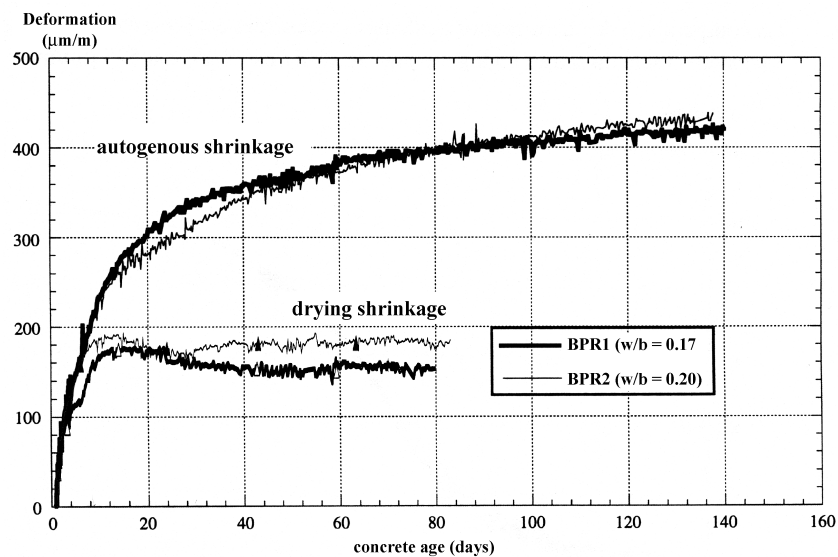


FIGURE 2.14: Autogenous and drying shrinkage of RPC (adapted from [Loukili96])

Schachinger et al. conducted linear autogenous shrinkage measurements on ultra-high performance concretes without fibres. The measurements started before setting of the UHPFRC. He confirmed that the major part of autogenous shrinkage occurs during 5 to 10 hours after setting. Then, the evolution slows down, but, it does not stabilize until the end of measurements at 56 days [Schachinger03].

Autogenous shrinkage was also measured for CEMTEC<sup>®</sup><sub>multiscale</sub> at the LCPC. The tests started 3 days after casting. The autogenous shrinkage was 500 µm/m after 325 days [Parant03].

*The results of shrinkage measurements show that the critical phase for these material is during the first 10 days after water addition. Therefore, good curing is essential during early age to prevent micro-cracking on the surface. Autogenous shrinkage deformations are high at very early age. Consequently, it is necessary to quantify the deformations from the setting point on.*

**Creep.** Compressive creep of RPC at several loading ages is shown in Figure 2.15. The creep coefficient ( $\epsilon_{\text{creep}} = \epsilon_{\text{el}} \cdot K_{\text{cr}}$ ) decreases from  $K_{\text{cr}} = 2.5$  to 0.6 with increasing age and stabilizes after 100 to 150 days (load level of 20%). RPC shows fast creep kinetics: 35% of the deformation occurs during the first 24 hours. The creep coefficient is smaller for lower w/b-ratios. Steel fibres reduce the creep compliance by 20 to 25%. [Cheyrezy01 Loukili96] The creep deformations are mainly attributed to viscoplastic CSH behaviour. The small creep compliance is explained by the fact that internal creep is high at early age due to the hygral stresses in the microstructure which arise with ongoing self-desiccation. Thus, the major part of creep is already finished when the UHPFRC is externally loaded. [Acker01]

The creep compliance was determined for CEMTEC<sup>®</sup><sub>multiscale</sub> at the LCPC. The specimens were loaded at 28 days to 45% of their compressive strength. The creep coefficient was  $K_{\text{cr}} = 1.0$ , and the creep compliance 45 µm/m/MPa, considering the elastic deformation [Parant03].

*No studies have been conducted for tensile creep of UHPFRC yet. Thus, it is difficult to estimate if tensile creep is of the same magnitude as compressive creep. It is known that tensile creep of normal strength concrete increases with decreasing cement content. i.e. with increasing interfaces between aggregates and cement. UHPFRC have only small aggregates, however, the steel fibres may have the same effect as aggregates, and a major part of tensile creep may have its origin at the interfaces between fibres and matrix.*

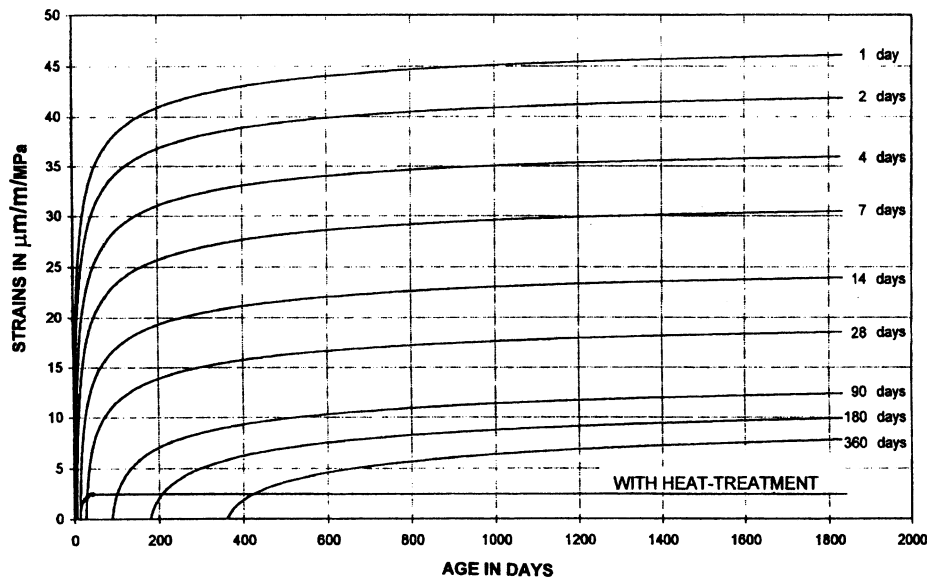


FIGURE 2.15: Creep deformation of RPC at different loading ages (from [Cheyrezy01])

#### 2.3.4.4 Other physical properties

**Porosity.** The cumulative porosity of UHPFRC was measured with mercury intrusion porosimetry (MIP) by Roux et al. for RPC subjected to different curing treatments (Figure 2.16a). Pores with sizes from 6 nm to 100  $\mu\text{m}$  can be measured with this test method. The cumulative porosity of RPC was less than 9% for RPC without heat treatment and pressing and less than 0.5% for RPC subjected to these curing methods. In comparison, normal strength concrete has a cumulative porosity between 10 and 15%. A threshold value was observed, below which the porosity increases rapidly. This porosity is called microporosity. Capillary porosity is very small or even absent in UHPFRC [Cheyrezy95, Roux96].

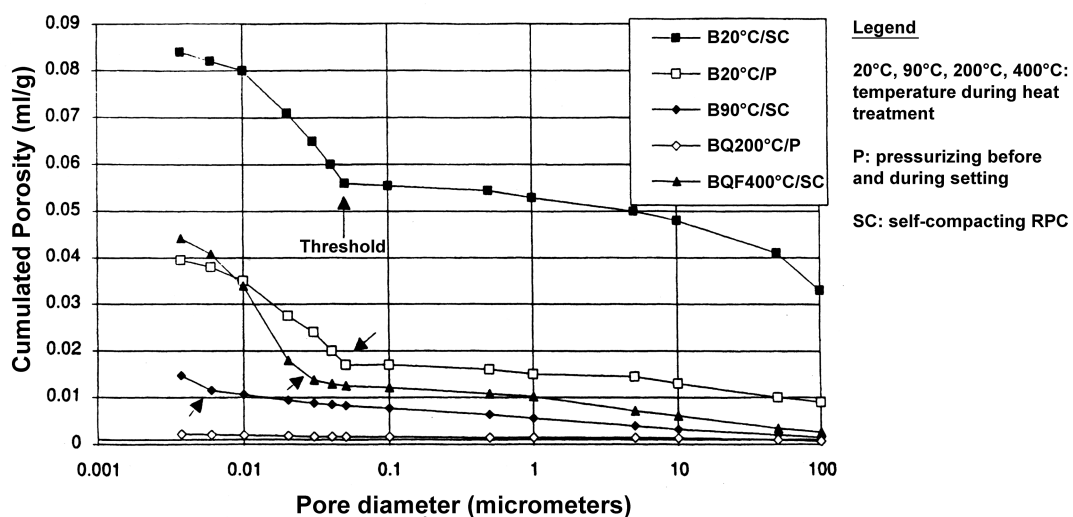


FIGURE 2.16: Cumulative porosity of UHPFRC (from [Cheyrezy95])

**Permeability.** Roux et al. also measured the air permeability on heat-treated sound RPC specimens. The permeability coefficient  $k = 2.5 \cdot 10^{-18} \text{ m}^2$  was 50 to 500 times lower than the one of normal strength concrete. The measured values were near the sensitivity threshold of the used test method.

Permeability measurements were conducted at the MCS on damaged and undamaged UHPFRC specimens [Charron04]. The investigated UHPFRC, CEMTEC<sub>multiscale</sub><sup>®</sup>, is identical to the one used in the experimental campaign of the present study. The damage, expressed by cumulated crack openings, was induced with the uniaxial tensile test described in Section 3.2.4. The displacement  $\Delta l$  refers to the deformation over 10 cm that was reached during the uniaxial tensile test just before unloading (Figure 2.17a), i.e. the reversible part of the deformation during unloading is included in the given values.

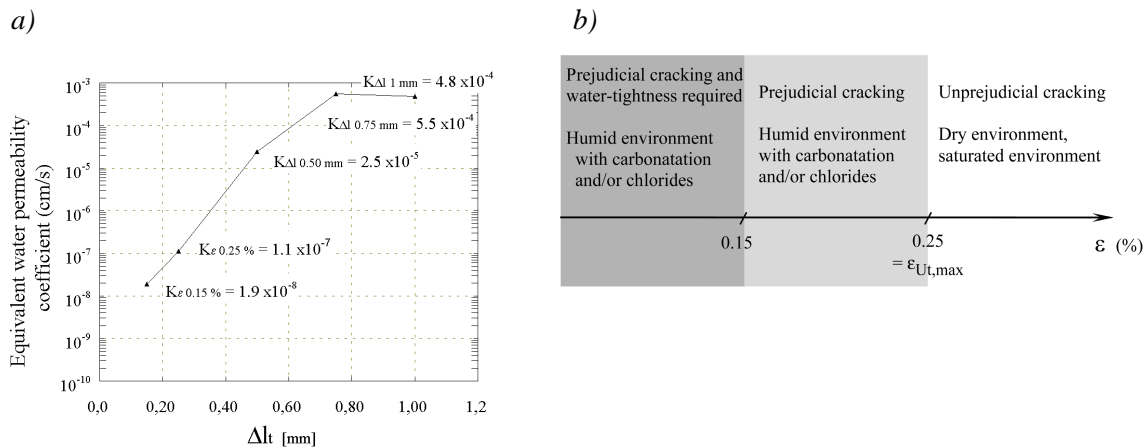


FIGURE 2.17: Permeability of CEMTEC<sub>multiscale</sub><sup>®</sup>: a) water permeability coefficients, b) proposed classes for structural application (after [Charron04])

The evolution of the water permeability for increasing tensile deformation  $\Delta l$  is shown in Figure 2.17a. In the hardening domain of the UHPFRC (see Figure 2.12), multiple cracking with small widths occurs, and the permeability remains small. Here, the permeability coefficient  $K_{\epsilon}$  refers to the deformation in the specimen  $\epsilon$ . When the UHPFRC is in the softening domain, a strong increase in crack width in a localized crack and consequently in the permeability coefficient were observed. The permeability coefficient  $K_{\Delta l}$  is referred to the deformation  $\Delta l$  measured during the uniaxial tensile test.

On the basis of the test results, durability and serviceability criteria for structural applications were defined by Charron (Figure 2.17b). If severe conditions such as water tightness are required, the deformation  $\epsilon$  is limited to 0.15%, a value that lies approximately at 70% of the hardening domain of the UHPFRC (see Section 3.2.4). In case of high requirements on permeability, e.g. structural elements in humid environment with carbonation and/or chlorides, the deformation is limited to the deformation at the end of the hardening domain  $\epsilon_{U_t, \max}$ , corresponding to 0.25% for the tested material. If the protection function of UHPFRC is of secondary importance, higher crack widths may be admitted.

**Water adsorption.** The water adsorption of RPC was measured by Roux et al. It was more than 15 times smaller with 0.2 kg/m<sup>2</sup> than for normal strength concrete after 20 days. This can be explained by the small porosity and the absence of capillary pores [Roux96].

**Chloride ions diffusion and migration, corrosion.** The chloride ingress into heat-treated, pressed RPC was measured with a steady-state chloride flow through potential differences. It was very low with an effective diffusion coefficient  $D_{\text{eff}} = 0.02 \cdot 10^{-12}$  m<sup>2</sup>/s, which was more than 30 times lower than for normal strength concrete [Roux96]. Roux measured also the corrosion rate of RPC. RPC has a very high ohmic resistance in comparison to normal strength concrete, which reduces the electrical current and the corrosion rate. The corrosion rate was not exactly determined, since the measurements attained the sensitivity threshold of the test method [Roux96].

The deterioration of damaged UHPFRC (CEMTEC<sub>multiscale</sub><sup>®</sup>) was investigated by Parant. Microcracks were created in plates under bending that were exposed to wetting-drying cycles (in NaCl-solution) in their loaded stage. The results showed that the effect of self-healing was more important than the effect of chloride ingress. The cracks were closed by new hydrates that could form due the water



supply of the NaCl solution. No significant corrosion was observed on the steel fibres in the UHPFRC [Parant03].

**Carbonation.** Roux et al. determined the resistance of RPC to the penetration of carbon dioxide by one natural and two accelerated carbonation tests. The carbonation was monitored by a phenolphthalein colour indicator. No carbonation was detected for the RPC, compared to a carbonation coefficient of 50 mm/year<sup>0.5</sup> for normal strength concrete in the accelerated test [Roux96].

**Freeze-thaw cycles.** Bonneau et al. investigated the resistance of RPC to freeze-thaw cycles according to ASTM C 666. The durability was evaluated after 300 freezing and thawing cycles in form of the ratio of the moduli before and after the cycles. No reduction of the moduli was observed [Bonneau97].

*The measurements of permeability and transport properties showed that the ingress of substances in the UHPFRC is significantly reduced when compared to normal strength concrete. Consequently, UHPFRC seem to be appropriate materials in case of high requirements on protection.*

### 2.3.5 Applications

UHPFRC were originally developed for the precast industry. The typical way to use UHPFRC is to produce precast elements that are assembled on the building site. The high strengths and the low permeability suggest the use of UHPFRC for zones subjected to detrimental substances or where high mechanical loads have to be introduced or transferred. UHPFRC have been applied for example for footbridges, beams in nuclear power plants, staircases and offshore structures [Cheyrezy97, Bekaert99, Behloul03, Aarup04]. They have not been cast in-situ yet. Moreover, the concept of UHPFRC is either to use them without additional reinforcement or in prestressed elements. To the author's knowledge, they have not been used in combination with rebar yet.

*UHPFRC material properties make them ideal materials for rehabilitation and in new composite "UHPFRC-concrete" elements. However, it has to be demonstrated that the outstanding properties of UHPFRC can be exploited in composite element with and without rebar in the UHPFRC layer.*

*Experimental campaigns have been conducted on some types of UHPFRC, however, there is still few knowledge of their material properties, in particular with regard to early age effects, viscoelasticity, tensile behaviour and the evolution of the material properties in time.*

## 2.4 Cementitious material-to-rebar behaviour

*This section can be seen as transition between material and structural behaviour. The bond model of rebar and the effect of fibre reinforced concrete (FRC) in structures consisting of reinforced cementitious materials, e.g. FRC with rebar, are described in brief.*

**Bond model.** The bond-slip relationship between rebar and concrete is described in four stages [fib10] (Figure 2.18):

- I. For low bond values ( $\tau \approx 0.2$  to  $0.8 \cdot f_{ct}$ ), the bond is due to chemical adhesion.
- II. When the force in the rebar increases, chemical adhesion breaks and microcracking occurs near the interface rebar-concrete and the force is transferred by the ribs of the rebar propping up against the concrete.
- III. For still higher bond stresses ( $\tau > 1$  to  $3 \cdot f_{ct}$ ), longitudinal cracks split radially.
- IV. After the maximum force is reached, the rebar is pulled out. Slip at failure increases with increasing confinement: For weak confinement, the longitudinal cracks break out through the concrete cover and the bond tends to fail abruptly. For confined bars, bond failure is caused by gradual bar pull-out as shown in Figure 2.18.

The bond-slip relationship applies in analogy to fibres.

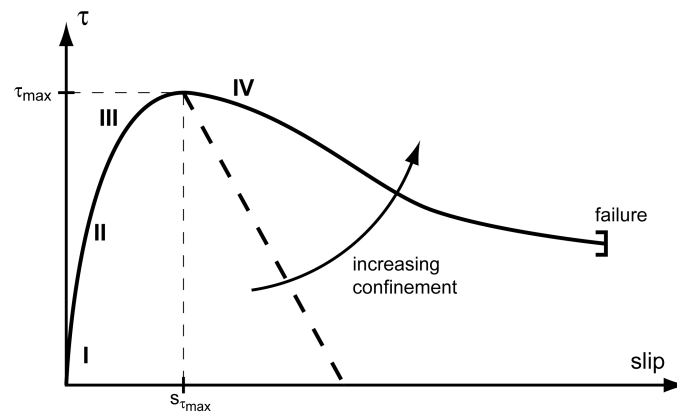


FIGURE 2.18: Conceptual local bond stress-slip behaviour in confined concrete

**Effect of SFRC and HPRCC.** HPRCC, e.g. SIFCON and ECC, in combination with rebar show a significantly increased bond strength, especially in the post-yielding regime. Microscopic discontinuities lead to activation of localized interfacial bond. The force increases after the yielding of the reinforcement until the maximum strength of the HPRCC is reached which is attributed to strain hardening. The use of steel fibres increases also energy and ductility of bond failure [Hamza96, Fischer02].

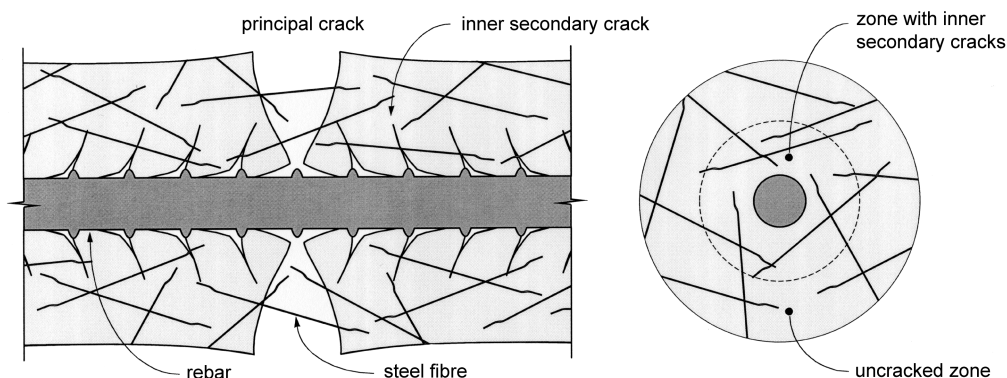


FIGURE 2.19: Effect of steel fibres on concrete-to-steel bond (from [Pfy103] on the basis of [Goto71])

Reinforced SFRC, e.g. structural elements consisting of SFRC and rebar, is characterized by significantly increased tension stiffening, since the steel fibres partially bridge cracks (Figure 2.19) [Abrishami97]. Crack width and spacing are reduced by the addition of steel fibres [Vandewalle00]. Visible cracks occur at a higher level (70% of the maximum force) than for normal strength concrete (30% of the maximum force) [Hamza96]. Pfy1 observed crack branching and late localization into equidistant macrocracks. Crack spacing and widths are already reduced by low fibre ratios, in parallel the stiffness is increased. The fibre effect is modelled with the extended tension chord model [Pfy103]. In case of ECC, no distinct first cracking load is observed. At the maximum force, multiple cracking is observed in the ECC with a width of 0.2 mm every 10 mm [Fischer02].

**Mechanically necessary concrete cover.** In normal strength concrete, the failure of the system rebar-concrete is caused by pull-out (and not by spalling) when the ratio concrete cover to bar diameter ( $c/d_s$ ) is higher than 1 to 2.5, depending amongst other parameters on rebar roughness and spacing. For typi-

cal parameters, the ratio was determined to  $c/d_s = 1.19$  [Schenkel98]. The addition of steel fibres reduces crack widths and spalling [Abrishami97, Hamza96].

*There exist no tests on reinforced UHPFRC to the author's knowledge. However, the behaviour of rebar in UHPFRC should be comparable to the one of reinforced SIFCON [Hamza96], if not even better due to the denser matrix of UHPFRC. Thus, bond between UHPFRC and rebar should be characterized by high bond strength and small slip. The spalling risk should be low due to the high amount of steel fibres in the UHPFRC and narrowly distributed fine cracks should form in reinforced tension chords. The mechanically necessary cover of UHPFRC should be approximately the rebar diameter ( $c/d_s = 1$ ).*

## 2.5 Deformation capacity

*From this section on, aspects on the structural level are described. Fundamentals on deformation capacity are discussed in this section with a special regard to the effect of steel fibres.*

**Ductility.** Ductility is the capacity of a material or a structure to dissipate energy by plastic deformation [Sigrist95]. Sufficient ductility of structures is necessary for redistribution of action effects in statically indeterminate systems, to announce failure by means of large deformations, for resistance against imposed deformations and for energy dissipation during impact or seismic loading [CEB242].

**Required rotation capacity.** Ductility of structures can be evaluated with deformation or energy criteria. Ductility of reinforced concrete members subjected to bending is often described by the rotation capacity [CEB242]. Studies were conducted to estimate the required rotation capacity for statically indeterminate systems in function of the degree of internal redistribution. Maximal required rotation capacities of a rotation of  $\theta = 0.03$  rad were found for statically indeterminate beams for a limit of the position of the neutral axis  $\xi = x/d \leq 0.5$  and a maximum moment redistribution of 25% [Cosenza91]. The required rotation capacity increases with increasing slenderness of a beam ( $l/d$ ) and with increasing moment redistribution, i.e. with decreasing redistribution degree. Furthermore, it depends on the static system [Cosenza91]. If linear-elastic design models are used, a certain rotation capacity is required because the actual behaviour differs from the assumed elastic behaviour. The required rotation capacity was evaluated to  $\theta = 0.01$  rad for  $\xi \leq 0.5$ .

**Available rotation capacity.** The available rotation capacity can be derived from the curvature distribution over the length of the structural member. For modelling, the curvature is assumed to be concentrated in plastic hinges (Figure 2.20a). The rotation capacity can be calculated in a simplified way by assuming a constant plastic curvature over the reduced length of the plastic hinge  $L_{hi}$  (Figure 2.20b). By integrating the curvature according to M- $\kappa$ -relationships over the plastic hinge  $L_{hi}$ , the rotation capacity is obtained.

The available deformation capacity of concrete elements under bending is determined by the reinforcement ratio and by the deformation capacity of the rebar. It is recommended to design the member in a way such that yielding of steel reinforcement in tension occurs before fracture of the concrete in compression. In this way, fracture is announced by large deformations and cracking.

**Deformation capacity of SFRC structures.** Pfyl investigated the behaviour of reinforced steel fibre reinforced concrete, i.e. structural elements with rebar and steel fibre concrete with steel fibre contents of 30 and 60 kg/m<sup>3</sup> [Pfyl03]. Tests on uniaxial tension elements and on bending beams showed that an increasing fibre content reduced crack spacing and increased the ultimate load, but also reduced the deformation capacity at failure, since the tension chord of the bending moment is reinforced by the steel fibres and premature failure may occur in the compression zone. The elements with high fibre content showed a softening behaviour after yielding of the steel rebar. This is due to the localization of deformation that occurs in fewer macrocracks than for comparable RC elements. Pfyl recommends to use SFRC in combination with rebar to enhance crack distribution and to guarantee sufficient deformation

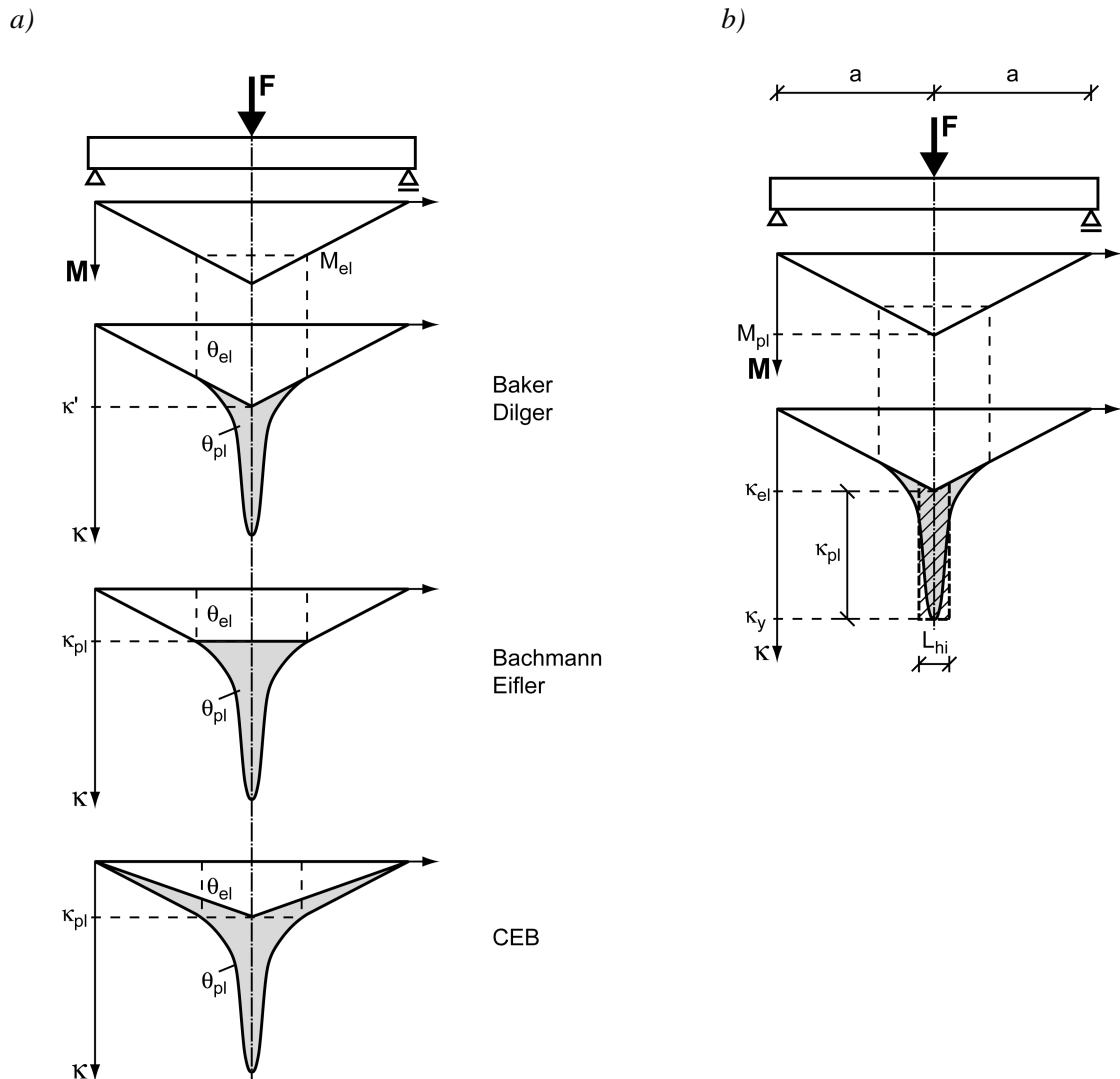


FIGURE 2.20: a) Definition of plastic hinges [CEB242], b) simplified definition of the plastic hinge after [Baker61] (from [CEB242])

capacity of the structural element. He suggests to design elements in such a way to ensure hardening behaviour in the structural element until fracture of the rebar.

The length of plastic hinges for SFRC members is estimated by Massicotte to  $L_{hi} = \frac{1}{2} \cdot (\text{depth of the structural element})$  for configurations without rebar and to  $L_{hi} = \max(\frac{1}{2} \cdot \text{depth of the structural element}; \text{crack spacing})$  for configurations with rebar [Massicotte03]; Casanova and Rossi propose  $2 \cdot (\text{length of the discrete crack})$  for SFRC structures without rebar [Casanova94] and Dupont  $2 \cdot (\text{height of the neutral axis})$  [Dupont03].

*The deformation capacity of structural elements consisting partially or totally of reinforced UHP-FRC has not been investigated. However, the high content of short fibres may lead to a reduction of the deformation capacity when softening in the UHPFRC occurs due to gradual fibre pull-out.*

## 2.6 Composite structural elements of reinforced cementitious materials

*The behaviour of composite elements consisting of reinforced cementitious materials is described in this section. First, the degree of restraint is discussed. Then, composite reinforced concrete (RC) elements are presented in brief with a focus on the aspects of time-dependent behaviour that are important for composite “UHPFRC-concrete” members and on failure modes. Finally, an overview of composite “ACM-concrete” elements is given concentrating on composite “UHPFRC-concrete” elements.*

### 2.6.1 Degree of restraint

In composite elements, the stress state in the new layer due to shrinkage can be estimated by the degree of restraint  $\mu$ . Shrinkage deformations of the new layer induce residual stresses in the structural element (Figure 1.5). The maximum tensile stresses build up in the new layer at the interface. They can be calculated by using the degree of restraint  $\mu$  (EQ. 2.3). The degree of restraint for composite slabs, consisting of two rectangles with an identical width, was calculated by [Silfwerbrand97], it was extended to more general cross-sections by [Bernard00] as developed in the following.

$$\sigma_{\text{new},2} = \mu E_{\text{new}} \varepsilon_{\text{free}} \quad (\text{EQ 2.3})$$

with  $\sigma_{\text{new},2}$  [MPa]: tensile stress in the new layer at the interface,  $\mu$  [-]: degree of restraint,  $E_{\text{new}}$  [MPa]: modulus of elasticity of the new layer,  $\varepsilon_{\text{free}}$  [-]: mean shrinkage strain in the new layer.

The degree of restraint is calculated with EQ. 2.4 under the following hypotheses:

- linear-elastic material behaviour,
- Poisson's ratio  $\nu = 0$ ,
- the cross-section of the new layer is rectangular, the cross-section of the substrate can be of any shape,
- plane sections remain plane (hypothesis of Bernoulli) and
- perfect adherence between new layer and substrate.

$$\mu = \frac{\sigma_{\text{new},2}}{\sigma_{\text{rest}}} = \frac{\sigma_{\text{rest}} + \sigma_N + \sigma_{M,2}}{\sigma_{\text{rest}}} = 1 + \mu_N + \mu_M \quad (\text{EQ 2.4})$$

The principle of the analysis consists in determining the tensile force  $N_t$  that is necessary to compensate the unrestrained shrinkage deformation  $\varepsilon_{\text{free}}$  in the new layer (Figure 2.21). The tensile force is balanced in the composite member by a compressive force  $N_c$  and a bending moment  $M_c$  acting in the centre of gravity (cg). The stress state in the composite element is determined by the superposition of  $N_t$ , and  $N_c$  and  $M_c$ .

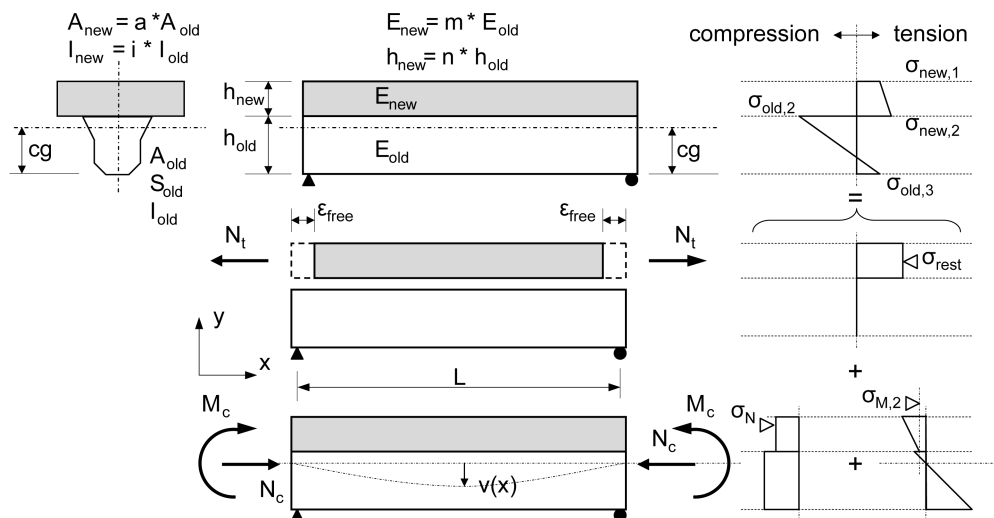


FIGURE 2.21: Normal stresses in a statically determinate composite beam (elastic stress-strain relation) (from [Bernard00])

**Statically determinate systems.** The degree of restraint  $\mu$  can be subdivided into the part of the axial force  $\mu_N$  and the part of the bending moment  $\mu_M$ . The equations for statically determinate beams (SD) are given in EQ. 2.5 and EQ. 2.6, the equation for the centre of gravity in EQ. 2.7. They apply to rectangular cross-sections of the new layer and cross-sections of any shape of the substrate.

$$\mu_{N,SD} = \frac{-m a}{1 + m a} \quad (EQ 2.5)$$

$$\mu_{M,SD} = \frac{-m a A_{old} \left( h_{old} \left( 1 + \frac{n}{2} \right) - cg \right) (h_{old} - cg)}{I_{old} (1 + m i) + A_{old} \left( cg - \frac{S_{old}}{A_{old}} \right)^2 + m a A_{old} \left( h_{old} \left( 1 + \frac{n}{2} \right) - cg \right)^2} \quad (EQ 2.6)$$

$$\text{with } cg = \frac{S_{old} + m a h_{old} A_{old}}{A_{old} (1 + m a)} \quad (EQ 2.7)$$

The degree of restraint in a statically determinate system  $\mu_{SD}$  is shown in Figure 2.22a for beams or slabs consisting of two rectangular cross-sections with the same width in function of the ratio of the thicknesses  $n$  and the ratio of the moduli of elasticity  $m$ . The degree of restraint is the highest for low ratios  $m$ , i.e. when the modulus of elasticity of the new layer is small, corresponding to the early age of the composite element. For composite “UHPFRC-concrete”, the final ratio  $m$  members lies between  $m = 1.2$  and  $2.0$  (for higher ages). The degree of restraint has the highest values for a ratio of the thicknesses  $n < 0.3$  to  $0.5$  (depending on  $m$ ). This indicates that tensile stresses and cracking risk are maximal for thin layers.

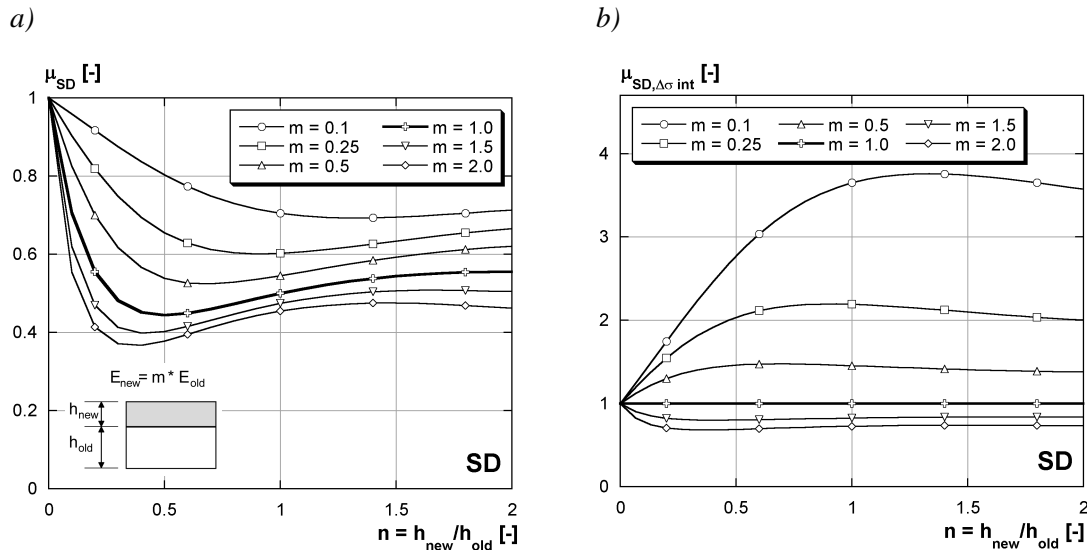


FIGURE 2.22: a) Degree of restraint of a statically determinate beam, b) relative stress difference at the interface between new layer and substrate

Figure 2.22b indicates the relative stress difference between old and new layer for statically determinate systems according to EQ. 2.8. At free ends, this stress difference induces stresses perpendicular to the interface ( $\sigma_y$ ) which are determinant for debonding due to shrinkage of the new layer (case 1 in Figure 1.5b). Consequently it can be used to determine the debonding risk. The latter is highest for low

values of  $m$ , i.e. at early age of the composite member and decreases with increasing  $m$  and age respectively.

$$\sigma_{\text{new},2} - \sigma_{\text{old},2} = \mu_{\text{SD}, \Delta\sigma_{\text{int}}} E_{\text{new}} \varepsilon_{\text{free}} \quad (\text{EQ 2.8})$$

**Statically indeterminate systems.** In statically indeterminate systems, the internal stresses due to restrained shrinkage are partially redistributed. The degree of restrained shrinkage is significantly increased. Yuan determined an increase of 30% in an example [Yuan94]. The effect of statically indeterminate systems is considered by factors  $\theta_N$  and  $\theta_M$  for axial and bending restraint respectively (EQ. 2.9, EQ. 2.10). These factors are the ratio between the statically indeterminate part of the reaction ( $N_{\text{SID}}$ ,  $M_{\text{SID}}$ ) and the reaction in case of total restraint ( $N_c$ ,  $M_c$ ). They are 0 for statically determinate systems and 1 in completely restrained systems.

$$\mu_{\text{SID}} = 1 + (1 - \theta_N)\mu_{N, \text{det}} + (1 - \theta_M)\mu_{M, \text{det}} \quad (\text{EQ 2.9})$$

$$\text{with } \theta_N = \frac{N_{\text{SID}}}{N_c} \quad \text{and} \quad \theta_M = \frac{M_{\text{SID}}}{M_c} \quad (\text{EQ 2.10})$$

The degree of restraint as it is presented here does not consider viscoelasticity and non-linear stress-strain distributions which would be the case in composite ‘‘UHPFRC-concrete’’ members. However, it is a simple tool for the estimation of the stress state in composite elements.

## 2.6.2 Composite RC elements

### 2.6.2.1 Processing

The durability of composite elements depends essentially on correct processing and has been extensively studied (e.g. by [Emmons00, Pigeon92, Schrader92]). The preparation of the contact surface is essential to guarantee monolithic behaviour under actions. Sandblasting and hydrojetting are the most adapted methods with regard to damage and roughness (e.g. [Courard99, Silfwerbrand90, Warner98, Zhu91]). The contact surface of the substrate should be humid, but not wet. In general, bonding agents and mechanical connectors are not necessary, if a surface preparation method is applied that creates sufficient roughness and if the design of the structural member is adapted in zones of force introduction [Bissonnette00, Bernard00]. A new concrete should be chosen whose properties are close to the substrate and good curing (minimum of 5 days) should be performed. A comprehensive overview of correct processing can be found in [Bernard00].

### 2.6.2.2 Time-dependent behaviour

The determinant time-dependent phenomena for composite RC members are deformations due to hydration effects, i.e. thermal deformations due to the heat release and autogenous shrinkage as shown by [Bernard00], and drying shrinkage in the long term.

**Thermal effects due to heat of hydration.** During hydration, heat is released in the new layer, first leading to a temperature rise and when the hydration reaction slows down to cooling of the element. The temperature increase is high in the new layer and relatively low in the substrate leading to a temperature gradient in the element. The evolution of maximum and minimum temperature in a composite element is schematically shown in Figure 2.23a. Due to the restraint, temperature rise induces compressive stresses in the new layer until time  $t_{\text{peak}}$  (Figure 2.23b). During cooling, tensile stresses build up in the new layer and may lead to cracking. The determinant parameter for residual thermal stresses is the *maximum temperature difference between old and new layer*  $\Delta T_{\text{o-n,peak}}$  [Bernard00]. Bernard proposed

a simplified approach to estimate the cracking risk due to early age thermal deformations and found a threshold value of  $\Delta T_{o-n,peak} \leq 12 \text{ }^\circ\text{C}$  to avoid cracking for average properties of normal strength concrete [Bernard00]. The temperature difference in composite elements becomes important for massive members such as curbs [Brühwiler00].

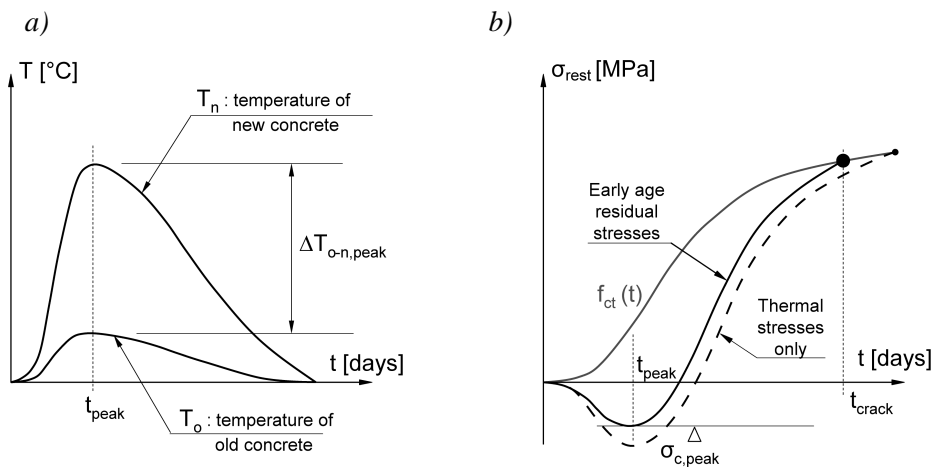


FIGURE 2.23: Early age behaviour of composite elements: a) temperature evolution, b) stress evolution in the new layer considering only thermal stresses and considering thermal stresses, autogenous shrinkage and viscoelasticity (adapted from [Bernard00])

The *cracking risk* is small for slender composite beams with a thickness ratio of new to old layer between  $h_{new}/h_{old} = 0.45$  and 1.1 under constant ambient temperature of  $20 \text{ }^\circ\text{C}$  [Bernard02]. However, ambient temperature and its variation may significantly increase the stresses due to thermal effects [Brühwiler00]. The cracking risk due to thermal stresses can be limited by adapting the temperature of the fresh concrete, by using an adapted low-heat concrete mix design, by heating the existing structural element during heat rise and by adapted curing. Further details about adequate methods can be found in [Bernard00, Bernard01, Brühwiler00].

**Autogenous Shrinkage.** Autogenous shrinkage is an important phenomenon that induces curvature and tensile stresses at early age, even for normal strength concrete with  $w/c = 0.5$ . It is mainly important during the first two days after casting of the new layer. Autogenous shrinkage reduces the compressive strength  $\sigma_{c,peak}$  and increases the tensile stresses in the new layer, i.e. the curve of stress evolution due to thermal effects is shifted towards tension (e.g. upwards in Figure 2.23b). The tensile stresses may lead to transverse crack formation in the composite element [Bernard02].

**Viscoelasticity.** The stresses in the composite element are partially relaxed by concrete viscoelasticity. Viscoelasticity is significant for early age concrete and decreases gradually. Ducret measured residual stresses in composite “reinforced concrete - steel” beams even at a concrete age of 28 days [Ducret97]. Viscoelasticity is higher in the new concrete layer and leads mainly to stress relaxation in the new layer of 50 to 70% after one year [Bernard00]. The importance of viscoelasticity on the reduction of the cracking risk in new layers is demonstrated by [Bernard00, Bissonnette00, Silfwerbrand87]. In consequence, Bissonnette proposes the concept of global deformation to evaluate stress state and cracking in composite elements.

**Drying Shrinkage.** Drying shrinkage is the most important phenomenon in composite members consisting of two layers of normal strength concrete. Various studies show its importance for thin repair layers and thicker structural layers (e.g. [Bernard00, Granju01, Martinola01, Sadouki97, Silfwerbrand97]). Drying shrinkage induces a moisture gradient in the new layer, leading to increased tensile stresses at the surface. Bernard determined the conditions under which transverse cracks form. Structural parameters such as geometry and static system and material parameters decide upon the cracking risk due to drying shrinkage. A comprehensive overview of drying and its influence on composite concrete elements can be found in [Bernard00].



Since drying shrinkage does not seem to play a major role in composite “UHPFRC-concrete” members, it is not discussed any further in this section and reference is made to the extensive literature. However, thermal effects and self-desiccation shrinkage are important in UHPFRC and may govern the behaviour of composite “UHPFRC-concrete” elements.

**Role of reinforcement.** Rebar in the new layer induces additional local restraint thus, increasing the cracking risk. In parallel, the deformations of the composite element are reduced. This is demonstrated for drying shrinkage by [Bernard03].

Steel fibres in the new layer reduce crack widths and spacing and debonding. For thin SFRC overlays, Chausson identified as most important factor the ratio post-cracking strength to tensile strength, since this ratio is determinant for the control of cracking [Chausson97]. The effect of materials with strain-hardening is discussed in Section 2.6.3.1.

**Modelling.** The time-dependent behaviour of composite concrete elements is either evaluated by analytical models or by FE-programs.

The *analytical models* are mainly developed to determine the residual stresses in the new layer and at the interface. In general, they consider uniform shrinkage and in some cases also creep [Silfwerbrand97, Yuan94].

*FE-programs* give the possibility to take into account thermal, hygral, chemical effects and the resulting deformations and crack formation either by the fictitious crack model or the crack band model. The options of the programs and their degree of couplings between the phenomena vary from program to program. Such models were developed and extended for example by [Bernard00, Emborg89, Femmasse04, Martinola01, Kranz99]. A detailed description of the models can be found in [Bernard00].

### 2.6.2.3 Failure modes

Composite elements consisting of normal strength reinforced concrete are designed in the same way as reinforced concrete structures, if monolithic behaviour is guaranteed. Residual stresses do not play a role in design, since they are small in the substrate in compression and tensile stresses of concrete are neglected at the ultimate limit state (ULS). This is demonstrated in [Silfwerbrand97]. Thus, nearly all investigations of the fracture behaviour of composite members focus on the evaluation of debonding.

**Debonding.** The properties of the interface zone depend on the design and processing. The influence of material parameters and surface preparation methods, partially in combination with connectors, on the debonding resistance has been extensively studied (e.g. by [Courard99, Randl00, Silfwerbrand90, Trausch01, Vaysburd01, Warner98]). By using adequate surface preparation methods (i.e. hydrojetting or sandblasting), the tensile strength in the interface zone amounts to approximately 60 to 70% of the concrete strength of the substrate or the new concrete [Bernard00a, Warner98]. Moreover, the modulus of elasticity of the new layer should be close to the one of the old layer ( $E = \pm 10$  GPa) in order to minimize the debonding risk [Emberson96].

Brenni conducted structural beam tests in order to determine the interface resistance by using different surface preparation methods and type of connectors. He concluded that best results are obtained by combining a high interface roughness with connectors. He proposed to design the composite members by exclusively considering the connectors and by neglecting the adherence between the two layers [Brenni95].

This approach is rather conservatory, since it has been shown that composite concrete elements may behave in a monolithic way without connectors [Bernard00, Silfwerbrand87]. Bernard showed that structural (geometry, static system) and material parameters influence the debonding risk and defined limit conditions to avoid debonding. His debonding criterion is conservatory - debonding already occurs when an interface crack starts to form. However, small interface cracks do not alter the structural response of the composite member. A design method is proposed for the determination of the thickness

of and the reinforcement ratio in the new layer by respecting the design moment and by preventing debonding [Bernard00, Habel00].

### 2.6.3 Composite “ACM-concrete” elements

#### 2.6.3.1 Composite “HPFRCC-concrete” beams

Composite “ACM-concrete” elements have been investigated using the HPFRCC ECC and SIFCON/SIMCON. The HPFRCC are used as thin overlays with thicknesses from 1 to 5 cm for deteriorated structures such as cracked pavements or bridge decks. Their tensile strain-hardening improves deformation and energy adsorption capacity. Thus, they are able to bridge cracks in the existing concrete substrate. The cracks in HPFRCC remain small (between 30 and 50  $\mu\text{m}$ ) and are densely distributed [Krstulovic96].

Promising results have been obtained in field studies with SIFCON. No damage and no debonding were observed in a thin pavement overlay (thickness: 2.5 cm) after 9 years of service life [Schneider92]. It is argued that the small crack widths diminish considerably the penetration of detrimental substances and thus, the deterioration of reinforcement in the composite element. [Li00, Krstulovic97, Krstulovic96].

Studies on chloride penetration into SIFCON show that the corrosion rate is reduced compared to SFRC, but, corrosion also occurs in non-damaged SIFCON elements [Kosa91]. This can be attributed to the porosity of the non-optimized SIFCON matrix and on possible shrinkage cracking at early age [Lemberg96]. The diffusion coefficient of sound ECC is similar to the one of concrete (with  $w/c = 0.35$ ) for  $RH < 65\%$ ; for  $RH > 65\%$ , the diffusion coefficient of ECC is higher than for concrete [Weimann03] and attempts are made to modify the ECC composition with internal water repellent agents in order to guarantee durability [Martinola02]. Consequently, HPFRCC are subjected to deterioration processes in time and should not significantly improve the durability of a structural element in the long term when compared to normal strength concrete.

*Existing research results show that tensile strain-hardening of HPFRCC is beneficial in composite elements with regard to crack widths. However, the relatively high permeability of ECC and SIFCON may reduce the protection function of the HPFRCC layer in the long term.*

#### 2.6.3.2 Composite “UHPFRC-concrete” beams

Composite “UHPFRC-concrete” beams were tested at the MCS in 3-point-bending in order to investigate the structural response and cracking (Figure 2.24) [Denarie01, Denarie03]. The used UHPFRC was a type of DUCTAL<sup>®</sup> with short steel fibres ( $l_f = 13 \text{ mm}$ ) [Orange00]. No rebar were placed in the UHPFRC layer. Reference beams in RC with a reinforcement ratio  $\rho = 0.8\%$  were also tested.

The results show that the maximum force of the beams was comparable for the RC beams and the composite beams (Figure 2.24). The stiffness of the composite beams was increased until the maximum force was reached. This is explained by the improved tensile properties of UHPFRC, in particular by the high tensile strength and by strain hardening increasing the deformation capacity of the UHPFRC before the formation of a localized macrocrack. However, the force decreased strongly after its maximum for the composite beams, while the RC beams showed hardening behaviour. Moreover, the measured crack openings increased slower for the RC beams than for the composite beams. This was due to the relatively small length of the steel fibres in the UHPFRC that were pulled out and could not transfer force through cracks with large widths.

The UHPFRC “CARDIFRC” is used as bonded strips in the tension chord for rehabilitation and improvement of existing concrete beams [Alaee03]. Rebar is incorporated in the existing concrete in the tension chord. The UHPFRC is cast separately and bonded to the concrete member with an epoxy adhesive. The tension side and in some cases also the sides of the beams are strengthened. The composite beams show monolithic behaviour under 4-point-bending until fracture. The maximum force of the composite beams is equal or higher than of the existing concrete member; however, the force-deflection curves show softening behaviour after the maximum force is reached.

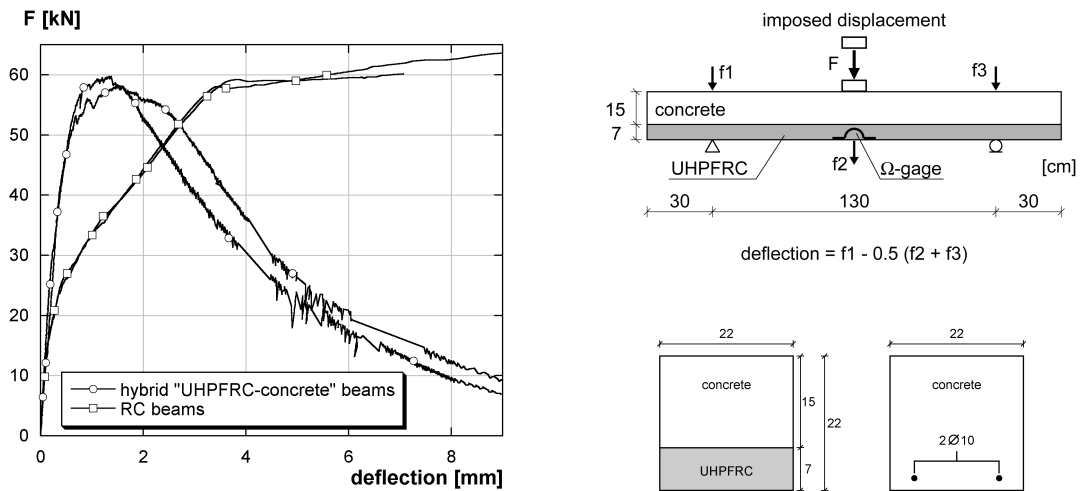


FIGURE 2.24: Structural response of composite "UHPFRC-concrete" beams in comparison to reinforced concrete beams (after [Denarie03])

The use of UHPFRC as bonded strips is promising, however, the epoxy adhesive used to bond the UHPFRC to the concrete may cause problems in terms of sufficient durability and the advantage of the good bond by casting the UHPFRC directly on the substrate cannot be exploited.

The results show that UHPFRC is a promising material for the rehabilitation of concrete beams. The advantage of UHPFRC when compared to HPRCC is their low permeability that prevents the ingress of detrimental substances. This should significantly increase the durability of composite "UHPFRC-concrete" members. However, the penetration of water to the interface zone of composite "UHPFRC-concrete" members has to be prevented by adequate design in order to prevent interface cracking as a consequence of water pressure.



## 3 Experimental investigation

The main results of the experimental campaign on composite “UHPFRC-concrete” elements are presented in this chapter. The first part of the experimental work is conducted to characterize the UHPFRC CEMTEC<sup>®</sup><sub>multiscale</sub> (Section 3.2) and to give an overview of the concrete properties (Section 3.3), the second part consists of the investigation of the structural behaviour of composite “UHPFRC-concrete” elements (Section 3.4). A more detailed description of the experimental campaign can be found in [Habel04].

### 3.1 Introduction

The objectives of the experimental campaign are the investigation of the structural behaviour of composite “UHPFRC-concrete” elements and the characterization of the UHPFRC properties. Thus, an experimental campaign is conducted with beam tests on composite “UHPFRC-concrete” elements and with material tests on UHPFRC and concrete. Only the part of the material test results on the concrete are presented that are needed as input values for the numerical simulation.

The material properties of UHPFRC are still little known and their properties may vary considerably for different kinds of UHPFRC. Material tests are conducted on the UHPFRC used in this study in order to evaluate its outstanding mechanical properties and its time-dependent behaviour. The study focuses on the evaluation of thermal and hygral changes and deformations at early age and on the tensile properties, determined by an original uniaxial tensile test.

The structural behaviour of composite “UHPFRC-concrete” beams is investigated to demonstrate that the combination “UHPFRC-concrete” is beneficial, i.e. that the beams show monolithic behaviour and that the outstanding properties of the UHPFRC are exploited in composite elements at early age, in the long-term and at fracture.

The measurements start with the casting of the UHPFRC layer. Thus, the early age of the composite elements is observed. At early age, the cracking risk is the highest due to thermal and autogenous deformations. Deformations and bending creep are investigated during long-term tests. Finally, cracking, deformations and evolution of force are observed during fracture tests.

The parameters of the composite “UHPFRC-concrete” elements are chosen to cover a wide range of possible applications. Thin UHPFRC layers are tested that have mainly a protection function. Thicker UHPFRC layers with and without reinforcement are also investigated for an additional increase in resistance and stiffness.

The results of the material tests are used as input values for the modelling of composite structural elements in Chapters 4 and 5. The beams also serve to validate the models.

### 3.2 Characterization of the UHPFRC

#### 3.2.1 UHPFRC composition

The UHPFRC is a self-compacting mix with one type of fibres of the family CEMTEC<sup>®</sup><sub>multiscale</sub>, developed at the LCPC [Rossi02]. Its detailed composition is given in Table 3.1. The cement is a CEM I 52.5 N with a high quantity of silicates and low a C<sub>3</sub>A content. The sand is very fine with an average grain size of 0.3 mm, and a maximum grain size of 0.5 mm. It also contains a high amount of silicates. The silica fume is pure with 93.5 % of SiO<sub>2</sub> and is a by-product of the zirconium industry. The steel fibres are short ( $l_f = 10$  mm) and straight with an aspect ratio  $l_f/d = 50$ . Their tensile strength is high ( $f_y \approx 1200$  MPa) so that the fibres are pulled out of the UHPFRC matrix and do not break.

TABLE 3.1: UHPFRC composition

	type	weight
Cement	CEM I 52.5 N CE PM-ES-CP2 NF, Lafarge, Le Teil	1051.1 kg/m <sup>3</sup>
Sand	Sand of Fontainebleau, MN 30 (< 0.5 mm)	732.5 kg/m <sup>3</sup>
Silica Fume	SEPR (median diameter: 0.5 $\mu$ m, specific surface: 12 m <sup>2</sup> /g, SiO <sub>2</sub> : 93.5%)	273.3 kg/m <sup>3</sup>
Steel fibres	straight, $l_f = 10$ mm, $\varnothing_f = 0.2$ mm	468.0 kg/m <sup>3</sup>
Superplasticizer	Chrysofluid OPTIMA 175	35.1 kg/m <sup>3</sup>
Total water		189.2 kg/m <sup>3</sup>
w/c		0.18
w/(c+SF)		0.14

### 3.2.2 Heat of hydration and evolution of the relative humidity

*Heat of hydration* is measured with semi-adiabatic tests on cylindrical specimens ( $\varnothing$  16 cm,  $l = 32$  cm) [Charif98]. The adiabatic temperature evolution, calculated on the basis of the tests, shows a nearly constant temperature until 24 hours, followed by a fast temperature increase until 36 hours (Figure 3.1a). Then, the temperature increase slows down until a final temperature of 115 °C. In comparison, the adiabatic temperature rise of the normal strength concrete is shown in the diagram. The first phase is the dormant period which is long for UHPFRC and which is attributed to the high amount of superplasticizer. The high maximum temperature results from the high cement content of the material.

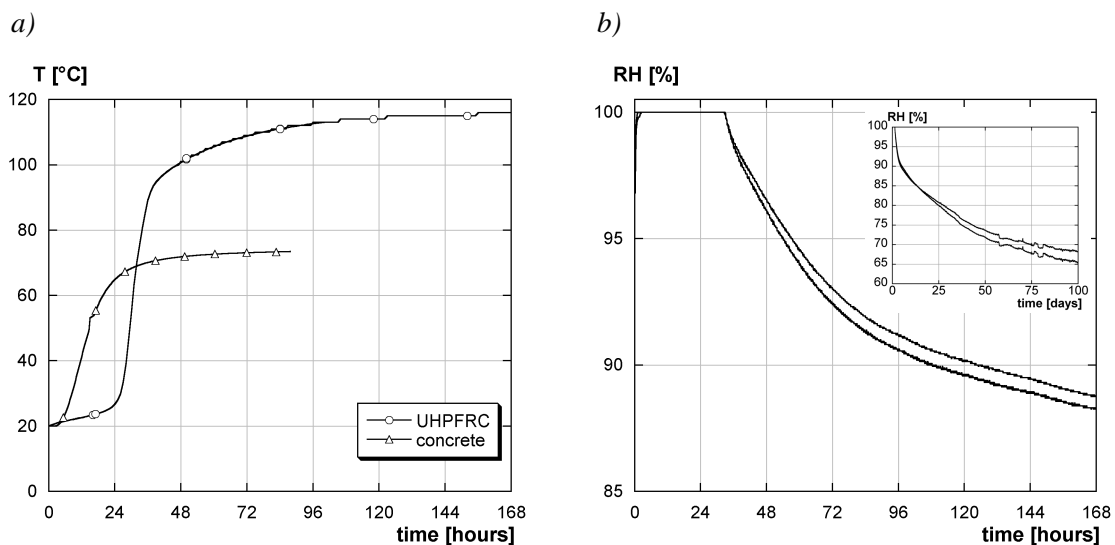


FIGURE 3.1: a) Adiabatic temperature rise of the UHPFRC compared to the concrete, b) evolution of the relative humidity (RH) in the UHPFRC

The evolution of the *relative humidity* (RH) in the sealed UHPFRC at early age is shown in Figure 3.1b; the detail shows the evolution of relative humidity during 100 days (the test set-up in [Habel04]). The relative humidity is constant at 100% during 33 hours and decreased to 88% after 168 hours (7 days). A decrease of the slope of the curve is observed after 72 hours. The w/b-ratio (0.14) is too low for complete hydration - the theoretical final degree of hydration is approximately 31% (after [Jensen01, Waller00]). The decrease of relative humidity starts at 33 hours. At this moment, the free water in the UHPFRC is consumed and menisci form in the capillary pores, leading to capillary tension in the UHPFRC and inducing chemical and macroscopic autogenous shrinkage. The lower the RH-content, the less water is available for hydration and the higher becomes the capillary tension in the pores until the hydration reaction is virtually stopped.

### 3.2.3 Compression properties

Compressive strength and secant modulus of elasticity (at 30% of the compressive strength, according to [EN206]) are determined on cylinders ( $\varnothing$  16 cm,  $l = 32$  cm). At 28 days, the average compressive strength is  $f_{U,c} = 168$  MPa and the secant modulus is  $E_{U,c} = 48$  GPa. Preliminary tests, conducted to determine the whole  $\sigma$ - $\varepsilon$ -curve for UHPFRC in compression, show that the stress rise is nearly linear-elastic until the maximum force is reached. The deformation-controlled tests indicate a strong force decrease beyond the maximum force. The specimen does not fracture suddenly, it is hold together by the confinement of the steel fibres.

### 3.2.4 Tensile properties

#### 3.2.4.1 General

The outstanding tensile properties are measured with uniaxial tests. Strain-hardening and the high tensile stresses of UHPFRC demand an efficient stiff test set-up that allows to record the whole force-displacement curve before and after the crack formation.

#### 3.2.4.2 Development of a uniaxial tensile test

A uniaxial tensile test is developed for UHPFRC. Prismatic specimens with a cross-section of  $20.5 \text{ cm}^2$  are built-in the testing machine by applying the “gluing without adherence” principle (Figure 3.2), developed in [Helbling87]: The glue (Figure 3.2b (d)) fills out the space between the specimen (Figure 3.2, (c)) and the surrounding metallic pieces (Figure 3.2, (a) and (b)). However, there is no adherence between the glue and the metallic pieces, and here the stress transfer is ensured by interlocking. The test is closed-loop displacement-controlled by the mean value of two LVDTs fixed on the specimen (Figure 3.2a, (f)).

The test set-up is stiff and bending in the specimen is virtually avoided during testing. In addition, the parameters of the closed-loop displacement-control on the specimen are adjusted to obtain stable tests before and after the formation of cracks. Further details can be found in [Habel04].

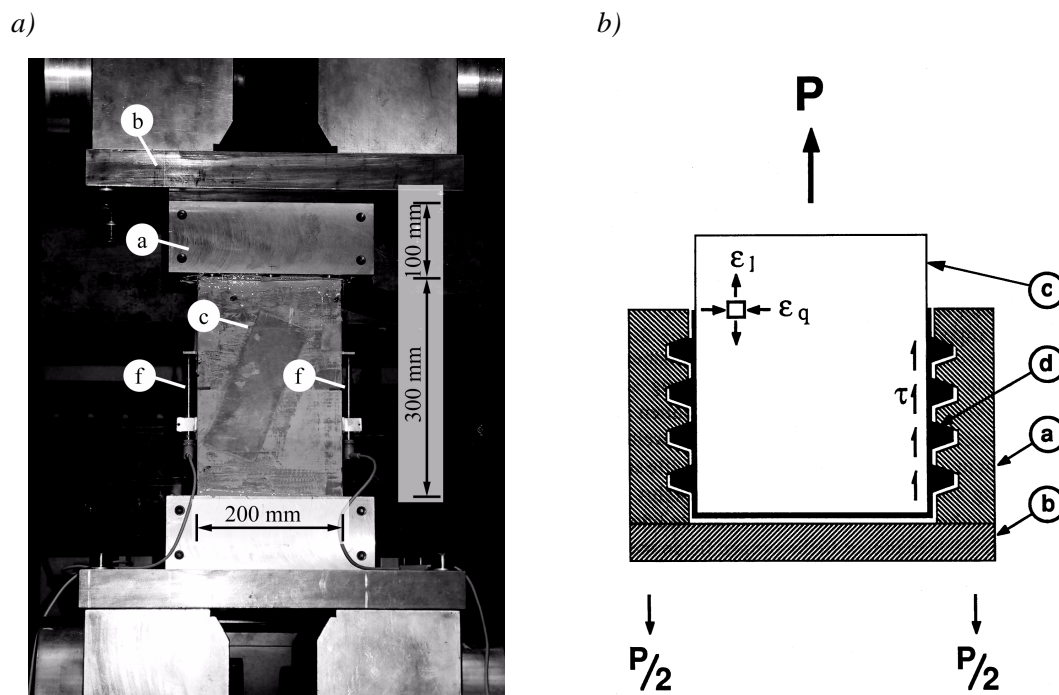


FIGURE 3.2: a) Set-up of the uniaxial tensile test, b) force introduction at the end of the specimen (from [Helbling87]): (a) surrounding metallic pieces with interlocking, (b) base plate, (c) test specimen, (d) glue, (e) testing machine, (f) LVDTs, controlling the test

### 3.2.4.3 Results and discussion

Uniaxial tensile tests are conducted on notched and on some dogbone prismatic specimens. As there are not enough results for dogbone specimens, the discussion concentrates on the results of notched specimens (Figure 3.2a, notch: 2 cm at each side). The test results show a nearly linear-elastic stress increase until the *first cracking strength*  $f_{U_t,1st}$ , followed by strain-hardening  $\epsilon_{U,hard}$  until a strain  $\epsilon_{U_t,max}$  of 0.28% at the *tensile strength*  $f_{U_t,max}$  (Figure 3.3). Crack localization occurs at the end of the strain-hardening domain. The displacement, measured with the LVDTs, before crack localization can be directly converted into deformation (Figure 3.3b). When a localized crack forms, the stress decreases monotonously until the fracture of the specimen at a crack opening  $w_{U_t,2}$ , corresponding approximately to  $l_f/2 = 5$  mm. The mean-stress-strain curve until  $\epsilon_{U_t,max}$  is shown in Figure 3.3b. The test set-up is stiff and there are only very small eccentricities during testing: at the tensile strength  $f_{U_t,max}$ , the maximum difference in the displacements between the two sides of the specimen is 40  $\mu\text{m}$ .

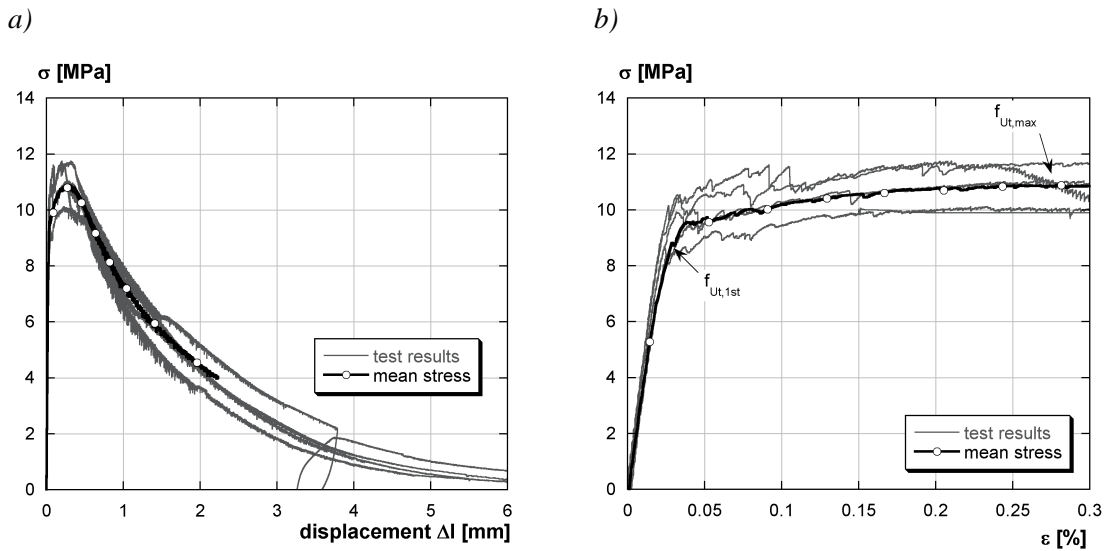


FIGURE 3.3: Tensile behaviour of the uniaxial tensile tests (at 28 days): a) stress-displacement curve, b) stress-strain curve before crack formation

In the *dogbone tests*, the strain at the tensile strength is only  $\epsilon_{U_t,max} = 0.1\%$  (mean value of only two tests), suggesting that the strain-hardening is overestimated with notched specimens.

The evolution of the *secant modulus* is investigated with cyclic tests. Figure 3.4a shows the secant modulus  $E_U$ , normalized on the non-damaged secant modulus  $E_{U0}$ , which is 48 GPa at an UHPFRC age of 28 days, versus the mean displacement, measured with the LVDTs (see Figure 3.2a (f)). A strong decrease of the secant modulus is observed until 0.2 mm when the secant modulus is at 15% of its initial value. The secant modulus is nearly constant at 10% of the initial secant modulus for displacements higher than 0.2 mm. The decrease coincides with the strain-hardening of the material. The decrease of the secant modulus indicates progressive damage in form of matrix cracking and progressive fibre pull-out. For displacements larger than 0.2 mm, the UHPFRC matrix is completely damaged in a localized crack. The force is transferred by the fibres that are gradually pulled out until the fracture of the specimen. The secant modulus decreases slowly.

At 28 days, the first cracking strength of the UHPFRC is  $f_{U_t,1st} = 9.1$  MPa, the tensile strength  $f_{U_t,max} = 11.0$  MPa and the fracture energy  $G_F = 20.2$  kJ/m<sup>2</sup>. The tensile strength is three to four times higher than that of the normal strength concrete. The outstanding UHPFRC tensile behaviour is best characterized by the fracture energy which is 100 times higher when compared to the normal strength concrete. The *evolution in time* of the mechanical properties is represented for the tensile strength in Figure 3.4b; it is similar for the other mechanical properties. A strength increase is observed until a specimen age of 90 days. Afterwards, the strength is virtually constant and the law proposed for normal strength concrete in [CEB204] to describe the evolution of the mechanical properties in time overesti-



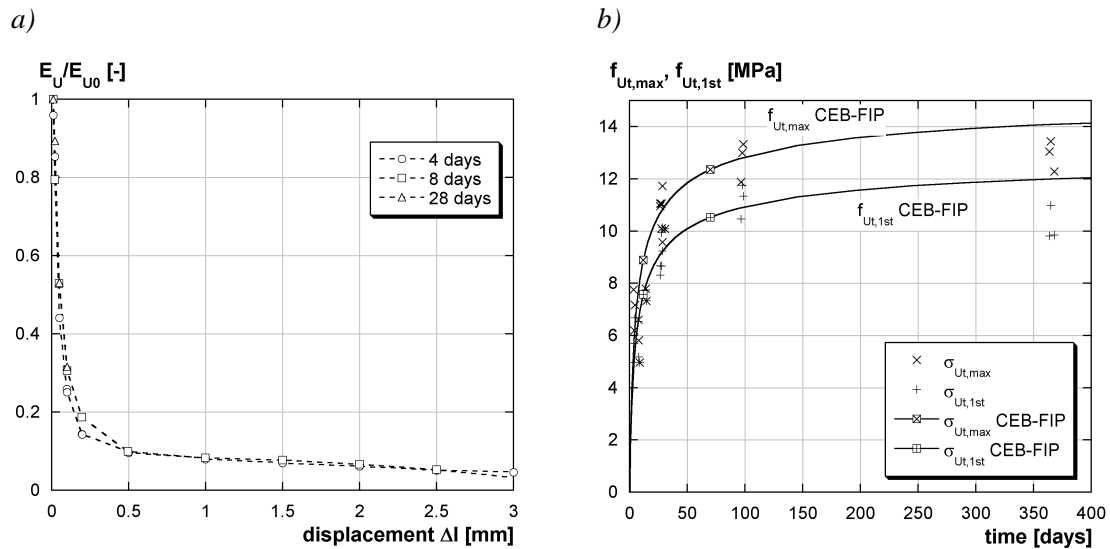


FIGURE 3.4: a) Evolution of the secant modulus with increasing displacement during the uniaxial tensile test, b) evolution of the tensile strength with age

mates the strength. The constant mechanical properties of UHPFRC beyond 90 days suggest that the hydration reaction stops after approximately 90 days due to water shortage.

### 3.2.4.4 Domains of cracking

In structural elements made of UHPFRC, different domains of cracking can be observed as described in Figure 3.5. The definition is an extension of the definition of the fictitious crack after [Hillerborg83].

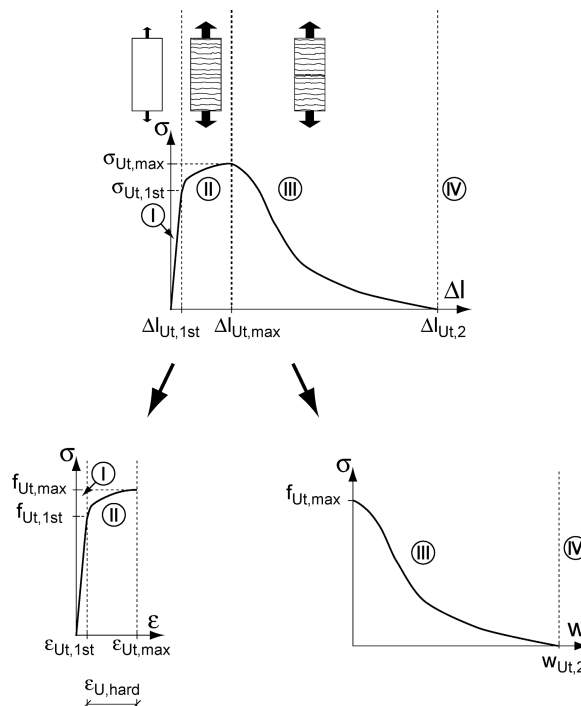


FIGURE 3.5: Crack definition in tension for a plain UHPFRC section

- *Domain I:* Prior to testing, cracks on the microscale of the matrix can exist. These cracks are called *preexisting microcracks*. During the initial part of the tensile behaviour, new *microcracks* form and

preexisting microcracks are activated and propagate. These microcracks are bridged and controlled by the steel fibres and the stiffness is not remarkably reduced (see Figure 3.4a).

- *Domain II*: After the quasi-linear behaviour, microcracks develop into macrocracks that are visible with the naked eye ( $w \approx 50 \mu\text{m}$ ). A significant reduction in stiffness is observed. The cracks are densely distributed so that the macroscopic deformation is still considered to be homogeneous for modelling. They are called *distributed macrocracks*. The deformation  $\varepsilon_{U,hard}$  is called magnitude of hardening.
- *Domain III*: Beyond the maximum force, localization of deformation occurs in one or few macrocracks, depending on the capacity of energy dissipation of each macrocrack. These cracks are *localized macrocracks*. The structural element fails in one of these cracks which is the *dominant localized macrocrack*.
- *Domain IV*: No more stresses are transferred through the localized macrocrack. At this stage, the crack is called *real crack*.

The crack definition can also be applied to one localized bending crack as described in Figure 3.6. The same four domains can be distinguished for this single crack. Furthermore, the apparent stiffness in the crack is shown in analogy to Figure 3.4a. It can be seen that the apparent stiffness is not remarkably reduced in domain I. In domain II, during hardening, the diminution of stiffness is strong, which indicates increasing damage of the matrix. In domain III, the stiffness is governed by fibres and its decrease is small until there is no apparent stiffness any more and a real crack exists (domain IV).

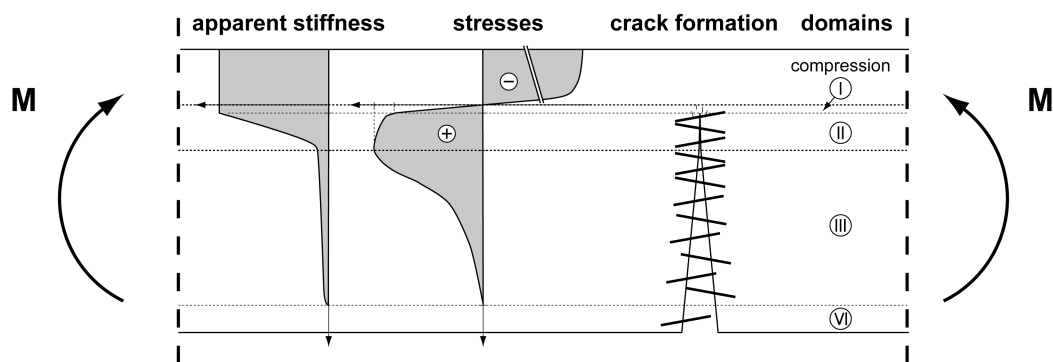


FIGURE 3.6: Localized crack in pure bending for a plain UHPFRC section

### 3.2.5 Free shrinkage

#### 3.2.5.1 Free autogenous shrinkage at early age

Linear free autogenous shrinkage tests were performed on the UHPFRC at early age at the university Laval, Québec, Canada. The cross-section of the specimen is  $5.5 \text{ cm}^2$ . The deformations are determined with two LVDTs that measure the displacement of two metallic rods placed in the specimen at a distance of 72 cm. Details of the test method can be found in [Charron03]. Measurements start two hours after the addition of water and are conducted for seven days. Two isothermal tests are performed at a temperature of  $20.5 \pm 0.75 \text{ }^\circ\text{C}$ .

The evolution of the autogenous shrinkage is shown in Figure 3.7. Shrinkage deformation has positive values in the diagram. In the beginning of the test until approximately 6 hours after the addition of water, slight shrinkage is observed (Figure 3.7a). From 6 to 31 hours, swelling occurs in the UHPFRC. Afterwards, monotonous shrinkage is measured until the end of the test. The swelling was also observed by Viviani for different types of concrete [Viviani04]. It may be attributed to crystallization processes, e.g. the formation of ettringite or CH crystals [Barcelo01]. It occurs before setting when the material is still soft and expansive hydration products may lead to a volume increase. The beginning of the shrinkage (at 31 hours) corresponds to the beginning of the RH-decrease due to self-desiccation

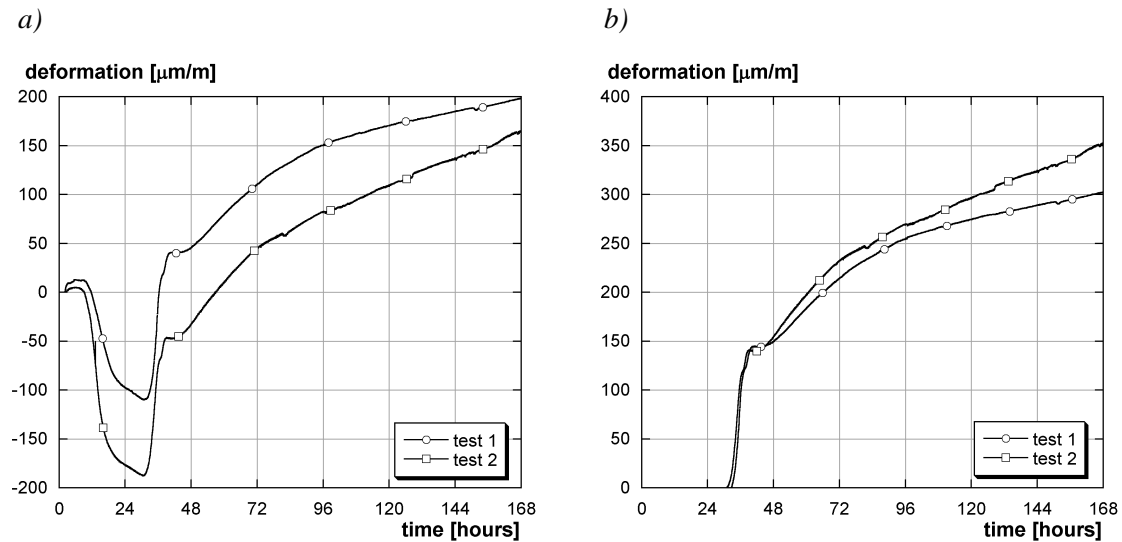


FIGURE 3.7: Free autogenous shrinkage deformation at early age: a) measured deformations, b) curves zeroed at the beginning of shrinkage (i.e. at the minimum of the curves in a)

(Figure 3.1b) and also to the beginning of setting. The autogenous shrinkage is  $325 \mu\text{m/m}$  at an UHPFRC age of 7 days (Figure 3.7b).

### 3.2.5.2 Free shrinkage tests on cylinders

Free shrinkage tests are conducted on drying and on sealed cylindrical specimens ( $\varnothing 11 \text{ cm}$ ,  $l = 22 \text{ cm}$ ) at a temperature of  $20 \text{ }^\circ\text{C} \pm 2 \text{ }^\circ\text{C}$  and a RH of  $40\% \pm 15\%$ . The shrinkage measurements start 54 hours after the casting of the UHPFRC when the major part of the heat of hydration is dissipated. A strong deformation increase is observed during the first 90 days (Figure 3.8a), followed by a stabilization at approximately  $360 \mu\text{m/m}$  for autogenous shrinkage and  $80 \mu\text{m/m}$  for drying shrinkage. Variations of the ambient climatic conditions are responsible for the fluctuations in the curves. The difference between drying and sealed specimens, i.e. drying shrinkage, is small. This indicates that the major part of shrinkage is caused by self-desiccation. Drying shrinkage develops mainly during the first 20 days. This suggests that the dense matrix of the UHPFRC allows only insignificant moisture exchange with the environment.

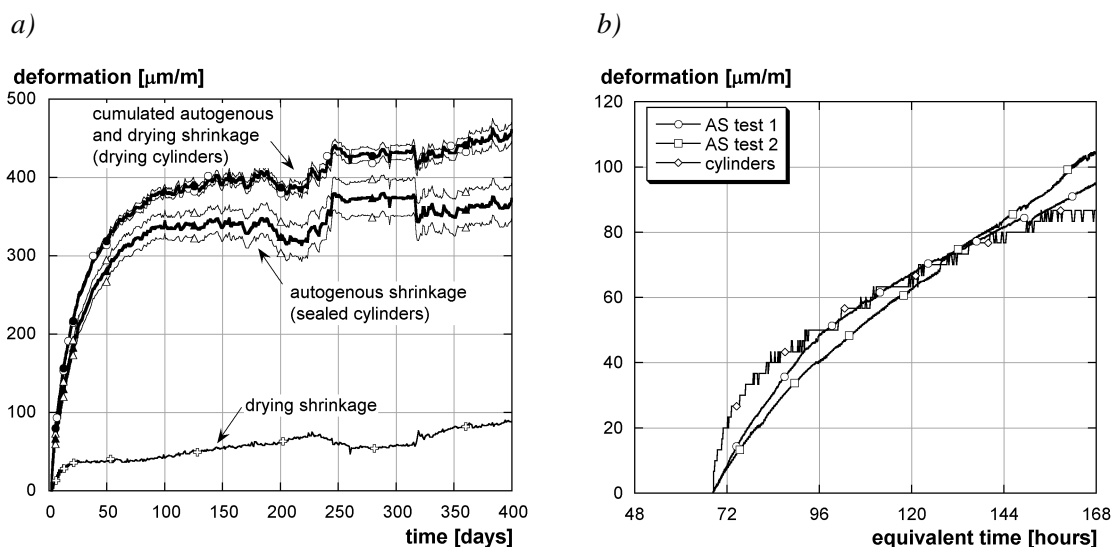


FIGURE 3.8: a) Shrinkage deformations of the UHPFRC, b) comparison between the results of the autogenous shrinkage tests and the cylindrical specimens

Figure 3.8b shows the comparison of the results of the autogenous shrinkage tests from Section 3.2.5.1 and the free shrinkage tests on the sealed cylinders at early age. The curves are zeroed at the beginning of the cylinder tests. The age of the cylinders is expressed by equivalent age or maturity (see Appendix A), since the cylinders are more massive and the heat of hydration leads to a higher temperature rise in the cylinders and a faster hydration kinetics which can be corrected by the equivalent age. The measurements on the cylinders correspond well to the measurements of the free autogenous shrinkage tests when considering the different test methods.

### 3.2.6 Viscoelastic behaviour

#### 3.2.6.1 Restrained autogenous shrinkage at early age

Restrained early age shrinkage tests were performed on two sealed UHPFRC specimens at the university Laval, Québec, Canada. They were conducted in the same campaign as the linear autogenous shrinkage tests (see Section 3.2.5.1). The specimen section is  $5.5 \text{ cm}^2$ .

**Test procedure.** The tests are performed according to the procedure described in Figure 3.9: The control system is activated when the strength of the material reaches  $0.01 \text{ MPa}$ . A deformation threshold is defined ( $\Delta\varepsilon_{\text{limit}} = 6 \mu\text{m}$ ). When the deformation reaches the threshold, it is set back to zero by increasing the stress in the material. The stress is held constant until the deformation threshold is reached again and creep curves develop between two load increments. Cumulated creep and shrinkage is measured with the restrained shrinkage tests.

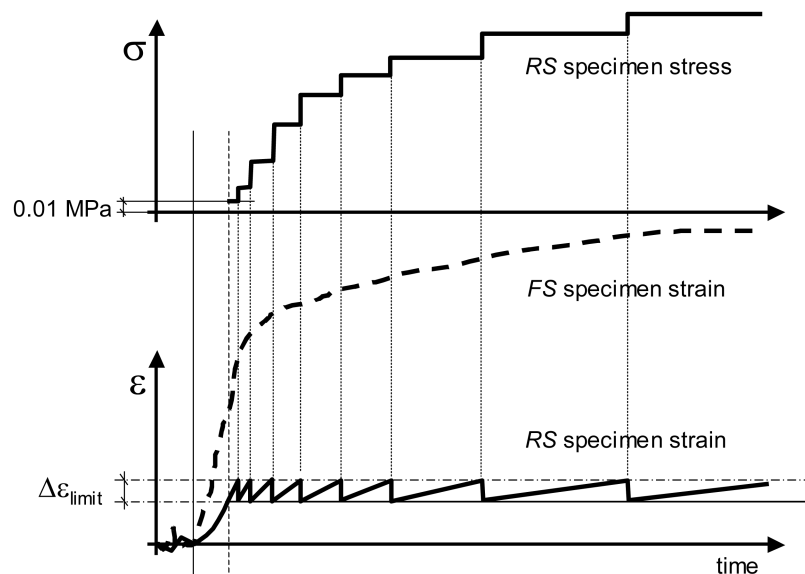


FIGURE 3.9: Schematic test procedure of the restrained shrinkage test (RS: restrained shrinkage, FS: free shrinkage) (from [Charron02])

As free autogenous tests are conducted in parallel, basic creep and autogenous shrinkage can be separated by assuming the principle of superposition ( $\varepsilon_{\text{rest}} = \varepsilon_{\text{cr}} + \varepsilon_{\text{shr}}$ ). The evolution of the Young’s modulus is evaluated when the restrained shrinkage deformation increments is zeroed ( $E_U = \Delta\sigma / \Delta\varepsilon_{\text{limit}}$ ). This method gives only a rough value of the secant modulus, but it indicates its kinetics. Details about test method and interpretation can be found in [Charron03].

Two tests are conducted at a temperature of  $20.5 \pm 0.75 \text{ }^\circ\text{C}$ . (see Section 3.2.5.1). The measurements start approximately two hours after casting and are performed for seven days. The results of the two tests are alike with a scatter of 10%. Thus, only the results of one test are described here (Figure 3.10).

**Results.** Figure 3.10a shows the evolution of axial stresses and secant modulus in the restrained specimen; Figure 3.10b shrinkage, cumulated creep and shrinkage, i.e. the results from the restrained shrinkage test, and the calculated creep deformation<sup>6</sup>.

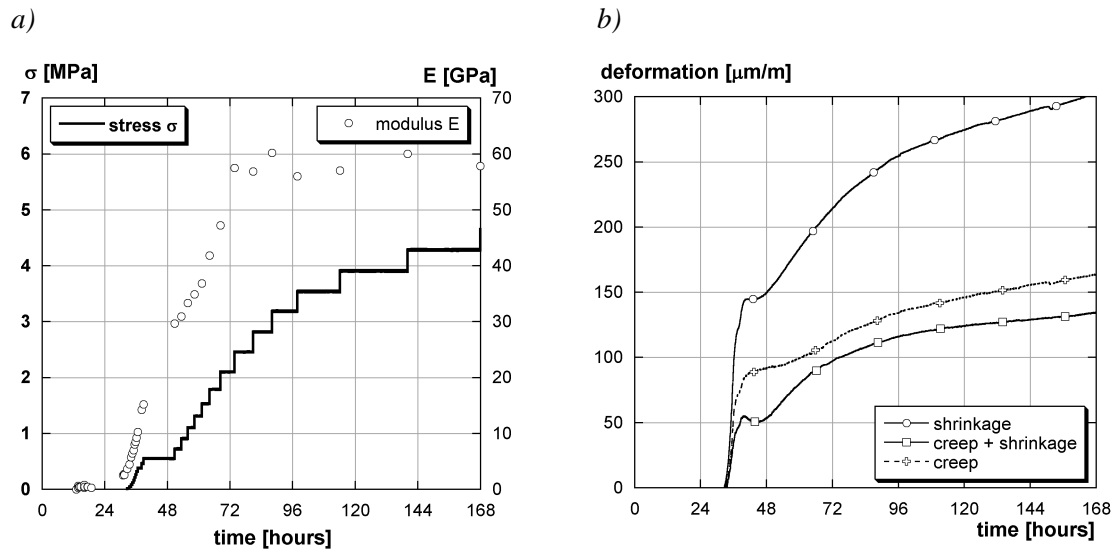


FIGURE 3.10: Results of the restrained shrinkage test: a) stress and calculated secant modulus, b) shrinkage, restrained shrinkage and tensile creep

Beyond 12 hours, the material strength is higher than 0.01 MPa and the deformations are reset to zero at each load increment, i.e. when the deformation threshold of 6  $\mu\text{m}/\text{m}$  is reached. Between 12 and 20 hours, the material is subjected to a small compression stress. However, the material is still soft during this period and setting has not started yet (see Section 3.2.2). This is confirmed by the low calculated secant modulus (Figure 3.10a). The apparent strength in the material may be attributed to interlocking of the steel fibres. In consequence, the evolution of restrained shrinkage is only considered from 31 hours on when tensile stresses build up, leading to tensile creep (Figure 3.10b).

The secant modulus increases strongly until approximately 72 hours. The time spans of the load increments increase with increasing UHPFRC age. This is explained by ongoing hardening, i.e. the material becomes stiffer and the rate of shrinkage deformation smaller. An exception is the period between 39 and 50 hours that is characterized by slight swelling. This physical phenomenon is observed during the free and restrained autogenous shrinkage tests. It may be due to topochemical reactions of inner CSH or to crystallization processes, as for example the formation of ettringite or CH crystals [Barcelo01].

In Figure 3.10b, free shrinkage, restrained shrinkage, i.e. creep + shrinkage, and the calculated creep deformations are zeroed at the beginning of shrinkage deformation at 31 hours. The creep deformations are approximately 60% of the free shrinkage deformations, attaining 160  $\mu\text{m}/\text{m}$  after 7 days for this test. The load level at the end of the restrained shrinkage test is approximately 60%.

### 3.2.6.2 Compression creep

Compression creep tests are conducted on cylinders in a climatic chamber at a temperature of 20°C  $\pm$  1 °C and a relative humidity of 60%  $\pm$  5%. In parallel, shrinkage deformations are measured. The cylindrical specimens ( $\varnothing$  6.9 cm,  $l$  = 22 cm) are loaded at the age of 6 days with a compressive stresses of 34 MPa and 58 MPa respectively. Considering a compressive strength at 3 days of 127 MPa, the load corresponds approximately to 27 % and 46 % of the compressive strength at the beginning of the test.

6. Shrinkage has positive values in the diagrams.

Figure 3.11 shows the creep compliance for the UHPFRC specimens. No distinction can be made between the drying and the sealed specimens, since the manual measurements are too imprecise for further conclusions. The mean creep compliance of the specimens is  $50 \mu\text{m}/\text{m}/\text{MPa}$  after 250 days. The slope of the creep compliance is increases monotonously until it becomes virtually constant at  $50 \mu\text{m}/\text{m}/\text{MPa}$  after approximately 100 days.

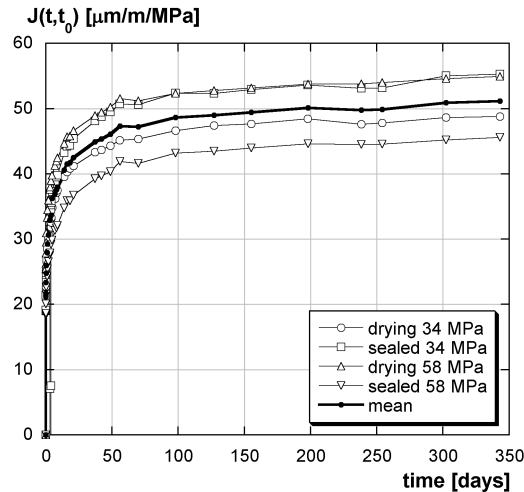


FIGURE 3.11: Compression creep compliance of the UHPFRC

### 3.2.7 Air permeability

The UHPFRC air permeability is measured with the Torrent test [Torrent92] at an UHPFRC age of 80 days. The results show an air permeability of  $k_T < 0.003 \cdot 10^{-16} \text{ m}^2$ . For some measurements, the resolution of the testing device is reached (at  $k_T = 0.001 \cdot 10^{-16} \text{ m}^2$ ). The very low air permeability is explained by the dense matrix of the UHPFRC. The measurements confirm the hypothesis that moisture exchange between UHPFRC and environment is small.

## 3.3 Concrete properties

*In this section, results for the concrete in the composite “UHPFRC-concrete” elements are presented. The chosen concrete is a normal strength concrete. Only the results that are necessary to understand and to simulate the behaviour of the structural elements are presented.*

**Mechanical properties.** The mechanical properties of the concrete are given in Table 3.1. Compressive strength and secant modulus at 30% are measured on cylinders with  $\varnothing 16 \text{ cm}$  and  $l = 32 \text{ cm}$  and uniaxial tensile strength on cylinders with  $\varnothing 11 \text{ cm}$  and  $l = 22 \text{ cm}$ . The softening diagram of the concrete is determined on notched plates with the test set-up described in Section 3.2.4. The normalized softening as well as the parameters for the deduced bi-linear softening diagram are shown in Figure 3.12a.

TABLE 3.1: Mechanical properties of the concrete

Property	at 28 days	at 90 days	at 365 days
Compressive strength $f_{cc}$	46.1 MPa	52.2 MPa	60.7 MPa
Secant modulus $E_{cc}$	37.8 GPa	39.3 GPa	41.6 GPa
Tensile strength $f_{ct}$	3.4 MPa <sup>a</sup>	3.4 MPa <sup>a</sup>	4.7 MPa

a. minimum boundary of the tensile strength, since some of the specimens fail at the glued surface and not in the concrete specimen during testing

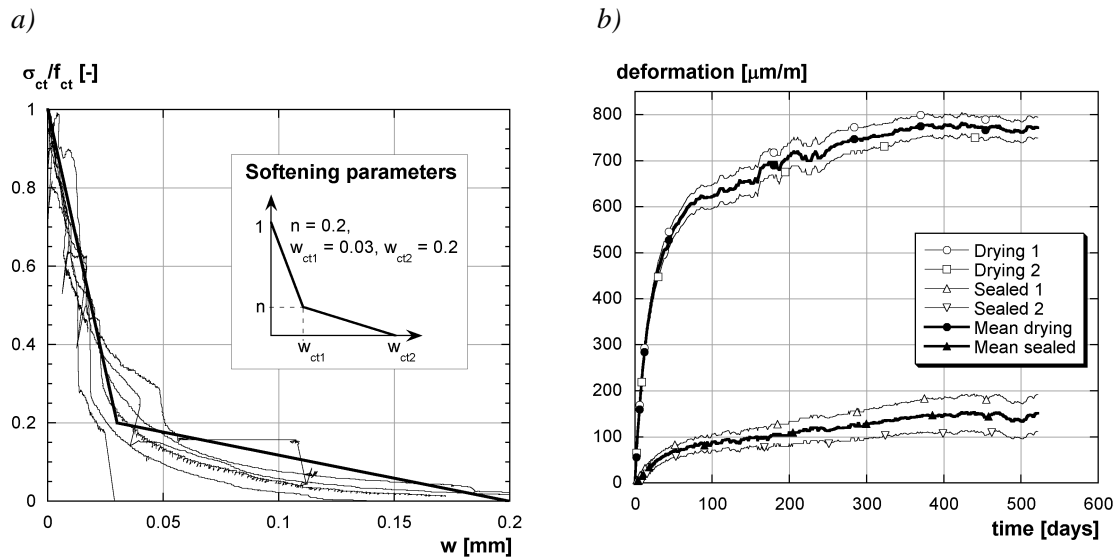


FIGURE 3.12: a) Softening behaviour of the concrete, b) drying shrinkage of concrete

**Time-dependent behaviour.** Free shrinkage deformations are determined on cylinders in the same way as for the UHPFRC (Section 3.2.5.2). The measurements start at a concrete age of 22 hours after casting. The results show that in contrast to UHPFRC, drying has a strong influence on the shrinkage deformations (Figure 3.12b). Autogenous shrinkage is approximately 5 times lower than drying shrinkage.

**Adherence strength at the interface.** The adherence strength at the interface is determined with uniaxial tensile tests on cylindrical specimens drilled out of composite “UHPFRC-concrete” blocks that are processed the same way as the composite “UHPFRC-concrete” beams. Fracture always occurs in the concrete layer at a distance of 0 to 2 cm from the contact surface. The surface preparation is of good quality, since nearly no fracture (< 5%) occurs at the contact surface. The mean adherence strength is 2.5 MPa.

## 3.4 Composite “UHPFRC-concrete” beams

### 3.4.1 Experimental program

The behaviour of composite “UHPFRC-concrete” elements is investigated on 15 full-size bending beams with a length of 5.40 m. The beams consist of an old layer of reinforced concrete that is more than 5 months old during testing and a new layer of UHPFRC (Figure 3.13). The contact surface of the concrete is prepared by hydrojetting. The structural behaviour of the beams is measured from the casting of the UHPFRC layer to an UHPFRC age of 11 to 12 weeks. After these early age and long-term tests, the beams are submitted to 4-point-bending fracture tests.

The variable parameters of the tests are the *thickness of the UHPFRC layer*  $h_U$ , the *presence of reinforcement in the UHPFRC layer*  $A_{s,U}$  and the *static system*. Three different thicknesses ( $h_U = 3, 5, 10$  cm) of the UHPFRC layer are investigated. Additional rebars  $A_{s,U}$  are placed in the UHPFRC layer of half of the beams with  $h_U = 5$  and 10 cm. The term “reinforcement in the UHPFRC layer” refers in the following to these rebars. The reinforcement ratio of the additional reinforcement corresponds to 2 Vol.-% of the UHPFRC cross-section.

**Early age and long-term tests.** A statically determinate and a statically indeterminate system are investigated (Figures 3.14 and 3.15). The statically determinate system consists of a single span beam with cantilevers on each side (Figure 3.14), the statically indeterminate system of a three span beam (Figure 3.15). Some of the statically determinate beams are loaded after 28 days to investigate bending

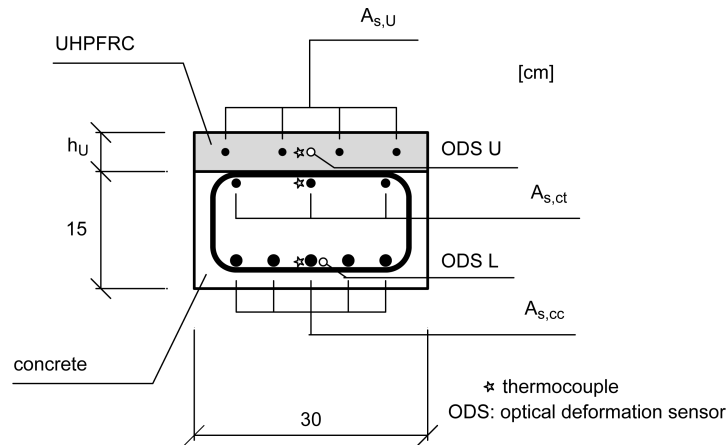


FIGURE 3.13: Cross-section of the composite “UHPFRC-concrete” beams

creep. The parameters of the experimental campaign and the chosen beam denominations are summarized in Table 3.2.

TABLE 3.2: Parameters of the composite “UHPFRC-concrete” beams

Name during long-term tests	Name during fracture tests	Static system	Thickness of the UHPFRC layer	Reinforcement in the UHPFRC layer	Creep loading	Calculated degree of restraint at 28 days
I3	NR3	determinate	3 cm	-	-	0.51
I3L	NR3	determinate	3 cm	-	2·10.2 kN	0.51
H3	NR3	indeterminate	3 cm	-	-	0.76
I5	NR5	determinate	5 cm	-	-	0.44
I5L	NR5	determinate	5 cm	-	2·7.5 kN	0.44
I5R	R5	determinate	5 cm	4Ø10	-	0.44
I5RL	R5	determinate	5 cm	4Ø10	2·7.5 kN	0.44
H5	NR5	indeterminate	5 cm	-	-	0.67
H5R	R5	indeterminate	5 cm	4Ø10	-	0.67
I10	NR10	determinate	10 cm	-	-	0.44
I10L	NR10	determinate	10 cm	-	2·16.1 kN	0.44
I10R	R10	determinate	10 cm	4Ø14	-	0.44
I10RL	R10	determinate	10 cm	4Ø14	2·16.1 kN	0.44
H10	NR10	indeterminate	10 cm	-	-	0.53
H10R	R10	indeterminate	10 cm	4Ø14	-	0.53

**Fracture tests.** 4-point-bending fracture tests are conducted on the beams after the long-term tests at an UHPFRC age of 90 days. The beams are tested with a set-up respecting the geometry of the statically determinate beams during the long-term tests and introducing tensile stresses in the UHPFRC layer (Figure 3.16). The tests are displacement-controlled by imposing the displacement of one of the two hydraulic jacks, placed at 30 cm from the ends of the beams. Both jacks are connected to the same hydraulic pumps and therefore apply the same force  $F$  onto the beams. The displacement rate of the controlled jack is 0.4 mm/min.

**Instrumentation.** During the early age and long-term tests, the temperature of the beams is measured with thermocouples at three depths (Figure 3.13). The deformations are followed with LVDTs and two



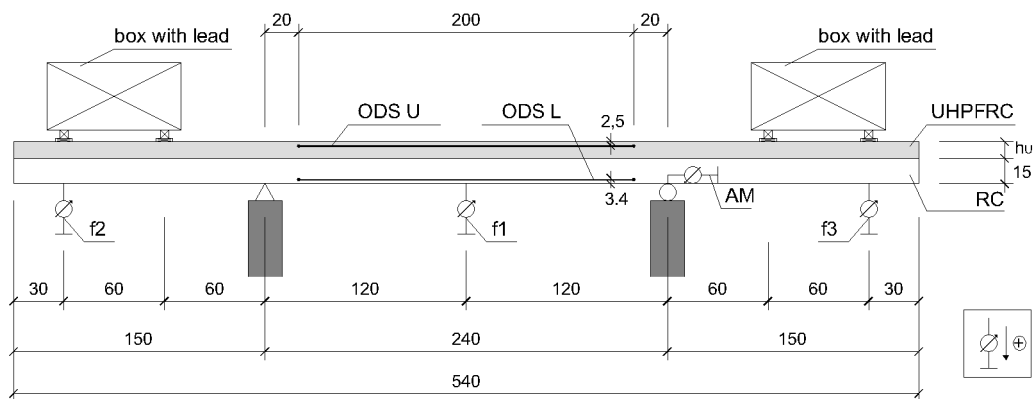


FIGURE 3.14: Test set-up of the early age and long-term tests for the statically determinate beams

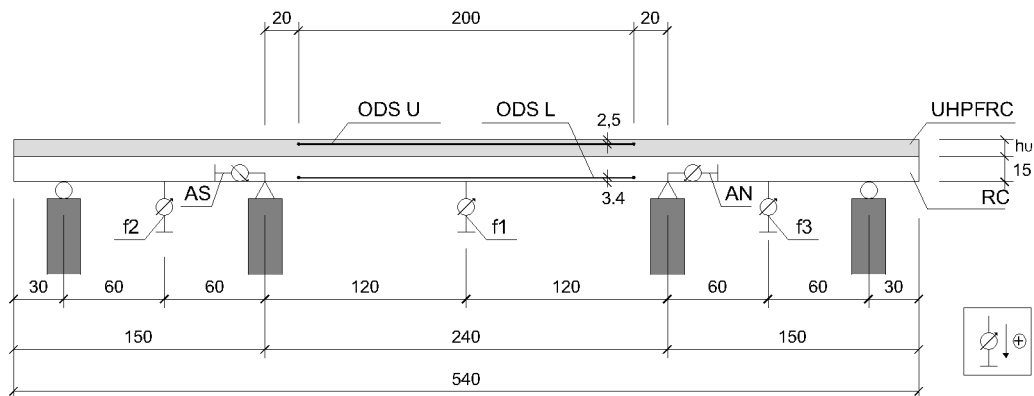


FIGURE 3.15: Test set-up of the early age and long-term tests: statically indeterminate beams

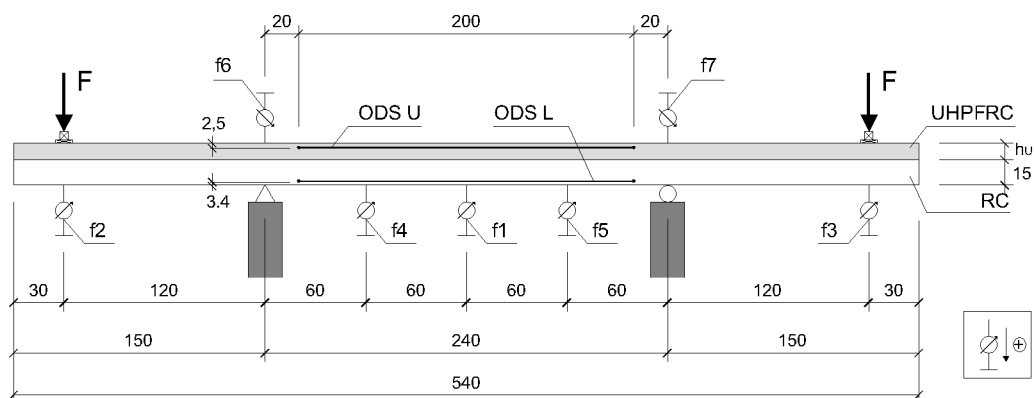


FIGURE 3.16: Test set-up of the fracture tests

optical deformation sensors (ODS), which measure the average deformation over a length of 200 cm in the central span (Figures 3.14 and 3.15). Furthermore, the cracking of the beams is observed visually. During the fracture tests, the deformations are measured with LVDTs and ODS (Figure 3.16). Crack formation is observed visually and the widths of localized macrocracks are followed with  $\Omega$ -gages, placed on the upper surface and on the sides of the beams.

### 3.4.2 Early age and long-term behaviour

#### 3.4.2.1 General behaviour

The general appearance of the central span deformations during the long-term tests is traced in Figure 3.17. The time is zeroed when the temperature in the UHPFRC layer reaches its maximum value, corresponding to approximately 1.5 days after casting of the UHPFRC layer. Figure 3.17a shows curves for statically determinate beams - one is subjected to bending creep after 28 days and one is not loaded; Figure 3.17b shows the curve for a statically indeterminate beam. All three curves are measured for the beams with  $h_U = 3$  cm.

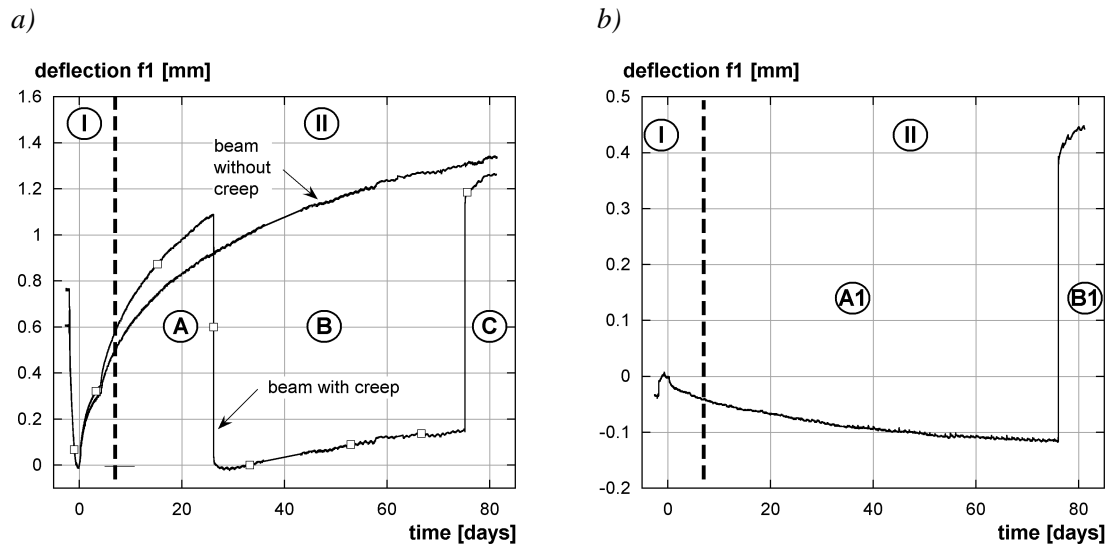


FIGURE 3.17: Typical deflection-time curves of: a) statically determinate beams (I3, I3L), b) statically indeterminate beams (H3)

Two main phases can be distinguished:

- I. *Early age*: A period of 7 to 9 days that is governed by the exothermal hydration reaction causing heat release and self-desiccation in the UHPFRC. The temperature and RH-changes lead to beam deformations. There is no clear transition between early age and long-term.
- II. *Long-term*: The evolution of the material properties and of the beam deformations due to the internal reactions of the materials of the beam slow down and the deformation rate decreases.

Some of the statically determinate beams are subjected to *bending creep*. Here, three test phases are distinguished:

- A. The beams remain unloaded.
- B. The beams are loaded 28 days after the casting of the UHPFRC layer.
- C. The load is removed 49 days later (at 77 days) and the creep recovery is measured.

For the *statically indeterminate beams*, two phases can be distinguished:

- A1. The deformations of the statically indeterminate beams are measured.
- B1. The recovery of the beams is monitored after removal of the external supports and one horizontal internal support, i.e. when the beams become statically determinate.

#### 3.4.2.2 Early age behaviour

**Temperature evolution.** The evolution of temperature and mid-span deflection during early age is shown in Figure 3.18 for a statically determinate beam with  $h_U = 5$  cm (I5). The time is zeroed just after the casting of the UHPFRC on the beam. The temperature of the UHPFRC at casting is approxi-

mately 25°C. During the dormant period of more than 24 hours, it cools nearly down to ambient temperature. The long dormant period is due to the high amount of superplasticizer. The acceleration of the hydration reaction induces a *temperature increase* until a maximum is reached after 38 hours. The maximum temperature in the UHPFRC layer ( $TC_U$ ) is 22.3 °C, 25.1 °C and 30.8 °C, for  $h_U = 3, 5,$  and 10 cm respectively. This corresponds to *temperature gradients* between  $TC_{s,1}$  and  $TC_U$  of 0.8 °C, 2.0 °C and 5.0 °C respectively [Habel04]. The temperature depends on the massiveness of the element: the thicker the element, the earlier starts the hydration reaction and the higher is the temperature rise.

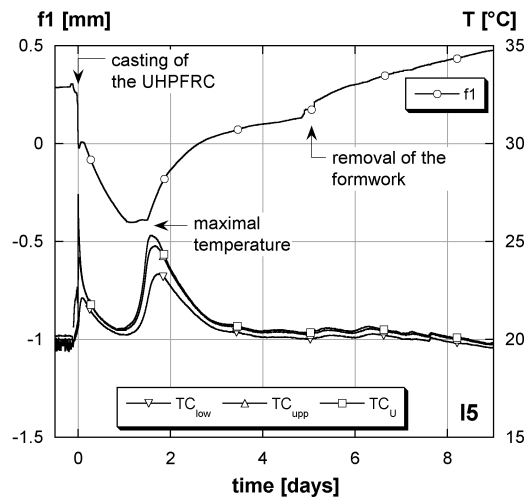


FIGURE 3.18: Temperature and central span deflection at early age, beam I5

**Deflections.** The deflection of the beam increases instantly during casting due to the dead weight of the UHPFRC. The deflections decrease until 26 hours, remain nearly constant for 12 hours and increase monotonously for an UHPFRC of more than 36 hours (Figure 3.18). During this period, an interaction between self-desiccation shrinkage and thermal expansion occurs. The self-desiccation shrinkage is higher than the thermal expansion. The maximum deflections are reached one hour after the maximum temperature is measured. Then, self-desiccation and temperature decrease lead to shrinkage and to an increase of the mid-span deflection. After 96 hours, the deflection continues to increase monotonously at a constant temperature of 20 °C which is attributed to shrinkage deformations: autogenous shrinkage and a minor part of drying shrinkage (see Section 3.2.5.2).

### 3.4.2.3 Influence of the static system

The influence of the static system is shown in Figure 3.19. The mid-span deflections  $f_1$  of the statically determinate beams (I) are much higher than those of the statically indeterminate beams (H) (Figure 3.19a): 10 times higher for  $h_U = 3$  cm (I3, H3) and 17 times higher for  $h_U = 10$  cm (I10, H10) at 70 days. Moreover, the mid-span deflections develop in the opposite sense for the two static systems as shown in Figure 3.20. The removal of the external supports and one horizontal internal support of the statically indeterminate beams after 77 days leads to a rise of the mid-span deflection. The deflection remains lower than for the statically determinate beams, indicating irreversible deformations due to the residual stresses caused by the statically indeterminate system. Without vertical restraint at the end supports, the beams curl in the same way as the statically determinate beams.

The axial deformations in the central span  $\epsilon_{ODS}$  are measured with the ODS ( $\epsilon_{ODS} = \frac{1}{2} (ODS_L + ODS_U)$ ). They are 5 to 15% higher for the statically determinate beams. However, the axial deformations are more sensible to the thickness of the UHPFRC layer than to the change of the static system. This indicates that the beams are only partially restrained in axial direction.

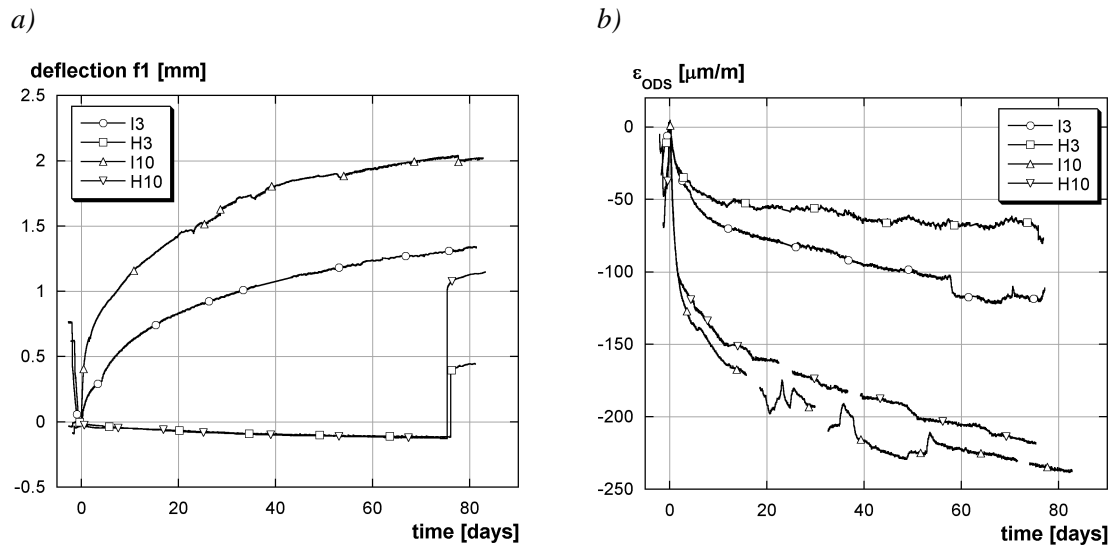


FIGURE 3.19: Influence of the static system: a) deflection  $f_1$ , b) axial deformation

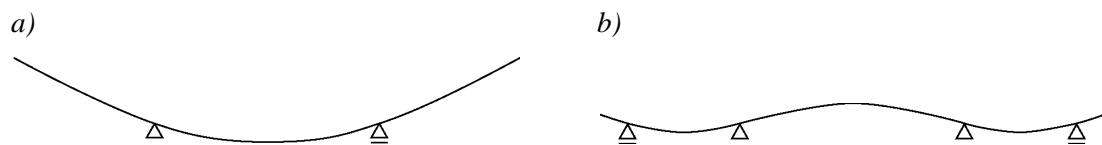


FIGURE 3.20: Deformations of the beams during the long-term tests: a) statically determinate beams, b) statically indeterminate beams (deflections are not scaled)

#### 3.4.2.4 Influence of the thickness of the UHPFRC layer

The thickness of the UHPFRC layer  $h_U$  influences considerably the deformations: the higher the thickness of the UHPFRC layer, the lower is the degree of restraint of the composite beams and the higher are the deformations. Furthermore, the temperature rise is higher in the thicker beams at early age.

The mid-span deflection of the statically determinate beams is two times higher for the beams with  $h_U = 10$  cm (I10) than for the beams with  $h_U = 3$  cm (I3) (Figure 3.19a). However, no significant difference is observed in the deflection of the statically indeterminate beams (H3, H10) (Figure 3.19a), indicating the efficiency of the vertical restraint in the UHPFRC layer.

The measurements of the ODS in the statically determinate beams show that the axial deformations near the bottom of the concrete layer (ODS L) are virtually independent on the thickness of the concrete layer, while the deformations in the UHPFRC layer (ODS U) are approximately 1.7 times larger for  $h_U = 10$  cm when compared to  $h_U = 3$  cm. This confirms that the deformations of the UHPFRC layer are mainly responsible for the beam deflections.

#### 3.4.2.5 Influence of reinforcement in the UHPFRC layer

Figure 3.21b shows that the deformations of the beams with reinforcement in the UHPFRC layer  $A_{s,U}$  (I5R, I10R) are smaller than of the beams without  $A_{s,U}$  (I5, I10) as shown for the curvature in the central span of the beams determined by the ODS ( $\kappa_{ODS} = (\text{ODS L} - \text{ODS U}) / (\text{distance between the ODS})$ ). The increase of curvature is higher for  $h_U = 10$  cm (-20%) than for beams (-5%) at 80 days. The difference in stiffness is explained by the reinforcement ratio and the beam geometry:  $A_{s,U}$  is situated near the upper surface of the UHPFRC layer and induces additional restraint. The static height and the reinforcement ratio is higher for the beams with  $h_U = 10$  cm. Thus, additional reinforcement ( $A_{s,U}$ ) restrains more efficiently the deformations in the UHPFRC layer for thicker UHPFRC layers.

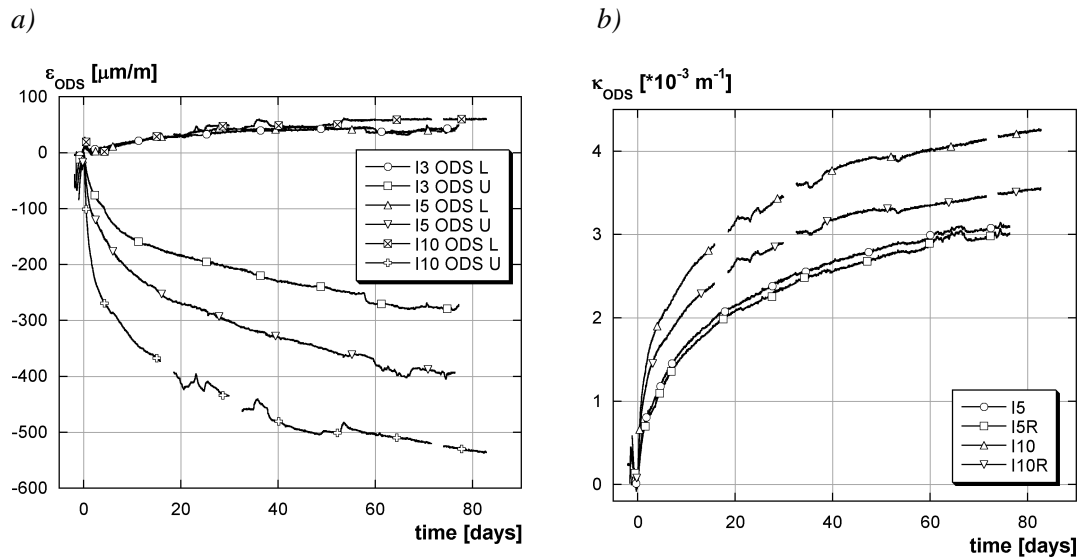


FIGURE 3.21: a) Influence of the thickness of the UHPFRC layer ( $h_U$ ), b) influence of reinforcement in the UHPFRC layer

### 3.4.2.6 Bending creep

Bending creep is investigated between 28 and 77 days, i.e. during 49 days, after the casting of the UHPFRC layer. During this period, the UHPFRC properties still change (see Section 3.2). There exist always a loaded and a non-loaded beam of the same configuration. The non-loaded beams are deformed by RH-changes due to drying and progressive hydration. The loaded beams are additionally deformed by an elastic and a time-dependent creep contribution due to the loading. The creep deformations are obtained by comparing the non-loaded and the loaded beams in the same way as described in Section 3.2.6.1. It must be stated that this method implies errors, since even two beams of the same configurations exhibit slightly different deformations as shown in Figure 3.17a for the beam I3 and I3L. The load level is fixed in relation to the tensile stress in the upper fibre of the UHPFRC layer. The additional tensile stress due to loading is 4.5 MPa for the beams with  $h_U = 5$  cm and 6 MPa for  $h_U = 3$  and 10 cm (calculated with a linear-elastic stress distribution).

The *creep compliance*  $J(t, t_0)$  is calculated for the beams (procedure described in [Habel04]). It expresses the creep strain per unit stress, independent on load and stiffness ( $EI$ ). So, it is possible to compare the different beam configurations on the basis of the creep compliance. Figure 3.22 shows the creep compliances for the mean value of the end deflections  $f_2$  and  $f_3$  of all the beams subjected to bending creep. The compliance is of the same magnitude for all the beams. The lowest creep compliance is found for beam I3 which has the lowest initial value as well as the lowest slope. The beams with  $h_U = 5$  and 10 cm have approximately the same initial values and the same slope. The creep compliance is within the range of composite RC beams tested by [Bernard00].

### 3.4.2.7 Cracking

*Surface cracks* with a width between 50 and 100  $\mu\text{m}$  are detected with the naked eye during the early age and long-term tests. Most cracks form during the 14 days after the casting of the UHPFRC layer and are orientated in transversal direction. No correlation between the test parameters and crack distribution is observed. The statically indeterminate beam with  $h_U = 3$  cm is an exception, since two transverse cracks (width  $\approx 100$   $\mu\text{m}$ ) due to early age deformations are observed. The reinforcement in the UHPFRC layer ( $A_{s,U}$ ) is placed near the upper surface. It induces additional restraint and provokes more surface cracks than in the beams without reinforcement in the UHPFRC layer.

Slight *interface cracking* is observed at the ends of some of the beams, however, no dependency on the beam configurations is discernible. The cracks are barely visible (width  $< 40$   $\mu\text{m}$ ) and occur always in the concrete at a distance of 0 to 2 cm from the contact surface. They can not be observed in cross-sectional cuts of the beams that are sawn after the fracture tests. The adherence at the hydrojetted con-

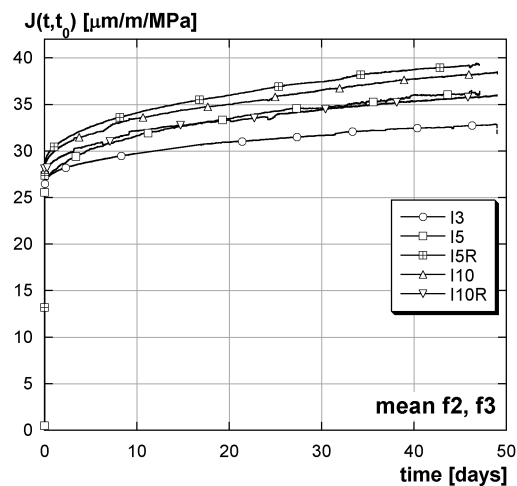


FIGURE 3.22: Creep compliances: mean values of deflections  $f_2$  and  $f_3$

tact surface between concrete and UHPFRC is very good, since no debonding cracks are observed directly at this contact surface. Thus, no stirrups or connectors between the UHPFRC and the concrete layer are necessary to guarantee monolithic behaviour.

### 3.4.3 Structural response under bending

#### 3.4.3.1 Beams without reinforcement in the UHPFRC layer (beams NR)

The fracture tests on the composite beams without reinforcement in the UHPFRC layer (NR) are characterized by an *increase in stiffness* for mid-span deflections (deflection =  $f_1 - 0.5 \cdot (f_6 + f_7)$ ) smaller than 20 mm (1/120) (Figure 3.23a): the thicker the UHPFRC layer, the higher is the increase in stiffness. The *maximum force* of the beams is increased for thicknesses of the UHPFRC layer larger than a threshold value  $h_{U,thr}$ , situated between 5 and 10 cm for the test series. The increase of the maximum force is followed by a rapid force decrease down to the force of the concrete section.

Widths of localized macrocracks are recorded with  $\Omega$ -gages that are placed on the upper side of the beams ( $\Omega_{upp}$ ), at the side of the beams near the interface ( $\Omega_{side}$ ) and at the interface ( $\Omega_{int}$ ) (Figure 3.23b). During the force rise, *distributed macrocracks* form in the UHPFRC until a deflection of approximately 4 mm (1/600). This corresponds to an *apparent strain-hardening* of the UHPFRC of nearly 1%. At the maximum force, the distributed macrocracks are spaced every 10 cm. Then, *one to two localized macrocracks* form in the UHPFRC layer with rapidly increasing localized macrocrack widths. The localized macrocrack widths, measured with  $\Omega_{upp}$  and  $\Omega_{side}$ , increase simultaneously, indicating that the localized macrocrack develops out of an existing distributed macrocrack.

*Interface cracks* ( $\Omega_{int}$ ) occur at a deflection of 6 mm. All the interface cracks are initiated by bending cracks: no debonding occurs due to shear stresses in the interface zone prior to transverse cracking. The interface crack develops into *debonding crack* that alters the structural behaviour of the beam: the UHPFRC layer does not transfer stresses any more, and fracture is governed by the reinforced concrete section. This explains also the rapid force decrease after the maximum force of beams NR10 ( $h_U = 10$  cm).

#### 3.4.3.2 Beams with reinforcement in the UHPFRC layer (beams R)

Reinforcement in the UHPFRC layer *increased the maximum force*: the maximum force is doubled for beams R5 ( $h_U = 5$  cm) and quadrupled for beams R10 ( $h_U = 10$  cm) when compared to the section without reinforcement in the UHPFRC layer respectively (Figure 3.24a). Furthermore, their *stiffness* is increased.

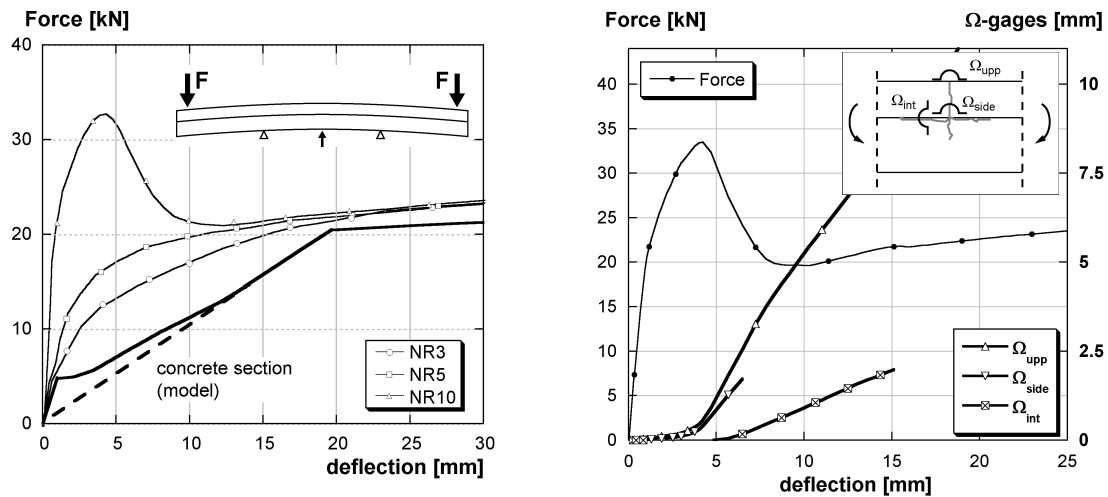


FIGURE 3.23: Beams without reinforcement in the UHPFRC layer: a) Force-deflection diagram (mean values), b) evolution of widths in a the localized macrocrack and in the caused interface crack (beam NR10)

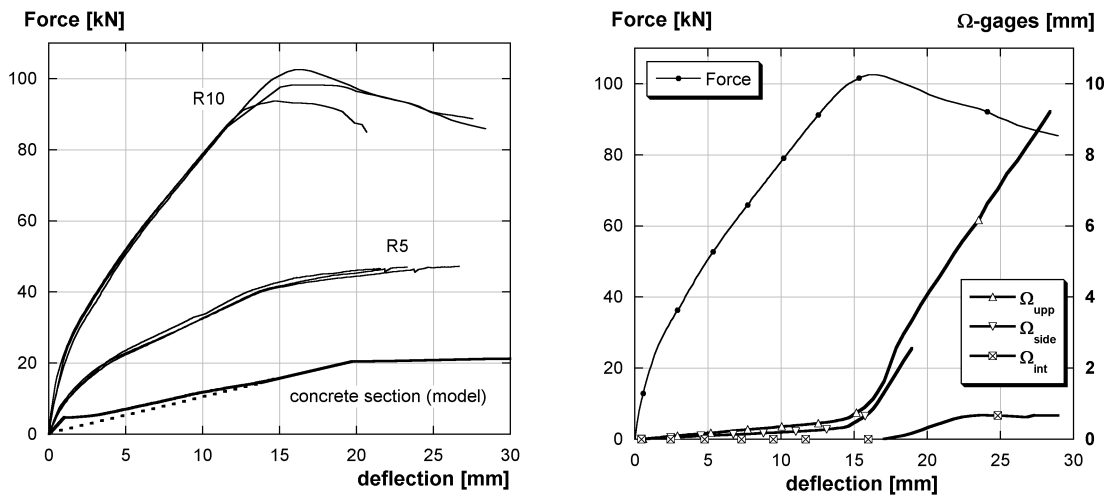


FIGURE 3.24: Beams with reinforcement in the UHPFRC layer: a) force-deflection diagram, b) evolution of the crack widths

One to four localized macrocracks form at a mid-span deflection of 15 mm (1/160) as measured with the  $\Omega$ -gages (Figure 3.24b). For smaller deformations, narrowly distributed macrocracks form, spaced every 3 cm at the maximum force (Figure 3.25). The *apparent strain-hardening* of the UHPFRC corresponds approximately to a deformation of 3‰ (deduced from ODS measurements), being *three times higher* than for the beams NR. This is due to the effect of the rebars in the UHPFRC layer ( $A_{s,U}$ ) that balance inhomogeneities in the UHPFRC tensile properties and lead to a distribution of deformations.

*Interface cracks* form at a deflection of 17 mm. Their crack widths and lengths remain virtually constant at 0.5 mm and 20 cm respectively. The interface cracks are small when compared to the debonding cracks of the beams NR. This is explained by the effect of the rebars in the UHPFRC layer ( $A_{s,U}$ ) that transfer a part of the tensile stress directly. Consequently, less stress have to be transferred through the interface. All interface cracks are provoked by bending cracks, no interface cracks are observed due to shear stresses in the interface zone.

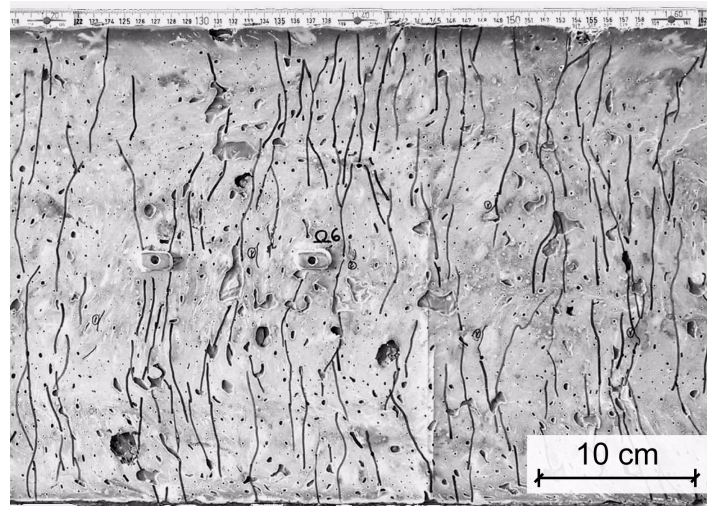


FIGURE 3.25: Distributed macrocrack pattern of the beams with reinforcement in the UHPFRC layer (beams R) at the maximal force (upper side of the beam)

### 3.5 Synthesis of the test results

#### 1. UHPFRC characterization

The material tests on the UHPFRC characterize the evolution of its physical properties, its mechanical properties and its time-dependent deformations:

- The investigated UHPFRC is self-compacting and has a good reproducibility.
- Initial setting occurs at an UHPFRC age between 30 to 32 hours. The long dormant period is attributed to the high amount of superplasticizer in the UHPFRC.
- Self-desiccation is high with a RH-decrease to 88% at an UHPFRC age of 7 days. It is due to the low water/binder-ratio of 0.14.
- Free autogenous shrinkage is high at early age (325  $\mu\text{m}/\text{m}$  at an UHPFRC age of 7 days).
- Creep deformations of approximately 60% of the free autogenous shrinkage deformations are measured for complete restraint at early age by means of restrained shrinkage tests. A cumulated stress of 4.2 MPa is necessary to restrain the deformations at an UHPFRC age of 7 days.
- An original UHPFRC tensile test is developed that allows to determine the UHPFRC tensile behaviour in a reliable way. The investigated UHPFRC has a magnitude of hardening of 2.8‰ for notched specimens and a tensile strength of  $f_{\text{U},\text{max}} = 11.0$  MPa at 28 days. Four different domains are defined for UHPFRC tensile behaviour and cracking.
- Mechanical properties (strengths and modulus of elasticity) and shrinkage deformations remain virtually constant beyond an UHPFRC age of 90 days.
- The UHPFRC has a very low air permeability ( $k_{\text{T}} < 0.003 \cdot 10^{-16} \text{ m}^2$ ). Thus, the exchange of substances between the UHPFRC and its environment is expected to be small. This confirms the protection function of UHPFRC, even for UHPFRC without heat treatment.

#### 2. Composite “UHPFRC-concrete” beams

- *Early age behaviour:* The maximum temperature rise in the UHPFRC layer is 10.8 °C and the temperature gradient is 5 °C for  $h_{\text{U}} = 10$  cm. The interaction of autogenous and thermal deformations is observed by means of beam deflections.
- *Deformations:* The major part of the beam deformations occurs until an UHPFRC age of 7 to 9 days and is attributed to autogenous and thermal deformations of the UHPFRC at early age.



- *Creep*: The creep compliance indicates that the creep deformations do not stabilize during the test period. The order of magnitude of the creep compliance is in the range of composite concrete elements.
- *Influence of the static system*: The bending deflections of the statically indeterminate beams ( $H$ ) are more than 10 times smaller than for the statically determinate beams ( $I$ ) during the long-term tests. The higher degree of restraint of beams  $H$  leads to higher stresses in the UHPFRC layer.
- *Influence of the thickness of the UHPFRC layer ( $h_U$ )*: The thicker the UHPFRC layer, the lower is the degree of restraint by the concrete substrate and the higher are the deformations. During the fracture tests, the stiffness of the beams is increased by a thicker UHPFRC layer. The resistance of the beams is increased for thick UHPFRC layers (see below).
- *Reinforcement in the UHPFRC layer ( $A_{s,U}$ )*: During the long-term tests, reinforcement in the UHPFRC layer induces additional restraint and reduces the beam deformations. The fracture tests show that reinforcement in the UHPFRC layer increases significantly resistance and stiffness of the beams. The cracks in the UHPFRC are more finely distributed and localized macrocracks appear at higher deformations near the maximum force of the beams, i.e. the apparent magnitude of hardening  $\varepsilon_{U,hard}$  is increased by a factor three.
- *Stiffness*: The stiffness of the composite “UHPFRC-concrete” members is significantly increased before the maximum force is reached when compared to the original reinforced concrete beam.
- *Resistance*: The resistance of the beams with reinforcement in the UHPFRC layer ( $R$ ) is significantly increased: it is two to four times higher for the investigated configurations when compared to the original reinforced concrete section. The resistance of the beams without reinforcement in the UHPFRC layer ( $NR$ ) is increased when the UHPFRC is higher than the threshold value  $h_{U,thr}$  ( $5 \text{ cm} < h_{U,thr} < 10 \text{ cm}$  for the tested beams).
- *Cracking*: During the long-term tests, only surface cracks are observed on the beams (crack widths  $< 0.1 \text{ mm}$ ). During the fracture tests, distributed macrocracks of small widths ( $< 0.1 \text{ mm}$ ) form with a crack spacing at the maximum force of 3 cm for beams with reinforcement in the UHPFRC layer ( $R$ ) and of 10 cm for beams without reinforcement in the UHPFRC layer ( $NR$ ). When the maximum force is reached, one to four localized macrocracks form. Failure, i.e. concrete crushing and fracture of the tensile rebars, occurs in one dominant localized macrocrack.
- *Interface cracks and debonding*: The beams exhibit monolithic behaviour during the long-term tests. Interface cracks are observed during the fracture tests: they develop into debonding cracks and lead to a loss of monolithic behaviour for the beams  $NR$ . The interface cracks do not alter the monolithic structural behaviour of the beams  $R$  and no debonding occurs for these beams.



## 4 Time-dependent behaviour of composite “UHPFRC-concrete” elements

*This chapter describes the time-dependent behaviour of composite “UHPFRC-concrete” members, i.e. deformations induced by early age and long-term volume changes of the UHPFRC. An outline of the problem is given in Section 4.1. The numerical model used for the study is presented in Section 4.2. In Section 4.3, the properties of UHPFRC are discussed with regard to the aspects that may be determinant in structural elements and to the numerical model. Finally, the time-dependent behaviour of composite “UHPFRC-concrete” elements and the influence of various parameters are investigated in Section 4.4.*

### 4.1 Importance of the time-dependent behaviour

The time-dependent behaviour such as early age and viscoelastic behaviour of UHPFRC is still not sufficiently known. High autogenous shrinkage and an increased heat of hydration when compared to normal strength concrete indicate larger deformations, however, UHPFRC have also higher strengths which allow them to withstand higher stresses due to restraint or loading.

The only attempt in modelling of UHPFRC has been undertaken for mechanical properties such as tensile and compressive behaviour (e.g. [AFGC02]), since UHPFRC have only been used in precast structures with heat treatment, reducing creep and shrinkage deformations to a minimum during service life. For composite “UHPFRC-concrete” structures without heat treatment, the time-dependent deformations have to be investigated and modelled in order to estimate deformations, stresses and possible damage in form of micro- or even macrocracking.

Modelling of the time-dependent behaviour of normal strength concrete is well known. The performance of models based on finite elements was demonstrated for example by Bernard who simulated the early age and long-term behaviour of composite RC beams [Bernard00]. UHPFRC properties differ from normal strength concrete and it has to be verified whether the models for normal strength concrete can be applied to UHPFRC

In consequence, the *aims* of this chapter are:

- to enhance the understanding of UHPFRC behaviour and to determine its importance for composite “UHPFRC-concrete” elements,
- to show whether the material laws for normal strength concrete can be applied for UHPFRC and to which extent UHPFRC behaviour can be modelled with an existing numerical model,
- to validate the numerical model with the results of the beam tests,
- to analyse and interpret the results of the early age and long-term beam tests by means of the numerical model and
- to estimate deformations, stresses, cracking tendency and their consequences for different parameters of composite “UHPFRC-concrete” members due to internal deformations.

### 4.2 Description of the numerical model

The time-dependent behaviour of structural elements consisting of cementitious materials is determined by the finite element program MLS of the company FEMMASSE [Femmasse04]. MLS uses material laws (on the macroscale) as input data to simulate the behaviour of structural elements. It was originally developed at the EPFL by [Roelfstra89]. Two-dimensional and rotationally symmetrical problems can be treated.

MLS considers hydration, hygral and thermal properties and the mechanical behaviour. The different material models have various couplings in order to simulate realistically the evolution of the proper-

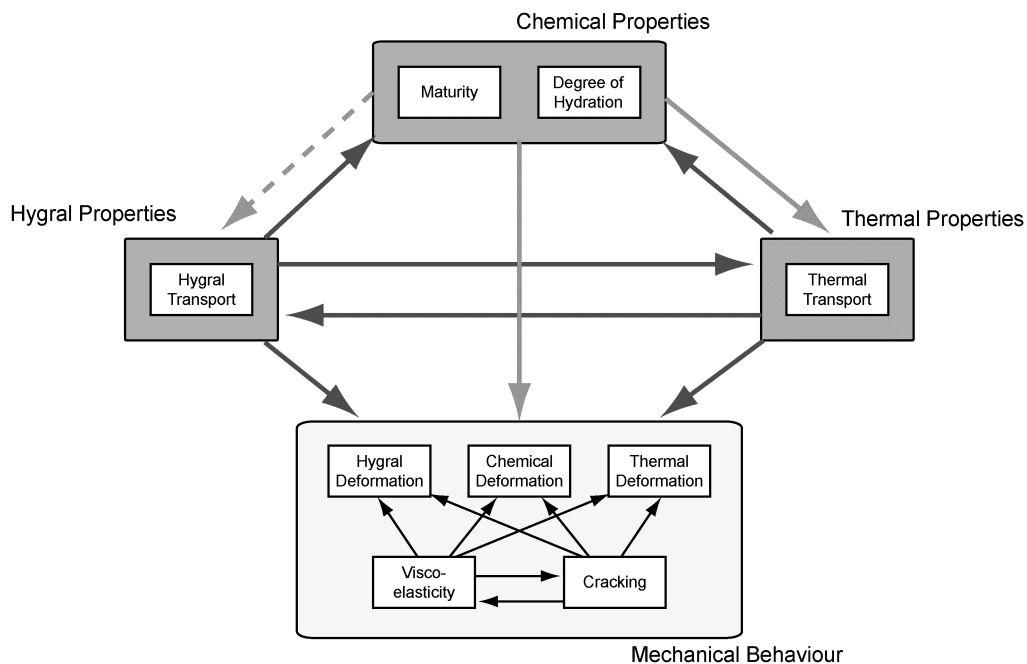


FIGURE 4.1: Simplified structure of MLS

ties of cementitious materials in time. A simplified overview of the couplings is given in Figure 4.1. A detailed description of the structure of MLS and of the used material models can be found in Appendix A.

The *hydration*, i.e. *chemical properties*, is expressed by the maturity method. Maturity is an equivalent time taking into account the temperature history in the element [Carino84]. The *thermal properties* comprise the evolution of the heat of hydration and the thermal transport. The *hygral properties* consider the moisture transport in the element and self-desiccation due to hydration. Finally, the *mechanical properties* consider the evolution of strengths and moduli as a function of maturity, deformations due to thermal and hygral changes, chemical deformation, cracking of the material and viscoelasticity. There are several couplings between the four main parts of the model, e.g. the evolution of the heat of hydration affects directly maturity and vice versa.

*Steel rebars* can also be introduced. They are defined as linear finite elements that are superimposed to the two-dimensional finite elements of the cementitious materials.

The use of a highly complex model like MLS requires extensive knowledge of material properties. Material characterization of UHPFRC is essential, since no test results have existed on several parameters of this material yet. Not all parameters can be determined by means of the experimental campaign and several hypothesis have to be made. The modelling of UHPFRC is discussed in Section 4.3.

## 4.3 Modelling of UHPFRC properties

### 4.3.1 Self-desiccation

The UHPFRC is subjected to significant self-desiccation from 32 hours on. This corresponds to the setting point, i.e. the beginning of the development of the mechanical properties as observed in the restrained shrinkage tests. Self-desiccation of normal strength concrete can be modelled with MLS, however, it is not possible to simulate self-desiccation of UHPFRC with this program. The desorption isotherms for the cementitious materials in MLS are calculated on the basis of mix parameters such as w/c-ratio, cement and air content with formulas developed by [Roelfstra89]. However, these formulas

for normal strength concrete do not apply to cementitious materials with low w/b-ratio ( $w/b < 0.23$ ) and that contain silica fume. In consequence, the hygral state in the UHPFRC cannot be simulated with MLS at present.

### 4.3.2 Thermal deformation

Thermal deformations at early age are mainly due to heat release during hydration. The heat of hydration with a total amount of  $H_T = 250'000 \text{ kJ/m}^3$  is approximately two times higher than for normal strength concrete. The models proposed in MLS to simulate the evolution of the heat of hydration do not well apply for UHPFRC because of its long dormant period ( $> 24$  hours). Thus, the adiabatic heat rise is given point by point for the numerical simulations on the basis of the semi-adiabatic tests from Section 3.2.2.

The evolution of the thermal dilation coefficient  $\alpha_T$  is not measured; it is estimated on the basis of the literature for concrete [Laplante94, Kada02] and is shown in Figure 4.2a. The initial thermal dilation coefficient is assumed to lie between  $40$  and  $60 \cdot 10^{-6} \text{ K}^{-1}$  and to decrease to its final value during the first hours of the acceleratory period (stage III); at maturities beyond  $36$  hours, it is estimated to be  $\alpha_T = 12 \cdot 10^{-6} \text{ K}^{-1}$  [AFGC02]. The thermal capacity is determined analytically to  $c_T = 2800 \text{ kJ/(m}^3 \text{ K)}$  by considering the thermal capacities of the UHPFRC constituents [DeLarrard99]. The thermal diffusivity is assumed to be  $\lambda_T = 2.4 \text{ W/(m K)}$ , a value slightly higher than for normal strength concrete because of the higher thermal conductivity of the steel fibres.

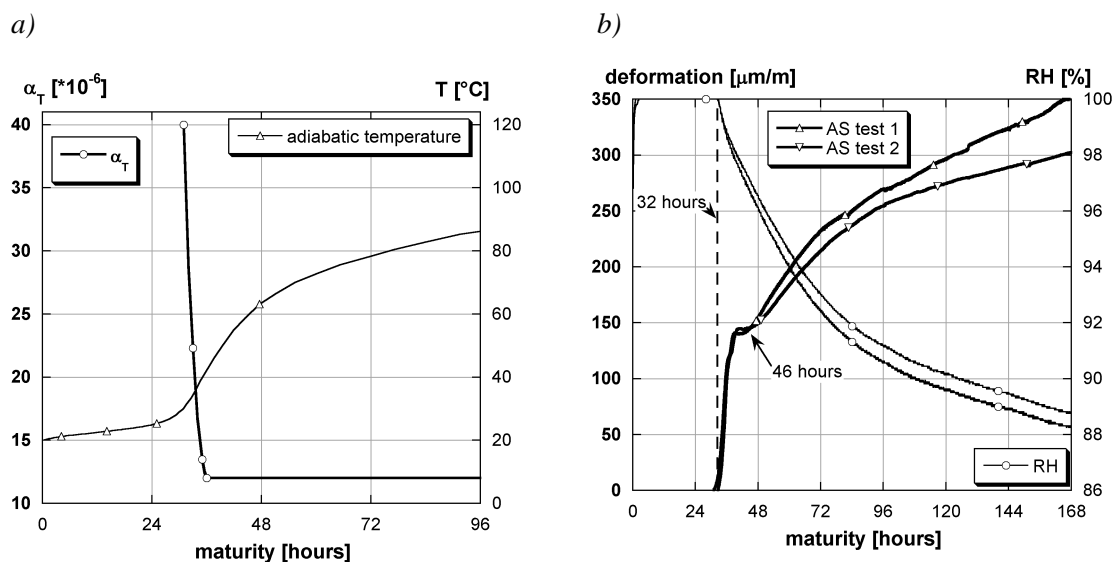


FIGURE 4.2: a) Evolution of the thermal dilation coefficient  $\alpha_T$  and adiabatic temperature rise due to the heat of hydration of the UHPFRC, b) evolution of autogenous shrinkage (AS) and self-desiccation (expressed by reduction of relative humidity RH)

### 4.3.3 Autogenous shrinkage

Autogenous shrinkage is larger for UHPFRC than for normal strength concrete. It is strong at early age ( $140 \mu\text{m/m}$  between 32 and 41 hours, Figure 4.2b) and may lead to stresses and microcracking in the material in case of restraint. Autogenous shrinkage consists to a major part of self-desiccation shrinkage. Figure 4.2b shows the evolution of autogenous shrinkage and self-desiccation of UHPFRC at early age. The decrease of relative humidity coincides with the beginning of autogenous shrinkage deformation at 32 hours. However, the autogenous shrinkage between 32 and 45 hours is not entirely explained by self-desiccation shrinkage. The kinetics of the two curves is different, i.e. the relative humidity decreases monotonously, whereas the rate of autogenous shrinkage becomes virtually zero between 39 and 46 hours. From 32 to 45 hours, the hydration reaction is strong and the rigid skeleton of UHPFRC forms. At the same time, the pore size distribution changes. It is impossible to predict autogenous shrinkage on the basis of material models considering the relative humidity as deduced from exist-

ing test results. Thus, it is proposed to define autogenous deformation point by point as “chemical shrinkage” in function of maturity.

Long-term autogenous shrinkage is measured on sealed cylinders (Section 3.2.5.2). The autogenous shrinkage rate is virtually zero after approximately 90 days. Again, the autogenous shrinkage is introduced point by point as “chemical shrinkage” in function of maturity.

#### 4.3.4 Drying shrinkage due to external drying

UHPFRC drying shrinkage occurs mainly during the first 10 to 15 days (see Figure 3.8a). It is approximately 4 times smaller than autogenous shrinkage. The drying shrinkage indicates that the permeability of the young UHPFRC is higher and that the young UHPFRC must be protected against drying by appropriate curing. Drying shrinkage cannot be modelled at the actual state of MLS, since the strong self-desiccation influences significantly the internal relative humidity and consequently, the exchange of moisture with the surroundings.

#### 4.3.5 Viscoelastic behaviour

The viscoelastic behaviour of the UHPFRC is modelled on the basis of two sets of experiments:

- at early age: restrained shrinkage tests (see Section 3.2.6.1) and
- in the long term: creep tests by Le Maou and co-workers (taken from [Parant03])

**Hypotheses for the modelling of early age viscoelasticity.** The viscoelastic behaviour of UHPFRC at early age is deduced from the restrained shrinkage tests described in Section 3.2.6.1 by making two major hypotheses:

1. The principle of superposition of creep and shrinkage deformation applies.
2. No damage occurs in the UHPFRC during the restrained shrinkage tests.

*Hypothesis 1 assumes that creep and shrinkage can be separated.* This point of view is generally accepted, however, Bazant and Chern found that creep is underestimated by the principle of superposition and that it can only be estimated correctly by considering the composite stress state resulting from shrinkage and creep simultaneously [Bazant87]. Creep and shrinkage deformations at early age depend strongly on the hydration process, i.e. on the changes of the structure of the cementitious material [RILEM02]. Internal stresses, e.g. generated by self-desiccation, lead to creep on the micro-level and influence significantly the viscoelastic response of the material [Acker01]. Consequently, this hypothesis is made for easiness of modelling. It is not totally supported as outlined above and has to be confirmed by further research.

*Hypothesis 2 assumes that no microcracking occurs during the restrained shrinkage tests.* However, the deformations were completely restrained during the tests and high stresses built up at early age. Figure 4.3 shows the evolution of the UHPFRC tensile strength and the stress in the UHPFRC during the restrained shrinkage tests. The evolution of the tensile strength is deduced from test results at 3, 8, 14 and 28 days, thus, the evolution at very early age (until 60 hours) is an approximation with the de Schutter model [DeSchutter96]. From 32 to 39 hours, the stress level in the material approaches the first cracking strength ( $f_{U_t,1st}$ ) and the probability of microcracking is high. However, the UHPFRC also hardens so that microcracks may be healed by ongoing hydration during this period. Consequently, hypothesis 2 may lead to an underestimation of early age cracking. Further investigations are necessary to determine whether microcracking is induced under restrained shrinkage conditions.

**Determination of the parameters of the Maxwell chains at early age.** Viscoelasticity is described in the numerical model by a generalized age-dependent Maxwell chain model. The parameters of the Maxwell chains are determined in two steps. First, specific creep curves for each stress increment are determined on the hypothesis that the creep curve of each load step is independent on the stress history. Then, time spans with similar creep behaviour are determined and the mean specific creep curve is calculated for each curve. These five specific creep curves are transformed into relaxation curves by an

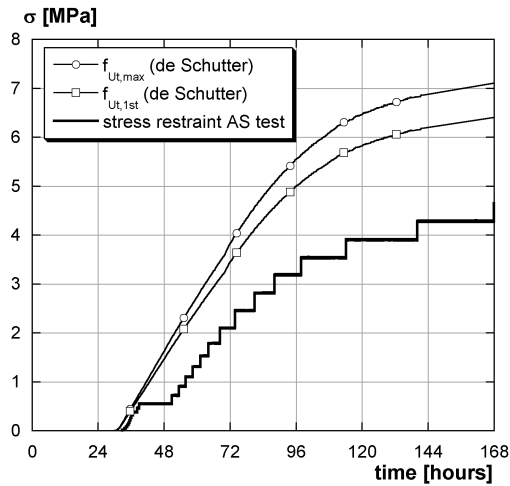


FIGURE 4.3: Evolution of tensile strength and of stress during the restrained shrinkage tests (UHPFRC tensile strength evolution determined by the de Schutter model [DeSchutter96] on the basis of uniaxial tensile test results on notched plates (see Section 3.2.4))

algorithm proposed by Bazant [Bazant72a]. The relaxation curves are approximated by Prony series that correspond to the mathematical formulation of the generalized Maxwell model (EQ. 4.1). The terms of the Maxwell chain are weighted by the factors  $\beta_i$  (for further details of the model see also Appendix A).

$$E(t) = E_c \cdot \left( \sum_{i=1}^m \beta_i \cdot e^{-\frac{t}{\tau_i}} \right) \quad \text{with} \quad \sum_{i=1}^m \beta_i = 1 \quad (\text{EQ. 4.1})$$

The first restrained shrinkage test is simulated with MLS using the Maxwell chains of this *first adaptation*. Similar to testing, the deformation of the restrained shrinkage specimen are reset to zero when the deformation threshold of  $6 \mu\text{m/m}$  is reached (see Figure 3.9 in Section 3.2.6.1) and the results are expected to remain between 0 and  $6 \mu\text{m}$ . Figure 4.4a shows the simulated restrained shrinkage deformation (1st adaptation) as well as the creep and shrinkage curves deduced from the restrained shrinkage test (see Section 3.2.6.1).

With the first adaptation, viscoelasticity of UHPFRC is underestimated, i.e. the total deformation (creep and shrinkage) of the UHPFRC is overestimated, from 32 to 36 hours. Viscoelasticity is overestimated, i.e. the total deformation is underestimated, between 36 and 44 hours and beyond 60 hours. The underestimation of viscoelasticity is explained by the strong hydration reaction during this period, leading to a fast evolution of the mechanical properties and of the creep kinetics. In this first step, the coefficients of the Maxwell chains are adapted from mean values of several creep curves and this procedure leads to an underestimation of viscoelasticity at the beginning of hardening. The overestimation of viscoelasticity between 36 and 44 hours and beyond 60 hours may be explained by the influence of the stress history: The first adaptation of the Maxwell chains is determined from mean curves over a time span without considering the stress history. However, the age dependent Maxwell chain model takes into account the stress history. The overestimation of viscoelasticity, i.e. the underestimation of deformations, is large and the Maxwell chains have to be re-adapted.

On the basis of the first adaptation, the *final Maxwell chains* are determined step-by-step on the basis of the results of restrained shrinkage test 1: The simulations start with a time span of the first 36

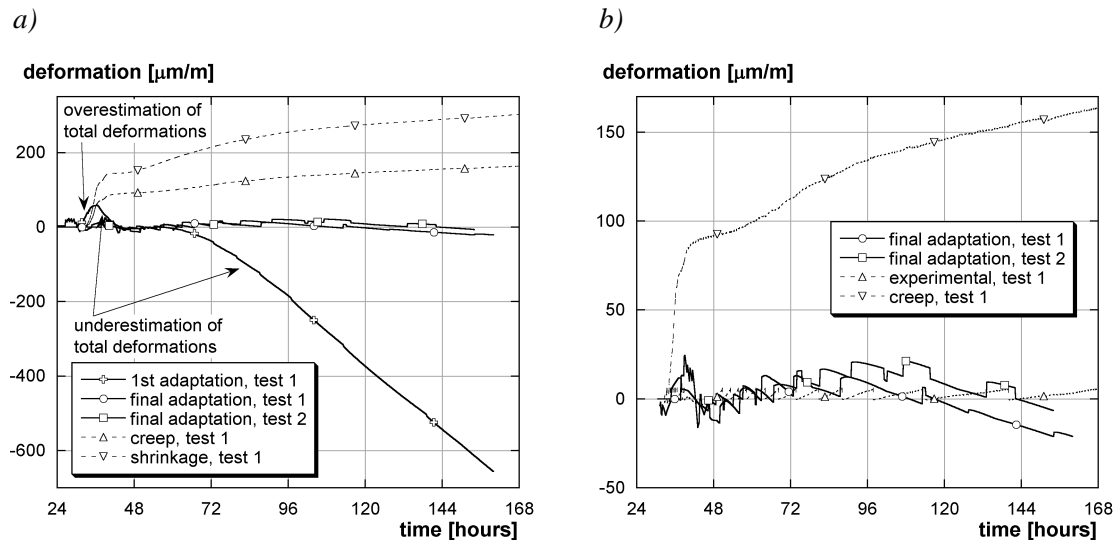


FIGURE 4.4: Simulation of the restrained shrinkage test with MLS: a) The simulation results with the 1st and the final adaptation of the parameters of the Maxwell chains are shown, in comparison to the calculated creep and the measured free shrinkage curves of test 1, b) The simulation with the final adaptations is shown in detail for both tests, in comparison to the targeted result of test 1 (experimental, test 1) and the calculated creep curve for test 1.

hours and the Maxwell chains are adapted for this time span. The time span is gradually increased and the Maxwell chains are adapted step-by-step. The time span between the individual Maxwell chains is reduced, since the time intervals of the first adaptation are too long to simulate well the evolution of viscoelasticity with increasing age. After the final adaptation of the Maxwell chains, the second restrained shrinkage test is simulated with these final Maxwell chains. Figure 4.4 shows that the first and the second restrained shrinkage test (test 1, test 2) are well simulated with the adapted Maxwell chains. The detail (Figure 4.4b) shows the comparison between the deformations measured during the restrained shrinkage test (experimental, test 1) and the simulations (final adaptation test 1, test 2). The scatter of the simulation is  $\pm 20 \mu\text{m/m}$ , compared to a deformation threshold of the test of  $6 \mu\text{m/m}$ . The results show that despite the weakness of the first hypothesis, early age creep can be well simulated with the proposed model.

Figure 4.5a shows the mean experimental relaxation curve for the period from 51 to 81 hours, deduced from the first restrained shrinkage test, the first adaptation of the Maxwell chain and the final Maxwell chains. It can be seen that in the first adaptation, only one Maxwell chain is used for this period, however, three Maxwell chains are used in the final adaptation. The relaxation potential of the final Maxwell chains is smaller than the one determined during the restrained shrinkage test for this period (Figure 4.4a). This result is expected, since viscoelasticity is overestimated with the first adaptation of the Maxwell chains.

**Early age UHPFRC viscoelasticity.** The specific creep behaviour at early age is shown for different loading ages in Figure 4.5b. The specific creep is high at early age with  $170 \mu\text{m/m/MPa}$  for a loading age of 36 hours and decreases to  $17 \mu\text{m/m/MPa}$  at 168 hours. A strong decrease of the creep rate is observed until 60 hours, corresponding to the period, during which the major part of hydration occurs. This confirms the observation that early age creep is directly related to the hardening of the cementitious material [DeSchutter02a].

**Comparison to concrete viscoelasticity at early age.** Figure 4.6 shows the comparison between UHPFRC and high strength concrete ( $w/c = 0.35$ ; cement content:  $460 \text{ kg/m}^3$ , maximum aggregate size: 10 mm,  $f_{cc} = 64$  and  $68 \text{ MPa}$  at 7 and 28 days respectively). The results of the high strength concrete were obtained with the same test set-up and under the same conditions as for the UHPFRC (i.e. by an isothermal restrained shrinkage test at  $20^\circ\text{C}$  under sealed conditions, see Section 3.2.6.1) and are taken from [Charron03].



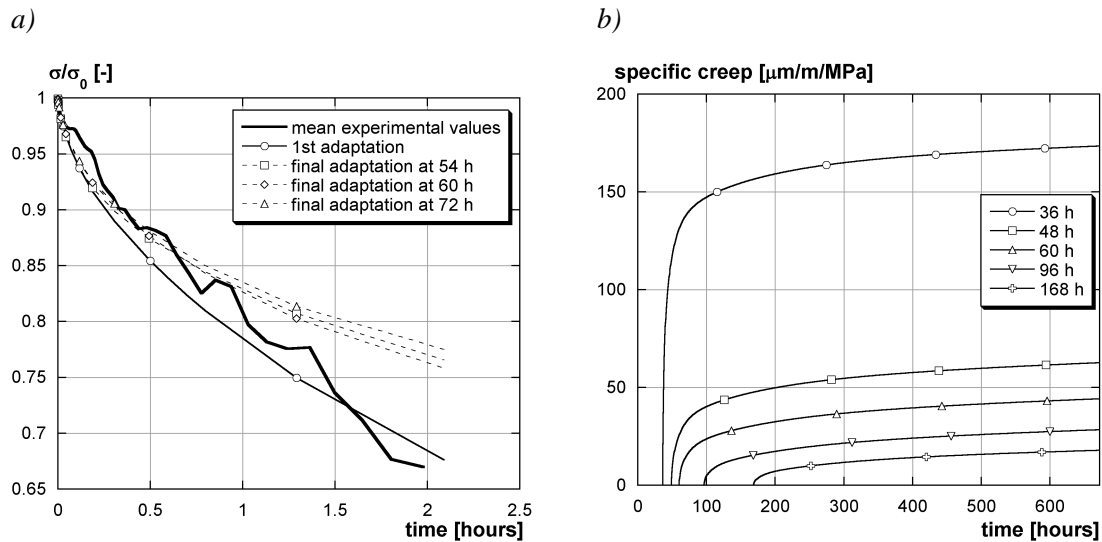


FIGURE 4.5: a) Adaptation of the relative UHPFRC relaxation curves with Prony series, b) evolution of the creep curves of the UHPFRC between 51 and 81 hours

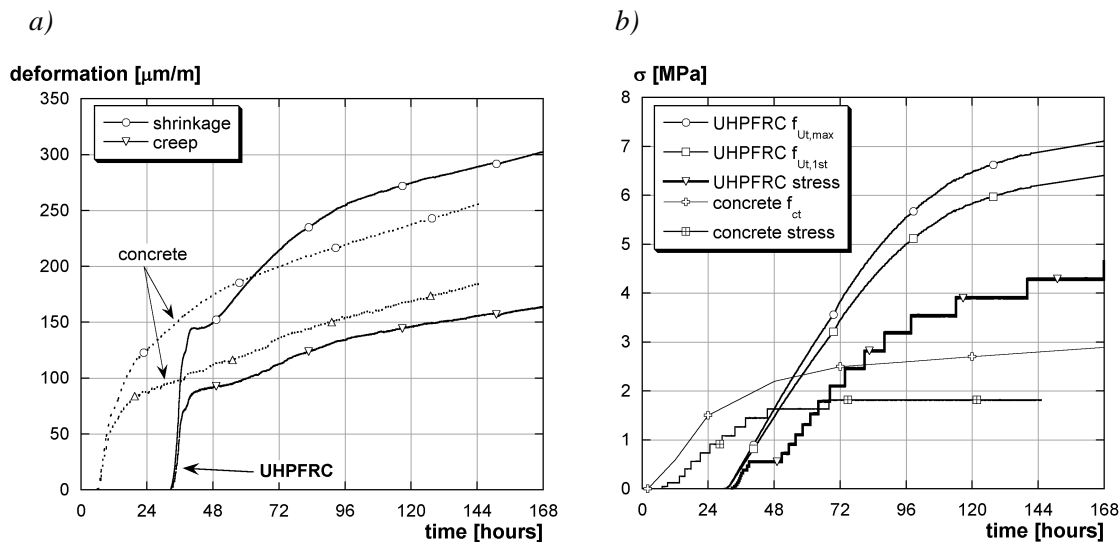


FIGURE 4.6: Early age viscoelasticity and autogenous shrinkage of UHPFRC and high strength concrete: a) shrinkage deformations, b) tensile stresses during restrained shrinkage tests and tensile strength evolution (UHPFRC tensile strength evolution directly deduced from uniaxial tensile tests on notched plates (see Section 3.2.4); concrete data taken from [Charron03])

The high strength concrete has a dormant period of 6 hours, which is 24 hours shorter than the UHPFRC. Its autogenous shrinkage deformation after 144 hours (120 hours of shrinkage evolution) amounts to 250  $\mu\text{m}/\text{m}$ . The UHPFRC shrinkage after 168 hours (120 hours of shrinkage evolution) is 300  $\mu\text{m}/\text{m}$  for a w/b-ratio of 0.14. This difference is small when compared to the difference of their water/binder-ratios and may be explained by the concrete mix parameters and by the restraint of the steel fibres in the UHPFRC: The relatively high autogenous shrinkage of the high strength concrete is due to its low w/c-ratio that prevents full hydration and leads to self-desiccation. Furthermore, the cement content and the maximum aggregate size of the concrete mix may reduce the effect of restraint by the aggregates: Loukili [Loukili96] showed that the addition of steel fibres reduced shrinkage deformations of UHPFRC of 10 to 20%. Moreover, autogenous shrinkage of UHPFRC decreases with decreasing w/b-ratio (for w/b-ratio < 0.26 [Cheyrezy01], see Section 2.3.4.3).

The autogenous shrinkage increase of the high strength concrete at the beginning of the measurements is slower than that of the UHPFRC. The UHPFRC shows a significant deformation increase between 32 and 40 hours, followed by a period where virtually no autogenous shrinkage occurs (40 to

48 hours). This phenomenon is typical for the investigated UHPFRC. It seems to be due to crystallization or topochemical reaction of the inner CSH (see Section 2.2.3.1 and [Barcelo01]) and not to temperature effects. The creep deformation after 120 hours of shrinkage evolution amounts to 160  $\mu\text{m}/\text{m}$  for the UHPFRC and to 180  $\mu\text{m}/\text{m}$  for the high strength concrete, indicating higher relaxation in the concrete specimen.

In the first hours of hardening, the stress rise in the high strength concrete is lower than that in the UHPFRC (Figure 4.6b). This is related to the stronger deformation increase of UHPFRC when compared to the high strength concrete during this period. It indicates that the probability of cracking is higher for the UHPFRC at the beginning of hardening. The stresses that develop in the high strength concrete are lower with 1.9 MPa than in the UHPFRC with 4.2 MPa at the end of the tests at 144 and 168 hours respectively. However, the tensile strength in the UHPFRC is also more than 2 times higher so that the relative stresses ( $\sigma_{ct}/f_{ct}$ ,  $\sigma_{Ut}/f_{Ut,1st}$ ) are of the same magnitude with approximately 65% at the end of the tests.

**Long-term UHPFRC viscoelasticity.** The parameters of the Maxwell chains for a loading age of 28 days are determined on the basis of compression creep tests performed on the multi-fibre variation of CEMTEC<sub>multiscale</sub><sup>®</sup> (tests performed by Le Maou and co-workers, taken from [Parant03]) (Figure 4.7). At present, no tensile creep data is available for this UHPFRC at higher ages. Thus, it is assumed that the creep of the CEMTEC<sub>multiscale</sub><sup>®</sup> used in this study is equal to the one used for the creep tests by Le Maou and that compressive creep is equivalent to tensile creep. The second hypothesis is necessary to relate the viscoelastic behaviour determined with the restrained shrinkage test to the viscoelastic behaviour determined at 28 days and to interpolate the viscoelastic behaviour for loading ages between 7 and 28 days.

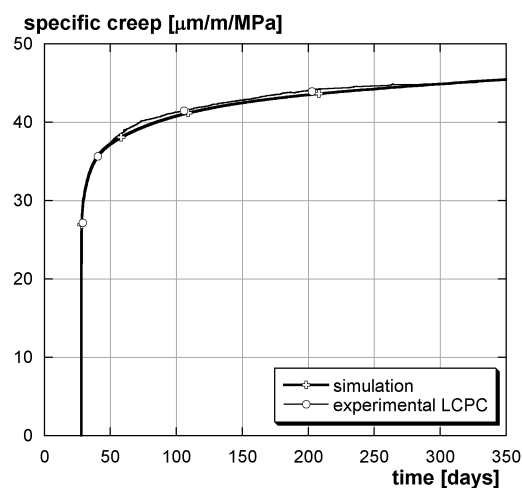


FIGURE 4.7: UHPFRC creep at 28 days including elastic deformation (experimental data from Le Maou and co-workers, taken from [Parant03])

The viscoelastic behaviour for ages beyond 28 days is extrapolated by assuming that the UHPFRC viscoelasticity evolves until an age of 90 days and stabilizes afterwards. This hypothesis is made because mechanical properties and shrinkage virtually stop after 90 days (Section 3.2). It is known for normal strength concrete that the viscoelasticity still evolves significantly at ages of several years [Neville70]. However, the hydration reaction of concrete also evolves several years, while it may be much shorter for UHPFRC due to its significant self-desiccation. Thus, the long-term viscoelastic behaviour of UHPFRC is assumed to be constant in a first approach for an loading age beyond 90 days.

### 4.3.6 Mechanical properties

The evolution of the mechanical properties such as strengths and secant modulus is determined on the basis of the test results and interpolated with the de Schutter and the CEB-FIP model (see Section 3.2). As the evolution of the mechanical properties virtually stops after 90 days, the values at 90 days are used to extrapolate strengths and moduli to higher ages. The first cracking strength for the simulation of composite “UHPFRC-concrete” members is estimated from the results of fracture tests on the composite beams to be 6.6 MPa at 90 days (see Section 5.2). Its time-dependent evolution is adapted by keeping the same kinetics as determined by the uniaxial tensile tests (see Figure 3.4b in Section 3.2.4.3)

The tensile behaviour is described in MLS by a linear-elastic stress rise (until the first cracking strength  $f_{Ut,1st}$ ) and a smeared crack model using a multi-linear  $\sigma$ - $w$ -law. The smeared crack model assumes a crack to be distributed over the width of the finite element  $L_{el}$ . The strain-hardening of UHPFRC is modelled as bulk deformation ( $\epsilon$ ) and must be transformed into a crack width  $w_{Ut}$  for input in MLS by means of the reference length  $L_{R,FE}$ . Accordingly, the equivalent strains in the smeared crack model for the hardening and for the softening part are determined by means of EQ. 4.2 and EQ. 4.3 respectively. For the numerical simulations, the reference length  $L_{R,FE}$  and the length of the elements  $L_{el}$  are assumed to be 10 mm which is considered to be an appropriate FE-size for the investigated structural elements [Wuest04].

$$\epsilon_{hard} = \frac{w_{Ut}}{L_{R,FE}} \quad (EQ\ 4.2)$$

$$\epsilon_{soft} = \frac{w_{Ut}}{L_{R,FE}} \cdot \frac{L_{R,FE}}{L_{el}} \quad (EQ\ 4.3)$$

## 4.4 Composite “UHPFRC-concrete” elements

### 4.4.1 Introduction

The time-dependent deformations in composite “UHPFRC-concrete” elements are modelled by considering thermal deformations, autogenous shrinkage and the viscoelastic behaviour. The tensile behaviour is modelled with a multi-linear and a bi-linear  $\sigma$ - $w$ -relationship for the UHPFRC and the concrete respectively.

**Material input.** The concrete properties are deduced from test results of the experimental campaign and from [Bernard00]. The parameters deduced from the experimental campaign are the evolution of the mechanical properties, the tensile behaviour, heat of hydration development and shrinkage. Concrete shrinkage deformations are assumed to be zero, since the concrete is older than 5 months at moment age of testing, and its autogenous shrinkage is very small at this age (approximately 20  $\mu\text{m}/\text{m}$  over a period of 90 days).

The hygral properties are not considered during the simulations (see Section 4.3.1), since the hygral state of the UHPFRC cannot be modelled with the available model. This simplification induces only a small error, since the concrete is assumed to be old in rehabilitation projects and its hygral state evolves very slowly. The hygral properties of UHPFRC are governed by self-desiccation. UHPFRC self-desiccation shrinkage is included in the autogenous shrinkage values (see Section 4.3.3). The simulation is based on the assumption of appropriate curing of the composite “UHPFRC-concrete” element, i.e. drying of UHPFRC is prevented. So, drying shrinkage of UHPFRC is assumed to be zero. In consequence, the hygral state should influence only marginally deformation and stress state in the composite “UHPFRC-concrete” elements. However, the situation changes for composite elements with new concrete substrates as discussed in Section 4.4.11.

Steel rebar with a yield strength of 500 MPa is the reinforcement in the elements; the bond stress-slip relationship is adjusted to UHPFRC and concrete.

All material input values can be found in Appendix B.

**Procedure.** The time-dependent behaviour of composite “UHPFRC-concrete” elements is discussed by means of the simulation and interpretation of the beams tested during the experimental campaign and by means of simulations on typical composite “UHPFRC-concrete” elements. Only some of the results are presented in this chapter. The simulation results of the time-dependent deformations for all beams can be found in Appendix D. The simulations on typical composite “UHPFRC-concrete” elements are used to interpret further the experiments and to investigate the influence of different parameters such as e.g. the reinforcement ratio in UHPFRC layer and the magnitude of autogenous shrinkage. During the experimental campaign, only deformations were measured, but no stresses and no microcracks (not visible with the naked eye) were observed. The numerical simulation allows to complete the missing information.

**Structural elements of the parametric study.** Three typical composite “UHPFRC-concrete” elements, shown in Figure 4.8, are chosen with regard to the work of [Bernard00]. Each element is simulated with three materials: (1) concrete, (2) concrete in the interface zone and (3) UHPFRC. The material properties are identical to the ones determined in the experimental campaign and can be found in Appendix B. The elements are sufficiently long to avoid the effect of boundaries on the stress distribution at mid-span ( $L > 3 \cdot h_{\text{tot}}$ ). The thickness of the old layer is fixed to 13 cm of concrete and 2 cm of interface concrete. The basic value for the thickness of the UHPFRC layer is 5 cm. The width of the cross-section is fixed to 100 cm, however, the simulation is two-dimensional, and the width is only important to evaluate support reactions and to determine the amount of reinforcement. The reinforcement in the concrete layer consists of two layers with a ratio of 0.8% (of  $A_c$ ) each. The reinforcement ratio in the UHPFRC layer  $\rho_{s,U}$  is also variable. Its basic value is  $\rho_{s,U} = 0\%$ . The thermal boundary conditions are kept constant during the simulations by considering an external temperature of 20 °C.

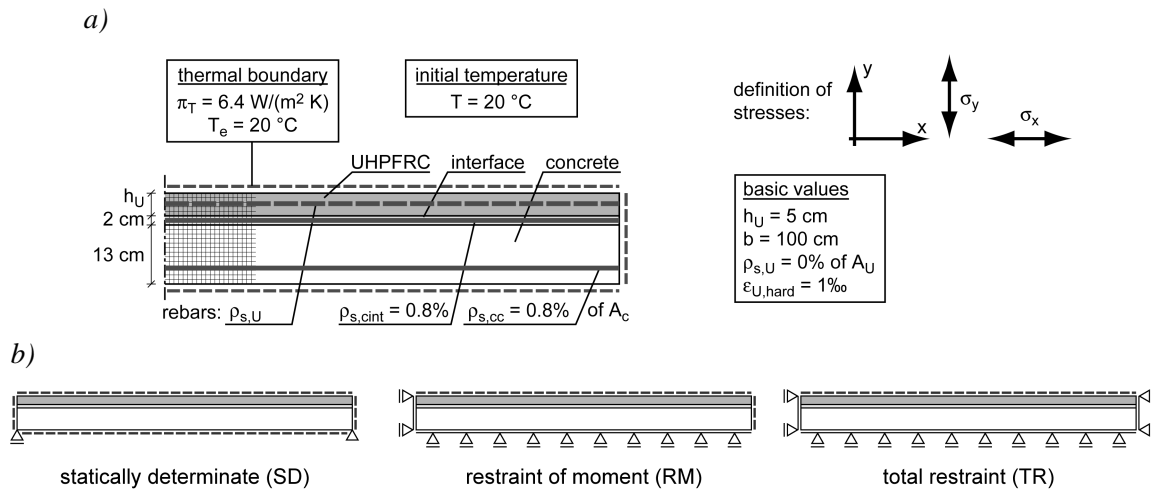


FIGURE 4.8: Basis of the numerical simulations: a) system and basic input values, b) static systems

Three static systems are considered (Figure 4.8b):

- a *statically determinate beam (SD)*, for which the degree of restraint is the lowest, since the UHPFRC layer is only restrained by the concrete layer and reinforcement ( $\mu = 0.45$  at 28 days),
- a beam, where *bending deformations are restrained (RM)*: here the element can only deform in axial direction ( $\mu = 0.73$  at 28 days),
- a *completely restrained beam (TR)* with a degree of restraint of  $\mu = 1$ .

**Definition of cracks and damage.** Cracking of UHPFRC is described by the same four domains as presented in Section 3.2.4.4.: Beyond the first cracking strength  $f_{U_t,1st}$ , when the UHPFRC is in the hardening domain ( $\epsilon_{U_t,1st} < \epsilon \leq \epsilon_{U_t,max}$ ), it is assumed that distributed macrocracks with small crack widths ( $< 50$  to  $100 \mu\text{m}$ ) form in the UHPFRC. Beyond the tensile strength  $f_{U_t,max}$  ( $\epsilon > \epsilon_{U_t,max}$ ), the UHPFRC exhibits softening and it is assumed that localized macrocracks form out of existing distributed macrocracks.

All simulations are performed with mean experimental values. No statistical variation is considered. It is obvious that the deterministic criterion for cracking does not correspond to the real material with its inhomogeneities and the resulting variations in tensile properties. However, the results of the simulation give an indication whether cracks form in the composite element.

*Damage* is used in two different contexts in this chapter:

- It is mostly used in relation with the UHPFRC layer. In this context, it signifies that the first cracking strength  $f_{U_t,1st}$  is reached and that distributed macrocracks of small widths form in the UHPFRC.
- Only in Section 4.4.9, where interface cracks and debonding are discussed, it is used to qualitatively describe the magnitude of cracking in the interface zone. The values used in this Section 4.4.9 for damage are directly obtained by the numerical simulation and describe the reduction of the modulus of elasticity when the concrete shows softening behaviour (for the definition of this damage see Figure A.3 in Appendix A).

#### 4.4.2 General description of the time-dependent behaviour of the beam tests

**Behaviour of a statically determinate beam (I5).** The beams of the experimental campaign are simulated in order to validate the numerical model and to interpret the results of the experimental study. Figure 4.9 shows the simulation results of the end-span deflection and the stress distribution in the mid-span section as a function of time for the statically determinate beam with  $h_U = 5 \text{ cm}$  (I5). The deflections of beam I5 are reproduced with the numerical simulation with a deviation smaller than 5%.

Figure 4.9 shows the individual contributions to the deflections in terms of thermal deformations, autogenous shrinkage and the influence of viscoelasticity on deflections. Thermal deformations are important during the first two days due to the strong heat release as a consequence of the hydration reaction. UHPFRC autogenous shrinkage is the main contribution to the deflections. The sum of thermal deformation and autogenous shrinkage deformation is smaller than the calculated total deformation. This is explained by the influence of the viscoelasticity which depends on the stress history in the specimen. The superposition of thermal and autogenous shrinkage deformations leads to a different stress history in the composite element than for the two separated components, altering the viscoelastic component.

When the viscoelasticity of the UHPFRC layer is not considered, the deflections are overestimated by 40%. The viscoelasticity of the UHPFRC layer relaxes the stresses in the UHPFRC layer, i.e. the UHPFRC layer deforms less and the beam deformations are smaller. The difference between the deflections with and without viscoelasticity demonstrates the importance of creep and relaxation for composite “UHPFRC-concrete” elements: the stresses in the UHPFRC layer are partially relaxed and the deformations of the element are smaller. The contribution of viscoelasticity may be important to delay or avoid the formation of distributed macrocracks and to reduce interface cracking. At early age however, it is not possible to distinguish between apparent and real creep mechanism at the present state (see Section 4.3.5) and the magnitude of microcracking in the UHPFRC cannot be determined.

The stress distribution in axial direction  $\sigma_x$  shows that the UHPFRC is in tension and the concrete in compression in its upper part and in tension in its lower part (see Section 2.6.1). The sudden change from tensile to compressive strength between UHPFRC and concrete layer at the interface leads to tensile stresses perpendicular to the interface at the free ends of the beams and is discussed in Section 4.4.9. The stresses in the cross section increase during testing which is mainly attributed to the autogenous shrinkage of the UHPFRC. The maximum tensile stresses are observed at the interface, i.e. at the bottom of the UHPFRC layer. However, the UHPFRC remains in the linear-elastic range

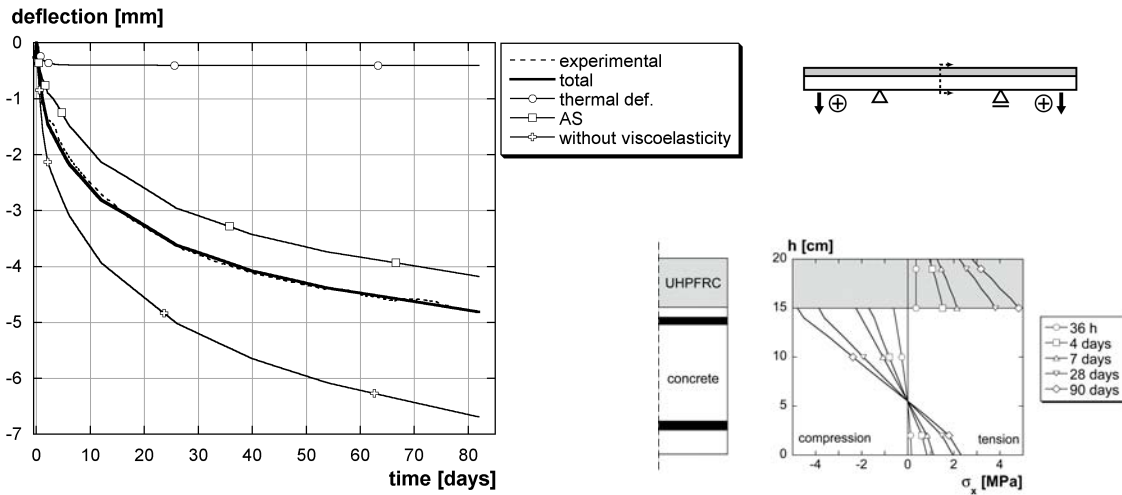


FIGURE 4.9: End span deflection and stress distribution at mid-span of the statically determinate beam with  $h_U = 5$  cm

( $\sigma_x < 0.6 \cdot f_{Ut,1st}$ ) during the whole test, i.e. no distributed macrocracks occur for this beam configuration.

**Behaviour of a statically indeterminate beam (H3).** The comparison between numerical simulation and test results is shown in Figure 4.10 for the statically indeterminate beam with  $h_U = 3$  cm which is the beam with the highest degree of restraint during the experimental campaign ( $\mu = 0.76$  at 28 days). Also, the recovery after the removal of the external supports and one horizontal internal support is simulated. The beam deformations before the removal of the external supports and one horizontal internal support ( $< 77$  days) are reproduced with the numerical simulation with a deviation smaller than 7%; the recovery is within the experimental scatter for the two lateral spans ( $f_2, f_3$ ) and overestimates the deformations of 0.15 mm in the central span ( $f_1$ ). This overestimation may be explained by the fact that a residual restraint remains in the central span after the removal of the external supports and one horizontal internal support. This residual restraint is probably produced by the support configuration of the beams (see Figure 3.15).

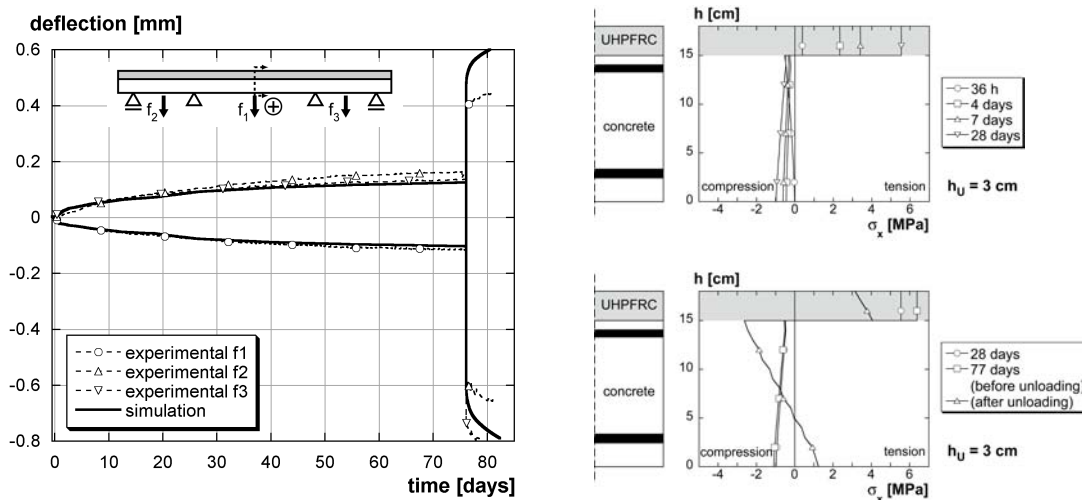


FIGURE 4.10: Deflections and stress distribution at mid-span of the statically indeterminate beam with  $h_U = 3$  cm

The stress distribution  $\sigma_x$  in the mid-span section of the beam shows nearly constant tensile stresses over the height of the UHPFRC layer and nearly constant small compressive stresses over the height of the concrete layer that increase in time. This indicates that the moment of the statically indeterminate beam is nearly completely restrained in the central span and that bending is restrained during testing. The calculated moment restraint for the given static system is 87.5% in the central span, i.e. the system corresponds here nearly to a built-in beam. The high degree of restraint leads to high tensile stresses in the UHPFRC layer, exceeding the first cracking strength  $f_{U,t,1st}$  for an UHPFRC age beyond 17.7 days. Consequently, the hardening of the beam is exploited from this age on. The maximum *exploitation of the magnitude of hardening* lies at  $EMH = (\epsilon_{tot} - \epsilon_{el}) / \epsilon_{U,hard} = 5\%$ , i.e. the hardening is exploited to a deformation of  $(\epsilon_{tot} - \epsilon_{el}) = 0.05\%$ , compared to the magnitude of hardening  $\epsilon_{U,hard} = 1\%$ . After the removal of the external supports and one horizontal internal support, the beam is statically determinate and the stress distribution corresponds to the one of the statically determinate beams. The tensile stresses in the UHPFRC decrease, while the stresses in the concrete increase (Figure 4.10).

The supports in the horizontal direction restrain the axial beam deformations only partially during the experimental campaign. Consequently, the horizontal supports are simulated by springs. The springs influence the ratio between end span and central span deflections: the higher the horizontal restraint, the lower is the mid-span deflection  $f_1$ . This ratio is used to estimate the spring constant  $k$  of the horizontal supports. The test results are well simulated for  $k = 210$  kN/mm, which is shown by the deflections in Figure 4.10 and by the horizontal displacements of the central supports shown in Figure 4.11. The horizontal displacements are well simulated when the beam is restrained. The deformations after the removal of the supports are underestimated. This may be explained by residual restraint of the supports as described above.

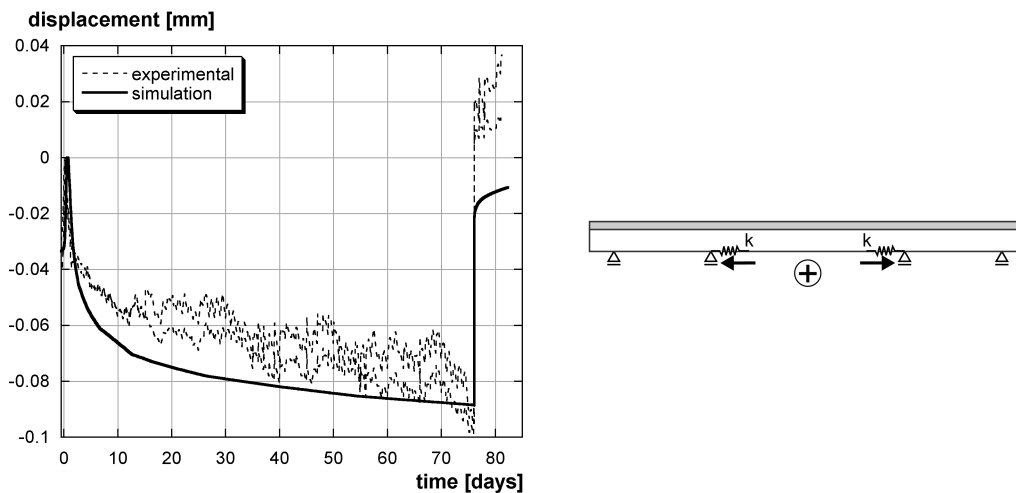


FIGURE 4.11: Horizontal displacements at the central supports of the statically indeterminate beam with  $h_U = 3$  cm (H3)

#### 4.4.3 Early age behaviour

**Early age behaviour of beams.** The temperature evolution in the beam section is correctly modelled for all beams for an age of the UHPFRC higher than 24 hours. Figure 4.12a considers as example a beam with  $h_U = 5$  cm (I5). Before 24 hours, the cooling of the UHPFRC layer down to the ambient temperature during the dormant period is too fast in the modelling. However, the UHPFRC is still soft during this period and the composite action in the beam is not yet active. Thus, the temperature evolution only becomes important at the beginning of the UHPFRC hardening, which coincides with the temperature rise at 24 hours when the temperature prediction is correct.

The mean value of the end span deflections ( $f_2, f_3$ ) is shown in Figure 4.12b. Differences between simulation and experimental results are observed prior to 24 hours. However, the UHPFRC has still not

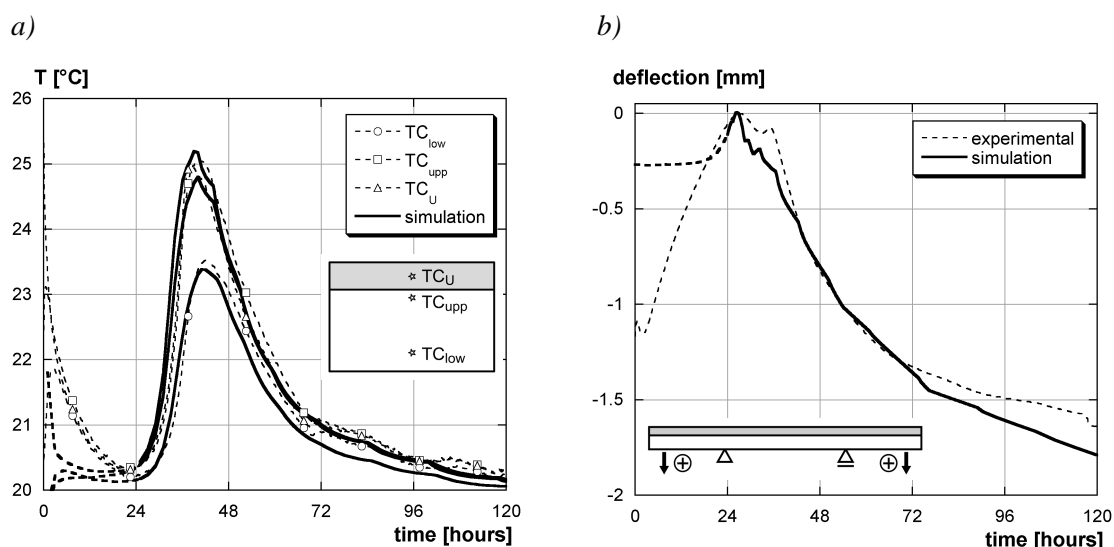


FIGURE 4.12: a) Early age temperature evolution in a beam for  $h_U = 5$  cm (I5), b) end span deflections at early age for the statically determinate beam with  $h_U = 5$  cm (I5)

set at this time and only small stresses are induced in the concrete ( $\sigma < 0.1$  MPa). The composite action of UHPFRC and concrete starts at approximately 26 to 30 hours, coinciding with the beginning of UHPFRC hardening. From 26 to 40 hours, the simulation overestimates the deformations by 0.2 mm. The second maximum observed during the beam tests at 35 hours occurs also in the results of the numerical simulation, but it is less pronounced. For higher ages, the simulation reproduces the experimental results with a deviation smaller than 10%.

The results indicate that the couplings between thermal and autogenous deformations at early age of UHPFRC can be described with the numerical model. The deflections of composite “UHPFRC-concrete” elements are predicted correctly as soon as the UHPFRC starts to set.

**Influence of thickness of the UHPFRC layer.** The thickness of the UHPFRC layer  $h_U$  and the thermal boundary conditions influence the temperature evolution due to heat of hydration in the composite “UHPFRC-concrete” element. The effects of a higher maximum temperature and temperature gradient over the depth of the composite element are discussed for different  $h_U$  by keeping constant boundary conditions.

The increase of thickness  $h_U$  leads to higher maximum temperatures and to higher temperature gradients between bottom face and UHPFRC layer due to heat of hydration (Figure 4.13). The increase of the maximum temperature ( $T_{max}$ ) is proportional to the increase of  $h_U$  and is explained by the heat transfer as for all concrete structures ([Bernard00]). The maximum temperature in the UHPFRC is reached at approximately 40 hours.

The maximum temperature gradient ( $\Delta T$ ) between bottom face and UHPFRC layers is reached at approximately 35.5 hours when the temperature at the bottom face of the beam is still close to the ambient temperature. However, this gradient occurs during the temperature rise, while the UHPFRC is still soft. Thus, the temperature gradient at the maximum UHPFRC temperature governs the tensile stress evolution in the UHPFRC. This is the gradient which is traced in Figure 4.13 ( $\Delta T$ ). The gradient increase is described as a function of  $h_U$  by a parabolic law, whereas the maximum temperature increases only linearly. When the element cools down to ambient temperature ( $> 40$  hours), the element contracts and the thermal deformations are superimposed to the autogenous shrinkage deformations, leading to an increase of the beam deformations. The temperature gradient is determinant for bending deformations, while the maximum temperature difference between the composite element and the external temperature governs axial deformations.

The impact of thermal deformations on composite “UHPFRC-concrete” elements is smaller than for composite RC elements. The couplings between autogenous shrinkage, thermal deformations and the evolution of mechanical properties and viscoelasticity do not allow to fix a criterion for maximum tem-



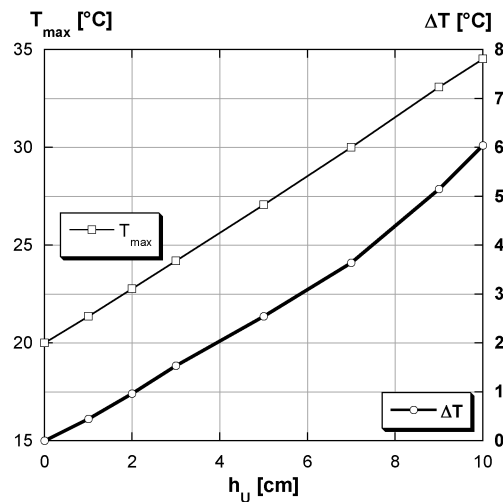


FIGURE 4.13: Maximum temperature and maximum temperature difference at early age as a function of the thickness of the UHPFRC layer

peratures as suggested by [Bernard00] for composite RC structures. However, the high autogenous shrinkage of UHPFRC seems to be predominant in composite “UHPFRC-concrete” elements (see Figure 4.9), at least for the investigated range of thicknesses  $h_U$ .

**Early age damage tendency.** At early age, the evolution of the modulus of elasticity and thus of the element stiffness is faster than that of the strengths (see Section 2.2.1.5). Furthermore, thermal and shrinkage deformations induce stresses in the UHPFRC in case of restraint. It has to be determined if the tensile strength is reached in the composite element and if cracks form at early age, since the latter may reduce the durability of the structural member.

Figure 4.14a shows the evolution of the first cracking strength  $f_{U,t,1st}$  and the tensile stresses at the top face and the interface in the UHPFRC for the statically determinate system SD and the completely strained system TR. The stresses of system SD reach a maximum at 36 hours, decrease in the following and increase again beyond 40 hours. The maximum is less significant for system TR and the stress increase is approximately three times higher than for SD for an UHPFRC age beyond 40 hours. The cracking strength at early age must be assumed, since tensile tests were only conducted on UHPFRC at 4 days and beyond. The evolution during the first 30 hours does not correspond to reality, since no tensile strength develops during the dormant phase; the linear increase during this period is chosen in order to avoid an important apparent damage in the simulation at very early age. Since the experimental results show no visible damage in the UHPFRC layer during the long-term tests, this hypothesis is justified at the present state of knowledge.

The relative stresses  $\sigma_x / f_{U,t,1st}$  are shown in Figure 4.14b. The relative stresses may be interpreted as the probability of cracking at early age, since all simulations are based on mean experimental values. The first cracking strength  $f_{U,t,1st}$  is assumed for this period and gives an indication of the stress level  $\sigma_x$ . The closer the value is to 100%, the more likely is the formation of microcracks. The relative stresses of SD have a maximum of 60% at 36 hours. It is possible that the first cracking strength  $f_{U,t,1st}$  is reached in this period which would indicate the formation of distributed macrocracks in the UHPFRC. The relative stress has a minimum between 40 and 43 hours. This is due to the kinetics of autogenous shrinkage that is nearly constant during this period and to the assumption that the mechanical properties continue to evolve. Consequently, stress relaxation occurs between 40 and 43 hours. Beyond 48 hours, the relative stress in the UHPFRC is nearly constant at early age with 22 and 40% at the top face and the interface respectively, and the probability of cracking is relatively low.

The relative stresses of the completely restrained system TR also attain a maximum at 36 hours, however, their magnitude of 50% is lower than for SD, indicating that the restraint seems to have a beneficial effect on the stress evolution at very early age. However, the calculated stress difference between

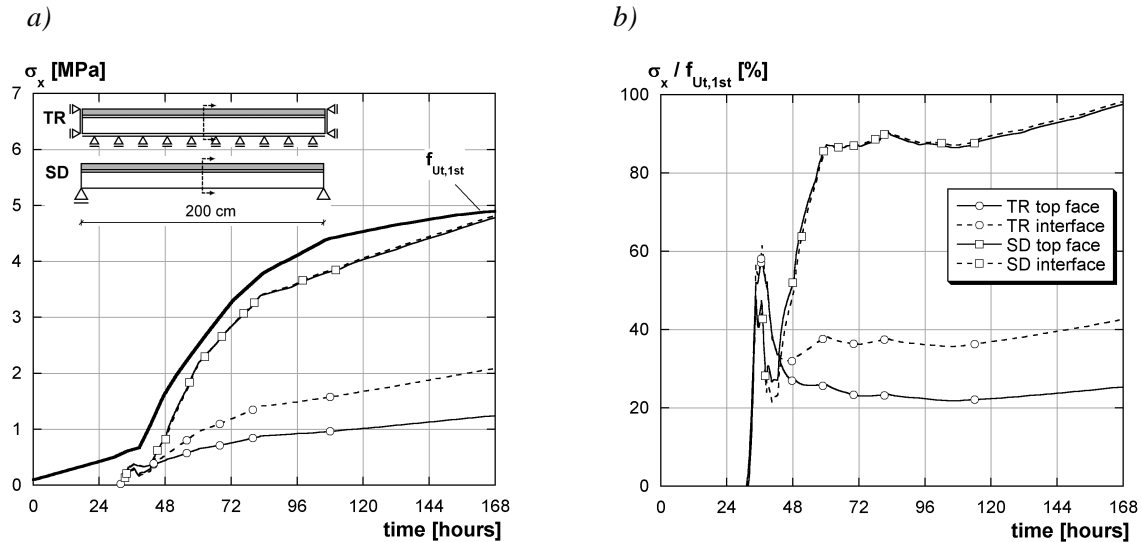


FIGURE 4.14: Early age: a) stresses  $\sigma_x$  the statically determinate system, b) relative stresses  $\sigma_x$  in the UHPFRC layer of systems SD and TR (legend is identical for both diagrams)

the two systems amounts only to 0.1 MPa and no firm conclusion can be drawn. The relative stresses of TR increase strongly beyond 40 hours, until they reach a value of 90% at 60 hours. At 168 hours, i.e. at 7 days, the relative stress is nearly 100% and the probability of the formation of distributed macro-cracks of small widths is very high for the completely restrained system.

The maximum at 36 hours for the two systems indicates that the probability of cracking is high at the beginning of UHPFRC hardening. At present, it is not known if cracks form during this period and if these cracks are healed with ongoing UHPFRC hydration. These questions are important for the prediction of durability of the composite “UHPFRC-concrete” structures, since early age damage may reduce the durability of structural elements as shown by [Bernard00]. They have to be answered by future work.

#### 4.4.4 Static system

**System description.** Three different static systems are discussed for the typical composite “UHPFRC-concrete” elements (Figure 4.8b). They are designed to differentiate between a statically determinate system (SD) where the UHPFRC layer deformations are only restrained by the concrete substrate, a system, where the bending moment is restrained (RM) and only axial deformations can occur and a system, where axial and bending moment deformations are restrained (TR). The evolution of the degree of restraint  $\mu$  for UHPFRC stress  $\sigma_x$  at the interface, i.e. the stress at the bottom of the UHPFRC layer, is shown in Figure 4.15a. The degree of restraint is determined with the formulas from Section 2.6.1 and is calculated for linear-elastic material behaviour. The formulas do not apply for damaged cross-sections, i.e. when the UHPFRC first cracking strength  $f_{U_t,1st}$  is reached. The initial degrees of restraint are 1 for all three systems, since the UHPFRC nearly does not have any stiffness before setting. With ongoing hydration, the stiffness of the UHPFRC increases and the restraint due to the concrete substrate decreases. The system SD has the lowest value with  $\mu = 0.45$ , followed by system RM with  $\mu = 0.73$  and the totally restrained system TR with  $\mu = 1$  ( $\mu$ -values for an UHPFRC age of 28 days).

**Stresses  $\sigma_x$  and deformations.** The UHPFRC tensile stresses  $\sigma_x$  at the interface are dependent on the static system (Figure 4.15b). The highest stresses occur for the completely restrained system TR in which the first cracking strength  $f_{U_t,1st}$  is reached at an UHPFRC age of 7 days. The first cracking strength  $f_{U_t,1st}$  is attained at 28 days for system RM, whereas it is never reached for system SD. However, the magnitude of hardening ( $\epsilon_{U,hard} = 1\text{‰}$ ) is only exploited to  $EMH = 5\%$  and to  $EMH = 2\%$  for systems TR and RM respectively.

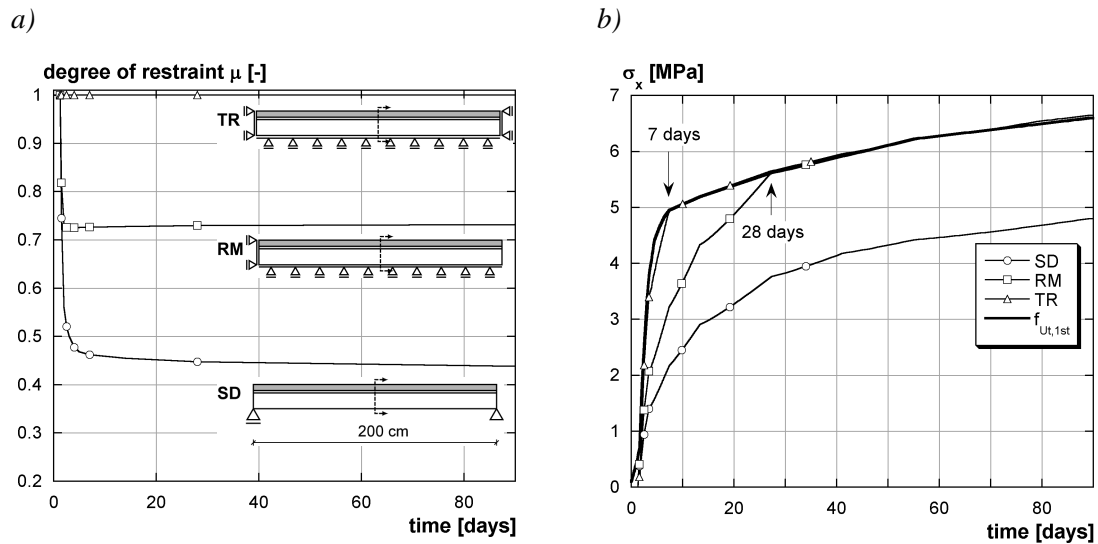


FIGURE 4.15: a) Evolution of the degree of restraint, b) UHPFRC stress  $\sigma_x$  at the interface for the different static systems

Figure 4.16 shows stress distributions  $\sigma_x$  and deformed systems in the cross-section at mid-span for the three static systems at different UHPFRC ages. The *beam SD* curls due to UHPFRC shrinkage and has a maximum deflection of  $1/1650$ . Its stress distribution shows gradients in the UHPFRC and in the concrete layer which are due to the bending deformation (see Section 4.4.2). The highest UHPFRC tensile stresses are observed at the interface. Moreover, the lower face of the concrete is in tension, however, its tensile strength is not reached.

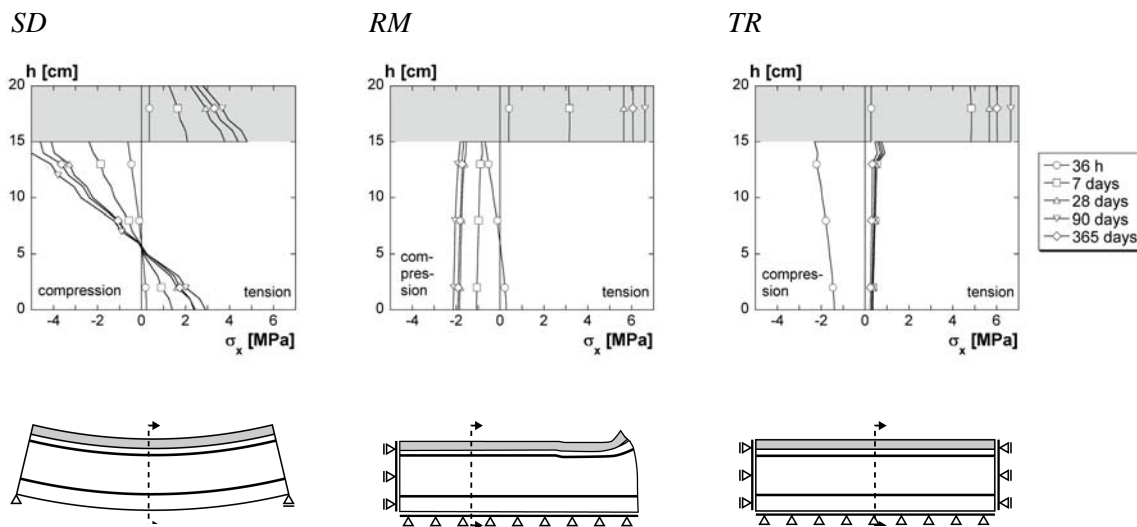


FIGURE 4.16: Comparison of the static systems: stress distributions and deformed systems

System *RM* can only deform in axial direction. It has nearly constant stress distributions  $\sigma_x$  in the UHPFRC and concrete layer, with the UHPFRC being in tension and the concrete in compression. The constant stresses in each layer indicate an efficient restraint of bending deformations. A stress gradient can be observed in the concrete layer for young UHPFRC (36 hours) which is attributed to the temperature gradient in the element due to the heat release during UHPFRC hydration. System *RM* deforms in axial direction. A deformation gradient can be observed at the free end, leading to tensile stresses perpendicular to the interface. The influence of the static system on debonding is discussed in Section 4.4.9.

No deformations occur in axial direction and in bending in system *TR*. The stress distribution  $\sigma_x$  in the UHPFRC layer is constant and only a small gradient is observed in the concrete layer. At early age,

the concrete layer is in compression (UHPFRC age of 36 hours). This occurs during the temperature rise in the element due to heat of hydration of the UHPFRC. The UHPFRC layer is in tension due to the interaction between autogenous shrinkage and thermal deformations. Beyond 36 hours, both UHPFRC and concrete layer are in tension. This is explained by the cooling of the element after the major part of the heat of hydration is released and by the UHPFRC shrinkage deformation. The tensile stresses in the concrete are small with maximum values of approximately 0.5 MPa. It must be noted that the completely restrained system TR is theoretical, since it is impossible to obtain total axial restraint in real structures. However, this system gives an upper boundary for stresses and possible cracking in the UHPFRC layer.

#### 4.4.5 Thickness of the UHPFRC layer

**Statically determinate beams of the experimental campaign.** Figure 4.17 shows the influence of the thickness of the UHPFRC layer on deflection and stress distribution for the statically determinate beams (I3, I5, I10) of the experimental campaign. The numerical simulation reproduces the test results with a deviation smaller than 5%. The end-span deflections of the beams become larger with increasing thickness. The comparison of the stress distribution  $\sigma_x$  of the beams with  $h_U = 3$  cm and 10 cm (I3 and I10) shows that UHPFRC stresses are higher and concrete stresses lower for thinner UHPFRC layers. The UHPFRC layer of  $h_U = 3$  cm is entirely in tension, with a maximal tensile stress of 5.6 MPa at 90 days; the UHPFRC of  $h_U = 10$  cm is only in tension in its bottom part and in compression on the upper face due to the strong curling deformation of the beams. The concrete stresses are higher for  $h_U = 10$  cm with a maximum value of 2.4 MPa at 90 days, compared to 1.7 MPa for  $h_U = 3$  cm. This is explained by the restraint of the UHPFRC by the concrete layer: the thicker the UHPFRC layer, the smaller is the influence of the concrete substrate and the smaller is the restraint in the UHPFRC layer. The simulation results suggest that the first cracking strength  $f_{U,t,1st}$  and the concrete tensile strength  $f_{ct}$  are not reached for the statically determinate beams during testing.

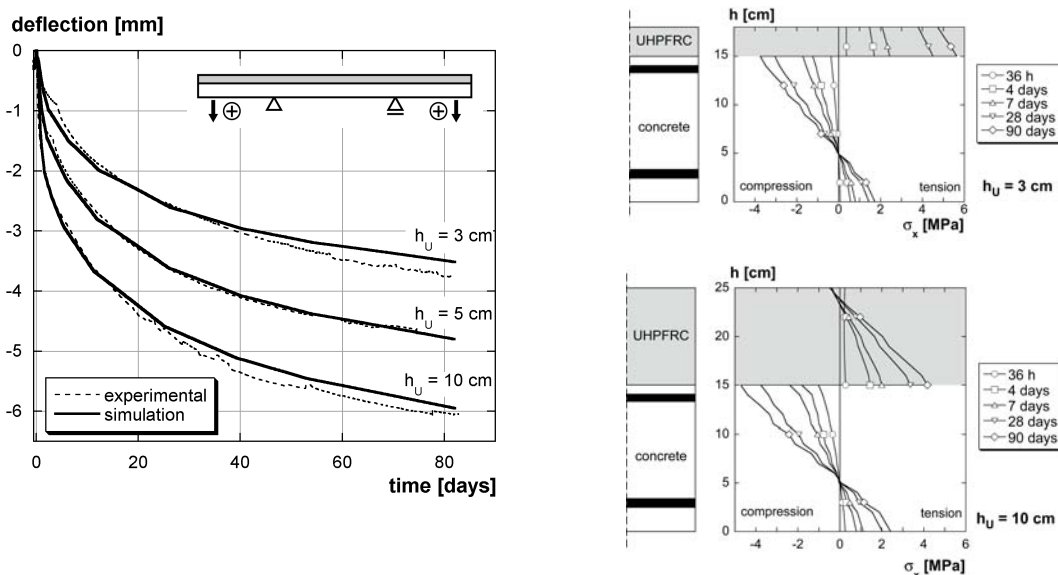


FIGURE 4.17: Influence of the thickness of the UHPFRC layer for the statically determinate beams of the experimental campaign

**Thin UHPFRC layers (system TR).** The beam tests have shown that the first cracking strength  $f_{U,t,1st}$  may be reached in composite “UHPFRC-concrete” members with thin UHPFRC layers. Thin UHPFRC layers with minimum thicknesses of approximately 1 cm may be applied as surface protection. Figure 4.18 shows the evolution of the UHPFRC stresses  $\sigma_x$  at the interface, i.e. the maximum tensile stress in the UHPFRC layer, for thin UHPFRC layers for system SD. For the given material parameters, the first cracking strength  $f_{U,t,1st}$  is reached for  $h_U = 1$  cm at an age of 26 days and the UHPFRC enters

the hardening domain beyond this age. The maximum relative stress ratio is  $\sigma_x/f_{U_t,1st} = 1.003$ , corresponding to a hardening deformation of 0.02‰ compared to a magnitude of hardening of  $\epsilon_{U,hard} = 1\%$ . Thus, only EMH = 2% of the hardening domain of the UHPFRC are exploited and few distributed macrocracks with small widths form (see Section 3.2.4.4). Consequently, the UHPFRC remains in the linear-elastic domain for  $h_U \geq 2$  cm for the investigated materials; distributed macrocracks of small widths form for  $h_U = 1$  cm.

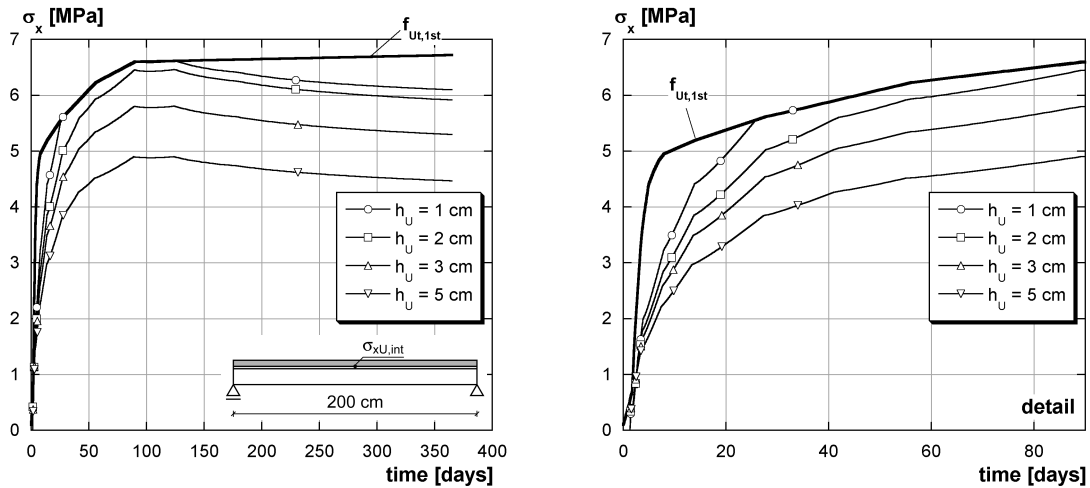


FIGURE 4.18: UHPFRC stress  $\sigma_x$  at the interface for thin UHPFRC layers

In this study, constant tensile properties are assumed over the whole depth of the UHPFRC layer. No segregation effects are considered in thicker layers which would lead to lower apparent tensile strengths on the top face of the UHPFRC layer. However, it is shown that the tensile stresses at the top face decrease significantly with increasing beam depth (see Figure 4.17). Therefore, no cracks should form in the UHPFRC layer of statically determinate systems due to slight fibre segregation.

#### 4.4.6 Reinforcement in the UHPFRC layer

**Statically determinate beams.** Reinforcement in the UHPFRC layer decreases the beam deformations as shown for the statically determinate beams with  $h_U = 10$  cm (I10, I10R) in Figure 4.19a. The numerical simulation predicts the effect of reinforcement with a deviation smaller than 5%, thus, the physical reality is well represented with the model of reinforcement.

Reinforcement does not only reduce the beam deformations, but it increases also the tensile stresses  $\sigma_x$  in the UHPFRC layer. The influence of the reinforcement on UHPFRC stresses is higher at the top face than at the interface: the stress differences are 1.5 MPa and 0.7 MPa at the top face and at the interface respectively for an UHPFRC age of 28 days. The UHPFRC cover of the reinforcement being assumed to be 2 cm, the stiff rebars ( $E_s = 205$  GPa  $\approx 4 \cdot E_U$ ) partially hinder UHPFRC deformations. The existing concrete substrate and the upper reinforcement in the concrete layer restrain more efficiently the interface than the top face deformations. Thus, the additional restraint by the reinforcement in the UHPFRC layer is more efficient at the free top face. Finally, it has to be noted that the beam without reinforcement in the UHPFRC layer (I10) is in compression on the top face, whereas the beam with reinforcement (I10R) is in tension.

**Static system (SD).** The influence of reinforcement in the UHPFRC layer is shown in Figure 4.20 for the statically determinate system (SD). The reinforcement ratio is varied between  $\rho_{s,U} = A_{s,U}/A_U = 0$  and 5%<sup>7</sup>. Higher reinforcement ratios lead to higher stresses  $\sigma_x$  in the UHPFRC layer and to smaller

7. 5% correspond to rebar with  $\varnothing 16$  mm @ 8 cm.

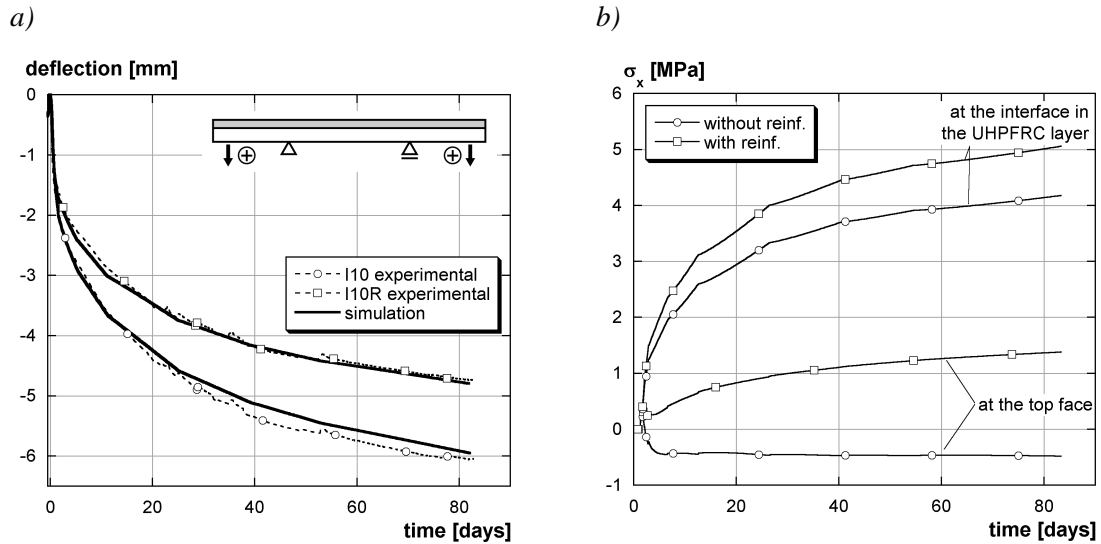


FIGURE 4.19: Influence of reinforcement in the UHPFRC layer for the statically determinate beams with  $h_U = 10$  cm (I10, I10R) of the experimental campaign

deflections. The stress differences between  $\rho_{s,U} = 0$  and 5% are 0.7 MPa and 0.4 MPa at the top face and at the interface respectively for an UHPFRC age of 28 days. However, the tensile stresses remain below the first cracking strength of the UHPFRC even for high reinforcement ratios for the given configuration. The deflections of the composite beam with  $\rho_{s,U} = 5\%$  are 20% smaller than of the beam without reinforcement in the UHPFRC layer. This means that reinforcement reduces considerably the deformations induced by internal UHPFRC deformations, without damaging the composite “UHPFRC-concrete” element.

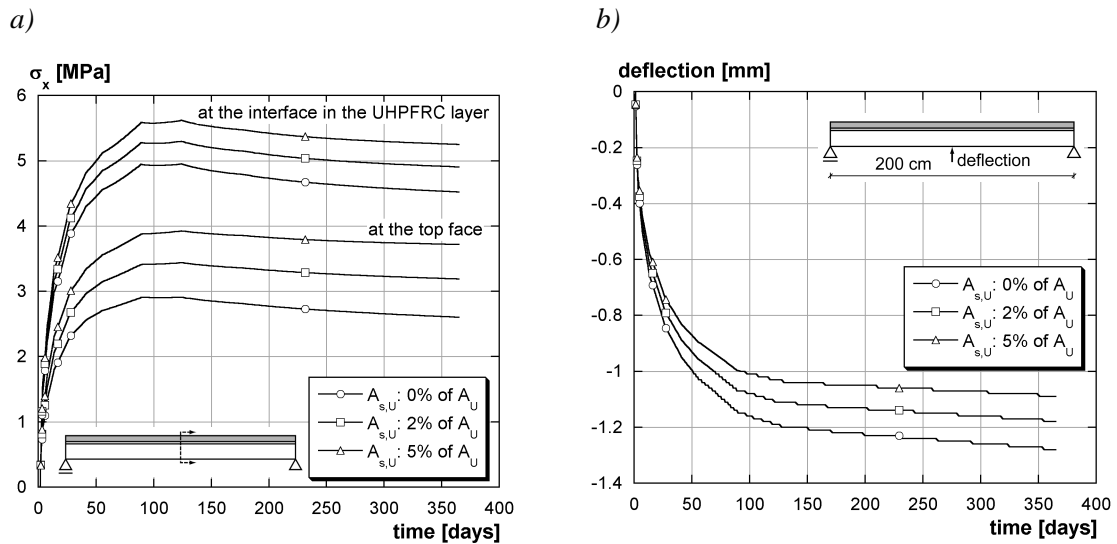


FIGURE 4.20: Influence of the reinforcement in the UHPFRC layer  $A_{s,U}$ : a) on the stresses  $\sigma_x$  in the UHPFRC layer, b) on the mid-span deflection

#### 4.4.7 Tensile strain-hardening of UHPFRC

Strain hardening is one of the main characteristic properties of UHPFRC. It is described by its magnitude  $\epsilon_{U,hard}$  and the ratio of the maximum tensile strength to the first cracking strength  $f_{U,max}/f_{U,1st}$ . The influence of strain hardening under tension is investigated by means of system TR, since this is the system, for which the magnitude of hardening is the most used. It is exploited to  $EMH = 5\%$  for the basic configuration as shown in Section 4.4.4.

**Magnitude of hardening.** The magnitude of hardening  $\varepsilon_{U,hard}$  is varied between 0.5 and 5‰. Pure strain softening, i.e.  $\varepsilon_{U,hard} = 0\%$ , is also discussed. The softening part of the UHPFRC tensile behaviour is kept constant for all simulations. The exploitation of the magnitude of hardening increases with decreasing  $\varepsilon_{U,hard}$ : EMH = 1% of the hardening domain are used for  $\varepsilon_{U,hard} = 0.5\%$  and EMH = 10.6% for  $\varepsilon_{U,hard} = 5\%$  (Figure 4.21). However, the state of deformations, i.e. the absolute value of deformations  $\varepsilon$  in the UHPFRC layer, remains virtually constant. This indicates that the equilibrium of deformations in the structural element is practically not influenced by the magnitude of hardening  $\varepsilon_{U,hard}$ , provided that the deformations in the UHPFRC do not exceed the magnitude of hardening.

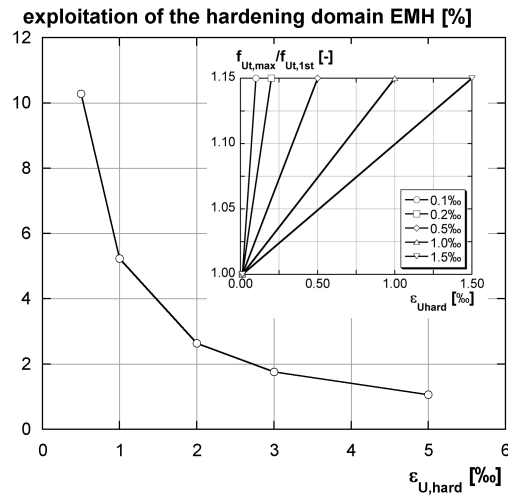


FIGURE 4.21: Influence of the magnitude of hardening on the exploitation of the hardening domain EMH

In case of  $\varepsilon_{U,hard} = 0\%$ , the material enters the softening domain when the first cracking strength is reached and localized macrocracks should form. However, no localized macrocracks, but a constant strain distribution over the whole length of system TR are obtained from the numerical simulation program. Even the introduction of an artificial error in form of a notch in the UHPFRC layer does not induce strain localization and cracking. In real structures, cracks form in weak sections, i.e. sections with smaller tensile strengths. However in the numerical model, the tensile strength is assumed to be constant over the whole length of the element and no crack localization can be modelled when a constant stress state exists in the element.

**Ratio  $f_{U_t,max}/f_{U_t,1st}$ .** The influence of the ratio  $f_{U_t,max}/f_{U_t,1st}$  is investigated for ratios between 1.00 and 1.15. When the ratio is below 1.00, there is no more strain hardening and softening occurs. The variation of the ratio  $f_{U_t,max}/f_{U_t,1st}$  does not have a significant influence (range of the exploitation of the hardening domain: EMH = 5%  $\pm$  0.5%) on the response of the composite element for the given actions: the actions consist of internal deformations in the UHPFRC layer, leading to stresses and strains in the composite element. These imposed deformations activate the deformation capacity of the structural member, and the stress state is a consequence of the equilibrium of deformations. Thus, the ratio  $f_{U_t,max}/f_{U_t,1st}$  does virtually not influence the response of the element due to imposed deformations in the simulations.

**Summary.** The variation of the hardening parameters does not change significantly the response of the structural system when only internal UHPFRC deformations are considered. However, the hardening parameters become more important when external loads are applied to the composite element (see Section 6.3.6). The exploitation of the magnitude of hardening before the application of loads and the resulting residual stresses may considerably affect the structural response of the composite “UHPFRC-concrete” element. This superposition has to be investigated in future work.

#### 4.4.8 Magnitude of autogenous shrinkage

Autogenous shrinkage is the major cause of UHPFRC internal deformations. The magnitude of autogenous shrinkage influences significantly residual stresses and deformations in composite “UHPFRC-concrete” elements. The autogenous shrinkage is varied between 250 and 1500  $\mu\text{m/m}$  (values at 28 days) by keeping the same evolution in proportion to the 28 days values as for the UHPFRC used in the experimental campaign (Figure 4.22a). The latter’s autogenous shrinkage is determined to be 475  $\mu\text{m/m}$  at 28 days. Magnitudes of autogenous shrinkage of 1500  $\mu\text{m/m}$  are very high and should occur rarely in cementitious materials, however, 1000  $\mu\text{m/m}$  may occur in UHPFRC with a very high cement content, e.g. for UHPFRC with all the sand replaced by cement.

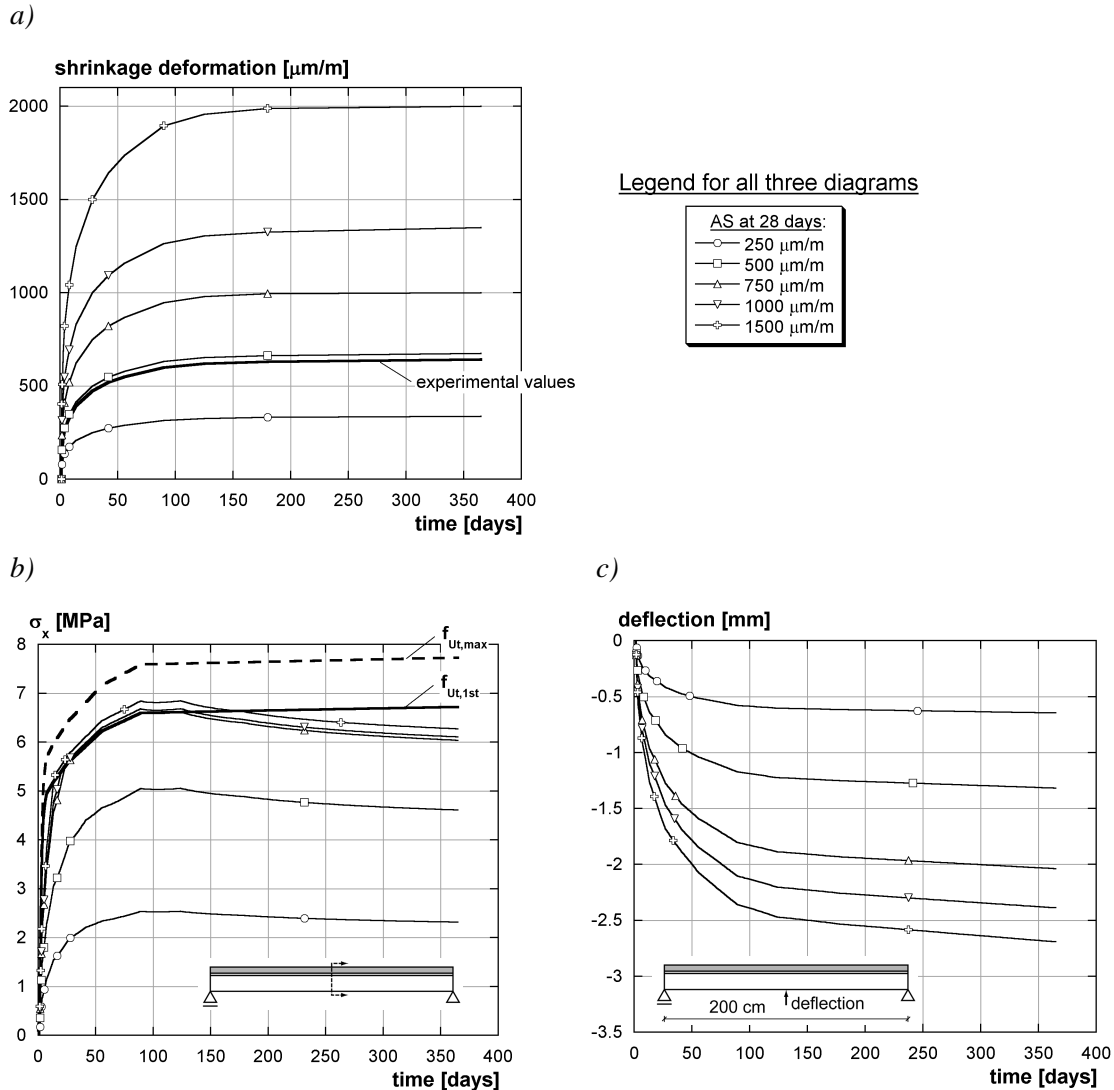


FIGURE 4.22: Magnitude of autogenous shrinkage: a) input values of UHPFRC autogenous shrinkage, b) UHPFRC stress  $\sigma_x$  at the interface (at the bottom of the UHPFRC layer), c) mid-span deflections for the statically determinate system SD

The viscoelasticity is assumed to be identical for all magnitudes of autogenous shrinkage (AS) during the simulation. However, UHPFRC with stronger autogenous shrinkage exhibit probably also stronger viscoelasticity, since creep and shrinkage depend on the same physical mechanisms. So stresses and possible cracking are probably overestimated for high autogenous shrinkage magnitudes.

**Stresses  $\sigma_x$ .** The influence of the magnitude of autogenous shrinkage is illustrated for the statically determinate system SD in Figures 4.22b and c. The maximum relative UHPFRC tensile stresses  $\sigma_x$  in axial direction are shown in Table 4.1: For an autogenous shrinkage of 250  $\mu\text{m/m}$ , the maximum tensile



stress attains 46.5% of the first cracking strength  $f_{U_t,1st}$ , while it reaches 100.3%, 101.3% and 103.7% for 750  $\mu\text{m/m}$ , 1000  $\mu\text{m/m}$  and 1500  $\mu\text{m/m}$  respectively. In comparison, the maximum tensile strength of the UHPFRC  $f_{U_t,max}$  is 115% of the first cracking strength  $f_{U_t,1st}$ . The first cracking strength  $f_{U_t,1st}$  in axial direction ( $\sigma_x$ ) is attained at the interface (at the bottom of the UHPFRC layer) for autogenous shrinkage magnitudes of 750  $\mu\text{m/m}$  and above (Figure 4.22b). That means that the UHPFRC enters the hardening domain and distributed macrocracks of small widths form (see Section 3.2.4.4).

**Exploitation of the hardening domain EMH.** Table 4.1 indicates also the exploitation of the hardening domain EMH, i.e. how many percent of the magnitude of hardening are used at the maximum relative stress. For magnitudes of autogenous shrinkage of 1000  $\mu\text{m/m}$  and 1500  $\mu\text{m/m}$ , the exploitation amounts to  $EMH = 9\%$  and  $25\%$  respectively. The hardening strain can be directly deduced from the exploitation of the hardening domain: the hardening strain is 0.25‰ for an exploitation of  $EMH = 25\%$  (magnitude of autogenous shrinkage: 1500  $\mu\text{m/m}$ ) with the magnitude of hardening being  $\epsilon_{U,hard} = 1\%$ . Charron showed that the permeability of UHPFRC increases in the hardening domain [Charron04]. Consequently, the exploitation of the hardening domain EMH may become a determinant factor when very low permeability is required.

TABLE 4.1: Magnitude of autogenous shrinkage

Autogenous shrinkage at 28 days [ $\mu\text{m/m}$ ]	$\sigma_x/f_{U_t,1st}$ [%]	exploitation of hardening domain EMH [%]
250	46.5	0
500	90.9	0
750	100.3	2
1000	101.3	9
1500	103.7	25

**Deflections.** The increase of autogenous shrinkage also leads to higher mid-span deflections of the composite “UHPFRC-concrete” element. The effect of an increase of autogenous shrinkage on the deflections is important for small magnitudes of autogenous shrinkage ( $< 750 \mu\text{m/m}$ ); it is lower for higher magnitudes of autogenous shrinkage ( $\geq 750 \mu\text{m/m}$ ): the difference in deflection of the composite member between 750 and 1000  $\mu\text{m/m}$ , i.e. the magnitudes of autogenous shrinkage with which the hardening domain is partially exploited, is approximately 2 times lower than between 250 and 500  $\mu\text{m/m}$ , i.e. the magnitudes for which the UHPFRC behaviour remains quasi-linear elastic. This is explained by the state of deformations in the UHPFRC layer: for high magnitudes of hardening ( $\geq 750 \mu\text{m/m}$ ), the first cracking strength  $f_{U_t,1st}$  is reached the first time at approximately 36 hours and the UHPFRC enters the hardening domain. The first cracking strength  $f_{U_t,1st}$  is again attained and exceeded from approximately 17 to 150 days. When the UHPFRC enters the hardening domain, its stiffness decreases and a part of UHPFRC deformations are balanced by the formation of distributed microcracks. This leads to a reduction of the deflection of the composite member.

The mid-span deflections for magnitudes of autogenous shrinkage of 1000  $\mu\text{m/m}$  and 1500  $\mu\text{m/m}$  are 1/1000 and 1/750 respectively. The stronger curling of the beams with increasing magnitude of autogenous shrinkage also leads to higher tensile stresses at the bottom part of the concrete layer, and cracks form in the concrete layer at high magnitudes of autogenous shrinkage ( $\geq 750 \mu\text{m/m}$ ).

**Summary.** The magnitude of autogenous shrinkage influences significantly stresses and deflections in composite “UHPFRC-concrete” elements. Therefore, the determination of autogenous shrinkage and viscoelasticity and their couplings is essential for the time-dependent behaviour of those elements. The simulations have shown that the UHPFRC, used in the experimental campaign, remains in the linear-elastic domain for statically determinate systems and is an appropriate material for composite “UHPFRC-concrete” elements.

#### 4.4.9 Interface cracks and debonding at free ends

**General.** *Debonding is the separation of old and new layer in the interface zone altering the response of the composite member, i.e. the element does not behave in a monolithic way any more.* In composite “UHPFRC-concrete” elements, high shear stresses may induce debonding at the interface. Local debonding may occur due to internal deformations at free ends or when macrocracks cross the entire UHPFRC layer and reach the interface.

*In this section, only local debonding at free element ends due to internal deformations is discussed for different parameters, since test results and numerical simulations show that no debonding cracks form in composite elements, subjected only to internal deformations.* Moreover, the previous sections demonstrate that no localized macrocracks form in the composite elements when only the time-dependent behaviour is considered. Thus, no interface cracks form at the tips of transverse cracks either. The debonding risk due to shear stresses and at the tip of localized macrocracks is discussed in Chapters 5 and 6.

Interface cracks and debonding due to internal deformations are determined by numerical simulations. Criteria are fixed to determine between interface cracks and debonding: *Local debonding occurs when crack length is  $l_i > 5$  cm or when the crack width  $w_i > 10$   $\mu$ m. Local debonding develops into debonding when the crack length does not become constant after 90 days.* This criterion is strict, since even larger cracks may not alter the structural response. However, the ingress of detrimental substances may be favoured for larger crack widths  $w_i$ .

Debonding is discussed by means of crack length, damage, crack width and its evolution in time. Damage is hereby defined as the reduction in stiffness after Figure A.3 in Appendix A. The crack length is the length of the elements in which damage occurs. The crack width is determined by the vertical deformation of the damaged interface at the end of the structural element. An overview of the influence of the different parameter on debonding is given in Table 4.2.

TABLE 4.2: Interface cracks and debonding at free element ends due to time-dependent internal deformations

static system	$h_U$ [cm]	$\rho_{s,U}$ [%]	magni- tude of AS <sup>a</sup> [ $\mu$ m/m]	crack length $l_i^b$				damage <sup>c</sup> [-]	time at initiation of interface crack [h]	debon- ding <sup>d</sup> [-]
				7 days [cm]	28 days [cm]	90 days [cm]	365 days [cm]			
SD	1	0	475	0	1	1	1	0.474	662	no
SD	2	0	475	0	1	1	1	0.783	276	no
SD	3	0	475	0	1	2	2	0.848	200	no
<b>SD<sup>e</sup></b>	<b>5</b>	<b>0</b>	<b>475</b>	<b>1</b>	<b>2</b>	<b>2</b>	<b>2</b>	<b>0.873</b>	<b>168</b>	<b>no</b>
SD	7	0	475	1	2	2	2	0.864	174	no
SD	9	0	475	0	1	2	2	0.832	230	no
SD	10	0	475	0	1	2	2	0.809	260	no
SD	5	2	475	0	2	2	2	0.869	172	no
SD	5	5	475	0	2	2	2	0.865	174	no
<b>RM</b>	5	0	475	1	2	3	3	0.912	144	no
SD	5	0	<b>250</b>	0	0	1	1	0.257	1128	no
SD	5	0	<b>500</b>	1	2	2	2	0.908	154	no
SD	5	0	<b>750</b>	1	3	5	5	0.987	83	yes
SD	5	0	<b>1000</b>	2	5	9	9	0.999	75	yes
SD	5	0	<b>1250</b>	2	8	12	13	1.000	68	yes
SD	5	0	<b>1500</b>	3	10	31	68	1.000	65	yes

- a. AS = autogenous shrinkage
- b. The crack length  $l_i$  is determined in steps of 1 cm.
- c. Damage refers to the damage definition in the FE-program MLS and describes the reduction of the secant modulus as shown in Figure A.3b in Appendix A. It cannot be directly converted into crack width and gives only a qualitative indication of debonding which is used to compare the influence of the different parameters. A damage of 1 corresponds to a real crack.
- d. Debonding occurs when the crack is longer than  $l_i = 5$  cm and its width larger than  $w_i = 10$   $\mu\text{m}$ .
- e. basic configuration

Interface cracks and debonding are induced by stresses perpendicular to the interface ( $\sigma_y$ ). At free ends, these stresses arise from stress differences in axial direction  $\Delta\sigma_x$  at the interface that occur in composite “UHPFRC-concrete” elements (see Figure 2.22b in Section 2.6.1). The magnitude of the stress difference  $\Delta\sigma_x$  stands in direct relation to the magnitude of interface cracks or debonding.

**Thickness of the UHPFRC layer  $h_U$ .** The ratio of the thicknesses of UHPFRC and concrete layer ( $h_U/h_c$ ) affects the degree of restraint and the stress distribution at the interface. The strongest interface cracking (expressed by the highest value of damage) is observed for  $h_U = 5$  cm, i.e.  $h_U/h_c = 1/3$  (Table 4.2), however, the differences are small for a thickness of the UHPFRC layer  $h_U$  between 2 and 10 cm ( $h_U/h_c = 2/15$  and  $2/3$ ). Only for  $h_U = 1$  cm, the interface crack is significantly smaller with a crack length of 1 cm and a damage value of 0.47 compared to damage values higher than 0.78 for higher thicknesses. The maximum at  $h_U \approx 5$  cm ( $h_U/h_c = 1/3$ ) is explained by the interaction of the eccentricity of the UHPFRC layer to the centre of gravity and the thickness of the UHPFRC layer. These two parameters influence the moment part of the stress difference  $\sigma_x$ , while the influence of the axial part of the stress differences is linear proportional to the ratio of the thicknesses of UHPFRC and concrete layer  $h_U/h_c$ .

The interface cracks begin to develop between 7 and 28 days (corresponding to 168 and 672 hours respectively). The time is related to the crack magnitude - the earlier the interface starts to crack, the larger is the crack width and the longer the length. So, the interface crack starts the earliest at 168 hours for  $h_U = 5$  cm. The crack width becomes constant at a width  $w < 10$   $\mu\text{m}$  for all  $h_U$  after approximately 90 days. This coincides with the time when the UHPFRC properties become constant. No debonding occurs.

**Reinforcement in the UHPFRC layer  $A_{s,U}$ .** Reinforcement in the UHPFRC layer does not have a significant influence on the formation of interface cracks at free ends (Table 4.2). This is observed during testing (see Section 3.4.2.7) and confirmed by the results of the numerical simulation. An increasing reinforcement ratio reduces slightly the risk of interface cracking: the damage decreases by 0.01. This negligible effect is explained by the fact that the reinforcement is embedded in the concrete and needs a certain anchorage length to develop its efficiency. Consequently, its influence on interface cracking at free end is small. However, the effect of reinforcement on local debonding due to transverse macrocracks for composite “UHPFRC-concrete” members under loading is important. It is discussed in Section 5.2.

**Static system.** The influence of the static system is shown for systems SD (statically determinate) and RM (restraint of moment). System TR (totally restraint) represents a totally restrained member without free ends and thus, without debonding at the free ends. The formation of interface cracks is more pronounced in the system with the restraint of moment (RM) than in the statically determinate beam (SD): crack form at 144 hours (6 days) for system RM and at 168 hours (7 days) for system SD (Table 4.2) and reaches a final length of 2 and 3 cm respectively. However, the crack does not propagate after 90 days and its width remains below 10  $\mu\text{m}$  for both static systems. No debonding occurs.

**Magnitude of autogenous shrinkage.** The magnitude of autogenous shrinkage is defined by its value at 28 days (see Section 4.4.8). It influences significantly debonding as shown in Table 4.2 and

Figure 4.23: Figure 4.23a describes the crack width as a function of time and Figure 4.23b the crack length  $l_i$  at several ages as a function of the magnitude of autogenous shrinkage.

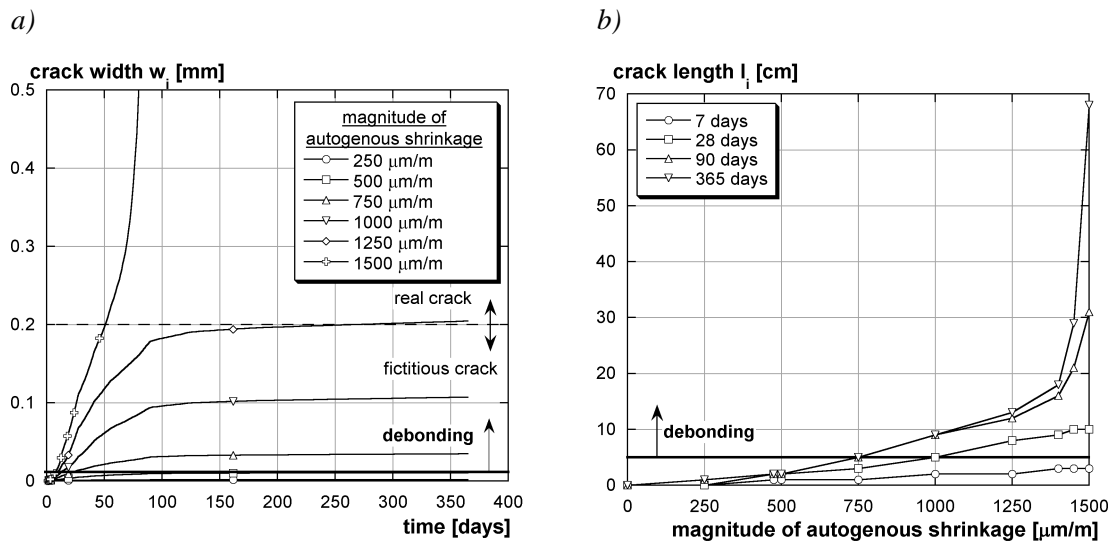


FIGURE 4.23: Influence of the magnitude of autogenous shrinkage on debonding

For small magnitudes of autogenous shrinkage ( $\leq 500 \mu\text{m/m}$ ), the crack width remains below  $10 \mu\text{m}$  and the crack length below 2 cm. For magnitudes of autogenous shrinkage between 750 and  $1000 \mu\text{m/m}$ , the interface crack length remains smaller than 10 cm and the width smaller than 0.1 mm: local debonding occurs. The crack width become visible, however, it is still small and the crack formation virtually stops after approximately 90 days. Considering the structural response, these magnitudes are between interface crack and debonding: the crack width increases, but the structural behaviour is not altered yet.

For high magnitudes of autogenous shrinkage ( $\geq 1250 \mu\text{m/m}$ ), the interface cracks develop into real cracks (see Section 3.2.4.4) with crack widths of more than  $0.2 \text{ mm}$  ( $> 10 \mu\text{m}$ ) and local debonding occurs. For a magnitude of autogenous shrinkage of  $1250 \mu\text{m/m}$ , the crack width stabilizes after approximately 90 days, however, for a magnitude of  $1500 \mu\text{m/m}$ , the crack width increases strongly and reaches a value of  $0.5 \text{ mm}$  after 80 days. Furthermore, the crack length does not stabilize, but increases with ongoing age. Here, debonding is strong and cancels the monolithic behaviour. Mechanical connectors or an appropriate element geometry are necessary to avoid debonding and to ensure the stress transfer between UHPFRC and concrete layer, e.g. by building an abutment at the free end as shown in Figure 4.24.

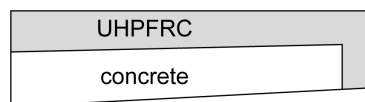


FIGURE 4.24: Abutment for the UHPFRC layer to prevent debonding (from [Bernard00])

**Conclusion.** The numerical simulations indicate no local debonding in the composite “UHPFRC-concrete” elements which is confirmed by the test results (except for high magnitudes of autogenous shrinkage). The simulated interface cracks lengths lie between 1 and 3 cm, with the maximum crack widths being smaller than  $10 \mu\text{m}$ , i.e. no real cracks form and no additional measures have to be taken to guarantee monolithic behaviour and durability. Only the magnitude of autogenous shrinkage influences significantly interface cracks and debonding: for high magnitudes ( $> 750 \mu\text{m/m}$ ), local debonding occurs and measures have to be taken to guarantee stress transfer between UHPFRC and concrete layer.

#### 4.4.10 Extrapolation to higher ages

The behaviour of composite “UHPFRC-concrete” elements is investigated experimentally over a period of 80 days. This period is determinant for those elements, since the major part of UHPFRC deformations and the evolution of its material properties occur during this time period. The evolution of residual stresses in such composite elements is important to predict crack formation.

The material tests on UHPFRC show that the mechanical properties (strengths and modulus) remain virtually constant and that shrinkage deformations are very small for UHPFRC ages beyond 90 days. Thus, the extrapolation of the material properties of UHPFRC is based on the assumption that all UHPFRC properties are constant for an UHPFRC age of more than 90 days. This hypothesis has to be verified by long-term tests, e.g. it is expected that the viscoelasticity becomes probably less important with increasing UHPFRC age.

Figure 4.25a shows the stress evolution  $\sigma_x$  in the composite element for the statically determinate system (SD, see Figure 4.8) over a time period of 10 years. The maximum stresses are obtained at an UHPFRC age of 4 months. They remain below the first cracking strength  $f_{U_t,1st}$  during the whole simulation period. The stresses relax with increasing age: the UHPFRC stress at the interface is 40% and the stress at the top face 30% of the maximum stress (after 4 months) at an UHPFRC age of 10 years. The concrete tensile stress  $\sigma_x$  at the bottom face relaxes to 40% of its maximum value.

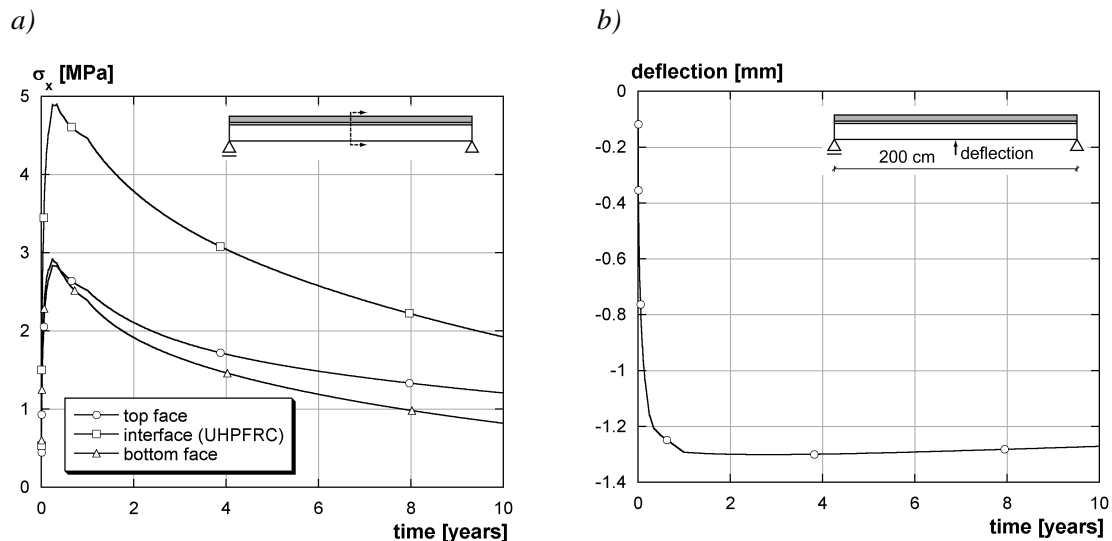


FIGURE 4.25: Extrapolation to higher ages (SD): a) stresses ( $\sigma_x$ ), b) mid-span deflection

Figure 4.25b shows the mid-span deflection of the system. The evolution is characterized by a strong deformation increase during the first 3 months (90% of maximum deflection), a slower increase until the maximum is reached at 2.7 years and then a slight decrease of deformations: the deflection after 10 years is 98% of the maximum deflection. For the given system, the maximum mid-span deflection corresponds to  $1/1500$ . The results indicate that the behaviour of composite “UHPFRC-concrete” elements due to internal deformations is most important during the first three months after its fabrication.

#### 4.4.11 Composite “UHPFRC-concrete” elements with a new substrate

The experimental campaign and the numerical simulations concentrate on composite “UHPFRC-concrete” elements with an “old” substrate, i.e. a concrete substrate sufficiently old ( $> 3$  months) that its material properties can be assumed to be constant and that do not shrink significantly. In this case, nearly all internal deformations are due to the UHPFRC. However, the structural behaviour changes significantly for new composite elements, with the concrete being only few days older than the UHPFRC. The major changes are:

- The residual stresses of concrete due to early age deformations before the application of the UHPFRC layer must be considered in the simulation.
- The relative humidity in the concrete is high (approximately 95 to 100%).
- Concrete strengths and modulus still develop significantly.
- The concrete deforms due to autogenous and drying shrinkage.
- The creep kinetics still changes significantly.

The actual state of the numerical model and the test results do not allow to predict reliably the behaviour of new “UHPFRC-concrete” elements. Thus, the following paragraphs give a qualitative description of the main differences between “old” and “new” concrete substrates.

The high relative humidity in the concrete leads to a moisture gradient between the UHPFRC and the concrete. The strong self-desiccation of UHPFRC reduces its internal relative humidity to 88% at 7 days and to 80% at 28 days (see Figure 3.1b), while the self-desiccation of concrete is slow or non-existent and its relative humidity remains at nearly 100%. Furthermore, drying shrinkage occurs for UHPFRC during the first 10 days, indicating that the permeability of the material is still sufficiently high to lose or uptake water. Consequently, the UHPFRC may suck water from the concrete due to the moisture gradient. The consequences of this moisture gradient have to be investigated.

In case of “new” composite “UHPFRC-concrete” elements, both materials shrink and their properties evolve. Consequently, the deformation gradient is lower and axial deformations are higher in case of statically determinate systems. The compatibility of deformations of new composite “UHPFRC-concrete” elements has to be verified: for example, the whole composite system has to be investigated with regard to cracking and debonding. The casting sequence depends on cracking and debonding risk. It must be determined whether it is more favourable to cast the UHPFRC or the concrete first.

The interface of new composite “UHPFRC-concrete” elements has to be considered in design. If such elements are for a new construction, the interface preparation method depends on which layer is cast first. A method should be chosen that does not damage the substrate. A possible preparation method for concrete would be the use of a surface retardant at the contact surface in order to easily remove the low-strength cement layer at the surface and to obtain roughness by laying the aggregates open. Surface preparation methods for UHPFRC have still to be investigated. The UHPFRC surface structure after application of a preparation method is influenced by the high amount of fibres and the absence of aggregates in UHPFRC and its appearance and roughness have to be determined.

## 4.5 Conclusions

1. *It is possible to model UHPFRC properties with the investigated numerical model except for self-desiccation.*
  - The viscoelastic behaviour of UHPFRC at early age and in the long-term can be described by an age-dependent generalized Maxwell chain model. However, the determination on the basis of the results of the restrained shrinkage tests does not allow to estimate damage in form of micro-cracking at very early age (< 40 hours).
  - Modelling of UHPFRC self-desiccation is not possible with the investigated numerical model. However, autogenous shrinkage can be directly introduced as time-dependent volumetric deformation.
  - A multilinear law is necessary to model UHPFRC tensile properties: The law introduced in the numerical model is appropriate, however, hardening and softening parts are not separated in the law and the tensile behaviour must be modelled by considering the FE-size, e.g. with two reference lengths. The modelling of crack localization in the softening part should be improved, e.g. by introducing a statistical variability.

2. *The time-dependent behaviour of composite “UHPFRC-concrete” elements is correctly predicted with the numerical model (with the exception of the hygral state).*

- The results of the beam tests are predicted by the numerical model with a deviation smaller than 15%. The validation is based on deflections. It shows that the time-dependent behaviour of composite “UHPFRC-concrete” beams can be simulated with parameters deduced from material tests.
- As the modelling of UHPFRC self-desiccation is not possible, the hygral state and resulting deformations in composite “UHPFRC-concrete” members cannot be modelled either. For new constructions, the hygral state is important and there is a research need to develop a hygral model that describes UHPFRC self-desiccation correctly. The hygral state is not determinant for modelling of composite “UHPFRC-concrete” members with the concrete layer being older than 5 months, e.g. for conservation projects, since the hygral state in the substrate evolves very slowly and autogenous shrinkage can be considered directly as volumetric deformation.

3. *The exploitation of the magnitude of hardening may be defined by  $EMH = (\epsilon_{tot} - \epsilon_{el}) / \epsilon_{U,hard}$*

- The parameter EMH describes the extent to which the hardening domain of the UHPFRC is exploited. The factor is used to indicate the strain state in the UHPFRC in the hardening domain and to estimate the reserve of strain in case of imposed deformations.

4. *Autogenous shrinkage of UHPFRC is determinant for the time-dependent behaviour of composite “UHPFRC-concrete” members.*

- Autogenous shrinkage is the major contribution to early age deformations for the investigated composite elements; thermal deformations due to heat of hydration are less significant for the investigated slender composite elements.
- The influence of autogenous shrinkage is important under isothermal conditions until the UHPFRC properties become virtually constant at 90 days.

5. *UHPFRC viscoelasticity leads to a significant relaxation of the stresses in composite elements.*

- The effect of UHPFRC viscoelasticity is important for the structural behaviour of composite elements: the residual stresses and deformations in the composite element are smaller, thus, reducing the risk of cracking.
- The stresses in the UHPFRC layer of the composite beams are significantly relaxed at early age (up to 60%) and the beam deformations are significantly reduced (to 40% for beam I5).
- Viscoelasticity leads to a relaxation of the residual stresses in the composite beam of 30 to 40% after 10 years as determined by the parametric study.

6. *Stress state and damage, i.e. stresses exceeding the first cracking strength, in the beams are determined by the numerical model.*

- The stresses remain below the first cracking strength  $f_{U,t,1st}$  for the statically determinate beams.
- The deformations in the UHPFRC layer of the statically indeterminate beams enter the hardening domain after approximately 20 days ( $\epsilon_{tot} > \epsilon_{U,t,1st}$ ). The magnitude of hardening is exploited to  $EMH = 5\%$ , i.e. the maximum total strain in the UHPFRC is approximately  $0.06\%$ <sup>8</sup>.
- The horizontal supports of the statically indeterminate beams are simulated by springs with a constant  $k = 210$  kN/mm, confirming the experimental observation that the central span is only partially restrained in axial direction.
- Rebars ( $A_{s,U}$ ) lead to increased tensile stresses in the UHPFRC layer of maximal 1 MPa. However, no additional damage is induced.

8. by making the assumption of an elastic UHPFRC deformation of approximately 0.01%.

7. *At early age and in the long-term, damage (i.e. stresses exceeding the first cracking strength) occurs in some cases.*

- Damage, i.e. the UHPFRC stresses exceeding the first cracking strength  $f_{U_t,1st}$ , occurs:
  - in statically determinate system with thin UHPFRC layers ( $h_U \leq 1$  cm),
  - for high magnitudes of autogenous shrinkage ( $\geq 750$   $\mu\text{m/m}$ ) and
  - in statically indeterminate systems (RM and TR).
- In thin UHPFRC layers ( $h_U = 1$  cm), the maximum exploitation of the magnitude of hardening is  $\text{EMH} = 2\%$ . For the completely restrained system (TR), the highest damage is observed with  $\text{EMH} = 5\%$ ; for the system with restraint of moment (RM),  $\text{EMH} = 1.3\%$  are used. Damage depends strongly on the magnitude of autogenous shrinkage: for magnitudes of 750 and 1500  $\mu\text{m/m}$ , the exploitation of the magnitude of hardening is determined to  $\text{EMH} = 2\%$  and 25% respectively.

8. *No debonding cracks form in general.*

- The interface cracks at free beam ends have lengths and widths smaller than 5 cm and 10  $\mu\text{m}$  respectively and do not alter the structural response of the composite beams, i.e. no debonding occurs.
- Debonding cracks only form for high magnitudes of autogenous shrinkage ( $\geq 750$   $\mu\text{m/m}$ ) and may lead to unstable debonding ( $\geq 1250$   $\mu\text{m/m}$ , see below).

9. *The mid-span deflections due to internal deformations remain below  $l/1000$ .*

- The mid-span deflections of the statically determinate system SD remain below  $l/1500$  for the investigated parameters. The deflections are only higher for high magnitudes of autogenous shrinkage ( $> 1000$   $\mu\text{m/m}$  at 28 days, f. ex.  $l/750$  for 1500  $\mu\text{m/m}$ ).
- The mid-span deflections of the beams of the experimental campaign due to internal deformations are smaller than  $l/1200$ .

10. *The magnitude of autogenous shrinkage of the UHPFRC should not exceed 1000  $\mu\text{m/m}$  at 28 days.*

- Magnitudes of autogenous shrinkage higher than 1250  $\mu\text{m/m}$  (at 28 days) lead to unstable debonding in the composite member.
- The exploitation of the hardening domain is important for high magnitudes of autogenous shrinkage ( $\text{EMH} = 25\%$  are exploited for 1500  $\mu\text{m/m}$ ). This means that there is pronounced formation of distributed macrocracks due to internal UHPFRC deformations.



## 5 Structural response

Chapter 5 treats the structural response of composite “UHPFRC-concrete” beams with the UHPFRC layer in tension. An analytical model is developed in Section 5.1 which predicts the force-deflection curves of composite beams. The model is validated with experimental results. In Section 5.2, the structural response of composite “UHPFRC-concrete” bending beams is discussed on the basis of the test results of Chapter 3. The reference length, being a significant parameter in the simulation of the structural response of structural members in bending, is discussed in Section 5.3.

### 5.1 Analytical model for bending

#### 5.1.1 General

The structural response of composite “UHPFRC-concrete” members is essential to predict forces and deformations under service conditions and at ultimate limit state. The flexural behaviour of composite “UHPFRC-concrete” elements may be determined by an *analytical cross-sectional model* and a kinematic hypothesis. The moment-curvature relationship is established for a section with the UHPFRC layer in tension (Figure 5.4). The analysis is based on an extension of the commonly used bending design model for reinforced concrete and considers the tensile behaviour of UHPFRC and of concrete.

#### 5.1.2 Hypotheses

The model for bending is based on the following hypothesis:

1. Plane sections remain plane (hypothesis of Bernoulli). This means that the adherence between the cementitious materials (concrete and UHPFRC) and the reinforcement is perfect and that the adherence at the interface between concrete and UHPFRC is perfect, i.e. no debonding occurs at the interface and the structural element shows monolithic behaviour
2. The behaviour of steel and cementitious materials are described with material laws.
3. The cross-section is in equilibrium, i.e. the equilibrium of forces and moment is stated.

#### 5.1.3 Description

##### 5.1.3.1 Material laws

The tensile behaviour of the UHPFRC is modelled in two parts: The material is considered as a continuum according to a bi-linear relation for strains smaller than  $\varepsilon_{U_t, \max}$  (Figure 5.1a). Beyond hardening at  $f_{U_t, \max}$ , the formation of a fictitious crack with an opening  $w$  is assumed following a bi-linear softening law (Figure 5.1a). The crack opening  $w$  is transformed into the strain  $\varepsilon$  by using the reference length  $L_R$  (EQ. 5.1) [AFGC02].

$$\varepsilon = \varepsilon_{U_t, \max} + \frac{w_{U_t}}{L_R} \quad (\text{EQ } 5.1)$$

with  $L_R$  [mm]: reference length,  $w_{U_t}$  [mm]: width of the fictitious crack.

The *reference length*  $L_R$  is a modelling parameter that is dependent on material properties and the beam configuration i.e. the geometry of the beam and the static system. It is used to transform the crack width ( $w_{U_t}$ ) into a deformation ( $\varepsilon$ ) which is necessary to determine the equilibrium of the model. The influences on the reference length are varied and it is not possible presently to determine the reference length for UHPFRC analytically. The reference length will be discussed in Section 5.3 in order to give indication about its determination.

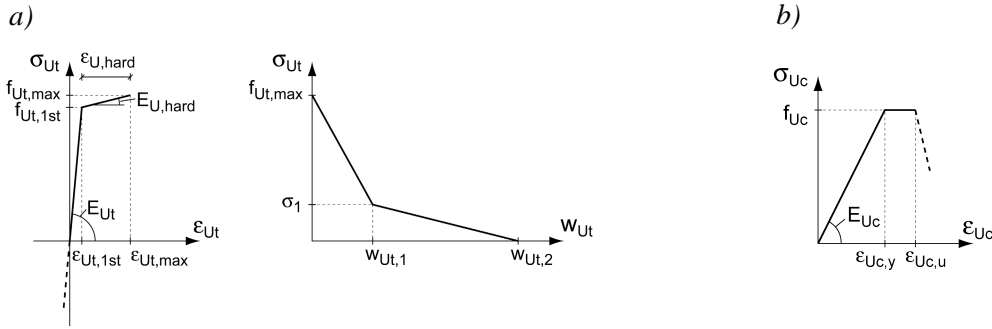


FIGURE 5.1: Material laws of UHPFRC: a) tensile behaviour - bi-linear continuum model for the linear-elastic and hardening domain and bi-linear softening diagram of the fictitious crack, b) compressive behaviour

The compressive behaviour of UHPFRC is modelled with a tri-linear diagram as proposed in [AFGC02] (Figure 5.1b). The linear-elastic stress rise represents well the test results. The plastic plateau is small or even non-existent, since the observed stress decrease is strong and the compressive behaviour rather brittle.

The compression of the concrete is modelled with a parabola diagram (Figure 5.2b) [Schläfli99]. The tensile behaviour of the concrete is modelled with a linear-elastic part and a bi-linear softening diagram (Figure 5.2a).

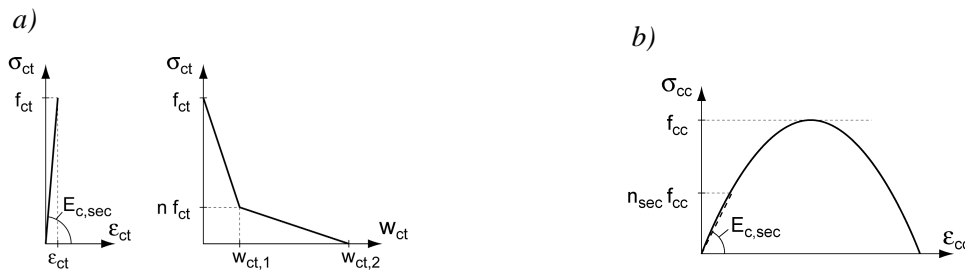


FIGURE 5.2: Material laws of the concrete, a) in tension, b) in compression

A bi-linear material law is assumed for the steel reinforcement (Figure 5.3a). It is symmetric in tension and compression. The reinforcements in the UHPFRC and the concrete layer may have different material properties.

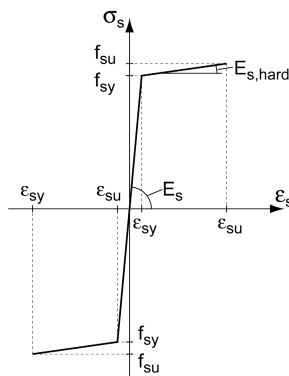


FIGURE 5.3: Material laws of the reinforcement

### 5.1.3.2 Kinematics

Strain and stress state in a section of a flexural “UHPFRC-concrete” element are calculated with the model given in Figure 5.4. The linear strain distribution allows to calculate the curvature  $\kappa$  (EQ. 5.2) and the stresses in the cross-section by using material laws.

$$\kappa = \frac{\varepsilon_{U,l} - \varepsilon_{c,upp}}{h_{tot}} \quad (EQ 5.2)$$

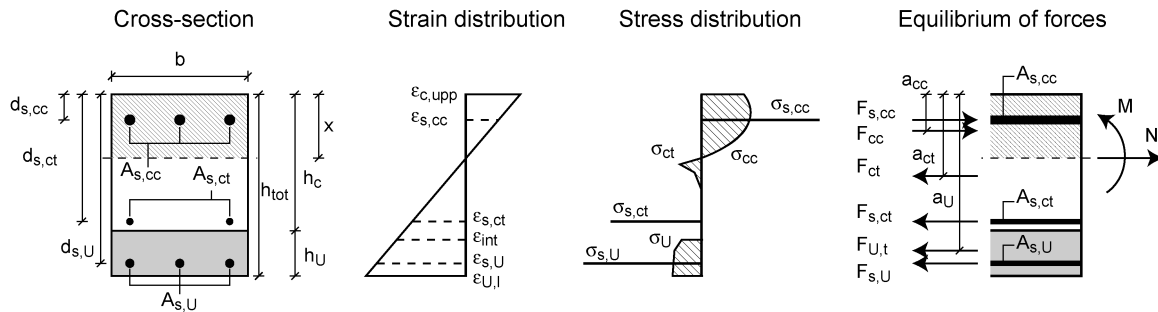


FIGURE 5.4: Definition of the analytical model

### 5.1.3.3 Equilibrium of internal forces and moment

The equilibrium of the normal forces is established in EQ. 5.3. The equilibrium of the normal forces is determined by iteration. The solution is obtained by varying the position of the neutral axis  $x$  on the cross section for a given strain at the bottom side of the beam  $\varepsilon_{U,l}$  until the equilibrium of the normal forces is reached. The strain distribution and the curvature  $\kappa$  are determined with  $x$  and  $\varepsilon_{U,l}$ . Finally, the moment is calculated with EQ. 5.10.

$$\sum F = F_{s,U} + F_{U,t} + F_{s,ct} + F_{ct} + F_{cc} + F_{s,cc} = N \quad (EQ 5.3)$$

with  $N$  [kN]: external normal force and

$$F_{U,t} = b \cdot \int_0^{h_U} \sigma_{U,t} dx \quad \text{force of the UHPFRC} \quad (EQ 5.4)$$

$$F_{s,U} = \varepsilon_{s,U} \cdot E_{s,U} \cdot A_{s,U} \quad \text{force of the reinforcement in the UHPFRC layer} \quad (EQ 5.5)$$

$$F_{s,ct} = \varepsilon_{s,ct} \cdot E_{s,c} \cdot A_{s,ct} \quad \text{force of the lower reinforcement in the concrete layer (in tension)} \quad (EQ 5.6)$$

$$F_{ct} = b \cdot \int_{h_U}^{h_{tot}-x} \sigma_{ct} dx \quad \text{tensile force of the concrete} \quad (EQ 5.7)$$

$$F_{cc} = b \cdot \int_{h_{tot}-x}^{h_{tot}} \sigma_{cc} dx \quad \text{compressive force of the concrete} \quad (EQ 5.8)$$

$$F_{s,cc} = \varepsilon_{s,cc} \cdot E_{s,c} \cdot A_{s,cc} \quad \text{force of the upper reinforcement in the concrete (in compression)} \quad (EQ 5.9)$$

$$\begin{aligned} M &= \sum M_i = M_{s,U} + M_{U_t} + M_{s,ct} + M_{ct} + M_{cc} + M_{s,cc} = \\ &= F_{s,U} \cdot d_{s,U} + F_{U_t} \cdot a_{U_t} + F_{s,ct} \cdot d_{s,ct} + F_{ct} \cdot a_{ct} + \\ &+ F_{cc} \cdot a_{cc} + F_{s,cc} \cdot d_{s,cc} \end{aligned} \quad (EQ 5.10)$$

#### 5.1.3.4 Moment-curvature diagram

The variation of the curvature allows to establish the moment-curvature relationship of the cross-section. By considering geometry and static system of the structural element, force-deflection curves can be derived.

The transition from the cross-sectional model to a structural element requires detailed knowledge of the distribution of curvature and stiffness over the length of the element. The deflection of the structural element can directly be deduced, when no fictitious cracks exist in the structural element, i.e. when the whole beam can be described with a continuum model (Figure 5.1a). When fictitious cracks form, i.e. softening of UHPFRC (Figure 5.1b), the distribution of the curvature is no longer proportional to the moment distribution. The fictitious crack width is distributed over the length of the plastic hinge  $L_{hi}$  (Figure 2.20b in Section 2.5). The length of the plastic hinge is dependent on the geometry of the structural element, on the crack path, on the bond-slip relationship between cementitious material and reinforcement and debonding in the interface zone. If the reference length  $L_R$  is known, the crack mouth opening displacement CMOD of the bottom side of the UHPFRC layer can be calculated using EQ. 5.11.

$$CMOD = (\varepsilon - \varepsilon_{U_t, max}) \cdot L_R \quad (EQ 5.11)$$

#### 5.1.4 Validation

The model is validated with composite beams tested at MCS and experimental results from the literature.

##### 5.1.4.1 Composite 3-point bending beams with UHPFRC [Denarie01]

Tests were conducted on 3-point composite bending beams, consisting of a layer of concrete and a layer of the UHPFRC Ductal<sup>®</sup> (Figure 5.5a). The UHPFRC layer was under tension during testing. Force, deflection and crack mouth opening displacements (CMOD') were measured during the tests. The crack mouth opening displacements CMOD' were determined with  $\Omega$ -gages and included the elastic deformation over the measuring base of 10 cm and the deformation of the localized macrocrack. Thus, the part of the elastic deformation has to be considered to deduce the CMOD. The force-deflection curves of the tests were simulated with the FE program MERLIN [Reich97]. The UHPFRC tensile behaviour was described by a multilinear hardening and softening behaviour (Figure 5.6a). The FE sim-

ulation considered a discrete crack model with a given crack path. Details on the tests and the FE simulation results can be found in [Denarie01].

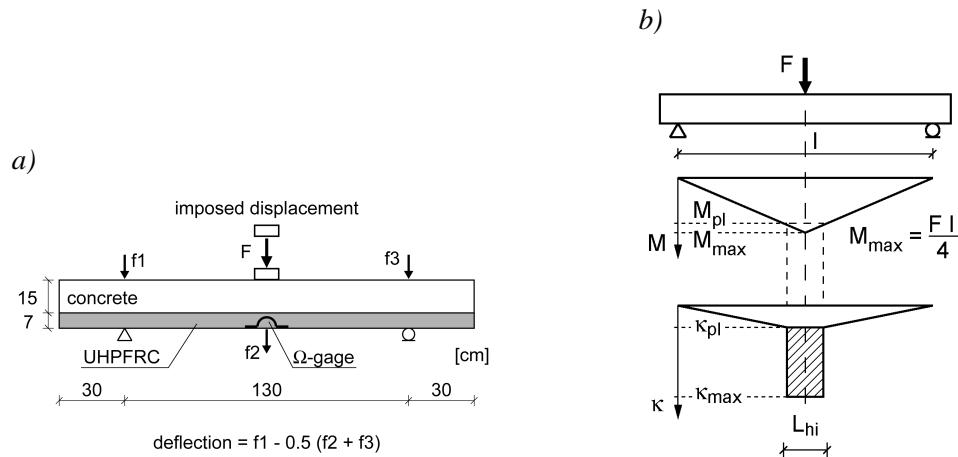


FIGURE 5.5: a) 3-point bending beam: system (after [Denarie01]), b) simplified curvature distribution for 3-point-bending beams

The analytical model is a cross-sectional model. Thus, the moment-curvature output of the model has to be transformed into a force-deflection diagram for a comparison with the test results. As the moment is not constant over the length of the beam, the length of the plastic hinge  $L_{hi}$  has to be determined (Figure 5.5b). The curvature in the plastic hinge corresponds to the one of the section with the localized macrocrack of the analytical model, while the curvature for the rest of the beam remains the one of the continuum section. The width of the plastic hinge is assumed to be the height of the beam  $L_{hi} = 22$  cm and the reference length  $L_R = 150$  mm. As the  $\Omega$ -gages measured also the elastic deformation before the formation of the localized macrocrack, this deformation has to be added to CMOD values, calculated with the analytical model and the numerical simulation.

The tensile behaviour of the UHPFRC is determined by means of uniaxial tensile tests as described in Section 3.2.4. The test results are shown in Figure 5.6. A hardening-softening diagram is adapted on the basis of the test results and serves as input for the analytical model (Table 5.1). The deformations that are needed in the continuum part of the model ( $\epsilon < \epsilon_{Ut,max}$ ) are deduced by assuming that the deformations during hardening are evenly distributed over the measuring base of the LVDTs during testing which is 10 cm. A displacement of the LVDT of 0.1 mm corresponds therefore to a deformation of 1‰ in the analytical model (Figure 5.6b). Figure 5.6 shows also the input values for the numerical simulation.

TABLE 5.1: Tensile input for the analytical model (see Figure 5.1)

$\epsilon_{Ut,1st} = 0.1\text{‰}$	$f_{Ut,1st} = 6.0$ MPa
$\epsilon_{Ut,max} = 1\text{‰}$	$f_{Ut,max} = 7.4$ MPa
$w_{Ut,1} = 1.9$ mm	$\sigma_1 = 2.5$ MPa
$w_{Ut,2} = 6.5$ mm	$\sigma_2 = 0$ MPa

The force-deflection curve can be reproduced with the analytical model and the FE simulation within the experimental scatter (Figure 5.7). The change of the slope in Figure 5.7 at a force  $F = 50$  kN is explained by the bi-linearity of the continuum model during hardening.

The force-CMOD' diagram in Figure 5.8a indicates good agreement between analytical model, FE simulation and experimental values. The CMOD' is underestimated with the analytical model for CMOD' higher than 225  $\mu\text{m}$  with a deviation of 10%. The CMOD'-deflection diagram shows a clear underestimation of the CMOD' of the analytical model by 40% (Figure 5.8b). The analytical model and the FE simulation predict the same values for CMOD' beyond 2.5 mm. The underestimation of

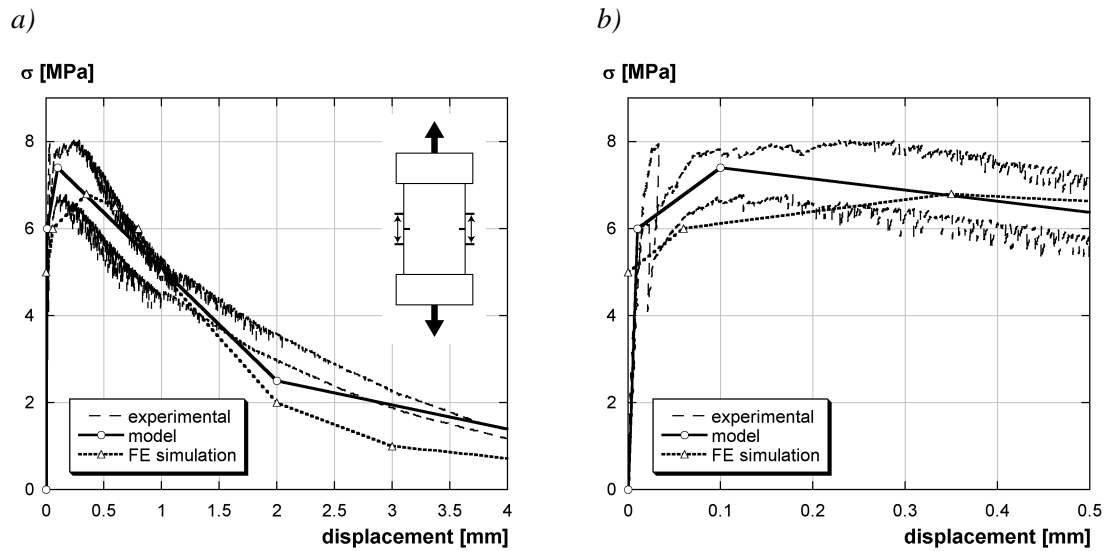


FIGURE 5.6: Tensile behaviour of the UHPFRC, a) Force-displacement diagram, b) detail

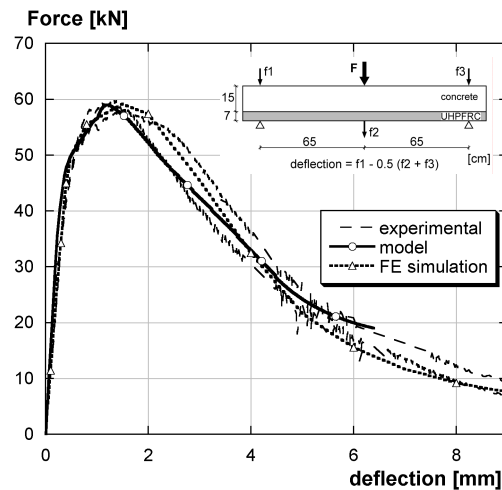


FIGURE 5.7: 3-point bending beams with UHPFRC: force-deflection diagram ( $L_R = 150$  mm), (test results and FE simulation from [Denarie01])

CMOD’ by the analytical model for small deflections can be explained by an overestimation of the hardening domain, i.e. in the model, localized macrocracks form at the end of the hardening domain (at  $\epsilon_{Ut,max}$ ). If  $\epsilon_{Ut,max}$  is overestimated, the localized macrocracks form at higher deflections than observed during the experiments. For higher deflections, the underestimation of the CMOD’ by the analytical model can be explained by an underestimated reference length  $L_R$ . Given the uncertainties of crack width measurements and the good correspondence between analytical model and numerical simulation, it can be concluded that the analytical model reproduces well the experimental results.

#### 5.1.4.2 Composite “SIMCON-concrete” beams

The behaviour of concrete beams strengthened with SIMCON was investigated by Krstulovic-Opara et al. [Krstulovic97]. The tensile behaviour of the SIMCON is modelled using experimental results (Figure 5.9a). On the basis of the tensile behaviour, the load-deflection curve of a plain SIMCON section (30.5 cm span, 10.2·5.1 cm<sup>2</sup> cross-section) in 4-point bending is calculated with the analytical model (Figure 5.9b) and compared to test results.

The tested 4-point-bending concrete beams have a square cross-section (15.2·15.2 cm<sup>2</sup>) (Figure 5.10, Section A). The same beams are strengthened with a SIMCON layer (thickness: 2.54 cm)

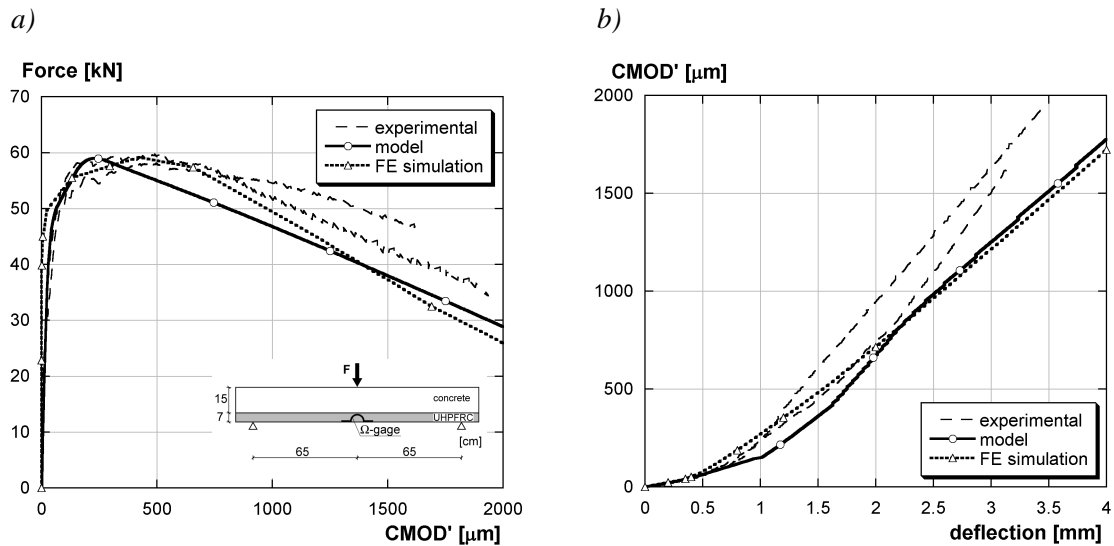


FIGURE 5.8: “UHPFRC-concrete” beams: a) force-CMOD diagram, b) CMOD-deflection diagram, (test results and FE simulation from [Denarie01])

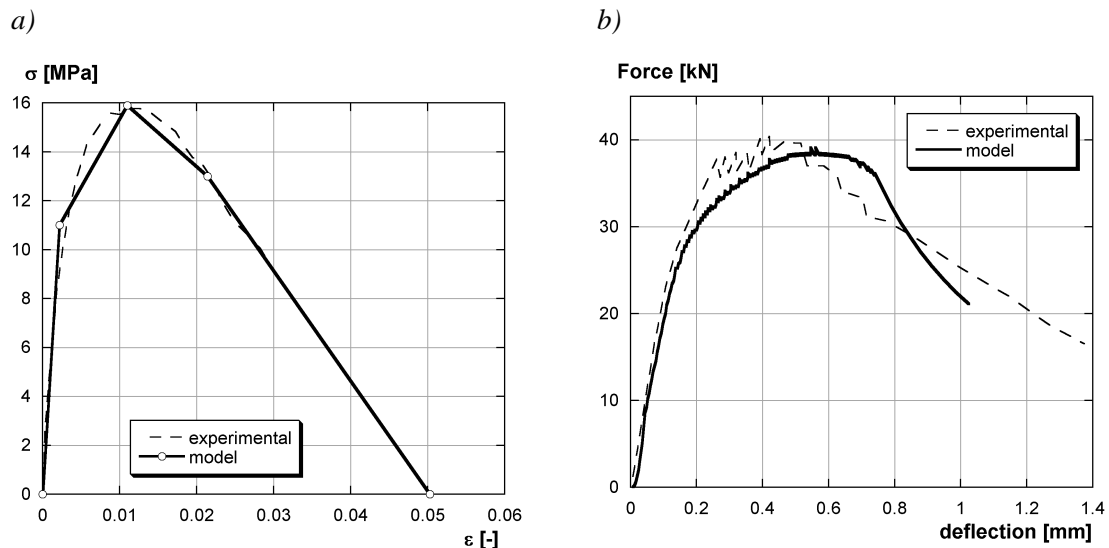


FIGURE 5.9: a) Tensile behaviour of SIMCON, b) flexural behaviour of SIMCON (test results from [Krstulovic97])

at their tensile chord (Figure 5.9, Section D). The curvature of the beams is calculated in the section of the constant moment in the middle of the beam. The prediction of the maximum moment is very good with a deviation smaller than 5%. The experimental results of section D show a force decrease after the maximum moment of 20 kNm at a curvature of  $3 \cdot 10^{-5} \text{ m}^{-1}$ , whereas the model indicates a small force increase. This is due to debonding between the SIMCON and the concrete layer that was observed in the experiments and which is not considered in the analytical model.

### 5.1.4.3 Conclusion

The analytical model is validated with test results obtained from composite bending beams. The model predicts well moment-curvature and force-deflection curves. The CMOD can also be estimated with the analytical model. The calculated CMOD are smaller than the measured values, however, they correspond well with the results of the FE simulation. Thus, the analytical model is adapted to predict the moment-curvature relationship of composite bending beams under the condition that monolithic behaviour of the beams is ensured.

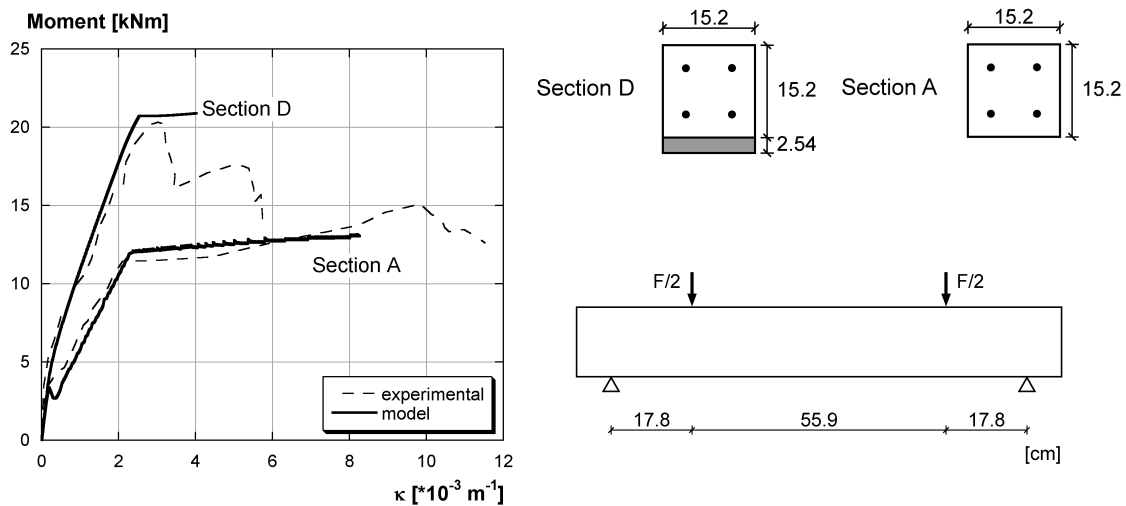


FIGURE 5.10: Composite “SIMCON-concrete” bending beams (test results from [Krstulovic97])

## 5.2 Structural response of composite “UHPFRC-concrete” beams

### 5.2.1 General

The structural response of composite “UHPFRC-concrete” beams is discussed by means of the results of the experimental campaign and the analytical model. The objectives are to determine the structural response of composite “UHPFRC-concrete” beams in order to predict deformations at SLS and deformation capacity and resistance at ULS. Therefore, the fracture mechanism of composite bending beams is discussed and different stages of fracture are distinguished. Furthermore, the usefulness of the analytical model is shown and the problem of the reference length is discussed on the example of the experimental results.

### 5.2.2 Beams without reinforcement in the UHPFRC layer (beams NR)

#### 5.2.2.1 Discussion of experimental results

Test results of composite “UHPFRC-concrete” beams and of material characterization (see Chapter 3) are compared by means of the analytical model. The material laws for the normal strength concrete and the steel rebars are directly deduced from the material tests and kept constant, since the deduction of material laws from the test results is well established. The UHPFRC tensile properties are determined by uniaxial tensile tests on notched specimens. However, it has to be investigated whether the uniaxial tensile test results can be directly converted to a material law. For the tensile test can also be interpreted as a test on a structural element, and the material law is deduced by making several hypothesis such as assuming the fracture surface to be the surface in the reduced cross-section (due to the notch) (see also Section 3.2.4). The structural response of composite “UHPFRC-concrete” beams is determined under pure bending.

Two approaches are chosen to determine UHPFRC tensile behaviour as described in Figure 5.11:

- In *approach I*, the tests results of the uniaxial tensile tests are used as input parameters for the analytical model and the simulated results are compared with the results of the beam tests.
- In *approach II*, the results of the beam tests are simulated by adapting the UHPFRC tensile properties. The tensile properties leading to the best fit with the experimental results are then compared to the tests results of the uniaxial tensile tests.

The input parameters for the analytical model can be found in Appendix E.1.



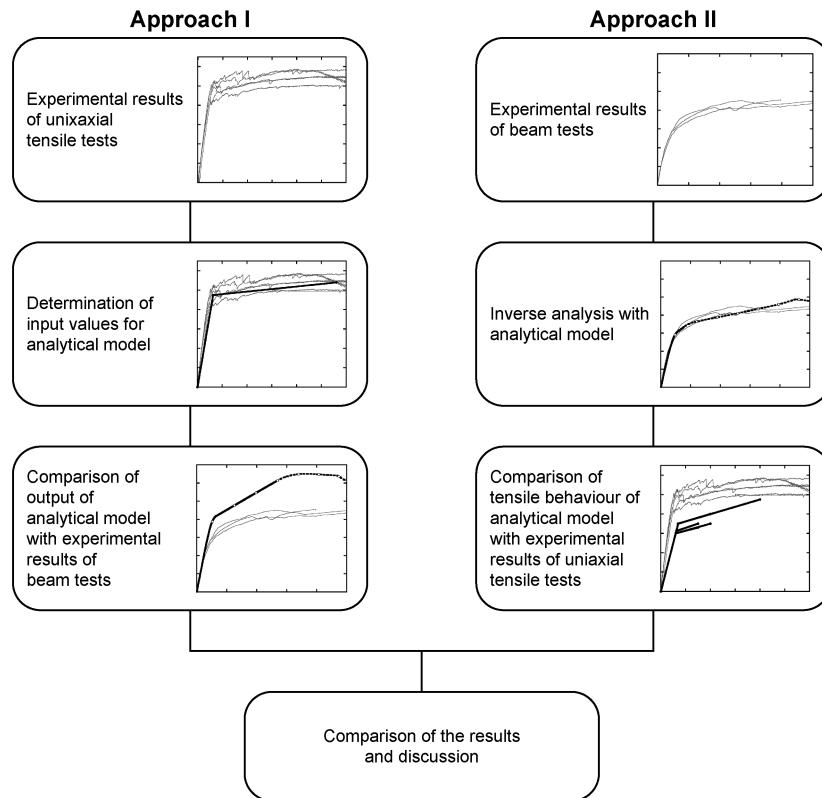


FIGURE 5.11: Approach for the comparison of the test results of the composite “UHPFRC-concrete” beams and of UHPFRC tensile behaviour

**Approach I: UHPFRC behaviour deduced from uniaxial tensile test.** The UHPFRC tensile behaviour is deduced from tests on notched specimens (Section 3.2.4). Mean values are determined and used in the analytical model (Figure 5.12).

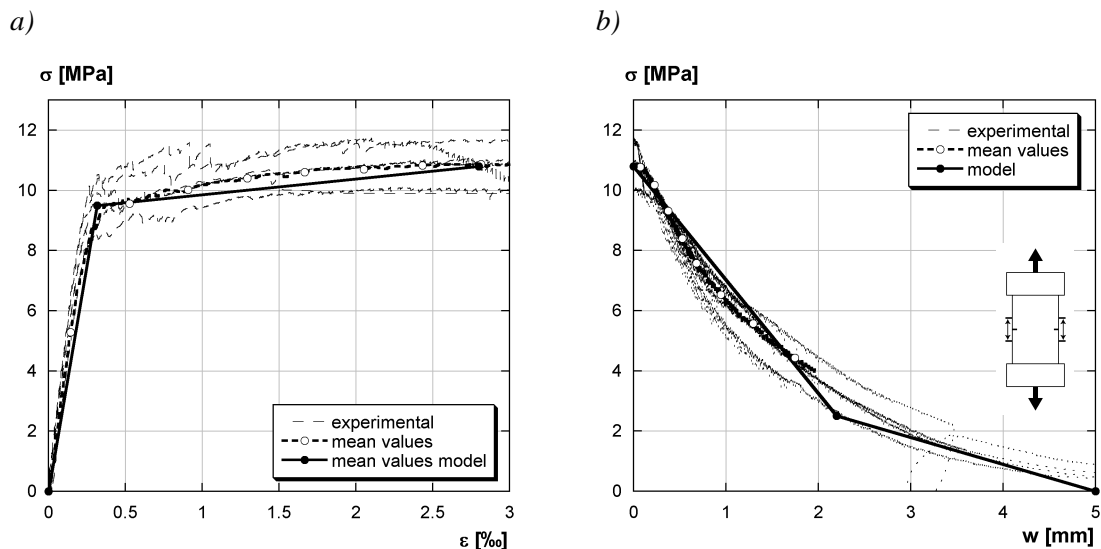


FIGURE 5.12: Tensile behaviour of UHPFRC - experimental results and modelling: a) hardening, b) softening

The comparison between experimental results and the results of the analytical model are shown in Figure 5.13. The analytical model puts out moment and curvature. The moment is transformed into the force to which the beams are subjected to during testing ( $F = M/1.2$  m, see Figure 3.16 in Section 3.4).

The mid-span deflection is determined by assuming a constant curvature over the entire central span of the beam. This assumption is correct before the formation of localized macrocracks ( $\epsilon \leq \epsilon_{U_t, \max}$ ). At the end of hardening of the UHPFRC, the experimental results show localization of deformation into one or several localized macrocracks that can be interpreted as plastic hinges, and the assumption of constant curvature induces errors in the determination of the deflection. The reference length  $L_R$  may not only be used to transform crack width  $w$  into strain (EQ. 5.1), but also to smear the concentrated deformations in the plastic hinges over the whole central span of the beam. This simplification is made because there is not sufficient experimental evidence to distinguish between the reference length  $L_R$  and the length of the plastic hinge  $L_{hi}$ . The transition from the continuum model to the fictitious crack model is illustrated in the diagrams. The part of the continuum model ( $\epsilon \leq \epsilon_{U_t, \max}$ ) is drawn with solid lines, the part of the fictitious crack model ( $\epsilon > \epsilon_{U_t, \max}$ ) with dotted lines.

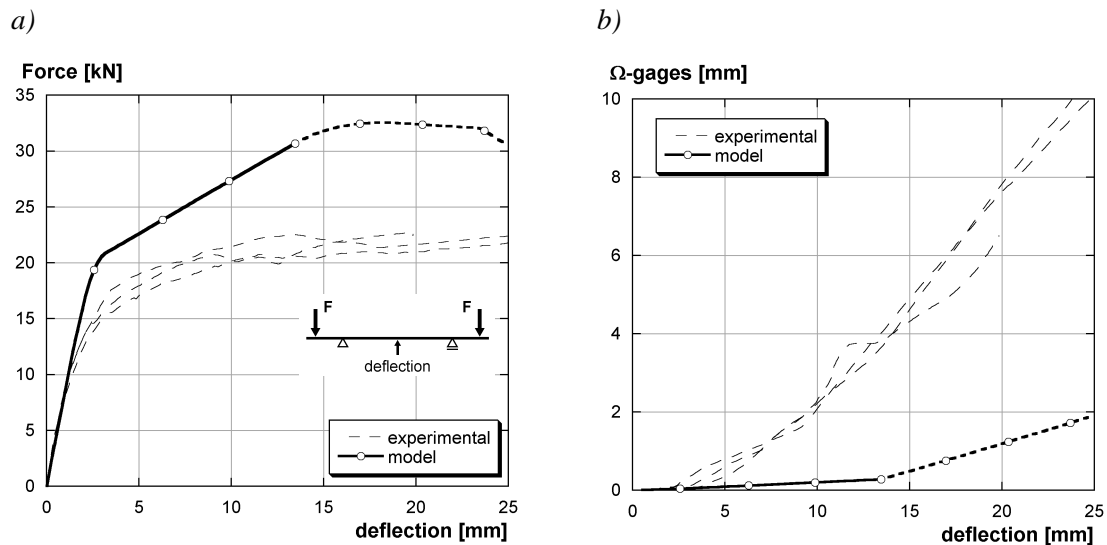


FIGURE 5.13: Comparison between experimental results and results of the analytical model (NR5) with tensile input derived from uniaxial tensile tests: a) force-deflection, b)  $\Omega$ -gages-deflection

Figure 5.13 shows that the analytical model overestimates the force of the beams NR5 with a maximum deviation of 30%. Localized macrocracks are observed at deflections of 4 mm during testing, while the model predicts 13.5 mm (Figure 5.13b). Furthermore, the calculated increase of macrocrack opening is smaller than in the experiments. These tendencies are confirmed by beams NR3 and NR10 (see Appendix E.2). The deviation of force is smaller for beams NR3 (10%). However, the overestimation of the deflection at the formation of localized macrocracks is equally high for all beams NR.

**Approach II: fitting of the beam tests by adapting the UHPFRC tensile behaviour.** The analytical model is used to determine the UHPFRC tensile behaviour by inverse analysis. Therefore, the results of the analytical model are fitted to the results of the beam tests by adapting the UHPFRC tensile behaviour.

Figures 5.14 to 5.16 show the comparison of test results and analytical model and Figure 5.17a the determined UHPFRC tensile behaviour. Only the hardening part is adapted; the softening part of the UHPFRC behaviour is not changed, but its magnitude is influenced by the reference length  $L_R$ . Prior to the formation of localized macrocracks, i.e. in the continuum part, the model reproduces well the results of the beam tests. Only the initial stiffness (for deflections smaller than 2 mm) is underestimated by the analytical model (Figures 5.15b). When the maximum force is reached, a dominant localized macrocrack forms and the model with the smeared curvature cannot predict the force-deflection curve any more, like for example, beams NR10 (Figure 5.14b).

The force-deflection curves of the beams NR3 suggest damage in form of microcracking: The maximum force of the three beams NR3 is nearly equal, however, the stiffness of the three beams is different. It is the lowest for the statically indeterminate beams (H3) and the highest for (I3). In beam H3,

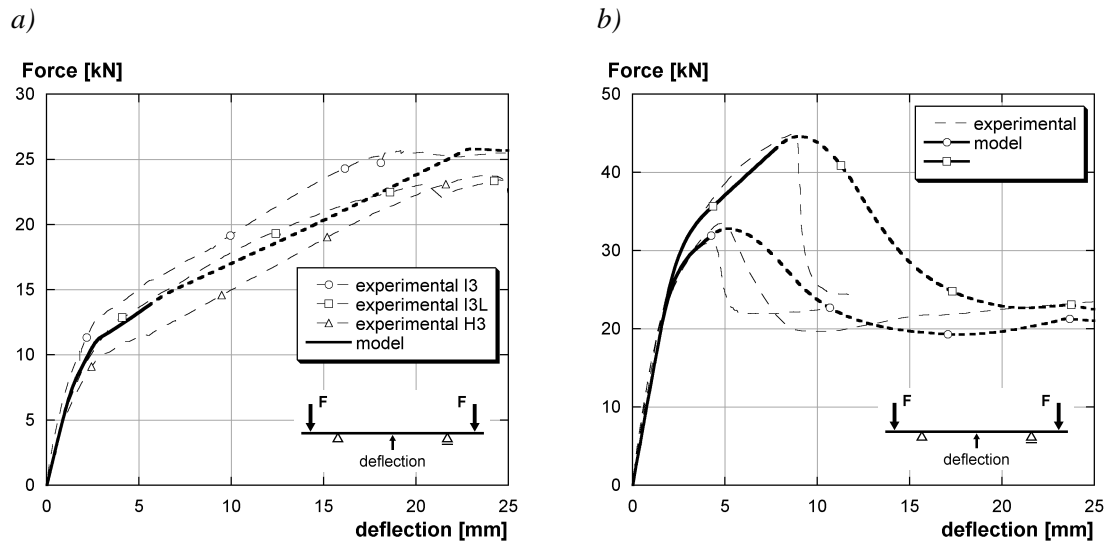


FIGURE 5.14: Comparison between experimental results and results of the analytical model with adapted input values: a) NR3, b) NR10

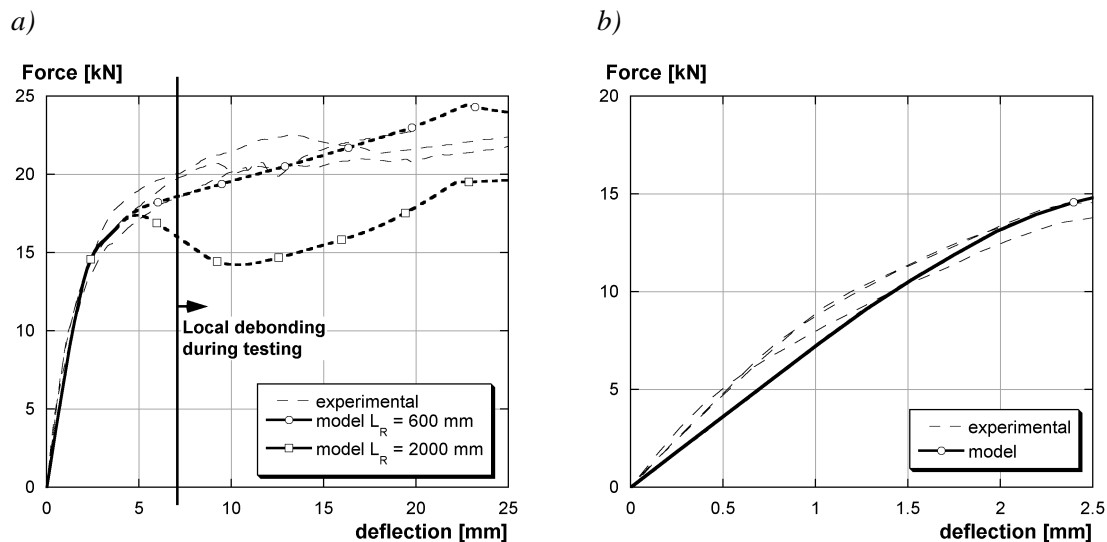


FIGURE 5.15: Comparison between experimental results and results of the analytical model with adapted tensile input values (NR5): a) overall force-deflection, b) initial part of force-deflection

microcracks have already formed during the long-term tests due to the static system (see Section 4.4). These cracks are barely visible with the naked eye, however, they reduce the stiffness of the beam during the fracture tests. Microcracking to a smaller extent also occurs in beam I3L, the beam subjected to creep, since its stiffness is lower than the one of the non-loaded beam I3. However, no difference in cracking is observed between beams I3 and I3L with the naked eye.

The strengths  $f_{U_t,1st}$  and  $f_{U_t,max}$  are approximately 33% lower than the mean experimental values (Figure 5.17). The approximation of the tensile behaviour requires an apparent secant modulus that is lower than the secant modulus observed in the tests (reduction of 50%). This corresponds to the underestimation of the initial stiffness of the beams (Figures 5.15b) and indicates non-linearity of the UHP-FRC tensile behaviour before the deformation  $\epsilon_{U_t,1st}$ . The slope of the hardening ( $E_{U,hard}$ ) is steeper than for the test results. The scatter  $f_{U_t,1st}$  for the different beams is of 1 MPa, the strain  $\epsilon_{U_t,max}$  is between 0.75‰ and 1‰, with one exception of NR10, where  $\epsilon_{U_t,max} = 2‰$  (dotted line in Figure 5.17). This high magnitude of hardening corresponds to the force-deflection curve in Figure 5.14b with a maximum force of 45 kN. This beam probably has a very homogenous UHPFRC layer with less weak spots than the other beams NR so that macrocrack localization occurs at a higher magnitude of harden-

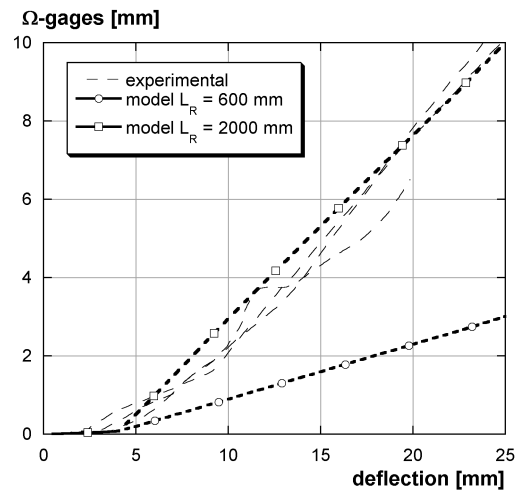


FIGURE 5.16: Comparison between experimental results and results of the analytical model with adapted tensile input values (NR5):  $\Omega$ -gages-deflection

ing. If this beam is not considered, a dependency of the strengths  $f_{U_t,1st}$  and  $f_{U_t,max}$  on the thickness of the UHPFRC can be observed: the thicker the UHPFRC layer, the lower are the strengths. This may be explained by the fibre segregation in the UHPFRC layer. It is not probable that the decrease in strengths is due to a size effect, since the size effect mainly occurs in brittle materials, while the deformation capacity of UHPFRC is rather high.

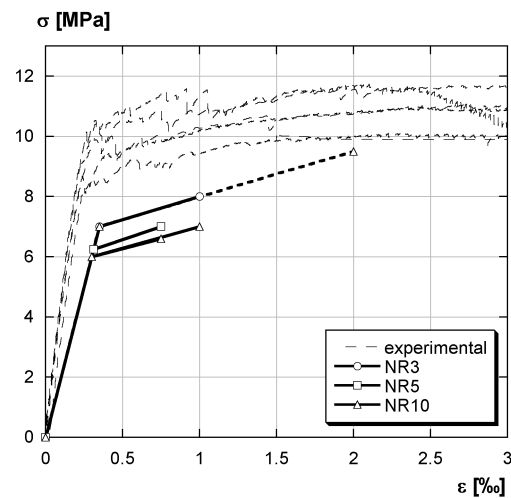


FIGURE 5.17: UHPFRC tensile behaviour determined by inverse analysis,

**Discussion of the tensile behaviour.** The significant difference between the UHPFRC tensile behaviour and the tensile behaviour determined by inverse analysis on the basis of the beam tests has several reasons:

- In the tensile test, the notch concentrates the fracture process into a given cross-section - not the weakest one, while in the 4-point-bending beams, the weakest sections fracture first. As a consequence, the tensile test tends to overestimate tensile properties.
- The reduction of the tensile strength of the UHPFRC of the beams may be due to fibre segregation in the UHPFRC. Fewer fibres are found near the top surface of the beams. This segregation is more pronounced for thicker UHPFRC layers. The observation that the UHPFRC tensile strengths, determined by inverse analysis, are higher for thinner layers substantiates this thesis.

- The lower apparent secant modulus and the steeper hardening modulus  $E_{U,hard}$  of the tensile properties found by inverse analysis may be due to residual stresses and the formation of microcracks in the UHPFRC layer due to the time-dependent behaviour of the composite elements during the 90 days prior to the fracture tests (see Chapter 4). This may also explain the non-linearity in the UHPFRC tensile behaviour for deformations smaller than  $\epsilon_{Ut,1st}$ .
- The analytical model only considers a bi-linear stress distribution in its homogenous part, i.e. before the localized macrocracks form. This simplification leads to an underestimation of the initial stiffness. However, a bi-linear model is assumed to be sufficiently exact to represent the tensile behaviour of UHPFRC before the macrocrack localization.

The differences between the tensile test results and the tensile properties, determined from the beam tests by inverse analysis, show that the material test results cannot be directly applied to structural elements. There is a need for further research into the deduction of UHPFRC tensile parameters for the analysis of composite “UHPFRC-concrete” elements.

**Reference length.** The calculated structural response after the formation of localized macrocracks depends on the reference length  $L_R$ . The force-deflection curve of beam NR is well reproduced with a deviation smaller than 10% for  $L_R = 600$  mm (Figure 5.15a). But, regarding the development of macrocrack width, the slope is strongly underestimated (Figure 5.16).

The evolution of macrocrack width is well reproduced with  $L_R = 2000$  mm (Figure 5.16), however, the force is underestimated in the force deflection diagram (Figure 5.15a). Thus,  $L_R = 2000$  mm can be interpreted as reference length that can be *applied to the cross-section with a localized macrocrack and that gives the average curvature over the length of the plastic hinge*  $\kappa_{hi}$  (Figure 5.18). It is called  $L_{R“hi”}$ .

$L_R = 600$  mm is the reference length for which the deflections over the central span can be best reproduced, but the macrocrack width is strongly underestimated. Here, the concentrated curvature of the plastic hinges is smeared over the entire central span of the beam to a smeared curvature  $\kappa_{sm}$ , and the reference length, *smeared over the entire central span*, is called  $L_{R“span”}$ .

It has to be stated that local debonding occurs for a deflection larger than 7 mm. The analytical model as cross-sectional model does not allow to reproduce three-dimensional macrocrack patterns. So, the calculated curves for deflections larger than 7 mm do not reproduce the observation during the experimental campaign, but indicate the structural response in case of monolithic behaviour (Figure 5.15b).

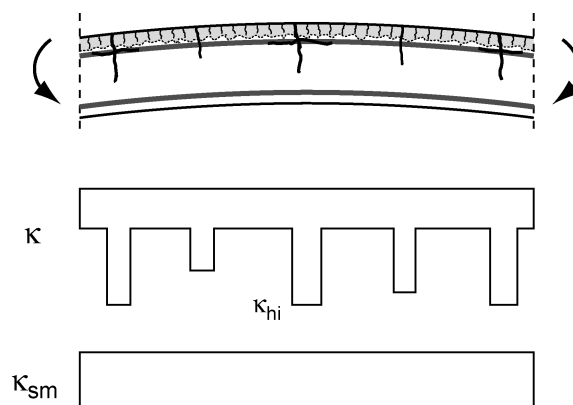


FIGURE 5.18: Smeared curvature over the central span of the composite “UHPFRC-concrete” beams

The influence of the reference length on the calculated structural response of the beam is illustrated by means of moment-curvature diagrams (Figure 5.19). Prior to the formation of localized macrocracks (continuous line of  $M$ ), the model output is identical for different reference lengths. After the formation of localized macrocracks (dotted line of  $M$ ), a smaller reference length leads to a slower stress decrease

after the formation of localized macrocracks, since a smaller reference leads to higher calculated deformations  $\epsilon$  for given crack widths (see EQ. 5.1). No more stresses are transferred in the UHPFRC layer ( $M_{U,t}$ ) at curvatures of  $\kappa = 80 \cdot 10^{-3} \text{ m}^{-1}$  and  $\kappa = 30 \cdot 10^{-3} \text{ m}^{-1}$  for  $L_R = 600 \text{ mm}$  and  $L_R = 2000 \text{ mm}$  respectively. The other parts of the moment like the moment due to the tensile reinforcement in the concrete layer  $M_{s,ct}$  remain identical for the two reference lengths.

The moment  $M$  of  $L_R = 600 \text{ mm}$  increases monotonously until the yielding of the reinforcement (Figure 5.19a). It decreases afterwards, since the transferred stresses in the UHPFRC still decrease and the hardening of the steel is small. The moment  $M$  for  $L_R = 2000 \text{ mm}$  decreases after the formation of localized macrocracks until a curvature of  $\kappa = 15 \cdot 10^{-3} \text{ m}^{-1}$  and increases afterwards to reach the moment due to the concrete in compression and the steel in tension (Figure 5.19b), which is identical to the one of a RC section.

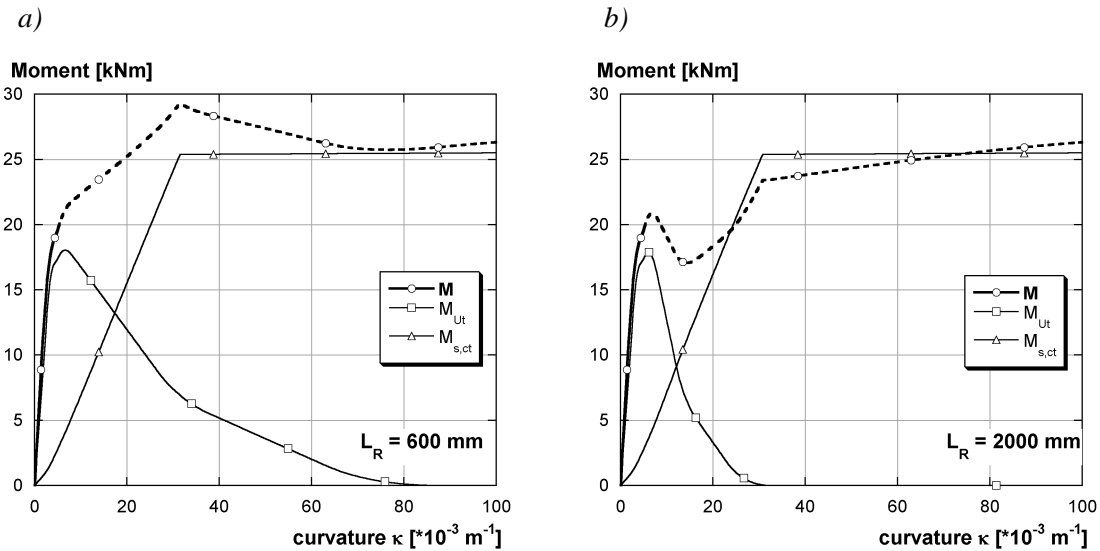


FIGURE 5.19: Behaviour of the analytical model for a)  $L_R = 600 \text{ mm}$ , b)  $L_R = 2000 \text{ mm}$

The reference lengths  $L_{R\text{“hi”}}$  and  $L_{R\text{“span”}}$  that are found for all beams NR with the analytical model are summarized in Table 5.2. The reference length  $L_{R\text{“hi”}}$  cannot be determined for beams NR3 because no measurements of macrocrack widths are available and  $L_{R\text{“hi”}}$  is determined on the basis of these test results. The length  $L_{R\text{“hi”}} = 2000 \text{ mm}$  is identical for NR5 and NR10. The length  $L_{R\text{“span”}}$  increases with increasing thickness of the UHPFRC layer, however, the value for NR10 can only be estimated, as the maximum force is reached just after the formation of localized macrocracks and the model is not appropriate to describe softening behaviour of the beams.

TABLE 5.2: Reference lengths for beams NR (determined by inverse analysis)

Beam	$L_{R\text{“hi”}}$ [mm]	$L_{R\text{“span”}}$ [mm]
NR3	-	250-500
NR5	2000	600
NR10	2000	1500 <sup>a</sup>

a. estimated value

A constant length  $L_{R\text{“hi”}}$  means that the transformation from macrocrack opening into strain seems to be independent on the thickness of the UHPFRC layer. The increasing  $L_{R\text{“span”}}$  for increasing thickness of the UHPFRC layer indicates that the deformation at localized macrocracks seems to be more concentrated for thicker UHPFRC layers, i.e. the length of the plastic hinge seems to be smaller for thicker UHPFRC layers. This may be due to the reinforcement  $A_{s,ct}$  in the concrete layer which is very close to the interface. The influence of the reinforcement on the deformations of the UHPFRC is more

pronounced for thin layers. So, deformations are better distributed in thinner UHPFRC layers. In thicker UHPFRC layers, maximum force and the formation of localized macrocracks are governed by the UHPFRC, and a localized macrocrack forms in the weakest section of the UHPFRC.

### 5.2.2.2 Structural response

On the basis of the test results and the analytical model, the structural response of the beams without reinforcement in the UHPFRC layer (NR) is described in five stages (Figure 5.20b and c).

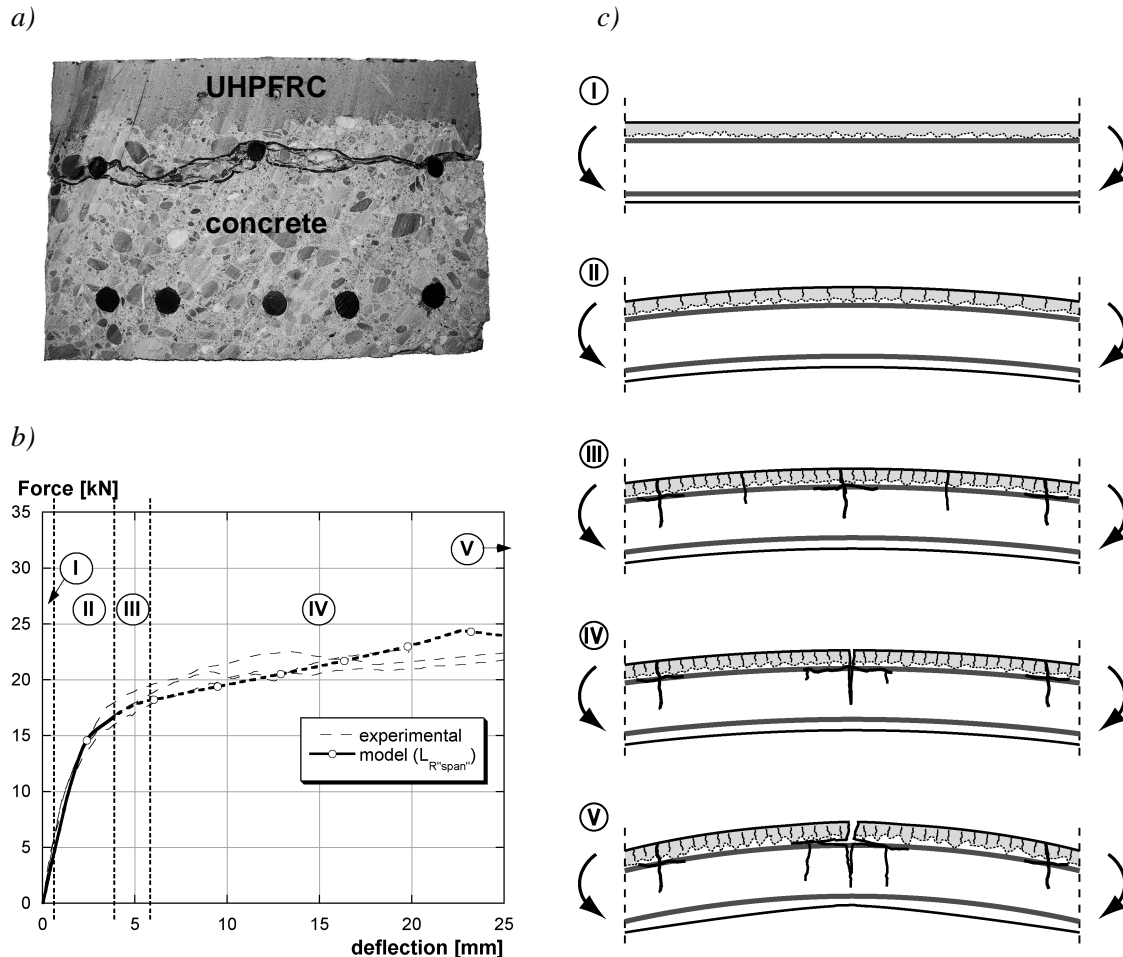


FIGURE 5.20: Structural response of beam NR: a) debonding in a cross-section near the localized macrocrack (picture taken after fracture tests, stage V), b) typical force-deflection diagram (NR5), c) evolution of the crack pattern

- I. At low forces, the beam shows *quasi linear-elastic behaviour*. No visible microcracks occur in the UHPFRC.
- II. Microcracks develop into *densely distributed macrocracks of small widths* ( $< 50 \mu\text{m}$ ). The deformations of the UHPFRC are simulated *homogeneously distributed* over the beam.
- III. *Localized macrocracks* develop out of distributed macrocracks at a mid-span deflection of  $1/600$  with a spacing larger than 100 cm. When the localized macrocracks reach the interface, *interface cracks* occur at the level of the tensile reinforcement in the concrete layer, placed near the interface (Figure 5.20a).
- IV. The force transmitted in the macrocracked UHPFRC layer decreases (softening behaviour of the UHPFRC), however, the overall force increases in the beam, since the tensile reinforcement of the concrete layer  $A_{s,ct}$  does not yield yet. More and more stress is transferred into this tensile reinforcement through the interface. The interface crack develops into *local debonding*. Length and width of

the debonding crack increase with increasing width of these flexural localized macrocracks. Secondary bending macrocracks form in the concrete layer. The tensile reinforcement in the concrete layer starts to yield (at a deflection of 22.5 mm). One *plastic hinge* forms.

- V. The composite beam *fails* by fracture of the tensile reinforcement in the concrete layer that is accompanied by concrete crushing in its final state.

The crack pattern is dependent on the *thickness of the UHPFRC layer*. If the UHPFRC layer is thin (e.g.  $h_U = 3$  cm), the tensile reinforcement in the concrete layer leads to localized macrocracking in the UHPFRC layer with reduced spacing (10 cm at maximum force after the experimental results). Less local debonding occurs, as the stresses that have to be transferred from the UHPFRC layer to the reinforcement in the concrete layer are small. The failure mode is similar to the one of RC beams. For thicker layers (e.g.  $h_U = 10$  cm), the influence of the tensile reinforcement in the concrete layer is small and localized macrocrack spacing is larger (40 cm at maximum force after the experimental results). Local debonding is pronounced, since more stresses have to be transferred through the interface when a localized macrocrack opens in the UHPFRC layer. Several macrocracks can form in the concrete layer in the debonded zone. These macrocracks extend the length of the plastic hinge  $L_{hi}$ . The influence of the thickness of the new layer on local debonding is also known for composite reinforced concrete elements [Bernard00, Habel00].

*Debonding* occurs always in the plane where the tensile reinforcement  $A_{s,ct}$  is located and not at the contact surface between UHPFRC and concrete (Figure 5.20a). This may be due to the reinforcement that weakens the concrete section. In the case of the composite beams, this plane is near the contact surface and the debonding crack weakens the bond between reinforcement and concrete. The reinforcement is still anchored in the sound concrete outside the debonded zones, it works in the debonded zone the same way as external reinforcement.

The *maximum force* of the composite beams is increased for UHPFRC layers that are thicker than a *threshold value*  $h_{U,thr}$ . The experimental results indicate that this value is between 5 and 10 cm for the given beam configuration (see Section 3.4.3).

### 5.2.2.3 Potential application

UHPFRC layers without reinforcement start to lose their resistance due to formation of localized macrocracks at relatively small deflections ( $1/600$ ). Therefore, thin UHPFRC layers should not be used to increase the resistance of a structural element. Thicker UHPFRC layers increase the fracture energy of the composite beams. This energy increase may be used to absorb accidental actions such as seismic actions or impacts.

## 5.2.3 Beams with reinforcement in the UHPFRC layer (R)

### 5.2.3.1 Discussion of experimental results

The same approach as for the beams NR is used to compare the experimental results by means of the analytical model (Figure 5.11).

**Approach I: UHPFRC behaviour deduced from uniaxial tensile test.** The mean values of experimental results of the uniaxial tensile tests (Figure 5.12) are used to simulate the force-deflection curves of the beams with reinforcement in the UHPFRC layer (R). Figure 5.21 shows the results for beams R5. The mean values of the UHPFRC tensile behaviour overestimate the force with a deviation of 20% at a deflection of 2 mm and of 15% at a deflection of 15 mm (Figure 5.21a). The formation of localized macrocracks at deflections between 13 and 17 mm (see Section 3.4.3) is predicted. The increase of crack width with increasing deflection is correctly modelled for a reference length of 1500 mm (Figure 5.21b). The force-deflection curve is also well determined with this reference length.

**Approach II: fitting of the beam tests by adapting the UHPFRC tensile behaviour.** The apparent tensile behaviour, determined by inverse analysis of the beams, is shown in Figure 5.23. It has a lower



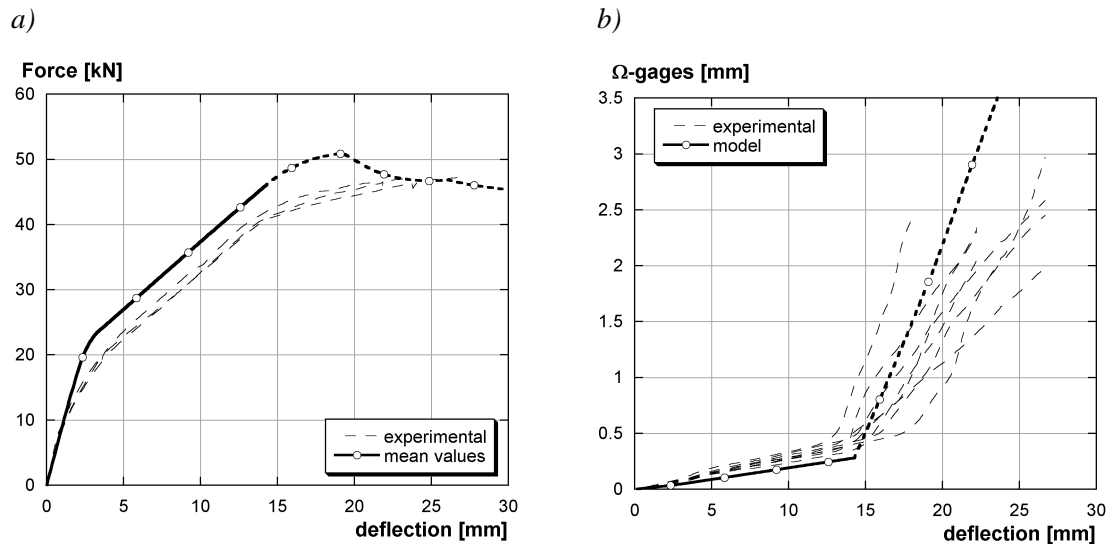


FIGURE 5.21: Comparison between experimental results and results of the analytical model (R5): a) force-deflection, b)  $\Omega$ -gages-deflection

apparent secant modulus (reduced by 50%) and lower strengths than the values derived from the uniaxial tensile test (reduction by approximately 33%). The hardening modulus  $E_{U,hard}$  is 30% higher for the tensile behaviour, determined by inverse analysis, than for the test results. The strain in the UHPFRC layer at the formation of localized macrocracks  $\epsilon_{Ut,max}$  is equal or even higher than indicate the tensile test results. The force-deflection curves of R5 and R10 are correctly modelled with the modified input values (deviation smaller than 5%) (Figure 5.22 and Appendix E.2). The formation of localized macrocracks and the increase of macrocrack width are predicted within the experimental scatter.

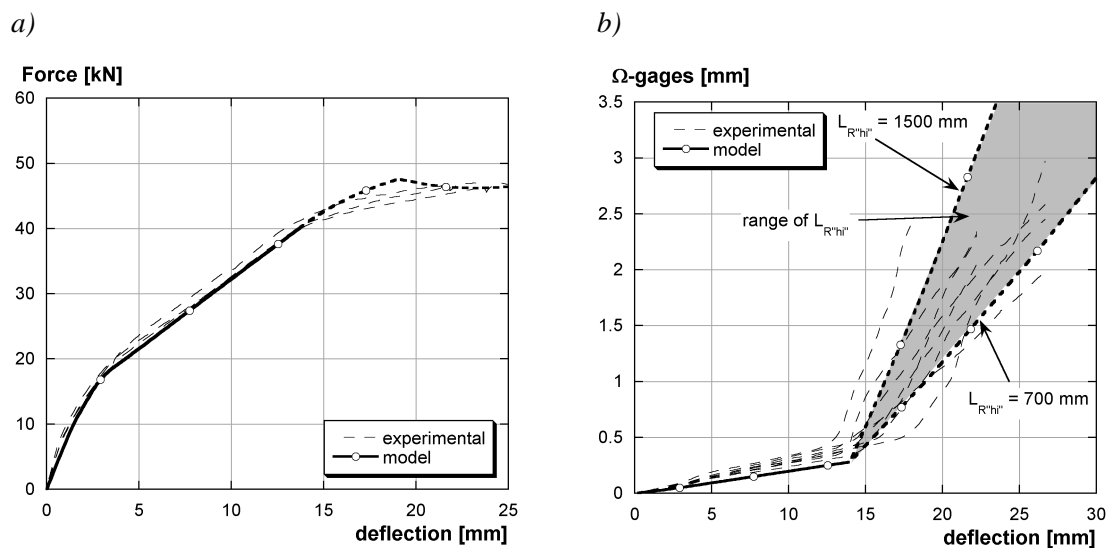


FIGURE 5.22: Comparison between experimental results and results of the analytical model with adapted input values (R5): a) force-deflection, b)  $\Omega$ -gages-deflection

**Composition of the bending moment.** Figure 5.24 shows the composition of the bending moment in the composite “UHPFRC-concrete” beam in a moment-curvature diagram. The main contributions to the bending moment are the moment due to the UHPFRC layers for small curvatures and the moments due to the tensile reinforcements for higher curvatures. The UHPFRC contributes mainly to the stress increase for curvatures smaller than  $4 \cdot 10^{-3} \text{ m}^{-1}$ . Then, the contributions of the tensile reinforcements  $A_{s,U}$  and  $A_{s,ct}$  become more and more important. The maximum moment is reached when the reinforcement  $A_{s,U}$  starts to yield.  $A_{s,ct}$  yields at a higher curvature, as it is nearer to the neutral axis of the beam. The moment  $M_{Ut}$  becomes zero at a curvature of  $55 \cdot 10^{-3} \text{ m}^{-1}$ . This is the moment when no more

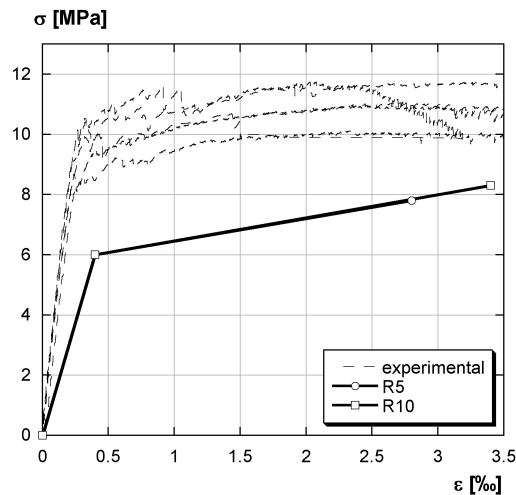


FIGURE 5.23: Apparent input data of the UHPFRC tensile behaviour

stresses can be transferred in the UHPFRC layer because the macrocrack opening is too large, and the bending moment  $M$  corresponds to the one of a RC beam with identical reinforcement configuration.

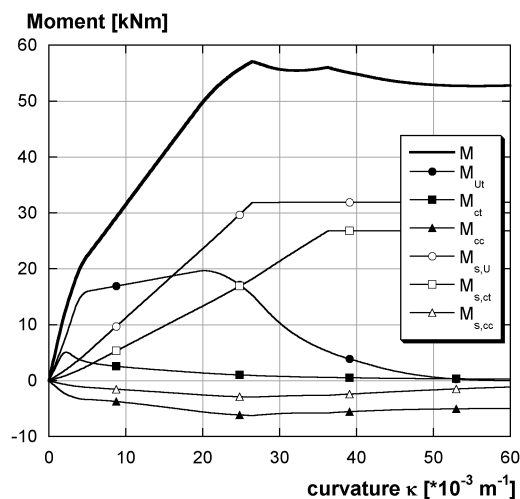


FIGURE 5.24: Composition of the bending moment

**Discussion.** The difference between the UHPFRC tensile behaviour observed with the uniaxial tensile tests and determined by inverse analysis on the basis of the beam results is explained by the same mechanisms as for beams NR (see Section 5.2.2.1). However, the difference in the magnitude of hardening seems to be smaller for beams R: the deformation at the maximum tensile strength, i.e. at macrocrack formation, is determined to be  $\varepsilon_{U_t, \max} = 2.8\text{‰}$  by the uniaxial tensile tests and to be  $\varepsilon_{U_t, \max} = 2.8\text{‰}$  and  $3.4\text{‰}$  determined by inverse analysis from the beam tests. This is due to the superposition of two independent phenomena: the increase of the apparent magnitude of hardening due to the notch in uniaxial tensile test specimens and the increase of the apparent magnitude of hardening in the beams due to the tensile rebars in the UHPFRC layer, i.e. two different phenomena that tend to compensate each other, but that do not stand in direct relation.

**Reference length.** The reference lengths  $L_{R\text{“span”}}$  are determined to 1500 mm and 2000 mm for R5 and R10 respectively. As macrocrack localization occurs near the maximum force, there is not enough experimental data to exactly determine  $L_{R\text{“span”}}$ . The reference length  $L_{R\text{“hi”}}$ , which is detected on the basis of crack width measurements of the  $\Omega$ -gages, varies between 700 and 1500 mm for R5 and

between 2000 and 2400 mm for R10. This high scatter of the reference length  $L_{R''hi''}$  that is directly determined on the basis of test results shows that the macrocrack width varies from crack to crack and that it is difficult to deduce a distinct value for the reference length  $L_{R''hi''}$ , but that  $L_{R''hi''}$  is better described by a range of values.

TABLE 5.3: Reference lengths for beams NR (determined by inverse analysis)

Beam	$L_{R''hi''}$ [mm]	$L_{R''span''}$ [mm]
R5	700 - 1500	1500
R10	2000 - 2400	2000

### 5.2.3.2 Structural response

The structural response of beams with reinforcement in the UHPFRC layer (R) is described in the same five stages as the beams without reinforcement in the UHPFRC layer (NR) (Section 5.2.2 and Figure 5.25) However, several important differences are observed in the structural response:

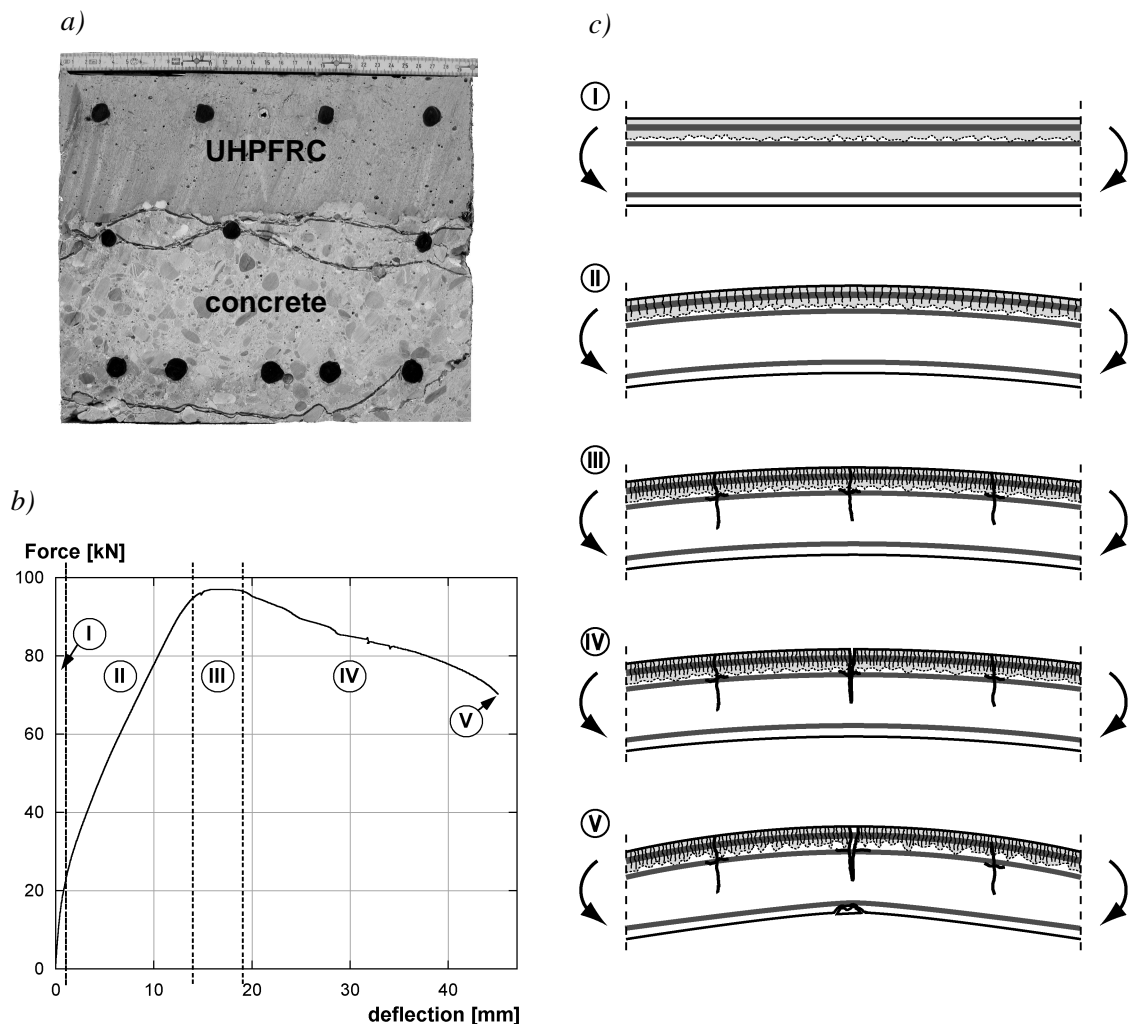


FIGURE 5.25: Structural response of beam R: a) interface cracks in a cross-section near a localized macrocrack (picture taken after fracture tests), b) typical force-deflection diagram (for beam R10), c) evolution of the crack pattern

- The *ultimate resistance* of beams R is increased when compared to beams NR: the force is two times higher for beams R5 than for NR5 and three times higher for R10 than for NR10.

- Localized macrocracks (transition from stage II to III) form at a *deflection* of  $l/160$ , just before the maximum force is reached. The deflection is approximately 3.5 times higher than for beams NR.
- *Interface cracks* form, but they are of a smaller length and width than in beams NR and *do not alter the structural response*. Thus, no debonding occurs.

**Interface cracks.** Interface cracks form at deflections of 13 to 17 mm, however, their crack width remains constant for deflections higher than 23 mm. In combination with visual observations during testing, it can be deduced that the beam fails in the vertical bending crack. This may be explained by the role of the reinforcement in the UHPFRC layer ( $A_{s,U}$ ) that transfers a big part of the tensile stresses directly through the localized macrocracks. Thus, less stresses have to cross the interface, and the interface cracks are significantly shorter and have smaller crack widths. Figure 5.26 shows schematically the stress distribution in a composite “UHPFRC-concrete” beam when the localized macrocrack reaches the interface. The stress deviation due to the crack provokes tensile stresses perpendicular to the interface zone. The magnitude of stress transfer is dependent on the cross-section geometry, the reinforcement ratio and the material types and cannot be derived by means of a simple analytical model. The same phenomenon has been observed for composite “RC-concrete” beams [Bernard00, Habel00].

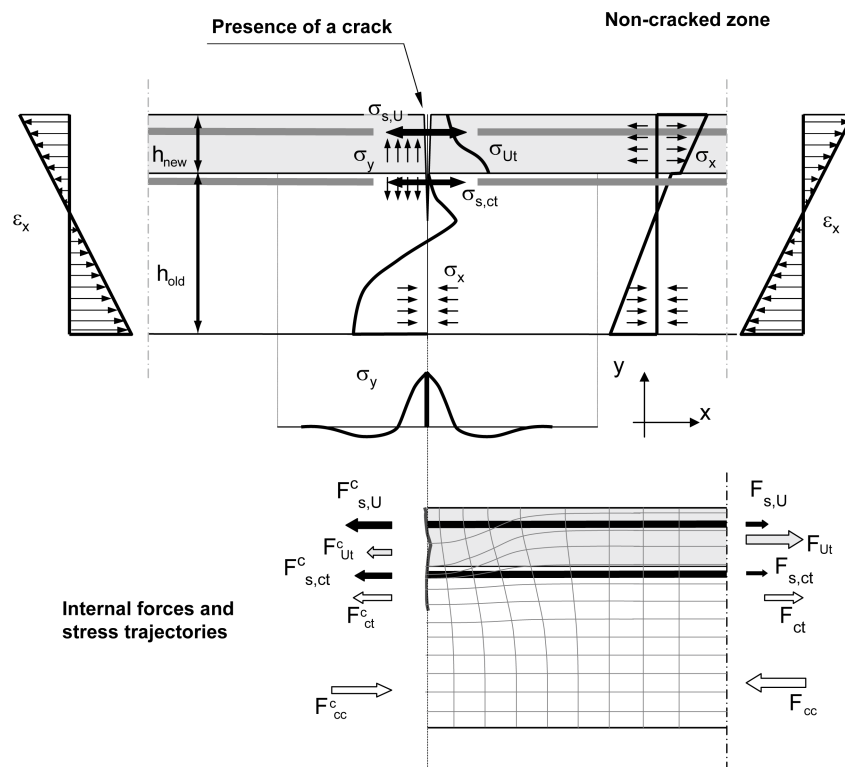


FIGURE 5.26: Stress distribution at a crack for composite “UHPFRC-concrete” elements (adapted from [Bernard00])

**Apparent hardening of UHPFRC with reinforcement.** The reinforcement in the UHPFRC layer ( $A_{s,U}$ ) can be seen as macroscale “reinforcing fibre” when compared to the small steel fibres in the UHPFRC (here:  $l_f = 10$  mm). The steel fibres act on the material level: They bridge microcracks and limit their propagation. When macrocracks form, the steel fibres bridge them until their width becomes too large and the fibres are gradually pulled out. At approximately half of the fibre length ( $l_f/2 = 5$  mm for the used UHPFRC), no more stresses are transferred through the crack.

Steel rebars can be seen as “macro-fibres” that bridge also macrocracks with large openings. In contrast to the steel fibres, the steel rebars are not pulled out, they yield and finally fail by fracture, leading to the failure of the structural element. During force rise, the steel rebars contribute to the distribution of

deformations and bridge macrocracks. Thus, narrowly distributed macrocracks form and macrocrack localization occurs at a higher deflection ( $l/160$ ) when compared to beam NR ( $l/600$ ).

The apparent magnitude of hardening is 3.5 times higher for the beams R than for the beams NR. This is observed during the beam tests (see Section 3.4.3) and is confirmed by the inverse analysis with the analytical model. The increase in the apparent magnitude of hardening underlines the beneficial effect of reinforcement not only on ultimate resistance but also on crack formation in the composite “UHPFRC-concrete” element.

**Softening behaviour of beams R.** The beams R may show softening behaviour after the maximum force. It is explained by the tensile behaviour of the UHPFRC: Force is still transferred in the UHPFRC when the reinforcement  $A_{s,U}$  yields. The decrease of stress that can be transferred through the localized macrocracks in the UHPFRC is higher than the stress increase due to the hardening of the steel rebars.

Whether softening or hardening occurs in the beams depends on the thickness of the UHPFRC layer and the reinforcement ratio  $\rho_{s,U}$ . For the tested beams, this softening behaviour is observed for beams R10, but not for beams R5.

### 5.2.3.3 Potential application

Composite “UHPFRC-concrete” bending elements with reinforcement in the UHPFRC layer show macrocrack formation at higher deflections ( $l/160$ ) than composite beams without reinforcement in the UHPFRC layer. Furthermore, the maximum force is increased when compared to the initial RC configuration. Thus, these configurations firstly increase the resistance and provide in addition an excellent protection against the ingress of detrimental substances. They are best used for strengthening of structures with high requirements on protection.

### 5.2.4 Macrocrack formation and deformation capacity

The composite “UHPFRC-concrete” beams are compared to RC beams in order to determine their differences in macrocrack formation and deformation capacity. This phenomenological description may be used as basis for estimations of the deformation capacity.

**Crack formation at stage II.** Figure 5.27a shows the pattern of the composite “UHPFRC-concrete” beams before the formation of localized macrocracks in pure bending (stage II, Figure 5.20b, c). In comparison, the macrocrack pattern of a RC beam is shown. It corresponds approximately to typical service conditions. The RC beam shows several bending macrocracks with equal spacing. The beam NR shows distributed macrocracks in the UHPFRC layer (width of the distributed macrocracks  $< 0.1$  mm). Average spacing of the distributed macrocracks in beams NR of the experimental campaign is 25 cm just before the formation of localized macrocracks (stage II, deflection  $l/600$ ). The crack spacing depends on the thickness of the UHPFRC layer [Habel04]. Beams R show narrowly distributed macrocracks before the formation of localized macrocracks. The experimental results indicate an average distributed macrocrack spacing of 20 cm at a deflection of  $l/600$  and of 3 cm at a deflection of  $l/160$ , just before the formation of localized macrocracks. The narrowly distributed macrocracks of beams R may be explained by the beneficial effect of the reinforcement in the UHPFRC layer (see Section 5.2.3).

The beam deformations at the moment of localized macrocrack formation are dependent on the tensile behaviour of the UHPFRC. The decisive parameter is the magnitude of hardening (see Figure 3.5), i.e.  $\epsilon_{U_t,max}$ , for a given beam configuration. The higher the value of  $\epsilon_{U_t,max}$ , the smaller is the distributed macrocrack spacing and the higher the beam deformation at the moment of localized macrocrack formation. The formation of localized macrocracks in RC beams is governed by the tensile behaviour of concrete, having a very low deformation capacity when compared to UHPFRC (concrete:  $G_F = 120$  J/m<sup>2</sup>, UHPFRC:  $G_F = 20'200$  J/m<sup>2</sup>). The first macrocracks occur at small deflections when the tensile strength of the concrete is reached (end of state I of the RC bending beam theory). All the cracks that form in the concrete are localized macrocracks and open gradually with increasing deformation. In con-

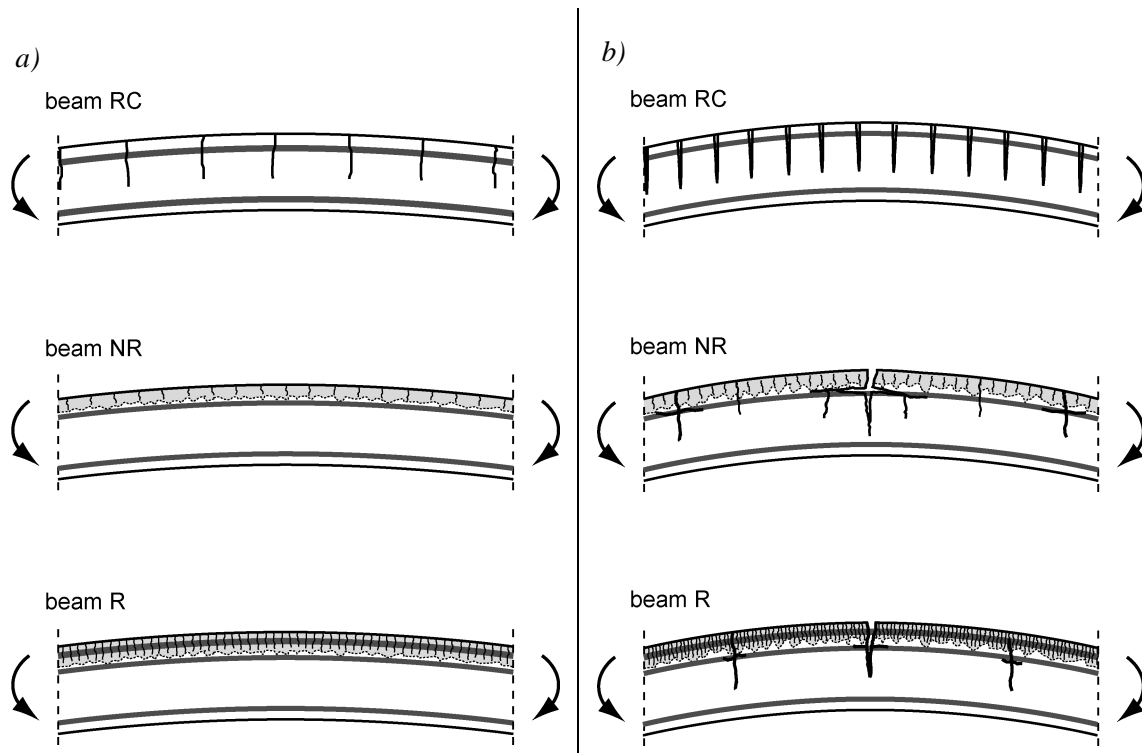


FIGURE 5.27: Comparison of crack pattern between RC and composite “UHPFRC-concrete” bending beams: a) at stage II, b) after yielding of the tensile reinforcement (stage IV)

trast, a distinction can be made between distributed and localized macrocracks in UHPFRC as described in Section 3.2.4.4.

**Crack formation after yielding of the tensile reinforcement.** Figure 5.27b shows the comparison of crack patterns between a RC beam and composite “UHPFRC-concrete” beams at yielding of the tensile reinforcement. The RC beam shows approximately equidistantly distributed macrocracks with similar widths. As the macrocrack formation in RC beams remains virtually constant after the yielding of the tensile reinforcement, i.e. no new macrocracks form, the structural response is governed by the tensile reinforcement and the concrete in compression.

The bending moment still increases slightly after the yielding (i.e. hardening) of the rebars due to the steel properties. The composite “UHPFRC-concrete beams” show narrowly distributed macrocracks, however, plastic deformations are concentrated in few or even only one localized macrocracks. The coexistence of these two types of macrocracks can be explained by the hardening domain of UHPFRC in tension and material inhomogeneities: Localized macrocracks form in weaker cross-sections, i.e. cross-section with a lower fibre content. The UHPFRC loses gradually its resistance in the localized macrocracks, i.e. softening in the UHPFRC occurs. Simultaneously, the UHPFRC in the other cross-sections is still in the hardening domain, and here only distributed macrocracks form. In consequence, plastic deformations are localized in few cross-sections, and the formation of plastic hinges can be observed.

The overall deflection of the composite “UHPFRC-concrete” beams in pure bending is smaller than those of RC beams at fracture.

**Hardening.** RC beams have a hardening behaviour until fracture, whereas composite “UHPFRC-concrete” beams may show a softening behaviour after the maximum force. Whether softening or hardening occurs in composite “UHPFRC-concrete” elements, i.e. whether the force decreases or increases after the maximum force, is dependent on the thickness of the UHPFRC layer and on the interaction between reinforcement and UHPFRC. It is investigated in the parametric study in Section 6.3.

**Deformation capacity.** The deformation capacity of composite “UHPFRC-concrete” beams differs from the one of RC beams. The hardening of the UHPFRC causes narrowly distributed macrocracks in the UHPFRC, and localization occurs at higher deformations than for RC elements, depending on the presence of reinforcement in the UHPFRC layer.

As fewer macrocracks localize in the UHPFRC beams than in RC beams, the deformations in composite “UHPFRC-concrete” beams may be lower at fracture depending on the static system. The length of the plastic hinges at the localized macrocracks is dependent on the beam geometry and on local debonding. If strong local debonding occurs, several localized macrocracks can form in the concrete (beam NR in Figure 5.27) and the length of the plastic hinge and the deformations of the beam are increased.

**Reinforcement in the UHPFRC layer.** Reinforcement in the UHPFRC layer (as beam R in Figure 5.27) increases the ratio of tensile reinforcement and the depth of the compressive zone ( $x/d$ ). Therefore, the deformation limit of concrete in compression is reached early and the deformation capacity of the beam is reduced at fracture. Furthermore, the bond between reinforcement and UHPFRC is stiffer and the bond stresses are higher than the bond between reinforcement and normal strength concrete. Thus, the length of force transfer between rebar and cementitious material is smaller for reinforced UHPFRC structures. Consequently, the plastic deformation of the rebars are concentrated over a smaller length and the length of the plastic hinge is reduced. The deformation capacity is important for ULS design and is discussed in Section 6.2.5.

## 5.3 Reference length

### 5.3.1 General

The reference length  $L_R$  is used to transform crack widths into deformations. It is needed for numerical simulations that use the smeared crack model and for analytical cross-sectional models like the one presented in this chapter. In case of analytical modelling, plastic hinges are assumed in zones where localized macrocracks form on the structural element in order to consider concentrations of curvature as shown in Figure 5.18. The *length of the plastic hinge*  $L_{hi}$  must also be determined. The two lengths depend on parameters such as fibre and cementitious matrix properties, cross-section geometry and static system. Consequently, they are not only material but also structural parameters.

### 5.3.2 Reference length values

**Literature.** In the literature, the reference length is often fixed to  $L_R = 2/3 \cdot (\text{depth of the structural element})$  under bending [AFGC02]. This value is empirical. Casanova and Rossi propose  $L_R = 2 \cdot (\text{length of the discrete crack})$  [Casanova94]. Massicotte distinguishes between SFRC bending elements with and without rebars: he suggests to use for the length of the plastic hinge  $L_{hi} = 1/2 \cdot (\text{depth of the structural element})$  for configurations without rebars and to  $L_{hi} = \max(1/2 \cdot \text{depth of the structural element}; \text{crack spacing})$  for configurations with rebars [Massicotte03]. Dupont proposes to use  $L_R = L_{hi} = 2 \cdot (\text{height of the neutral axis})$  for SFRC concrete with and without rebars [Dupont03] which is close to the approach of [Casanova94].

**Composite “UHPFRC-concrete” beams in 3-point-bending.** Tests on composite “UHPFRC-concrete” beams in 3-point-bending without reinforcement are modelled to validate the analytical model (see Table 5.4 and Section 5.1.4.1). The reference length is determined to  $L_R = 220 \text{ mm}$ , being equivalent to the beam depth when a length of the plastic hinge equal to  $2/3$  of the beam depth ( $L_{hi} = 150 \text{ mm}$ ) is assumed. These values for  $L_R$  and  $L_{hi}$  are close to values proposed in the literature.

**Composite “UHPFRC-concrete” beams in 4-point-bending.** The experimental campaign on composite “UHPFRC-concrete” elements in 4-point-bending is used to determine the reference length  $L_R$  on the basis of crack width measurements ( $L_{R,“hi”}$ ) and on the basis of force and deflection measure-

TABLE 5.4: Reference lengths for composite “UHPFRC-concrete” beams, determined with the analytical model

Beam	$L_{R\text{“hi”}}$ [mm]	$L_{R\text{“span”}}$ [mm]	$L_{\text{hi}}$ [mm]
4-point-bending NR3 (Section 5.2.2)	-	250-500	-
4-point-bending NR5 (Section 5.2.2)	2000	600	-
4-point-bending NR10 (Section 5.2.2)	2000	1500 <sup>a</sup>	-
4-point-bending R5 (Section 5.2.2)	700 - 1500	1500	-
4-point-bending R10 (Section 5.2.2)	2000 - 2400	2000	-
3-point-bending (Section 5.1.4.1)	220	-	150

a. estimated value

ments by assuming a constant curvature over the whole central span ( $L_{R\text{“span”}}$ ) (see Table 5.4 and Section 5.2).

The *reference length over the hinge*  $L_{R\text{“hi”}}$  exhibits a large variability with values between 700 and 2400 mm. As it is determined directly on crack width measurements, it includes also the large variability of these measurements. This means that no precise value for  $L_{R\text{“hi”}}$  can be determined on the basis of crack width measurements on the upper side of the beams. *There exists rather a range of values for this reference length.* However, the values of  $L_{R\text{“hi”}}$  determined in this study, are still considerably higher than the values in the literature or for the composite 3-point bending beam without reinforcement.

The *smear reference length*  $L_{R\text{“span”}}$  increases with increasing thickness of the UHPFRC layer. It is longer for the beams with reinforcement in the UHPFRC layer (R). However, no analytical relationship can be established between thickness of the UHPFRC layer and  $L_{R\text{“span”}}$  at the present state. Moreover, the reference length  $L_{R\text{“span”}}$  is specific to the given static system, since the curvature is smeared over the whole zone of the constant moment.

The high values for the reference lengths of the composite beams may be explained by:

- the *presence of tensile reinforcement* in form of rebars in the structural element and in particular in the UHPFRC layer: Rebars in the UHPFRC layer increase considerably the apparent magnitude of hardening (see Section 5.2.3.2).
- the influence of *interface cracks and local debonding*: Local debonding alters the structural response and violates hypothesis 3 for the analytical model (see Section 5.1.2). Thus, it is impossible to accurately compare the analytical model to the test results when local debonding occurs.
- the influence of the *static system*: The composite beams are subjected to 4-point-bending, i.e. a constant moment forms in the central span, leading to a high volumetric energy dissipation in the hardening zone.

### 5.3.3 Determination of the reference length

The reference length is above all an artefact of analytical and numerical models that is needed to transform crack width into deformation in cross-sectional and smeared crack models respectively. Its determination is necessary for the modelling of localized macrocracks in UHPFRC members. The reference length can be determined on the basis of test results as shown in this chapter ( $L_{R\text{“hi”}}$ ) or by assuming crack geometry and hypotheses of analytical models as shown by [Casanova94] and [Wuest04]. Material and structural parameters are mixed up in the reference length. Therefore, it is difficult to deduce it directly from test results, but it must be calculated by making several assumptions.

The length of the plastic hinge  $L_{\text{hi}}$  intervenes when the results of the cross-sectional model are extrapolated to the third dimension, i.e. over the length of structural members. The length of the plastic hinge is a simplified approach to determine non-elastic beam deformations and is for example necessary for the calculation of force-deflection diagrams. Also, the length of the plastic hinge  $L_{\text{hi}}$  depends on material and structural parameters.



The necessity of two lengths to describe force-deflection curves on the basis of an analytical model complicates the determination of the reference length by test results: It is difficult or even impossible to accurately record cracking in UHPFRC under pure bending as for example in the composite “UHP-FRC-concrete” beams of this study, since not all distributed macrocracks can be followed precisely (due to their high number) and since every macrocrack in the UHPFRC opens with a different rate (see the scatter of  $L_{R\text{“hi”}}$  in Table 5.4). In consequence, assumptions must be made either for one of the two lengths or for the coupling between the two lengths.

It is possible to combine the two values  $L_{R\text{“hi”}}$  and  $L_{hi}$  into one value which is called  $L_{R\text{“span”}}$  in this study. However, this value is bound to the specific beam configuration and should not be used for the extrapolation to other cross-section geometries and static systems.

For the tested beams, the domain between the formation of a localized macrocrack in the UHPFRC layer and of an interface crack at the crack tip of this macrocrack is small. In this domain, all model hypotheses are valid and the reference length depends only on the vertical bending crack formation. When interface cracks form, the hypothesis of perfect bond between UHPFRC and concrete layer is strictly speaking violated. The influence of interface cracking can be considered in an adapted reference length and the analytical model can still predict force-deflection curves.

### 5.3.4 Prospects

The reference length is an artefact for modelling of structural concrete elements. It combines material and structural parameters. Therefore, it is difficult to determine this parameter on the basis of the existing test results. The problem of the reference length can be avoided by using numerical simulation with the discrete crack model (e.g. [Reich97]).

The reference length for smeared crack models in *FE-programs* depends on the element size and the definition of the model for the tensile behaviour. The major problem of FE-programs using the smeared crack model is the difficulty to obtain stable calculations and crack localization when material models considering hardening-softening laws are used (see Chapter 4).

The reference length that is necessary for the *analytical model* can be derived on the basis of the results of experiments and the numerical simulation. There exist only few studies about the determination of the lengths  $L_R$  and  $L_{hi}$  for plain FRC members with and without rebars (e.g. [Massicotte03] and [Dupont03]). An approach is described in [Wuest04] from [Denarie04] to deduce the reference lengths on the basis of tensile and 4-point-bending test results. In this approach, it is distinguished between bulk energy dissipation  $G_V$  in form of finely distributed macrocracks in the domain of hardening, i.e. before the formation of localized macrocracks, and surface energy dissipation  $G_F$  in the localized macrocrack as schematically shown in Figure 5.28. The idea of distinguishing between these two kinds of energy dissipation was proposed for the crack band model by [Bazant98] and was already suggested by [Hillerborg83]. The deformation  $\varepsilon_{Ut}$  in the domain of hardening is deduced by assuming homogenous deformations over the measuring basis of the uniaxial tensile test as described in EQ. 5.12.

$$\varepsilon_{Ut} = \frac{\Delta l}{\text{measuring basis}} \quad (EQ\ 5.12)$$

The crack width  $w_{Ut}$  is directly deduced by making the hypothesis that the deformation concentrates in the crack after macrocrack localization. The reference length  $L_R$  is used to transform the crack width  $w_{Ut}$  into deformations for the cross-sectional analytical model and is determined by calculating the dissipated energy of the structural element and by considering for the UHPFRC bulk and surface energy dissipation. This approach seems to be promising for the deduction of  $L_R$  and  $L_{hi}$  in composite “UHP-FRC-concrete” members subjected to bending and should be investigated further.

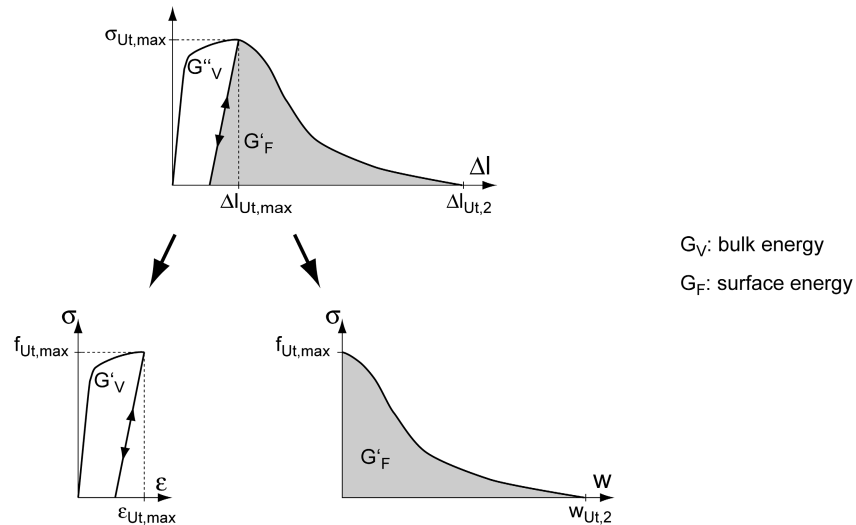


FIGURE 5.28: Schematic representation of the approach to determine the reference length  $L_R$  ([Denarie04, Wuest04])

## 5.4 Conclusions

### 5.4.1 Structural response of composite “UHPFRC-concrete” beams

#### 1. Beams without reinforcement in the UHPFRC layer (NR)

- Stiffness is increased in composite “UHPFRC-concrete” elements when compared to reinforced concrete elements.
- The resistance of composite “UHPFRC-concrete” elements is increased for UHPFRC layers thicker than the threshold  $h_{U,thr}$  ( $5 \text{ cm} < h_{U,thr} < 10 \text{ cm}$ ).
- Finely distributed macrocracks of small widths form in composite “UHPFRC-concrete” elements under service conditions, while discrete cracks with larger crack widths form in reinforced concrete elements.
- The apparent tensile strengths in the UHPFRC beams, deduced by inverse analysis, are approximately 33% lower than the ones determined by uniaxial tensile tests on notched specimens. The differences in the UHPFRC tensile behaviour in the composite beams and the uniaxial tensile test may be explained by the effect of the notch in the uniaxial tensile test that forced the crack into one section, by slight fibre segregation in the UHPFRC layer of the beams and by pre-existing cracks with small widths that formed during the long-term tests.
- Local debonding occurs in all the beams NR and is always initiated by localized macrocracks. It alters the structural response of the composite “UHPFRC-concrete” beams.

#### 2. Beams with reinforcement in the UHPFRC layer (R)

- The resistance of the beams is significantly increased due to the reinforcement in the UHPFRC layer.
- The stiffness of the composite “UHPFRC-concrete” element is increased when compared to reinforced concrete elements of the same geometry.
- The reinforcement in the UHPFRC layer delays the formation of localized macrocracks and leads to an apparent magnitude of hardening of the UHPFRC that is three times higher in beams R than in beams NR.

- The differences in the UHPFRC tensile behaviour between the composite beams and the uniaxial tensile tests may be explained in the same way as for beams NR (see above), however, the UHPFRC exhibits a higher apparent magnitude of hardening due to the effect of the rebars  $A_{s,U}$ .
- Interface cracks are less pronounced in beams R than in beams NR because (1) the reinforcement in the UHPFRC layer transfers part of the tensile stresses through the crack and (2) less tensile stresses pass through the interface. The interface cracks do not significantly alter the structural response.

### 5.4.2 Modelling

#### 1. Analytical model

- It is possible to predict the moment-curvature relationship of composite “UHPFRC-concrete” elements subjected to bending with the analytical model developed in this study. The analytical model, which is an extension of the bending model of reinforced concrete, is based on simple hypotheses.
- Force-deflection curves can be determined by making a hypothesis on the curvature distribution over the length of the structural element.
- Crack widths can be deduced in a simple way from the results obtained with the model.
- The least known parameters of the model are the reference length  $L_R$  that is necessary to transform crack width into deformation and the length of the plastic hinge  $L_{hi}$ .

#### 2. Reference length

- The reference length is an artefact for modelling that is necessary to transform crack width into deformation. It is essential to determine the reference length to predict the deformation capacity of composite “UHPFRC-concrete” bending elements with the analytical model.
- The reference length is not a single value, but lies within a range of values. This is observed by the determination of the reference length on the basis of crack widths (i.e.  $L_{R^{“hi”}}$ ).
- The reference length, determined from the composite “UHPFRC-concrete” beams, is significantly higher than indicated in the literature. This may be due to the cross-section geometry of the composite system, to the presence of tensile reinforcement in form of rebars and to the formation of interface cracks and debonding effects that are considered correctly in the model by using an adapted reference length.
- The approach to consider energy dissipation as described in [Wuest04] (from [Denarie04]) of plain UHPFRC specimens seems to be promising for its determination in case of composite “UHPFRC-concrete” elements.
- The importance of the reference length  $L_R$  underlines the research need for its determination.



## 6 Design of composite “UHPFRC-concrete” elements

Chapter 6 describes the design of composite “UHPFRC-concrete” elements. Conceptual design of three basic configurations is presented in Section 6.1. Limit state criteria for serviceability and ultimate limit states are discussed in Section 6.2. Rules for efficient design of composite “UHPFRC-concrete” elements are defined in Section 6.4 on the basis of the parametric study from Section 6.3 and the results of Chapter 4.

### 6.1 Conceptual idea

UHPFRC may extend durability and increase stiffness and resistance in composite “UHPFRC-concrete” elements. On the basis of the results of Chapter 5, three basic configurations emerge (Figure 6.1): one for protection purposes (P), one that can be designed either only for protection or additionally for an increase in resistance (PR) and one for protection and increase of resistance (R).

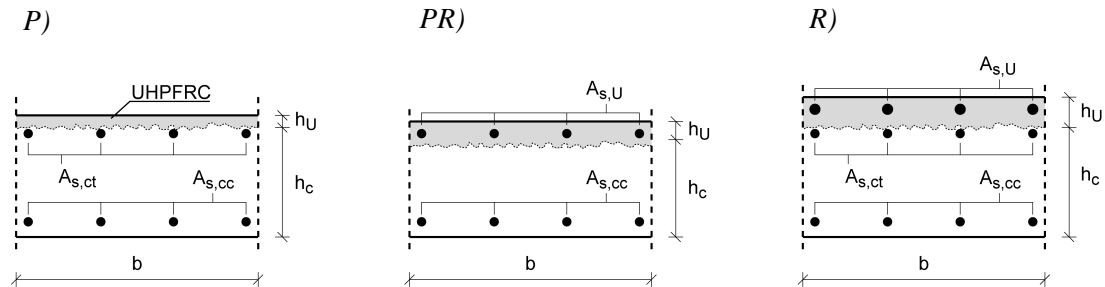


FIGURE 6.1: Investigated configurations: P) for protection function, PR) for protection and in some cases for resistance and R) for increase of resistance and protection function (in case of negative bending moment  $M$ )

- The *first configuration* (P, Figure 6.1) is a concrete section with a thin UHPFRC layer. The tensile reinforcement is situated near the interface in the concrete layer. This configuration corresponds to the beams NR of the experimental campaign. Such cross-sections are used when the deterioration of the tensile reinforcement of the existing RC structure ( $A_{s,ct}$ ) is non-existent or small and sufficient resistance is ensured. Finally, they are adapted for new constructions.
- The *second configuration* (PR, Figure 6.1) represents the case when tensile reinforcement is placed into the UHPFRC layer to replace the existing strongly deteriorated rebars. The tensile reinforcement in the concrete layer is completely laid open by a surface preparation method and the existing reinforcement or newly placed reinforcement lie in the UHPFRC layer. This configuration has the protection function as main aspect, however, it is possible to increase the ratio of the tensile reinforcement and so the resistance. It is also recommended for new constructions.
- The *third configuration* (R, Figure 6.1) is designed to increase the resistance of the structural element. The cross-section consists of a reinforced concrete section and a reinforced UHPFRC layer. This type of cross-sections is used when the principal aim is to increase the resistance of an existing structure. At the same time, the protection function of the UHPFRC is exploited.

The *interest* in the use of composite “UHPFRC-concrete” elements lies in structural elements and components that are exposed to detrimental substances, e.g. to chlorides and sea water (see exposure classes in Swisscode 2 [SIA262] and Section 6.2.3.2), and that are submitted to increased mechanical loads. The term “increased mechanical loads” is used to describe the situations when an increase in resistance without an increase in dead weight is required and at points of concentrated loads introduction. Finally, composite “UHPFRC-concrete” structures are appropriate when high energy absorption capacity is required. Consequently, these elements may be used in bridge decks, slabs in car parks and retaining walls, where de-icing agents with chlorides can cause reinforcement corrosion, or in seismic

zones. Another possible application is the use of composite “UHPFRC-concrete” elements in industrial plants that process substances that can be detrimental to concrete and its reinforcement. Finally, “UHPFRC-concrete” elements are promising in marine environment where salt water leads to chloride ingress into the concrete. In particular, the use of composite “UHPFRC-concrete” elements is appropriate for quays and other structures that are submitted to changing salt water level, e.g. due to tidal movements.

## 6.2 Verification of composite “UHPFRC-concrete” structural elements

### 6.2.1 General

The aim of this chapter is to give the *basis for the design of composite “UHPFRC-concrete” elements*. Also, the determination of UHPFRC properties is discussed in brief.

The verification of composite “UHPFRC-concrete” elements is described in this chapter. *Durability, SLS and ULS criteria* are defined. Durability verifications concentrate on the limitation of crack formation and width in order to limit the ingress of detrimental substances. SLS verifications include deformations and water tightness. At ULS, the bending verification focuses on the negative bending moment, i.e. the UHPFRC layer is in tension, but a positive bending moment verification is also proposed. A basic shear verification is proposed to avoid debonding in the interface zone.

A *high quality execution*, i.e. the processing of the composite “UHPFRC-concrete” elements by respecting the actual state of the art, is essential and a condition for validity of the proposed verification. Consequently, the discussion of partial safety factors in Section 6.2.5.3 does not consider uncertainties of the material properties due to execution not respecting certain quality management.

### 6.2.2 Material properties of UHPFRC

The material characterization of UHPFRC (see Section 3.2 and [Habel04]) suggests that the *variability of UHPFRC test results is of the same order of magnitude as for normal strength concrete*. The high amount of steel fibres in the UHPFRC reduces the probability of inhomogeneous fibre distribution. Thus, the same safety concept is proposed for UHPFRC as for normal strength concrete, i.e. the use of the lower 5%-fractile of test results as characteristic value for material properties as proposed in codes. The requirements on the homogeneity of the test results remain identical to the one of normal strength concrete, as described in codes. These requirements are based on the limited test data available for UHPFRC; they may be adapted by further test results.

However, in contrast to normal strength concrete, the *way of casting* influences the fibre orientation and the properties of UHPFRC can vary significantly according to the load direction [Wuest04]. *UHPFRC are anisotropic materials* just like as other fibre reinforced concretes. The anisotropy is depending on the way of casting and element geometry. This must be considered for the experimental determination of the UHPFRC material properties, e.g. the specimens for the uniaxial tensile tests were cast in the same way as the UHPFRC layer of the composite “UHPFRC-concrete” beams in the experimental campaign described in Chapter 3. The anisotropy of the UHPFRC may be treated in two ways: either the lowest values are taken for design, either, the stress flow in the element is known and the strengths are defined in function of the anisotropy of the material. The first choice gives conservative values that may lead to a significant underestimation of the mechanical properties. Therefore, it is proposed to consider these values only when the stress flow in the material cannot be clearly determined. When the stress flow is known, it is proposed to consider the anisotropy for the determination of the material properties.

## 6.2.3 Durability

### 6.2.3.1 General

Durability is defined based on definitions given in codes (e.g. [SIA260, Brühwiler04]): *Structures are durable when they meet the requirements of serviceability and structural safety throughout their design service life according to the planned use without unforeseen maintenance.*

Durability is characteristic for the structural member. It is the basis for design, since structural members are designed in their undamaged state. Consequently, durability has to be ensured with appropriate measures during design, construction and use of the structure. The condition has to be fulfilled that the required durability of the structure is longer than the design service life [Brühwiler04].

The aim of this study is to provide sufficient durability during design service life. Thus, all necessary measures have to be taken to limit damage in a way such that the structure fulfils the SLS and ULS criteria during the design service life. The durability verifications discussed in this chapter are permeability and limitation of crack widths. It is clear that these verifications alone do not guarantee durable structures. For example, adequate structural conception and design of construction details as well as quality control are also essential for durable structures.

### 6.2.3.2 Hazard scenarios

The permeability of UHPFRC is very low (see Sections 2.3.4.4 and 3.2.7 and [Charron04]). Thus, deterioration mechanisms that are provoked by the ingress of aggressive substances do not reduce durability in sound UHPFRC. However, these substances may reach concrete and reinforcement and provoke damage when full depth cracks exist in the UHPFRC. The durability of composite “UHPFRC-concrete” structures may be reduced in case of the following hazard scenarios:

- *Chloride ingress:* The ingress of chlorides may provoke reinforcement corrosion which reduces the resistance of the structural member. It is favoured by cracks. When there is reinforcement in the interface zone of the concrete layer, interface cracks are detrimental for the structure, since they allow the chlorides to spread over the rebar on the whole length of the interface crack. Thus, the crack widths of UHPFRC have to be verified in case of exposition classes XD2 and XD3 according to Swisscode 2 [SIA262]. The penetration of sea water into the structure is comparable to chloride ingress. Crack widths have to be verified in case of exposition class XS3 to prevent corrosion of the reinforcement [SIA262].
- *Freeze-thaw cycles:* The danger of spalling due to frost action is prevented in UHPFRC without localized macrocracks because of its low permeability. A potential danger exists when water can penetrate into macrocracks and freeze in them. Freeze-thaw cycles in interface cracks may be detrimental, since the splitting effect during freezing increases the interface crack width and its length. Thus, interface cracks have to be limited in case of exposition classes XF3 and XF4 [SIA262].
- *Carbonation:* Corrosion in cementitious materials can also be provoked by the depassivation due to carbonation and the resulting change of the pH. Exposure classes XC3 and XC4 are critical [SIA262]. However, test results show that the carbonation rate of UHPFRC is small or non-existing (see Section 2.3.4.4, [Roux96]). Thus, no explicit verification is necessary.

### 6.2.3.3 Permeability

The permeability of cementitious materials is responsible for the ingress of detrimental substances. It is determined by measurements of water capillarity [EN206] or air permeability [Torrent92]. Several classes are distinguished for permeability in relation to the exposure class. Durability is guaranteed by prescribing a combination of permeability limit and thickness of the cover concrete in relation to the exposure classes [Brühwiler04]. The permeability of UHPFRC is generally very low, thus, providing an excellent protection function against the ingress of detrimental substances and freeze-thaw cycles.

#### 6.2.3.4 Limitation of crack widths

The durability of structures is among other factors dependent on the crack width as shown in the discussion of the hazard scenarios. The limitation of crack widths is based on permeability measurements and the discussion in [Charron04] (see Section 2.3.4.4). In general, severe durability requirements are fulfilled by respecting the condition that no localized macrocracks form in the UHPFRC, i.e. that the UHPFRC deformations stay within the magnitude of hardening  $\varepsilon_{U,hard}$ . This criterion applies to the discussed hazard scenarios, and the verification is proposed in form of deformation limitation of the UHPFRC (EQ. 6.1):

$$\varepsilon_U \leq \varepsilon_{U,t,max} \quad (EQ\ 6.1)$$

The deformation of the UHPFRC  $\varepsilon_U$  is determined on the level of serviceability.

### 6.2.4 Serviceability limit state (SLS)

#### 6.2.4.1 General

Serviceability limit states are verifications that mainly ensure the “functioning of the structure or structural members under normal use” [EC01]. In particular, the verifications of functionality should be performed for stiffness in terms of deformations, vibrations and water tightness. In this study, only *stiffness* and *water tightness* are discussed; the verification of vibration is equivalent to the one of concrete structures and is not presented here.

#### 6.2.4.2 Stiffness

Sufficient stiffness which is often expressed by a *limit of deformations* is dependent on the type of structure. Indicative values of limits of deformations are given in codes. The codes distinguish between deformations due to rare, frequent and quasi-permanent actions [SIA260]. The deformations are calculated on the basis of load cases according to codes (e.g. in [SIA261]). Time-dependent deformations such as creep and shrinkage have to be considered in the determination of quasi-permanent deformations.

The determination of *time-dependent deformations* requires knowledge of early age deformations such as thermal deformations due to heat of hydration and autogenous shrinkage as well as long-term shrinkage and creep deformations. These deformations should be determined by numerical modelling, as demonstrated in Chapter 4, since they are dependent on material properties, cross-section geometry and static system. The creep kinetics decreases strongly at early age. The later the composite “UHPFRC-concrete” structure is externally loaded, the smaller are its elastic and creep deformations. It may even be appropriate to apply external loads only after 90 days when the evolution of the UHPFRC properties has virtually stopped.

The *stiffness of composite “UHPFRC-concrete” members with the UHPFRC acting as tension chord is increased* due to the increased modulus of elasticity and the outstanding tensile properties of UHPFRC when compared to normal strength concrete. No localized macrocracks form generally in typical “UHPFRC-concrete” elements under bending. The UHPFRC can be seen as continuum under service conditions, while the stiffness of reinforced normal strength concrete structures is considerably reduced due to the formation of macrocracks. Consequently, the deformations of composite “UHPFRC-concrete” members are smaller than for reinforced concrete structures for the same loading under service conditions. They may be determined with the analytical model.

The stresses in the *reinforcement* during serviceability are limited to the elastic range. Inelastic deformations lead to high deformations in the structural member and may violate SLS deformation criteria.



### 6.2.4.3 Water tightness

Water tightness is required for applications such as water reservoirs. The limit permeability has to be fixed for water tightness in terms of limit tensile deformation of UHPFRC. A lower limit of the water tightness is to limit the UHPFRC tensile deformation to the elastic domain (EQ. 6.2).

$$\varepsilon_U \leq \varepsilon_{Ut,1st} \quad (\text{EQ. 6.2})$$

Higher tensile UHPFRC deformations may be admitted when tests on the UHPFRC are conducted to determine the permeability in function of deformation as described in [Charron04]. For the UHPFRC, used in the experimental campaign, Charron defined a limit deformation of 70% of  $\varepsilon_{Ut,max}$  ( $\varepsilon = 0.15\%$ ) for water tightness for the UHPFRC used in the experimental campaign of this study (see Section 2.3.4.4). However, this limit varies for each kind of UHPFRC and has to be determined individually for each UHPFRC at the present state of knowledge.

### 6.2.5 Ultimate limit state (ULS)

#### 6.2.5.1 General

The structural element must *provide sufficient resistance with respect to the determinant hazard scenarios*. Furthermore, the *deformation capacity must be sufficient* to absorb imposed deformations and to allow stress redistribution. As the UHPFRC with or without reinforcement strengthens the tensile chord of the structural element and the compression zone remains usually unchanged, the deformation capacity is reduced for composite “UHPFRC-concrete” elements in bending when compared to the original RC element, since premature fracture of the concrete in compression may occur.

Partial safety factors are applied to verify the structural safety at ULS. Partial safety factors are used on the resistance side for material properties  $\gamma_m$  and model uncertainties  $\gamma_R$ . The partial safety factors on the action side are independent on the used material and are not discussed any further.

#### 6.2.5.2 Failure modes

Composite “UHPFRC-concrete” beams have different possible failure modes in bending, illustrated in Figure 6.2.

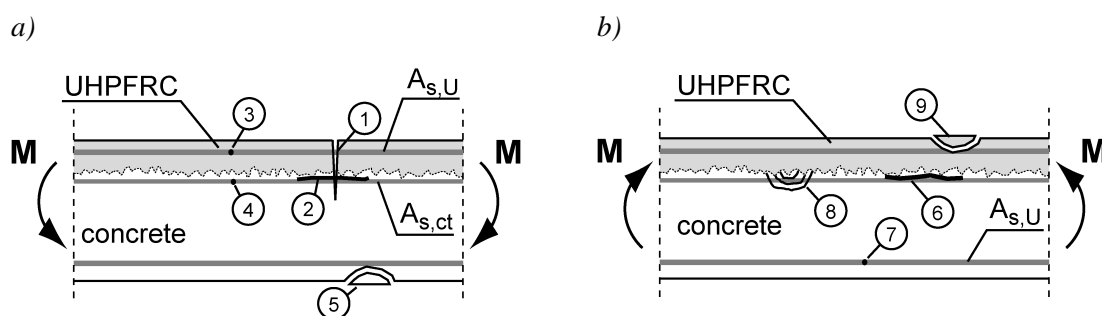


FIGURE 6.2: Failure modes of composite “UHPFRC-concrete” beams for a) a negative, b) a positive bending moment

**Negative bending moment.** Five failure modes are distinguished for the negative bending moment (Figure 6.2a):

1. *Fracture of the entire UHPFRC layer.* (formation of a localized macrocrack)
2. *Debonding at the interface.* (loss of the monolithic behaviour)
3. *Fracture of the reinforcement  $A_{s,U}$ .*
4. *Fracture of the reinforcement  $A_{s,ct}$ .*

### 5. Fracture of concrete in compression.

Fracture of concrete in compression (5) leads to brittle fracture of the element and should not become the determinant failure mode. Debonding (2) should also be avoided, since monolithic behaviour is important for the structural behaviour of the composite element. Thus, composite elements should be designed in a way that either the fracture of the UHPFRC layer (1) or fracture of tensile reinforcement ((3) or (4)) become decisive.

Several strategies may be applied to determine the *design failure mode*. In case of composite elements with reinforcement in the UHPFRC layer (configurations PR and R), either fracture of the UHPFRC layer (1) or fracture of the reinforcement in the UHPFRC layer (3) is determinant, depending on the reinforcement type and the UHPFRC. In case of composite elements without reinforcement in the UHPFRC layer (configuration P), either failure mode (1) or (4) become determinant. If the UHPFRC layer is considered for design, the failure mode depends on the geometry of the element and on reinforcement and UHPFRC properties. If failure mode (4) becomes determinant, the debonding risk (2) is high.

**Positive bending moment.** Four failure modes are distinguished for the positive bending moment (Figure 6.2a):

6. *Debonding at the interface.* (loss of the monolithic behaviour)
7. *Fracture of the reinforcement*  $A_{s,cc}$ .
8. *Fracture of concrete in compression.*
9. *Fracture of UHPFRC in compression.*

The design failure mode for the positive bending moment should be fracture of the reinforcement  $A_{s,cc}$  (7). Fracture of concrete and UHPFRC in compression ((8), (9)) should be avoided, since they provoke brittle fracture of the element. Monolithic behaviour is lost when debonding (6) occurs. Consequently, this failure mode should not become determinant either.

#### 6.2.5.3 Discussion of partial safety factors

The design of composite “UHPFRC-concrete” elements requires consideration of partial safety factors for the material “UHPFRC” and for the modelling of structures with UHPFRC.

**Factor  $\gamma_M$ .** The partial safety factor  $\gamma_M = \gamma_m \cdot \gamma_R$  unites the partial safety factors of material and modelling. It represents the partial safety factor of the resistance side of the verification. Codes define the partial safety factor for concrete to  $\gamma_c = 1.5$  [SIA260].

**Factor  $\gamma_m$ .** The partial safety factor of the material considers the variability of the material on condition that good execution is ensured. It does not consider the variability due mediocre processing of the structural member. As the variability of UHPFRC is comparable to the one of normal strength concrete, the partial safety factors  $\gamma_m$  that are defined for normal strength concrete can be applied to UHPFRC when appropriate test methods to determine the UHPFRC are used (see Section 6.2.2).

**Factor  $\gamma_R$ .** Modelling of composite “UHPFRC-concrete” elements in bending is comparable to the modelling of RC elements. The discussion of the analytical model in Chapter 5 has shown that the reference length is of great importance. This reference length is better known for RC than for UHPFRC. Therefore, the uncertainties of modelling are higher for “UHPFRC-concrete” sections. It is impossible to determine the impact of the model uncertainty on the safety factor at the present state of knowledge. Consequently, it is proposed to be conservative in the determination of the reference length  $L_R$  and to keep the same partial safety factor for model uncertainties.

**Factor  $\gamma_U$ .** On the basis of the discussion, a partial safety factor for UHPFRC of  $\gamma_U = 1.5$  is proposed. An extensive material characterization of UHPFRC is necessary to verify the hypothesis of the partial safety factor.

### 6.2.5.4 Verification of the negative bending moment

**Concept.** A *verification in two steps* is proposed for the verification of the negative bending moment. In a first time, a *simplified moment verification* gives a conservative estimation of the bending moment. This verification is easy to conduct. If the simplified verification is not fulfilled, a detailed verification is proposed that allows an exacter determination of the negative bending moment. The *detailed verification* may be used for example in case of heavily loaded bridge decks, where limiting factors demand an optimum use of materials.

**Detailed moment verification.** This bending moment verification demands detailed knowledge of the required deformation capacity. The required deformation capacity of a structural element is dependent on the static system and the chosen analysis method.

The *resistance* and the *available rotation capacity* are determined by moment-rotation ( $M-\theta$ ) curve which are deduced either in an experimental campaign or analytically by knowing the reference length  $L_R$  and the length of plastic hinges  $L_{hi}$ . When the values are determined experimentally, the characteristic moment-rotation curve has to be determined by considering the variability of the test results and specific factors inherent to the test method. When the  $M-\theta$  curve is determined analytically, a moment-curvature ( $M-\kappa$ ) curve can be transferred into a moment-rotation curve by distributing the curvature in the crack over the plastic hinges and assuming a linear curvature distribution in the other zones of the structural element as shown in Figure 5.5 in Section 5.1.4.1.

The *required rotation capacity* is dependent on the static system. Statically determinate systems are designed with the maximum moment  $M_{max}$  (Figure 6.3a). Different analysis methods may be used for the design of statically indeterminate beams: In case of linear analysis, the required rotation capacity remains small and the structure is designed for the maximum moment. In case of linear analysis with limited redistribution or plastic analysis, the required rotation capacity must be determined and the characteristic moment is determined after Figure 6.3: If the required rotation  $\theta_{req}$  is smaller than the rotation at the maximum moment, the characteristic moment is equal to the maximum moment. If the required rotation  $\theta_{req}$  is larger than the rotation at the maximum moment, the characteristic moment is the moment corresponding to  $\theta_{req}$ .

The design moment is determined with EQ. 6.3.

$$M_{Rd} = \frac{M_k}{\gamma_U} \quad (EQ\ 6.3)$$

with  $M_{Rd}$  [kNm]: design value for the ultimate moment,  $M_k$  [kNm]: characteristic value for the ultimate moment,  $\gamma_U$  [-]: partial safety factor for UHPFRC.

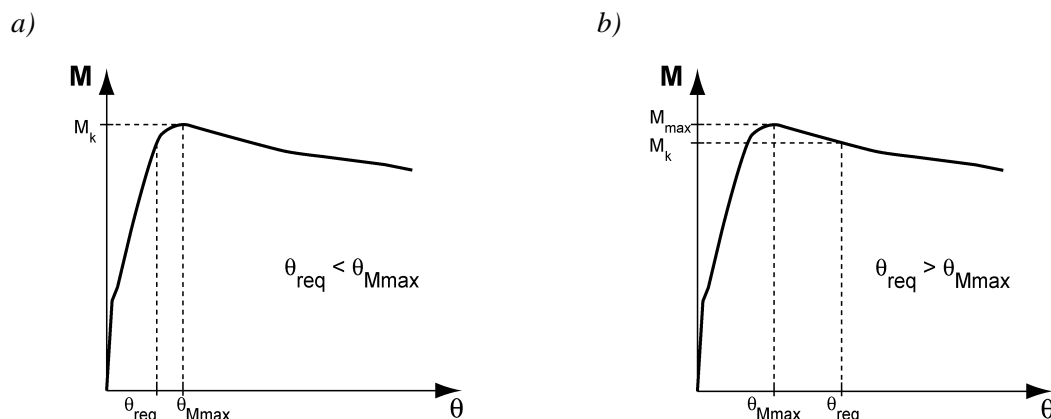


FIGURE 6.3: Definition of the characteristic moment in function of the rotation capacity

The detailed moment verification demands several parameters that are difficult to determine such as the reference length, length, number and position of plastic hinges and the required rotation capacity. Consequently, the effort of the detailed moment verification is high.

**Simplified moment verification.** The simplified verification is similar to the bending verification for RC structures, since it neglects the UHPFRC tensile strength. For configurations P and PR, the design corresponds exactly to bending verifications after codes, for configuration R, the two layers of tensile reinforcement have to be considered (Figure 6.4). The design ultimate moment is determined with EQ. 6.3. The concrete compression zone may be simplified, as indicated in codes, e.g. Swisscode 2 proposes a parabola-rectangle or a rectangle diagram [SIA262].

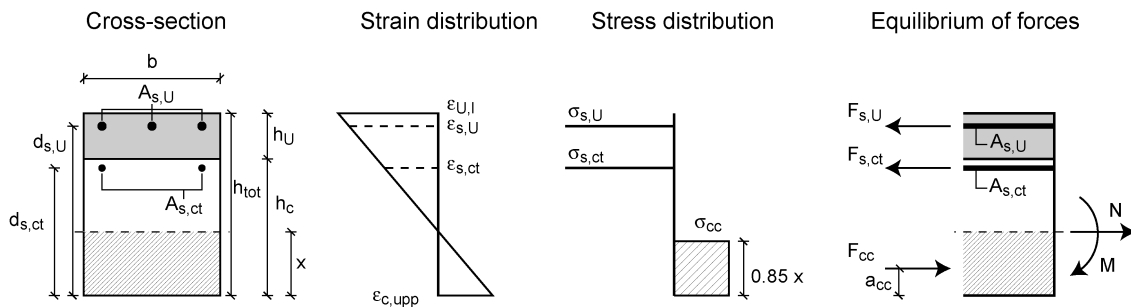


FIGURE 6.4: Simplified verification of the negative bending moment

The deformation capacity has to be verified. Swisscode 2 proposes a criterion based on the depth of the compression zone. If EQ. 6.4 is fulfilled, the rotation capacity is verified, if EQ. 6.5 applies, the rotation capacity has to be verified.

$$\frac{x}{d} \leq 0.35 \quad (\text{EQ 6.4})$$

$$0.35 < \frac{x}{d} \leq 0.5 \quad (\text{EQ 6.5})$$

### 6.2.5.5 Verification of the positive bending moment

The positive bending moment is determined with the material laws described in Section 5.1.3.1 (Figure 6.5). The deformation capacity is estimated in analogy to the negative bending moment on a  $M-\theta$ -curve.

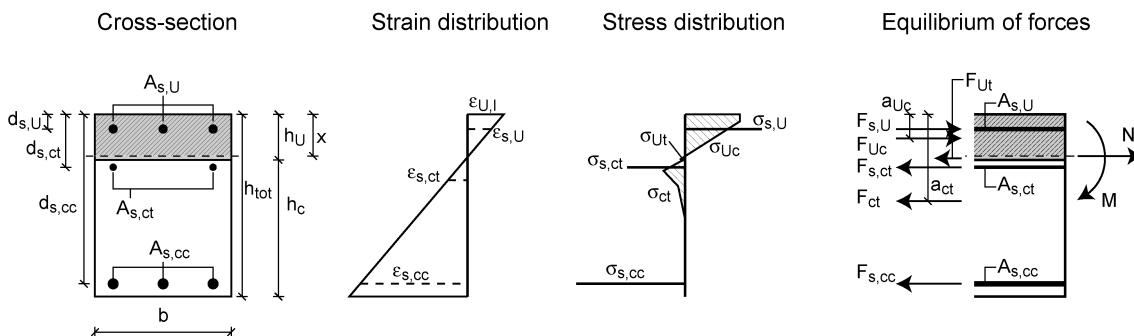


FIGURE 6.5: Detailed verification of the positive bending moment

The moment may also be determined in a simplified way by considering only the reinforcement  $A_{s,cc}$  and the UHPFRC in compression as shown in Figure 6.6. This verification gives a good estimation of the moment at yielding of the reinforcement. However, hardening due to the reinforcement  $A_{s,ct}$  is not considered. It must be verified that the compression zone is entirely in the UHPFRC layer. If this is not the case, the concrete in compression must be included. Sufficient deformation capacity is verified with the depth of the compression zone after Swisscode 2 (EQ. 6.4, EQ. 6.5).

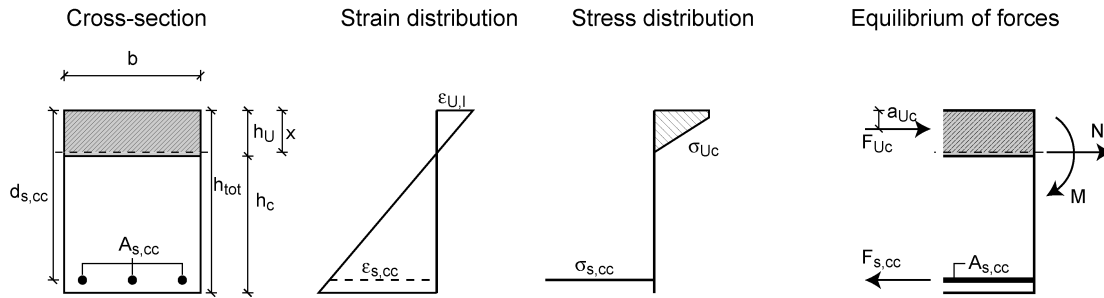


FIGURE 6.6: Simplified verification of the positive bending moment

### 6.2.5.6 Shear

Reflections about shear stresses and possible verifications are made in this chapter. The reflections are only qualitative and do not lead to an explicit shear verification. At present, there is not enough experimental, analytical and numerical evidence to propose a shear verification.

Shear stresses have to be verified for composite “UHPFRC-concrete” beams to avoid debonding in the interface zone. The shear stresses at the interface are difficult to determine, since the composite “UHPFRC-concrete” systems has a complicated geometry and as the material laws are non-linear.

The shear stresses may be calculated in the *elastic state* with EQ. 6.6 by considering the difference in stiffness between the UHPFRC and the concrete layer. However, this calculation is simplified and does not represent the real stress state. Moreover, it does not consider stress deviations due to localized macrocracks. The shear stresses may also be estimated by the means of stress fields as presented for example in [Brenni95] or by FE-simulations.

$$\tau = \frac{Q \cdot S_{eq}}{I_{eq} \cdot b} \quad (EQ 6.6)$$

with  $\tau$  [MPa]: shear stress,  $Q$  [N]: shear force,  $S_{eq}$  [mm<sup>3</sup>]: equivalent section modulus,  $I_{eq}$  [mm<sup>4</sup>]: equivalent moment of inertia,  $b$  [mm]: width.

The determination of the stress state in the interface zone and the risk of debonding when *localized macrocracks reach the interface* is not trivial, since it depends on the static system and geometric and material parameters. It may be determined with numerical FE-simulations. The experimental campaign shows that debonding is critical for the *beams without reinforcement in the UHPFRC layer* when the contribution of the UHPFRC layer is considered (see Section 5.2). If the debonding risk cannot be calculated, it is proposed to neglect the UHPFRC layer for the determination of bending moment and shear stresses. Few interface cracks occur in the *beams with reinforcement in the UHPFRC layer* and do not alter their structural response. Thus, when beams with a similar configuration are used, the probability of debonding in the interface zone due to localized macrocracks that reach the interface is small and may not be verified.

## 6.2.6 Example

### 6.2.6.1 Description

**General.** The structural response of composite “UHPFRC-concrete” beams in a statically indeterminate system is illustrated by means of an example. The example focuses on the resistance to bending. The influence of softening behaviour and reduced deformation capacity of the negative bending resistance on the system response is discussed in order to determine an appropriate design method. The case of an increased deformation capacity of the negative bending moment is investigated in addition. Finally, the detailed determination is compared to the simplified method which is based on the theories of elasticity and plasticity.

**System and input parameters.** The statically indeterminate system of the example is commonly used to illustrate the theory of plasticity [Muttoni97]. It consists of a vertically supported two span beam that is modelled by a single span beam built-in at one end and supported vertically at the other end (Figure 6.7a). The beam is loaded with two concentrated forces in the third points of the span. In the linear-elastic case, the minimum moment forms at the built-in support at point A and the maximum moment at point C.

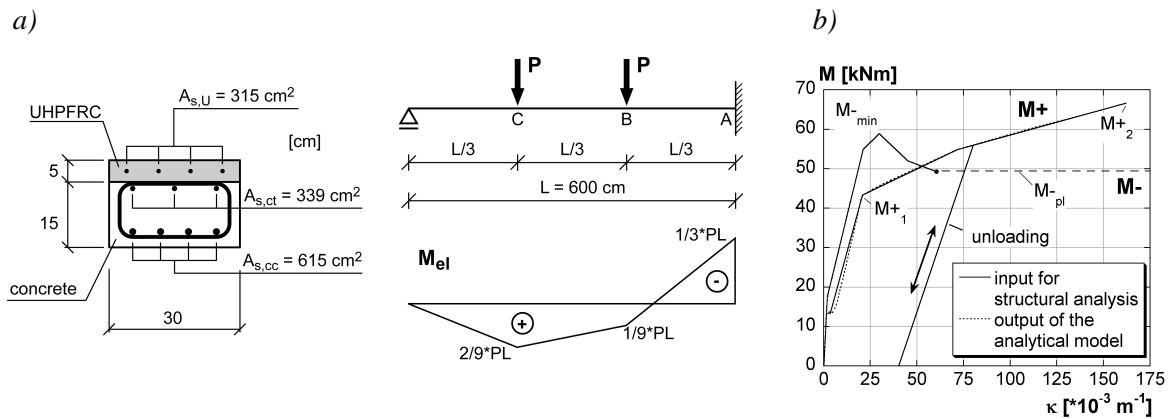


FIGURE 6.7: Input data for the example: a) system, b)  $M$ - $\kappa$ -curves for positive and negative bending resistance ( $M+$  and  $M-$  respectively)

The cross-section is a reinforced composite “UHPFRC-concrete” section, similar to section R5 of the experimental campaign under a negative bending moment (see Section 3.4.1). However, the lower reinforcement  $A_{s,cc}$  is reduced to  $615 \text{ cm}^2$  ( $\rho_{s,cc} = 1.2\%$ ) (Figure 6.7a). The material properties of the example are identical to the ones of the experimental campaign and can be found in Appendix E.1. The hypotheses described in Section 5.1.2 are also valid for the present example.

The  $M$ - $\kappa$ -curves for the negative and the positive bending resistance are determined by using the analytical model from Chapter 5 and shown in Figure 6.7b. Final failure is always due to fracture of the concrete in compression at  $-3.5\%$  because the strain at rebar fracture is assumed to the high value of  $\epsilon_{Uk} = 10\%$ ; the strain in the tensile reinforcement at concrete fracture in compression is  $\epsilon_s = 2.3\%$  for the positive bending resistance and  $\epsilon_s = 0.8\%$  for the negative bending resistance.

The positive bending resistance ( $M+$ ) increases monotonously. Two criteria are defined for the positive bending resistance: the point of yielding of the reinforcement  $A_{s,cc}$  at  $M_{+1} = 43 \text{ kNm}$  at a curvature  $\kappa_{+,2} = 21 \cdot 10^{-3} \text{ m}^{-1}$  and the point of fracture of the concrete in compression  $M_{+2} = 66 \text{ kNm}$  at a curvature  $\kappa_{+,2} = 160 \cdot 10^{-3} \text{ m}^{-1}$ .

The negative bending resistance ( $M-$ ) has a higher stiffness than the positive bending resistance until the minimum moment  $M_{-min} = -59 \text{ kN}$  at a curvature  $\kappa_{-,min} = 30 \cdot 10^{-3} \text{ m}^{-1}$ . Then, softening occurs in  $M-$  until the fracture of concrete in compression at a resistance of  $M_{-pl} = -50 \text{ kNm}$  and  $\kappa_{-,min} = 60 \cdot 10^{-3} \text{ m}^{-1}$ . This softening behaviour is significantly influenced by the reference length as discussed in Chapter 5.

The reference length is fixed to  $L_R = 700$  mm for this example. The case of an increased deformation capacity of the negative bending resistance is investigated assuming a constant negative bending resistance, i.e. ideal plastic behaviour, for curvatures  $\kappa \geq 60 \cdot 10^{-3} \text{ m}^{-1}$ .

The unloading path for both bending resistances is assumed with an unloading factor of 0.5, i.e. the curvature at completely unloaded state is 0.5 times the curvature of before unloading.

**Solution procedure for the detailed determination.** In this example, force  $P$  and curvature  $\kappa$ , rotation  $\theta$  and deflection distributions are determined by iteration and by increasing the force by increments  $\Delta P$ : The equilibrium of energy (virtual work) over the beam length is determined for the force  $P$  on the basis of the  $M$ - $\kappa$ -curves and the resulting variation of stiffness ( $EI$ ). For this, the beam is divided into several elements<sup>9</sup>.

In a first model, the calculations are stopped when the limit curvature of the negative bending resistance is reached in point A, i.e. at  $\kappa_{\min} = 60 \cdot 10^{-3} \text{ m}^{-1}$ . In a second model, the influence of the increased deformation capacity of the negative bending resistance is investigated (dotted line in Figure 6.7b).

### 6.2.6.2 Results and discussion

**Model one: initial negative bending resistance.** In this paragraph, the structural response of the composite beam is discussed for the given static system until the criterion for failure in compression is reached at  $\kappa_{\min} = 60 \cdot 10^{-3} \text{ m}^{-1}$ . Figure 6.8 shows the relationships between bending moments  $M_A$ ,  $M_B$  and  $M_C$ , force  $P$  and maximum deflection ( $w$ ) over the beam. Figure 6.9 shows curvature ( $\kappa$ ), rotation ( $\theta$ ) and deflection distributions over the length of the beam for different forces  $P$ . The maximum force  $P_{el} = 28$  kN is reached when the negative moment in point A is equal to the minimum negative bending resistance  $M_{\min} = -59$  kNm. This occurs at a maximum deflection of  $w = 3.6$  cm, corresponding to  $l/170$  (Figure 6.8a). The positive moments remain smaller than the first criterion for the positive bending resistance  $M_{+1} = 43$  kNm.

The negative bending resistance decreases for increasing curvature, i.e. softening occurs in point A, and a hinge forms (Figure 6.9a). In this example, the  $M$ - $\kappa$ -curve of the negative bending resistance is followed until the curvature  $\kappa_{\min} = 60 \cdot 10^{-3} \text{ m}^{-1}$  is reached. For this curvature, the force decreases to  $P_{\min} = 23$  kN and  $w = 2.9$  cm.

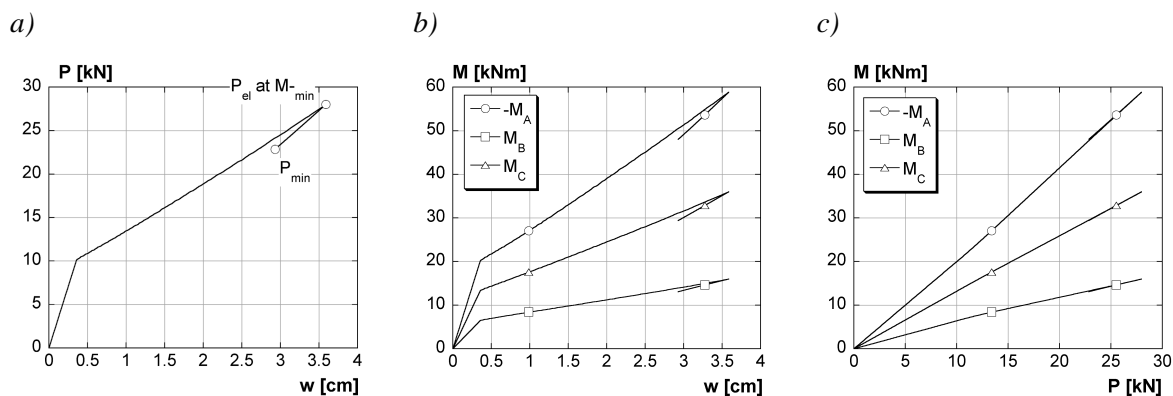


FIGURE 6.8: Results of the example (until fracture at point A when the negative bending resistance reaches its deformation limit of  $\kappa_{pl} = 60 \cdot 10^{-3} \text{ m}^{-1}$ ): a)  $P$ - $w$  curve, b)  $M$ - $w$  curves, c)  $M$ - $P$ -curves ( $w$ : deflection)

At the maximum force of  $P_{el} = 28$  kN, maximum values are reached for all moments ( $M_A$ ,  $M_B$ ,  $M_C$ ) and deflection. For higher curvatures in point A, curvature and rotation increase in the element at point A and decrease in the rest of the beam, leading to a decrease of force  $P$  and deflection. Thus, fracture would occur at the maximum force  $P_{el} = 28$  kN and the maximum deflection of 3.6 cm for imposed

9. here 100 elements are chosen, however, also the calculation with 15 elements gives comparable results.

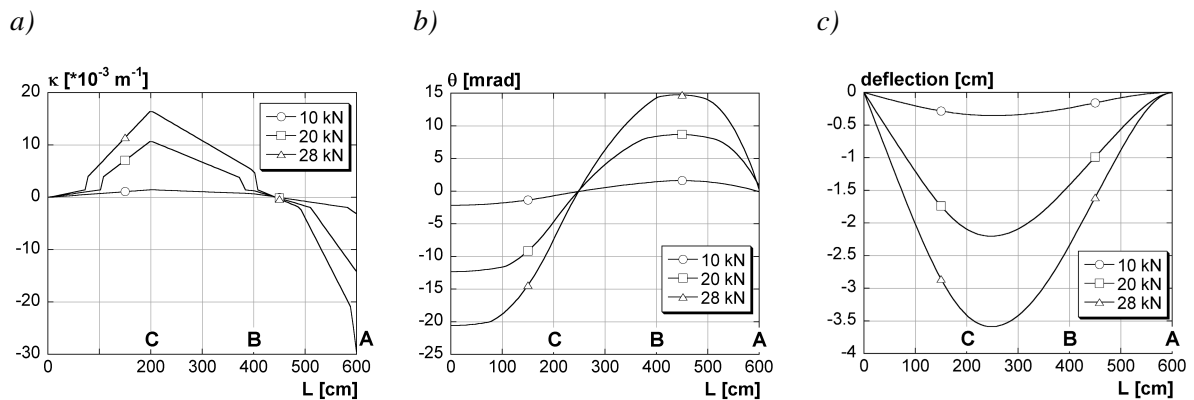


FIGURE 6.9: a) Curvature, b) rotation and c) deflection of the beam at different forces  $P$  before the maximum moment  $M_{-max}$  is reached in point A

loading and imposed deformations (in points B and C) respectively. This also means that the softening behaviour of the negative bending resistance could not be exploited.

**Second model: negative bending resistance with increased deformation capacity.** In the second model, the deformation capacity of the negative bending resistance is assumed to increase at a constant resistance ( $M_- = -50$  kNm) for curvatures  $\kappa \geq 60 \cdot 10^{-3} \text{ m}^{-1}$ . Such an increase in the deformation capacity may be obtained by strengthening of the compression zone in point A, for example by adding an UHPFRC layer to the compression zone and thus creating a sandwich element. In this way, early failure of the cross-section in compression can be prevented. The assumed constant negative bending resistance corresponds to the formation of an ideal plastic hinge in point A.

Figure 6.10 shows that an increased deformation capacity of the negative bending resistance leads to a higher ultimate load of the system (Figure 6.10b). Beyond  $P_{min}$ , the force  $P$  increases monotonously until the fracture criterion in point C are reached (Figure 6.10a). Simultaneously, the stiffness of the beam decreases. The force amounts to  $P_{+,1} = 30$  kN and  $P_{+,2} = 41.8$  kN for the first ( $M_{+,1} = 43$  kNm) and the second criterion ( $M_{+,2} = 66$  kNm) respectively. The force  $P_{+,1}$  is only 2 kN higher than the force  $P_{el} = 28$  kN determined with the first model. The maximum force  $P_{+,2}$  is 50% higher when compared to  $P_{el}$  and the deflection is with  $w_{+,2} = 33$  cm ( $l/20$ ) approximately 10 times higher than at  $P_{el}$ .

When the plastic moment is reached in point A, the static system changes due to the plastic hinge to a statically determinate system. This is expressed by a change in the slope of the  $M$ - $P$ -curves in Figure 6.10c: The negative moment in point A ( $M_A$ ) remains constant, while the slope of the positive moments in points B and C ( $M_B$  and  $M_C$ ) is increased after the formation of a plastic hinge.

The moment distribution is shown in Figure 6.10d for a force of  $P_{min} = 23$  kN, i.e. at a curvature of  $\kappa_{,pl} = 60 \cdot 10^{-3} \text{ m}^{-1}$  in point A, and at the maximum force  $P_{+,2} = 41.8$  kN, i.e. when the limit curvature of  $\kappa_{+,2} = 160 \cdot 10^{-3} \text{ m}^{-1}$  in point C is reached. The evolution of the moments shows that the positive moments increase with increasing force  $P$ , while the negative moment remains constant in point A. At  $P_{min} = 23$  kN, the moment distribution still corresponds to the linear-elastic distribution as shown in Figure 6.7b, whereas the influence of the plastic hinge in point A leads to increased positive moments for  $P_{+,2} = 41.8$  kN.

Figure 6.11 shows the evolution of curvature ( $\kappa$ ), rotation ( $\theta$ ) and deflection over the length of the beam after the formation of the plastic hinge in point A (i.e.  $P \geq 23$  kN). Curvature, rotation and deflection are very high for forces  $P \geq 30$  kN which indicates important deformations of the beam.

It must be stated that this calculation does not entirely correspond to reality, since the assumption of ideal plastic behaviour in point A for  $\kappa \geq 60 \cdot 10^{-3} \text{ m}^{-1}$  leads to the hypothesis of the possibility of infinite rotations in point A and to very high deformations over the beam. However, no construction material behaves in an ideal plastic way and deformations in a real structure are limited by the fracture of the cross-section.



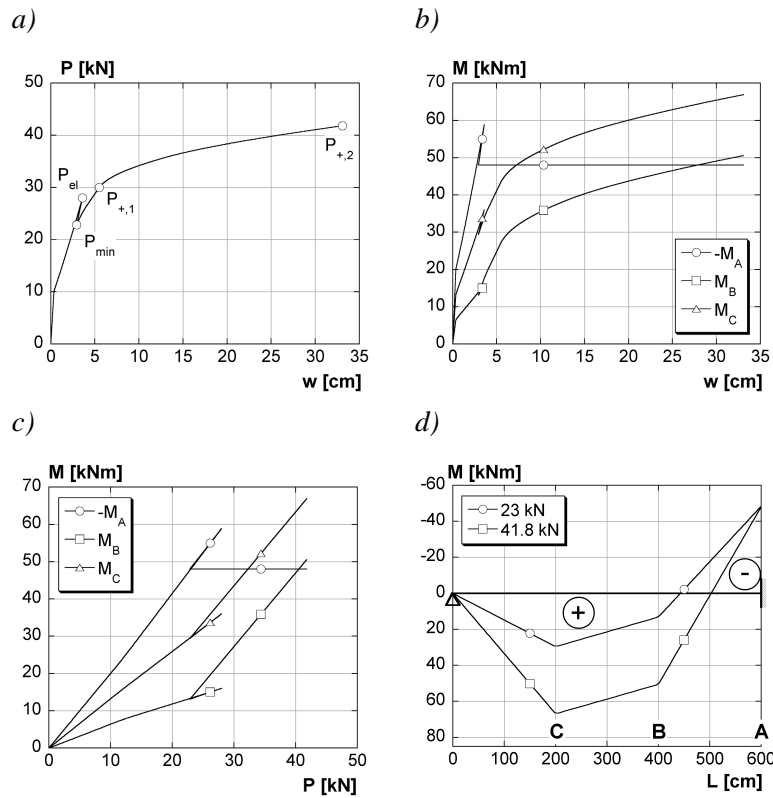


FIGURE 6.10: Results for an increased deformation capacity of the negative bending resistance: a)  $P$ - $w$  curve, b)  $M$ - $w$  curve, c)  $M$ - $P$ -curve, d) moment distribution over the beam ( $w$ : deflection)

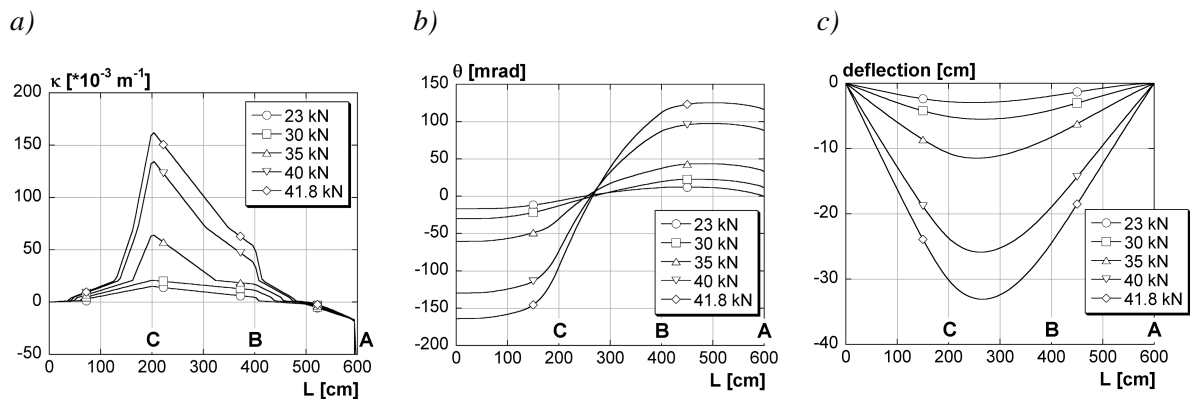


FIGURE 6.11: a) Curvature, b) rotation and c) deflection of the beam at different forces  $P$  when a plastic hinge has formed in point A

**Comparison with simplified calculation.** The ultimate load of the system may also be calculated in a simplified way by the theories of elasticity and plasticity, i.e. the ultimate load is determined by assuming constant stiffness ( $EI$ ) over the beam and by assuming linear-elastic and ideal plastic material behaviour. The investigated static systems are described in Figure 6.12.

The lower limit of the maximum force  $P$  is determined with the theory of elasticity. It occurs when the bending resistance is reached in one section of the system: In the given system (Figure 6.12), the bending resistance is first reached in point A at a force of  $P_{el} = (3 \cdot M_{-max})/L = (3 \cdot 59)/6 = 29.5$  kN, compared to a force  $P_{el} = 28$  kN in the detailed calculation (see first model). The maximum positive moment occurs in point C with  $M_C = 2/9 \cdot P_{el} \cdot L = 2/9 \cdot 28 \cdot 6 = 37.3$  kN. It is smaller than the positive bending resistance at yielding of the reinforcement  $A_{s,cc}$ , called  $M_{+1}$ .

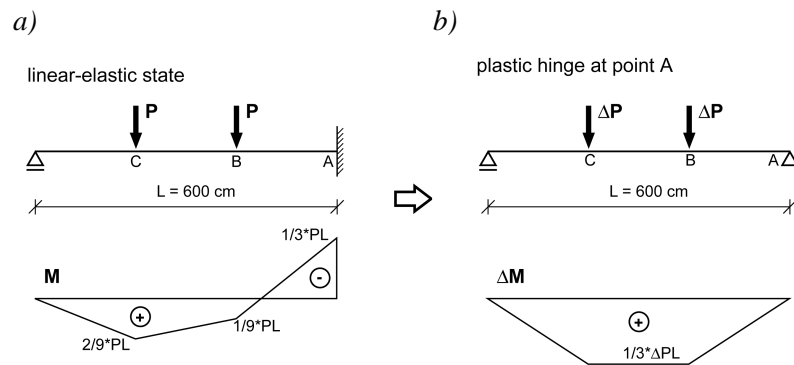


FIGURE 6.12: Static systems for simplified calculation: a) linear-elastic state, b) statically determinate system after the formation of a plastic hinge in point A

$P_{\min}$  occurs at a negative bending moment in point A at  $M_A = -48$  kNm. It is determined to  $P_{\min} = 24$  kN and to 23 kN by the simplified (Figure 6.12a) and the detailed models respectively. The positive moment is  $M_C = 32$  kN at  $P_{\min}$ .

At  $P_{\min}$ , a plastic hinge is assumed in point A and the system changes to a statically determinate system as presented in Figure 6.12b. The force  $P$  can be increased until positive bending resistance is reached in point C:

- The positive bending resistance  $M_{+1} = 43$  kNm is attained at a force  $P_{+,1} = P_{\min} + \Delta P = 29.5$  kN (with  $\Delta P = (3 \cdot (M_{+1} - M_{C,\min})) / L = (3 \cdot (43 - 32)) / 6 = 5.5$  kN and  $P_{\min} = 24$  kN).  $P_{+,1}$  is determined to 30 kN with the detailed calculation. Thus, the force  $P_{+,1}$  is approximately equal to the force  $P_{el}$  which is the maximum force from the elastic calculation.
- The positive bending resistance  $M_{+2} = 66$  kNm is attained at a force  $P_{+,2} = 41$  kN which corresponds well to the value of 41.4 kN calculated by the detailed method.

The results show that the ultimate load  $P$  can be determined reliably with the theories of elasticity and plasticity.

### 6.2.6.3 Conclusion

For the given configuration, static system and material properties, the following results are obtained:

- In the first model, the deformation capacity of the negative bending resistance is limited to  $\kappa_{\min} = 60 \cdot 10^{-3} \text{ m}^{-1}$ . The results show that the ultimate load  $P$  is limited by the negative bending resistance in point A. The deformation capacity of the negative bending resistance in the softening part cannot be exploited, since beam deflections and force  $P$  decrease both during softening for the given system and the beam would fail under imposed loads and deformations.
- In the second model, the deformation capacity of the negative bending resistance is increased by assuming ideal plastic behaviour of the negative bending resistance in point A, and a mechanism can form with plastic hinges in points A and C. As a consequence, the ultimate load is significantly increased (by 50%) when the positive bending resistance ( $M_{+2}$ ) is reached. However, the assumption of an ideal plastic hinge in point A does not correspond to reality and the rotation capacity in the structure must be verified.
- The comparison of the detailed models with analyses based on the theory of elasticity and plasticity shows that these simple methods are appropriate for the determination of the ultimate load.

## 6.3 Parametric study

### 6.3.1 Scope

A parametric study is conducted with the analytical model for the negative bending moment (see Section 5.1) in order to investigate the influence of geometric parameters and to define requirements on the used materials in order to determine composite elements that exploit efficiently the used materials. Slender composite “UHPFRC-concrete” bending elements are investigated. More specifically, the study shall answer the following questions for the three configurations defined in Figure 6.1:

- What geometry is efficient and what reinforcement ratio in the UHPFRC layer is necessary?
- How do the tensile properties of the UHPFRC influence the structural response?
- What type of reinforcement interacts best with the UHPFRC?
- What is the influence of the concrete strength in compression on the structural response?

Only the negative bending moment, i.e. the UHPFRC layer as top layer of the composite beam in tension, is examined in the parametric study. This bending moment is determinant, since cracking in the UHPFRC layer influences SLS, ULS and durability. Under positive bending, the UHPFRC with its high compressive strength increases slightly the ultimate moment. However, no change in permeability is expected, for the UHPFRC is in compression and no cracks form.

The results of the parametric study are discussed for configuration R (Figure 6.1), since this configuration is designed for protection and strengthening and covers the widest range of applications. The results apply also to cross-sections P and PR. When differences in the results are observed for the other configurations, the differences are explicitly discussed.

### 6.3.2 Basic parameters

The chosen basic parameters of the material behaviour are representative for reinforcement steel B500 [SIA262], normal strength concrete and UHPFRC. The geometric parameters approach typical bridge decks as described in [Broquet99].

The *basic parameters* of the reference case are:

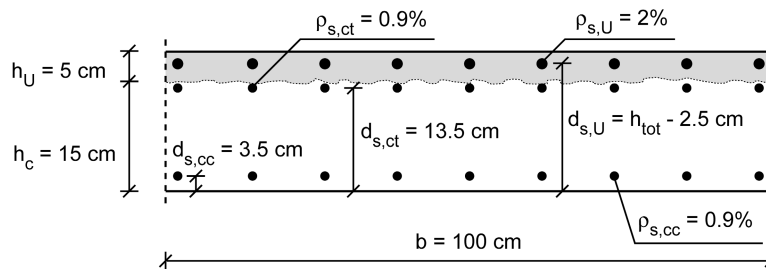


FIGURE 6.13: Basic structural parameters

- the *cross-section geometry* of the structural element (Figure 6.13):
  - $b = 100$  cm,
  - $h_U = 5$  cm,
  - $h_c = 15$  cm,
- the *reinforcement ratio* (Figure 6.13):
  - $\rho_{s,U} = 2\%$  of  $A_U = b \cdot h_U$ ,
  - $\rho_{s,ct} = 0.9\%$  of  $A_c$  with  $A_c = b \cdot d_{s,ct}$ ,
  - $\rho_{s,cc} = 0.9\%$  of  $A_c$  with  $A_c = b \cdot d_{s,cc}$ ,
- the *position of the reinforcement* (Figure 6.13):
  - $d_{s,cc} = 3.5$  cm,

$$d_{s,ct} = 13.5 \text{ cm},$$

$$d_{s,U} = h_{tot} - 2.5 \text{ cm},$$

- *material properties of the UHPFRC* (see Figure 5.1):

$$E_U = 50 \text{ GPa},$$

$$f_{U,c} = 150 \text{ MPa},$$

$$f_{U_t,1st} = 6 \text{ MPa},$$

$$f_{U_t,max} = 8 \text{ MPa},$$

$$\varepsilon_{U_t,max} = 1 \text{ ‰ for configurations without } A_{s,U} \text{ (P) and for } \varepsilon_{U_t,max} = 2 \text{ ‰ for sections with } A_{s,U} \text{ (PR, R)}^{10},$$

$$\sigma_1 = 2.5 \text{ MPa},$$

$$w_{U_t,1} = 2 \text{ mm},$$

$$w_{U_t,2} = 6.5 \text{ mm},$$

$$L_R = 400 \text{ mm}^{11},$$

- *material properties of the concrete* (see Figure 5.2):

$$E_{cc} = E_{ct} = 35 \text{ GPa},$$

$$f_{cc} = 40 \text{ MPa},$$

$$f_{ct} = 3 \text{ MPa},$$

$$n = 0.33,$$

$$w_{ct1} = 0.03 \text{ mm},$$

$$w_{ct2} = 0.2 \text{ mm},$$

$$\text{corresponding to } G_F = 145 \text{ J/m}^2$$

- *material properties of the reinforcement* (see Figure 5.3):

$$E_s = 205 \text{ GPa},$$

$$f_{sy} = 500 \text{ MPa},$$

$$f_{su} = 550 \text{ MPa},$$

$$\varepsilon_{su} = 10\%,$$

- the *normal force* on the section:  $N = 0 \text{ kN}$ .

### 6.3.3 Curve description

The  $M$ - $\kappa$ -curves of a composite “UHPFRC-concrete” section resulting from the basic values, a composite “RC-concrete” section and a reinforced concrete (RC) section are shown in Figure 6.14. The composite “UHPFRC-concrete” section corresponds to configuration R. The composite “RC-concrete” section is identical to configuration R, but it consists of two layers of normal strength concrete. The “RC-concrete” section is used to investigate the effect of the use of UHPFRC instead of normal strength concrete. The RC section represents the cross-section before the application of an UHPFRC layer and is used to analyse the increase in stiffness and resistance of composite “UHPFRC-concrete” sections.

The  $M$ - $\kappa$ -curve of the composite “UHPFRC-concrete” element is traced with a dotted line after the formation of localized macrocracks because the appearance of the curve depends strongly on the hypothesis of the reference length  $L_R$ , which is not well known for UHPFRC (see Section 5.3). Consequently, this part of the curve represents an estimation. Since the reference length can be more or less accurately determined for concrete [Schläfli99], the curve of the concrete section is traced as solid line even after the formation localized cracks.

10. The differentiation between the configurations with reinforcement in the UHPFRC layer and without reinforcement in the UHPFRC layer is made to consider the influence of reinforcement in the UHPFRC on crack formation, as reinforcement in the UHPFRC layer increases the magnitude of hardening  $\varepsilon_{U,hard}$ .

11. The chosen reference length is smaller than the reference lengths determined for the beams in 4-point-bending in Chapter 5 and may overestimate the moment after the formation of localized macrocracks. The reference length is discussed in Chapter 5 and is not discussed any further in this section.

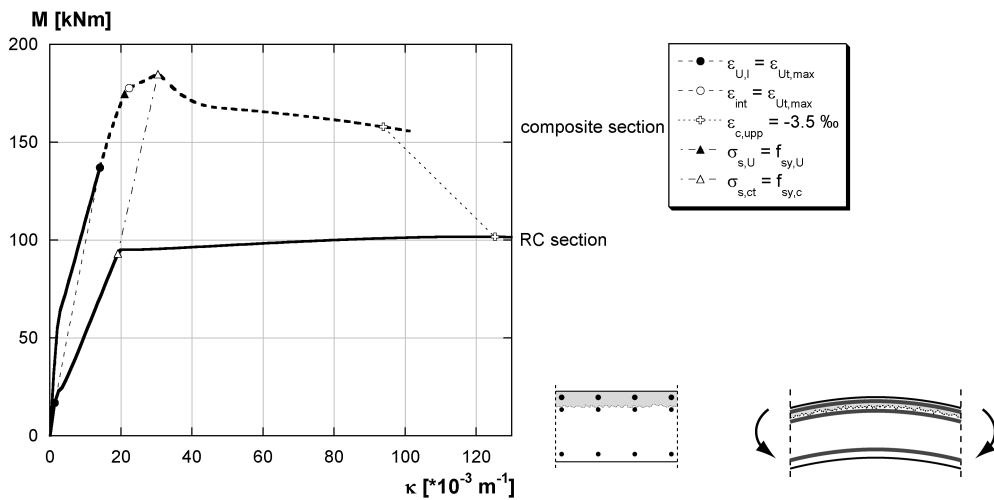


FIGURE 6.14:  $M$ - $\kappa$ -curves for the basic values of the parametric study and for the concrete section

Several stages can be distinguished on the curves in Figure 6.14:

- i. A *localized macrocrack starts to form at the upper side of the UHPFRC layer*, i.e. at  $\varepsilon_{U,l} = \varepsilon_{Ut,max}$  (●). This criterion concerns the crack width restriction. Before the formation of localized macrocracks, the permeability of the UHPFRC remains low and the protection function of the cross-section is still ensured (see Section 6.2).
- ii. The *localized macrocrack reaches the interface*,  $\varepsilon_{int} = \varepsilon_{Ut,max}$  (○), i.e. the localized macrocrack crosses the whole UHPFRC section. This criterion is important to evaluate the protection function of the UHPFRC layer, since localized macrocracks represent preferential paths for the penetration of water and aggressive substances. If localized macrocracks cross the whole UHPFRC layer, these substances may penetrate to the concrete layer, and the protection function for the RC section of the UHPFRC layer becomes ineffective. This criterion is also important to evaluate debonding: Interface cracks occur always after localized macrocracks have reached the interface and may alter the structural response of the element.
- iii. The *reinforcement in the UHPFRC layer* ( $A_{s,U}$ ) *starts to yield*,  $\sigma_{s,U} = f_{sy,U}$  (▲).
- iv. The *tensile reinforcement in the concrete layer* ( $A_{s,ct}$ ) *starts to yield*,  $\sigma_{s,ct} = f_{sy,c}$  (△).

Depending on the configuration of the cross-section (P, PR or R), criterion iii and iv indicate the yielding of the reinforcement that induces irreversible plastic deformations into the cross-section.

- v. *Fracture of the concrete in compression* at  $\varepsilon_{c,upp} = 3.5 \text{ ‰}$  (⊕). This criterion leads to the final fracture of the structural member. It indicates the deformation capacity, which is important for ULS design. The value of  $\varepsilon_{c,upp} = 3.5 \text{ ‰}$  is assumed and corresponds to the prescriptions of codes [SIA262]. It does not correspond entirely to the chosen parabolic modelling of concrete in compression. However, it gives a conservative indication for normal strength concrete.

Due to the high value of the strain at maximum tensile strength of the rebar  $\varepsilon_{su} = 10\%$ ; the fracture of the rebars becomes never determinant in the parametric study.

Regarding the curve of the composite “UHPFRC-concrete” section presented in Figure 6.14, it can be observed that localized macrocracks form first in the UHPFRC layer (criterion i (●)). Then, the reinforcement in the UHPFRC layer yields (criterion iii, ▲), just before the localized macrocrack reaches the interface (criterion ii, ○). The reinforcement in the concrete layer yields afterwards (criterion iv, △). Concrete fracture (criterion v, ⊕) occurs at a curvature of  $82 \cdot 10^{-3} \text{ m}^{-1}$ , which is nearly three times larger than the curvature at criterion iv.

The  $M$ - $\kappa$ -curve of the concrete section serves as reference curve. The beginning of yielding of the tensile reinforcement ( $A_{s,ct}$ ) is taken as reference point for the *normalization of the curves*

(Figure 6.15). So, the increase in stiffness and maximum moment of the composite “UHPFRC-concrete” section can be evaluated in comparison to the original concrete section.

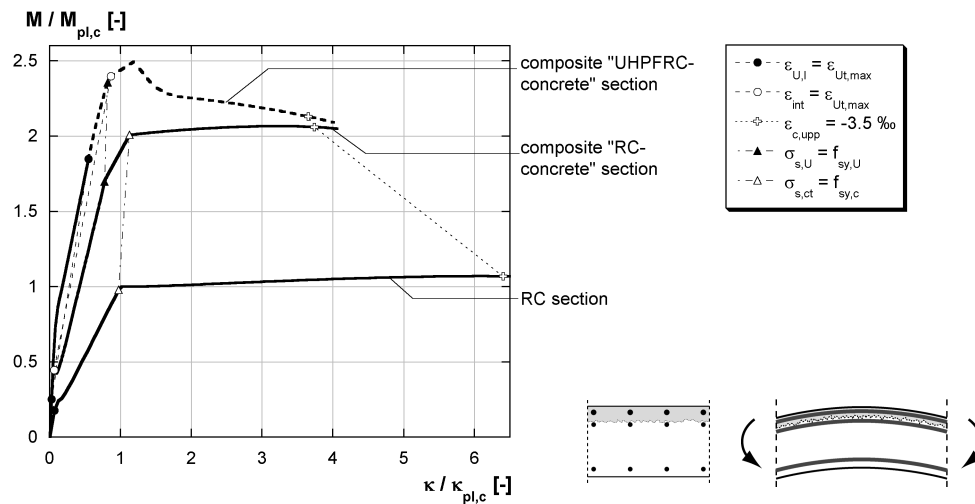


FIGURE 6.15: Normalized  $M$ - $\kappa$ -curves for the basic values of the parametric study and for the concrete section

### 6.3.4 Configuration of the cross-section

The parametric study is conducted for the three basic configurations P, PR and R as presented in Section 6.1. Figure 6.16 shows the  $M$ - $\kappa$ -curves for the basic values of the three configurations with the same depth ( $h_U = 5$  cm).

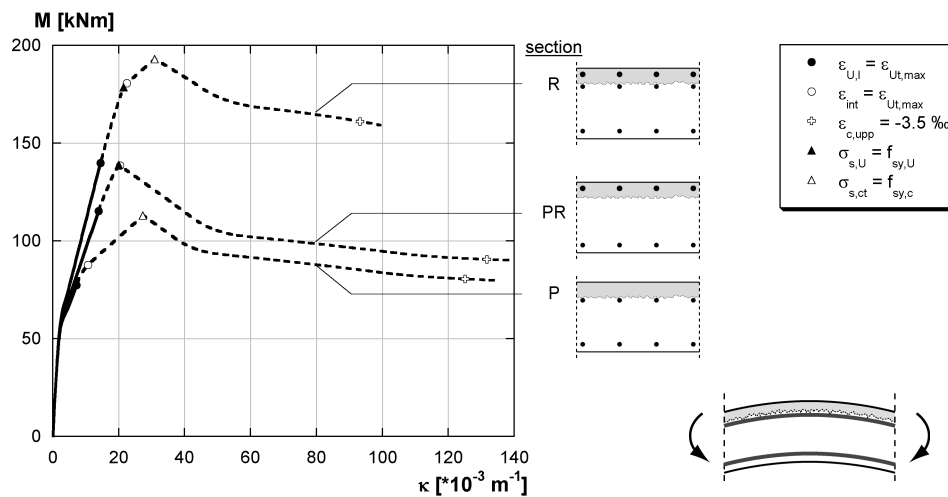


FIGURE 6.16: Moment-curvature relations for cross-section configurations P, PR and R

*Configuration P* is designed for protection purposes. Therefore, its main interest lies in its cracking behaviour and not in the ultimate moment. The latter corresponds to the one of the original concrete section at fracture of concrete in compression when the crack in the UHPFRC is so large that no more force can be transferred through it. So, durability and SLS are most important for configuration P.

*Configuration PR* is mainly designed for protection purposes. If the reinforcement in the UHPFRC layer is identical to the one of the existing section in terms of ratio and position, the ultimate moment corresponds to the one of the existing concrete section. This is not the case in Figure 6.16, since the static height is higher and the reinforcement ratio is lower when compared to the original concrete sec-

tion. This simplification is made in order to keep the same basic values for the three configurations. For configuration PR, durability and SLS are essential, but ULS is also of importance.

As the tensile reinforcement of PR is incorporated in the UHPFRC layer, the magnitude of hardening  $\varepsilon_{U,hard}$  is increased and localized macrocracks form at a higher curvature and moment than for section P. For the basic parameters, the formation of localized macrocracks in section PR (●) occurs at a higher moment than the ultimate moment at fracture of the concrete layer.

*Configuration R* is designed for increase of resistance *and* for protection. It has the highest moment of the three configurations at concrete fracture in compression (⊕). The resistance is increased, however, the deformation capacity is reduced. This can be explained by an increase of the tensile chord under negative bending moment, leading to an increase of the depth of the compression zone. Compared to configurations P and PR, configuration R has a higher stiffness. The reinforcement in the UHPFRC layer increases the deformation at localized macrocrack formation  $\varepsilon_{Ut,max}$  (●) compared to configuration P. Durability, ULS and SLS have to be investigated in detail for configuration R.

The *maximum moment* of the three configurations occurs when all the tensile reinforcement yields ( $\Delta$ ). Beyond the maximum moment, the increase of the force in the tensile reinforcement is small and the UHPFRC is already cracked. The force transferred by the UHPFRC decreases faster than the stress increase in the tensile reinforcement: the bending moment decreases, i.e. softening occurs.

### 6.3.5 Influence of the cross-section geometry

**Thickness of the UHPFRC layer.** The influence of the thickness of the UHPFRC layer  $h_U$  is shown for configurations P and R in Figures 6.17 and 6.18 respectively. The thickness is varied between 1 and 5 cm for configuration P and between 4 and 10 cm for configuration R. The minimum thickness of configuration R is limited by the rebar diameter and the UHPFRC cover of the rebar which is necessary to guarantee force transfer between rebar and UHPFRC and which is assumed to be 1.5 cm.

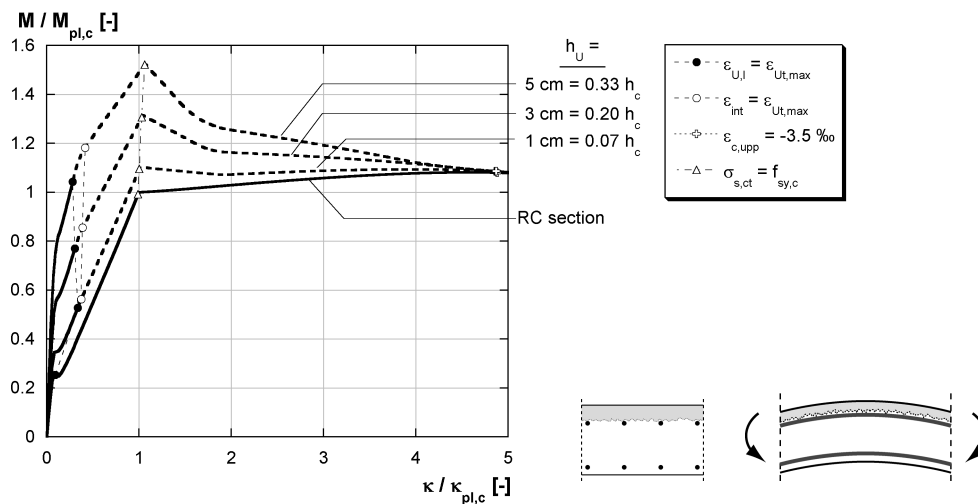


FIGURE 6.17: Influence of the thickness of the UHPFRC layer - configuration P

A thicker UHPFRC layer increases the stiffness before the formation of localized macrocracks. Moreover, those cracks form at higher relative moments for higher  $h_U$ . The localized macrocrack forms at nearly the same curvature for different  $h_U$ . The moment at concrete fracture (⊕) is independent on  $h_U$  for P. In configuration R, it increases with increasing  $h_U$ . Thicker UHPFRC layers in R lead to an increase of the static height of the reinforcement  $A_{s,U}$ , since the thickness of the UHPFRC cover is kept constant. Also, the static height of this reinforcement increases with increasing  $h_U$ , leading to an increase in resistance. The behaviour of configuration PR is the comparable to the one of configuration R.

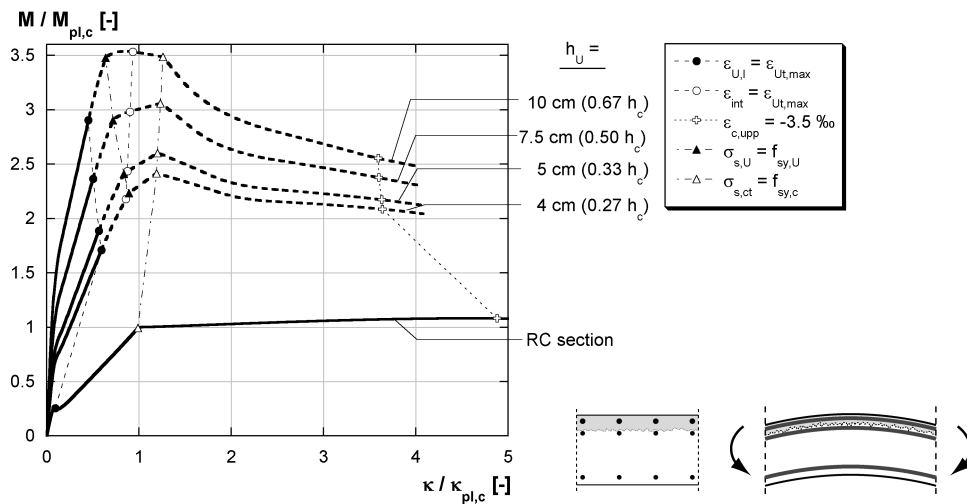


FIGURE 6.18: Influence of the thickness of the UHPFRC layer - configuration R

An increasing thickness  $h_U$  is favourable, since it leads to smaller deformations for a given moment and to a formation of localized macrocracks at higher moments. For configuration P, however, the moment at formation of localized macrocracks (●, durability and SLS criterion) may be close to the moment at fracture of the concrete in compression (⊕, ULS criterion) and the maximum moment, and it may not be possible to fully exploit the UHPFRC properties in the composite element. The same tendency is observed for configuration R, but in a less pronounced way.

**Reinforcement ratio in the UHPFRC layer.** The concrete section is efficiently strengthened by adding reinforcement in the UHPFRC layer (Figure 6.19). An increasing reinforcement ratio in the UHPFRC layer ( $\rho_{s,U}$ ) leads to an increase in resistance, but also to a reduction of deformation capacity. The resistance of a configuration with  $\rho_{s,U} = 5\%$  (of  $A_U$ ) (corresponding to  $\varnothing 16 \text{ mm} @ 8 \text{ cm}$ ) is more than two times higher than that of a configuration with  $\rho_{s,U} = 2\%$  (corresponding to  $\varnothing 16 \text{ mm} @ 20 \text{ cm}$ ) however, the relative rotation capacity is reduced from 3.6 to 2.4 (-50%). Thus, the maximum amount of reinforcement  $A_{s,U}$  may be limited by the required rotation capacity.

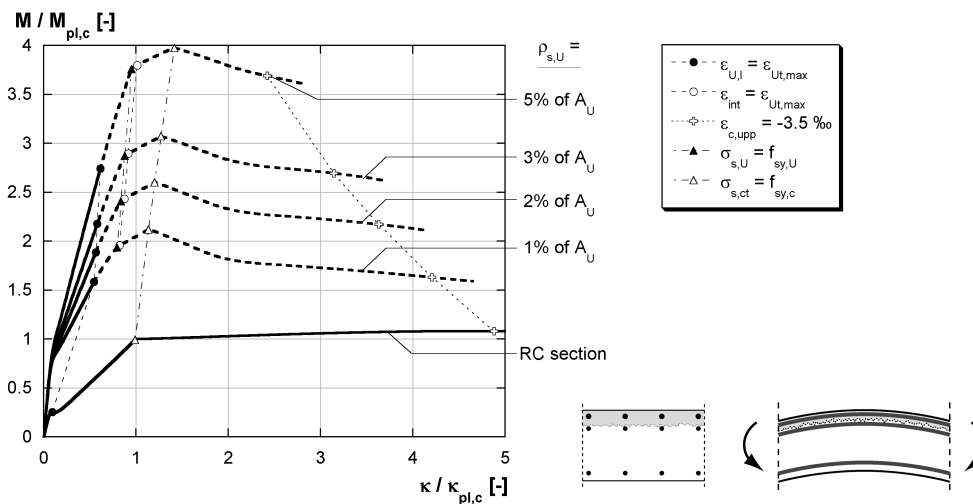


FIGURE 6.19: Influence of the reinforcement ratio in the UHPFRC layer

The increase of reinforcement in the UHPFRC layer leads to a higher stiffness of the section. The bending moment at the formation of localized cracks (●) is increased, while the curvature at this point



increases only slightly. The ratio between the moment of formation of localized macrocracks and the moment at concrete fracture ( $M_{U_t, \max} / M_{e_c, \text{upp}} = -3.5\%$ ) decreases with increasing reinforcement ratio, so that the verification of crack widths becomes more critical with increasing reinforcement ratio.

The fracture of the compression zone leads to final fracture of the section. The depth of the compression zone is calculated using an equivalent static height  $d_{\text{eq}}$  that considers the two reinforcement layers in tension  $A_{s,U}$  and  $A_{s,ct}$  (Table 6.1). The consideration of the equivalent static height is justified because the two reinforcement layers yield before the fracture of concrete in compression occurs. It is shown that the depth of the compression zone is always smaller than 0.35. The ductility criterion according to EQ. 6.4 is therefore fulfilled for reinforcement ratios up to  $\rho_{s,U} = 5\%$  for the given geometric configuration. The limit curvature at concrete fracture is only half of the limit curvature of the RC section and corresponds to curvatures of  $\kappa = 62 \cdot 10^{-3} \text{ m}^{-1}$  and  $\kappa = 125 \cdot 10^{-3} \text{ m}^{-1}$  respectively.

TABLE 6.1: Depth of the compression zone for the curves of Figure 6.19

reinforcement ratio $\rho_{s,U}$	RC section	1% of $A_U$	2% of $A_U$	3% of $A_U$	5% of $A_U$
depth of the compression zone $x/d_{\text{eq}}$	0.16	0.22	0.24	0.27	0.35

### 6.3.6 Influence of the tensile properties of the UHPFRC

#### 6.3.6.1 Contribution of the UHPFRC

The contribution of UHPFRC in composite “UHPFRC-concrete” elements is demonstrated in Figures 6.14 and 6.15 for configuration R and in Figure 6.17 for configuration P. The moment at fracture of concrete in compression ( $\oplus$ ) is not or only slightly increased by the use of UHPFRC for the given material parameters (3% for R and 0% for configuration P). However, if only a low rotation capacity is required, the increase of the maximum moment can be exploited. If the required rotation capacity corresponds for example to a relative curvature of 2.5, the design moment may be increased by 10% for configuration R and by 12% for configuration P ( $h_U = 5 \text{ cm}$ ) respectively when compared to the original RC section.

The main contribution of UHPFRC is the increase in stiffness for small curvatures, i.e. under service conditions. Moreover, localized macrocracks form at a higher moment and curvature than in RC sections. The moment of configuration R is increased by 50% for a relative curvature of  $\kappa/\kappa_{pl,c} = 0.5$  compared to the corresponding “RC-concrete” section. Moreover, the “UHPFRC-concrete” section does not show localized macrocracks, whereas the “RC-concrete” section has localized macrocracks at this curvature. The UHPFRC leads also to an increase in resistance, i.e. a higher maximum moment which may be exploited when sufficient deformation capacity is guaranteed.

#### 6.3.6.2 Influence of UHPFRC tensile properties

**Secant modulus.** The secant modulus  $E_{U_t}$  of the UHPFRC indicates the apparent initial stiffness of the UHPFRC layer (Figure 6.20). Undamaged UHPFRC have secant moduli between 30 and 80 GPa, depending on the UHPFRC composition. When the UHPFRC is damaged, e.g. due to microcracking of the matrix at early age (see e.g. Chapter 4), the secant modulus is reduced. The lower boundary of this damage for the UHPFRC that is used in the experimental campaign is 5 GPa (see Figure 3.4a in Section 3.2.4.3), which is the value of the apparent stiffness of a specimen in uniaxial tension at the maximum tensile strength ( $f_{U_t, \max}$ ).

Figure 6.20 shows that the influence of the secant modulus is only significant for small curvatures ( $\kappa/\kappa_{pl,c} < 0.6$ ) and before the formation of localized macrocracks. For values from 30 to 80 GPa, the loss of stiffness due to a lower secant modulus can only be seen for curvatures  $\kappa/\kappa_{pl,c} < 0.1$ . The difference in stiffness is small when the entire hardening domain is considered. However, a stronger reduction of the secant modulus ( $E_{U_t} < 30 \text{ GPa}$ ) due to damage considerably reduces the stiffness of the composite element under service loads. For a relative moment  $M/M_{pl,c} = 1$ , the relative curvature for

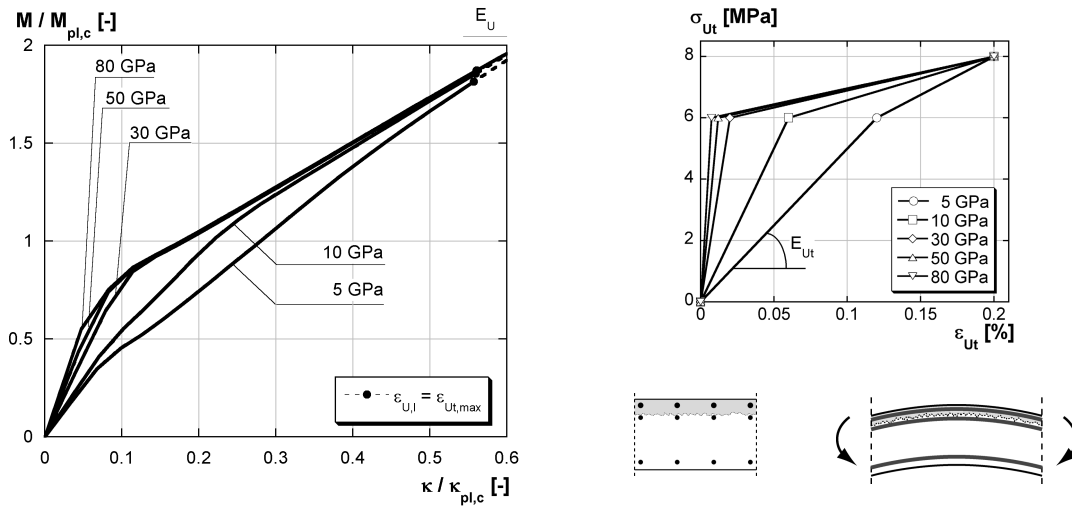


FIGURE 6.20: Influence of the secant modulus of the UHPFRC

$E_{Ut} = 10$  GPa is increased by 23% and for  $E_{Ut} = 5$  GPa by 58% respectively when compared to a curvature for  $E_{Ut} = 50$  GPa.

This underlines the importance of the estimation of microcracking at early age and in the long-term in composite “UHPFRC-concrete” elements. The influence of the secant modulus is important for SLS, more precisely for the limit of deformations.

**First cracking strength.** The first cracking strength ( $f_{Ut,1st}$ ) is varied between 6 and 14 MPa (Figure 6.21). The strain at the formation of localized macrocracks  $\epsilon_{Ut,max}$  and the modulus of hardening  $E_{U,hard}$  are kept constant.

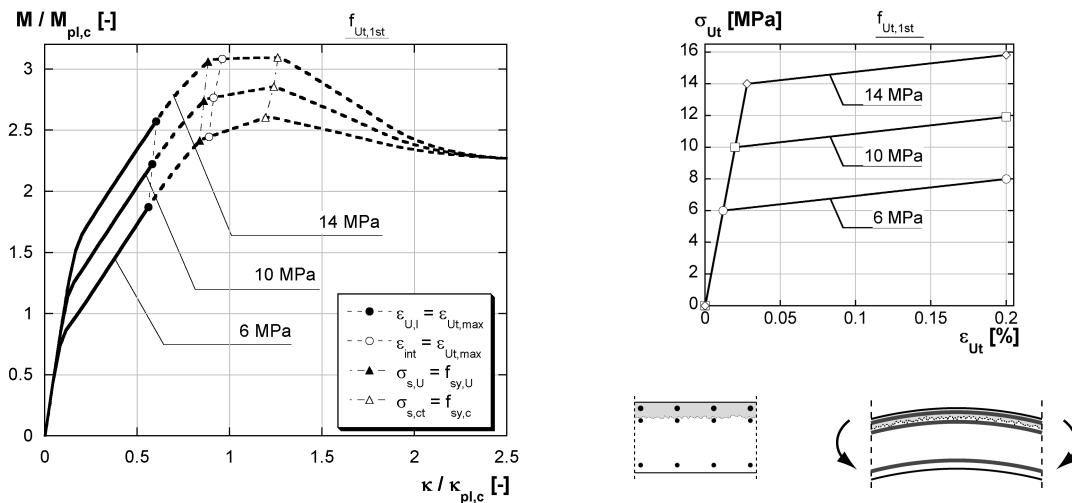


FIGURE 6.21: Influence of the strength at the formation of distributed macrocracks in the UHPFRC

The increase of the first cracking strength  $f_{Ut,1st}$ , leads to an increase in stiffness of the composite element. The increase of the moment is 19% from  $f_{Ut,1st} = 6$  to 10 MPa for a given curvature of  $\kappa/\kappa_{pl,c} = 0.5$ . The moment at the formation of localized macrocracks (●) and the maximum moment are increased for higher  $f_{Ut,1st}$ . However, at the failure moment at fracture of concrete in compression (⊕), the moments are identical, since the influence of the change of the first cracking strength  $f_{Ut,1st}$  can

only be observed for relative curvatures that are smaller than 2.5. Thus, the increase of  $f_{U_t,1st}$  is mainly important under service loads and for the maximum moment.

**Magnitude of hardening.** The magnitude of hardening indicates the domain of localized macrocrack formation and is also important to evaluate the interaction between reinforcement and UHPFRC. It is varied between  $\epsilon_{U,hard} = 0$  to 1.5% (Figure 6.22).

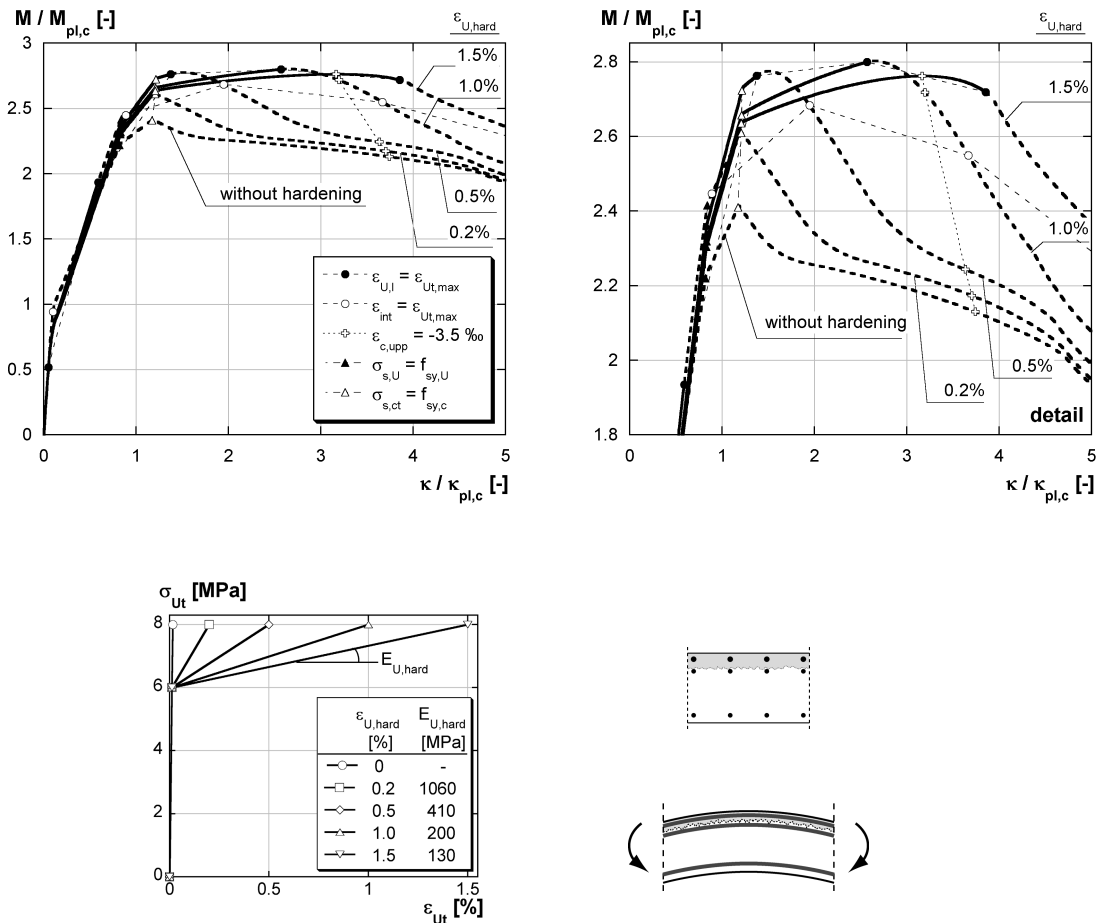


FIGURE 6.22: Influence of the magnitude of hardening of the UHPFRC

$\epsilon_{U,hard} = 0$  signifies that no hardening occurs; the material exhibits linear elastic stress increase, followed directly by softening behaviour. This configuration has the lowest resistance, since softening, i.e. the formation of localized macrocracks, starts at the smallest deformation and moment ( $M/M_{pl,c} = 0.5$ ). The maximum moment occurs when all the reinforcement yields (at  $\Delta$ ).

For  $\epsilon_{U,hard} = 0.2\%$ , localized macrocracks form at a relative moment of  $M/M_{pl,c} = 1.93$ , before the yielding of the reinforcement. The maximum moment occurs at the yielding of all tensile reinforcement (at  $\Delta$ ,  $M/M_{pl,c} = 2.6$ ) as for  $\epsilon_{U,hard} = 0$ .

For  $\epsilon_{U,hard} = 0.5\%$  and  $\epsilon_{U,hard} = 1.0\%$ , localized macrocracks form after the yielding of the entire tensile reinforcement ( $\bullet$  after  $\Delta$ ). The higher the magnitude of hardening  $\epsilon_{U,hard}$ , the longer is the apparent plateau until the maximum moment. The bending moment decreases rapidly after the formation of localized macrocracks, until the fracture of the concrete in compression occurs. The decrease is more pronounced for lower magnitudes of hardening  $\epsilon_{U,hard}$  (decrease of 23% for  $\epsilon_{U,hard} = 0.5\%$  compared to 3% for  $\epsilon_{U,hard} = 1.0\%$ ).

For  $\epsilon_{U,hard} = 1.5\%$ , the UHPFRC is still in the hardening domain when the concrete fails in compression ( $\oplus$ ). After the yielding of the entire tensile reinforcement ( $\Delta$ ), a plateau can be observed, until

the maximum moment occurs at the fracture of concrete in compression. In this case, the fracture of the structural element is not announced by localized macrocracks, but only by beam deflections.

The higher the magnitude of hardening, the later the localized macrocrack reaches the interface (○). The test results show that interface cracks and debonding under loading form only when localized macrocracks have propagated to the interface. Thus, a high magnitude of hardening delays also the formation of debonding cracks: for  $\epsilon_{U,hard} \geq 1\%$ , concrete fracture in compression (⊕) occurs before the cracks reach the interface and no interface cracks and debonding should occur in the structural element.

The deformation capacity, expressed by curvature at concrete fracture in compression, decreases for an increasing magnitude of hardening. This can be explained by the contribution of UHPFRC when the concrete fails: the higher the magnitude of hardening  $\epsilon_{U,hard}$ , the more force is still transmitted through the UHPFRC layer and the stronger is the tension chord under negative bending moment, leading to a reduction of deformation capacity.

The variation of the magnitude of hardening  $\epsilon_{U,hard}$  shows that the most favourable behaviour for the given configuration is obtained for  $\epsilon_{U,hard} = 1.0\%$ : The  $M-\kappa$ -curve shows slight moment increase after the yielding of the reinforcement and before the formation of localized macrocracks. Concrete fracture occurs after the formation of localized macrocracks, however, the fracture moment at ⊕ is only 3% smaller than the maximum moment. The deformation capacity is improved when compared to a smaller magnitude of hardening. A higher magnitude of hardening (e.g.  $\epsilon_{U,hard} = 1.5\%$ ), for which concrete fracture in compression occurs before the formation of localized macrocracks, indicates that the tensile behaviour of UHPFRC cannot be fully exploited.

The maximum moment increases with an increasing magnitude of hardening up to  $M/M_{pl,c} = 2.8$  at  $\epsilon_{U,hard} = 0.5\%$ . At this magnitude of hardening, yielding of the entire tensile reinforcement occurs just before the formation of localized macrocracks (△ before ●). For higher magnitudes of hardening, the maximum moment depends on the interaction between the hardening of UHPFRC and of steel and it remains virtually constant.

The magnitude of hardening influences durability, SLS and ULS considerations. For small magnitudes ( $\epsilon_{U,hard} < 0.2\%$ ), the crack width criterion may become critical. The magnitude of hardening influences also the fracture moment and so the ULS.

**Softening.** UHPFRC softening is dependent on fibre type, ratio and composition. The size of softening, i.e. the crack widths  $w_{Ut,1}$  and  $w_{Ut,2}$  are varied with a constant ratio  $w_{Ut,1}/w_{Ut,2}$  (Figure 6.23). The crack width  $w_{Ut,2}$  is dependent on the fibre length  $l_f$  and corresponds approximately to  $l_f/2$ . The crack widths have to be transformed into deformations for the analytical model with the reference length  $L_R$  (see Section 5.1.3). Thus, the presented  $M-\kappa$ -curves in Figure 6.23 are dependent on the reference length. The importance of the reference length is discussed in Chapter 5 and is not discussed any further here.

Softening influences the  $M-\kappa$ -curve *after* the formation of localized macrocracks and is only important for ULS considerations. Larger crack widths  $w_{Ut,1}$  and  $w_{Ut,2}$  increase the maximum moment and the moment at fracture of the concrete in compression (⊕), since more stress can be transferred for a given crack width. Therefore, longer fibres are favourable for the ultimate bending moment: the higher  $w_{Ut,1}$ , the smaller is the moment decrease after the maximum moment. For  $w_{Ut,1} = 8$  mm, the stress decrease is very small and the cross-section approaches an ideal plastic behaviour, while a moment decrease of 17% (between the maximum moment and the moment at fracture of the concrete in compression) is observed for  $w_{Ut,1} = 1$  mm.

### 6.3.7 Influence of the concrete strength

The influence of concrete strength in compression ( $f_{cc}$ ) is investigated, since even normal strength concretes in existing bridges often attain strengths up to 80 MPa with increasing age. The  $M-\kappa$ -curves are determined for concrete strengths from 40 to 80 MPa. Figure 6.24 is determined with a parabolic material law for concrete in compression (see Section 5.1.3) and with an adapted secant modulus for the concrete according to EQ. 6.7. The differences in deformation capacity of the different concretes in

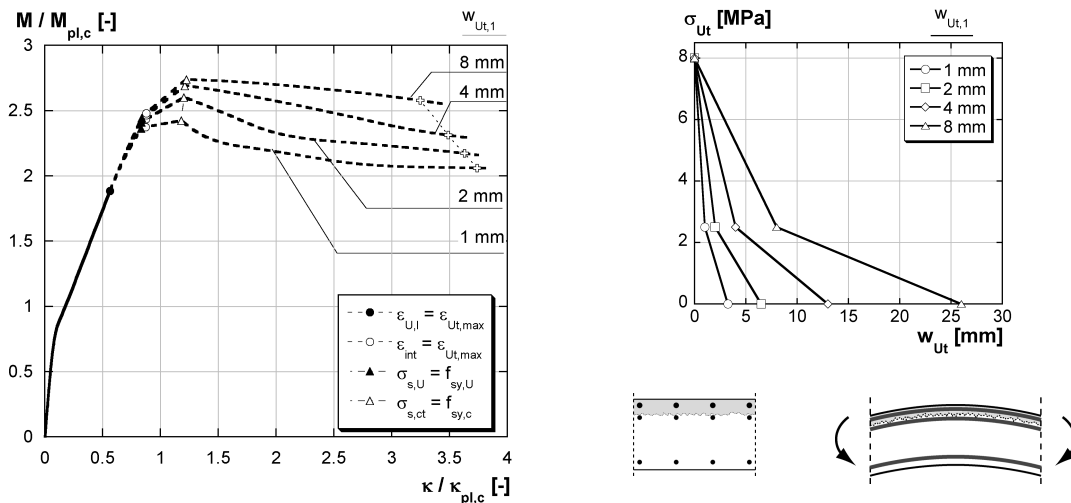


FIGURE 6.23: Influence of softening of the UHPFRC

compression are not considered in the diagram, but the criterion for concrete fracture at  $\epsilon_{c,upp} = -3.5\%$  is applied, which is conservative for the discussed concretes.

$$E_c = 10 \cdot \sqrt[3]{f_{cc}} \tag{EQ 6.7}$$

with  $E_c$  [GPa]: secant modulus.  $f_{cc}$  [MPa]: concrete compressive strength

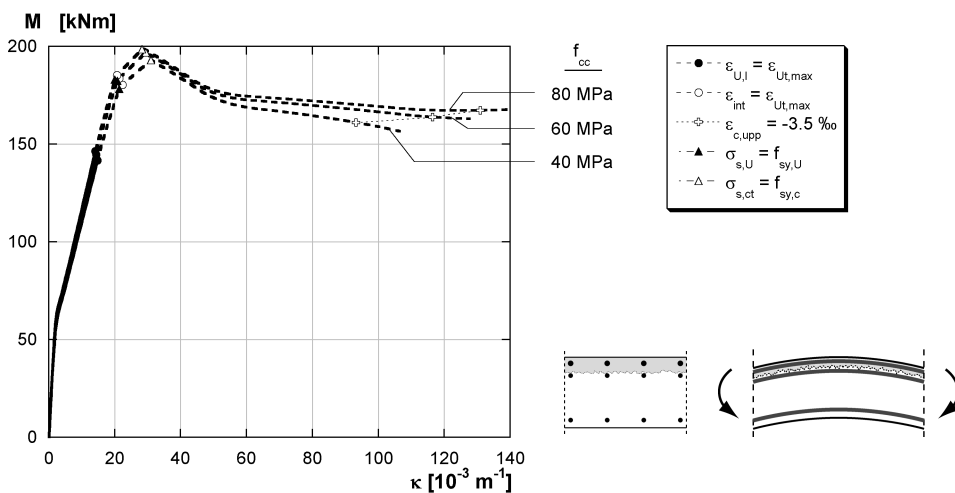


FIGURE 6.24: Influence of the concrete strength in compression

The influence of the concrete strength in compression is small. No significant increase in resistance ( $< 3\%$ ) is observed for an increase of the compressive strength  $f_{cc}$  from 40 to 80 MPa, however, the curvature at fracture of the concrete in compression, which is assumed to be  $-3.5\%$ , is increased for higher compressive strengths: by 40% for an increase of  $f_{cc}$  from 40 to 80 MPa. For a higher concrete strength in compression acts as reinforcement of the compression zone of the bending element and therefore leads to an increase in deformation capacity. In reality, concretes with smaller strengths have higher deformation capacities, thus, the curvature at failure is larger for the beam configuration with lower concrete compressive strengths than assumed in this study.

### 6.3.8 Influence of the type of reinforcement in the UHPFRC layer

In this section, the influence of the reinforcement type in the UHPFRC layer is investigated. In addition to traditional steel rebars with  $f_{yk} = 500$  MPa (e.g. B500 of Swisscode 2 [SIA262]), steel rebars with higher yield limits as well as rebars made of composite materials are considered. The calculations are based on the hypothesis of perfect bond between cementitious material and reinforcement and no conclusions can be drawn with respect to the different bond behaviour of rebars made of steel and composite materials.

**Yield strength of reinforcement in the UHPFRC layer.** The yield strength of steel rebars is varied between  $f_{sy,U} = 300$  and 900 MPa (Figure 6.25). The hardening modulus after yielding  $E_{s,hard}$  as well as the deformation  $\varepsilon_{s,U}$  are kept constant, i.e. the behaviour after yielding is identical.

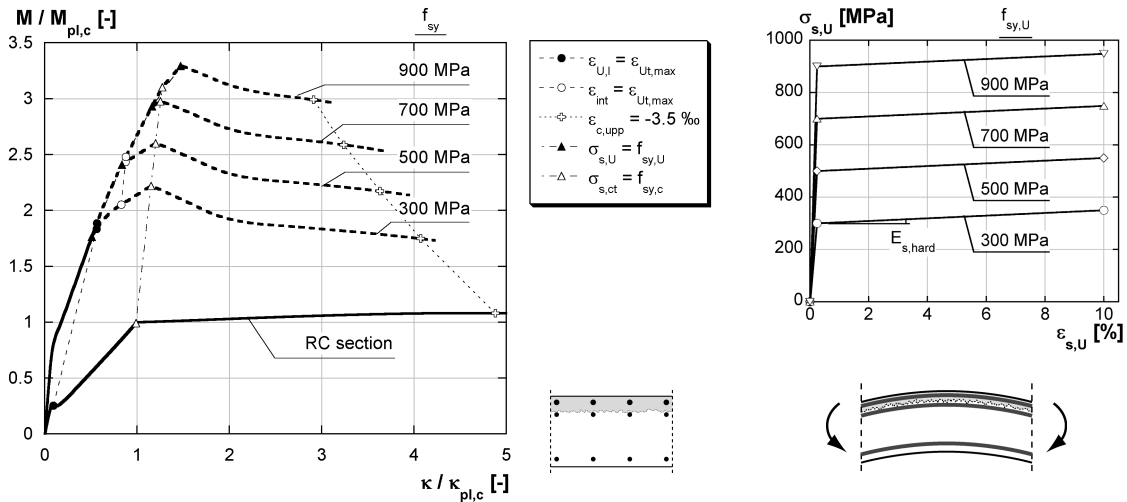


FIGURE 6.25: Influence of the yield strength of the reinforcement in the UHPFRC layer

The influence of the yield strength  $f_{sy,U}$  is only relevant for relative moments  $M/M_{pl,c} > 1.8$ , thus, the influence of the yield strength is here important for ULS considerations. A higher yield strength increases the maximum moment and the moment at fracture of the concrete in compression. Since the tension chord is strengthened under a negative bending moment, the deformation capacity is reduced. Comparing  $f_{sy,U} = 500$  to 900 MPa, the bending moment at concrete fracture in compression is increased of 42%, whereas the curvature is reduced by 25%.

**Different reinforcement types.** In this section, the steel B500 is compared to rebars made of composite materials as reinforcement in the UHPFRC layer  $A_{s,U}$  (Figure 6.26). Rebars made of composite materials have a linear elastic tensile behaviour up to fracture without plastic or hardening domain. Thus, sudden fracture of the structural elements occurs when the tensile strength of the composite rebars is reached. Carbon Fibre Reinforced Composites (CFRC) have a high tensile strength ( $f_{sy} = 1500$  MPa) and a modulus of  $E_s = 120$  GPa, Glass Fibre Reinforced Composites (GFRC) have a tensile strength of  $f_{sy} = 1000$  MPa and a modulus of  $E_s = 45$  GPa. Aramide Fibre Reinforced Composites (AFRC) have material properties that lie between the properties of CFRC and GFRC and are not discussed here.

Fracture of the structural element is caused by fracture of concrete in compression ( $\ominus$ ). The deformation capacity is reduced for GFRC and CFRC rebars compared to B500, while the bending moment at concrete fracture is increased. This is due to the higher tensile strengths of the rebar materials: at fracture of the concrete in compression ( $\sigma_{s,U} = 1030$  MPa for CFRC,  $\sigma_{s,U} = 555$  MPa for GFRC when compared to  $\sigma_{s,U} = 505$  MPa for B500). Moreover, the bending moment CFRC increases continuously until fracture, the one of GFRC has a small decrease at  $\kappa/\kappa_{pl,c} = 1.9$ , before increasing until fracture, whereas the moment of B500 decreases after the yielding of the reinforcement ( $\Delta$ ) until fracture. The

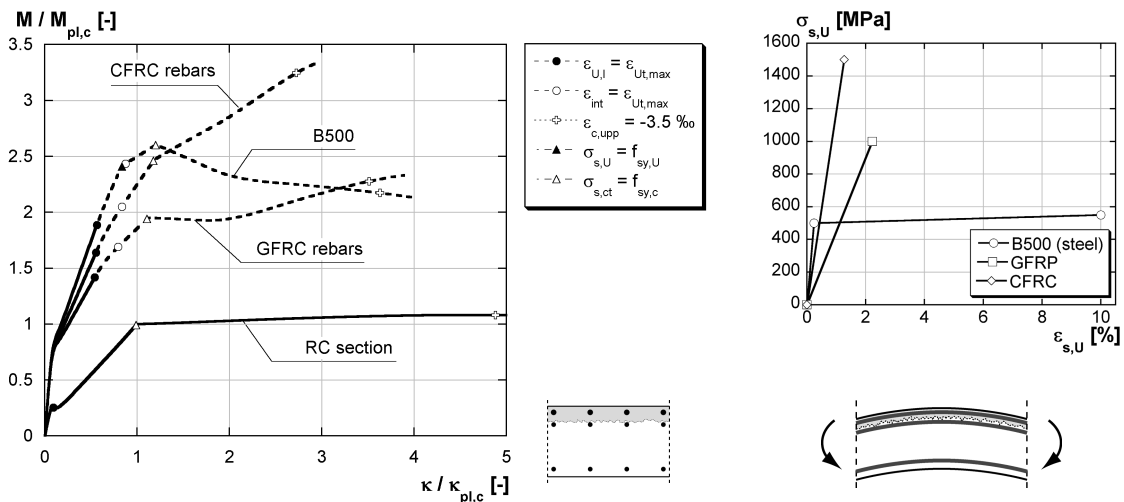


FIGURE 6.26: Comparison of reinforcement with different materials

decrease of the B500 can be explained by the low hardening modulus after yielding: the force increase in the steel rebars is lower than the force decrease in the UHPFRC layer for increasing curvature. The tensile behaviour of the composite materials is linear elastic, thus, the initial moduli of the rebars are preserved until their fracture. It can be deduced that for the given configuration, a modulus slightly higher than 45 GPa is necessary to guarantee a monotonously increasing bending moment until fracture.

Since the modulus of the composite materials is lower than that of steel, the stiffness of the structural element is reduced. The bending moment at the formation of localized macrocracks is reduced (reduction of 33% for GFRP and 16% for CFRC compared to B500).

The use of composite materials as reinforcement in UHPFRC layers is promising, since the moment increases continuously until fracture. However, their lower initial moduli decrease the stiffness under service conditions, consequently, deformations increase under imposed load.

**Adapted steel tensile behaviour.** On the basis of the discussion in the preceding paragraphs, steel reinforcement with an adapted hardening tensile behaviour is proposed for configuration R (Figure 6.27). The tensile behaviour of the steel reinforcement interacts strongly with the tensile behaviour of the UHPFRC (in this configuration, with the softening behaviour), since localized macrocracks form before yielding of the reinforcement in the UHPFRC layer.

The material steel is chosen, since it has the highest modulus of elasticity and thus, the highest stiffness before yielding, i.e. under service conditions. The yield strength  $f_{sy,U}$  is reduced to 400 MPa, so, the condition of the formation of localized macrocracks before the yielding of the reinforcement is fulfilled (● before ▲ and △), and the M- $\kappa$ -curve has the same stiffness for the adapted steel as for the configuration with B500. The hardening modulus  $E_{s,hard}$  is increased compared to B500 in order to avoid a moment decrease after yielding of the tensile reinforcement (at △) until fracture. The necessary hardening modulus is  $E_{s,hard} = 45$  GPa for the given UHPFRC properties. Thus, the bending moment at yielding of the reinforcement (△) is identical to the one for B500. However, the higher hardening modulus leads to higher stresses in the reinforcement at fracture ( $\sigma_{s,U} = 835$  MPa for the adapted steel, compared to  $\sigma_{s,U} = 505$  MPa for B500) and the deformation capacity is reduced.

The adaptation of the steel tensile behaviour shows that it is possible to optimize the interaction between UHPFRC and steel. Here, the adaptation is shown for a bi-linear tensile behaviour of the steel. A real plastic plateau of the moment-curvature relationship after yielding of the reinforcement can be obtained by further adjusting the tensile behaviour of steel after yielding (e.g. approximation with a multi-linear material law).

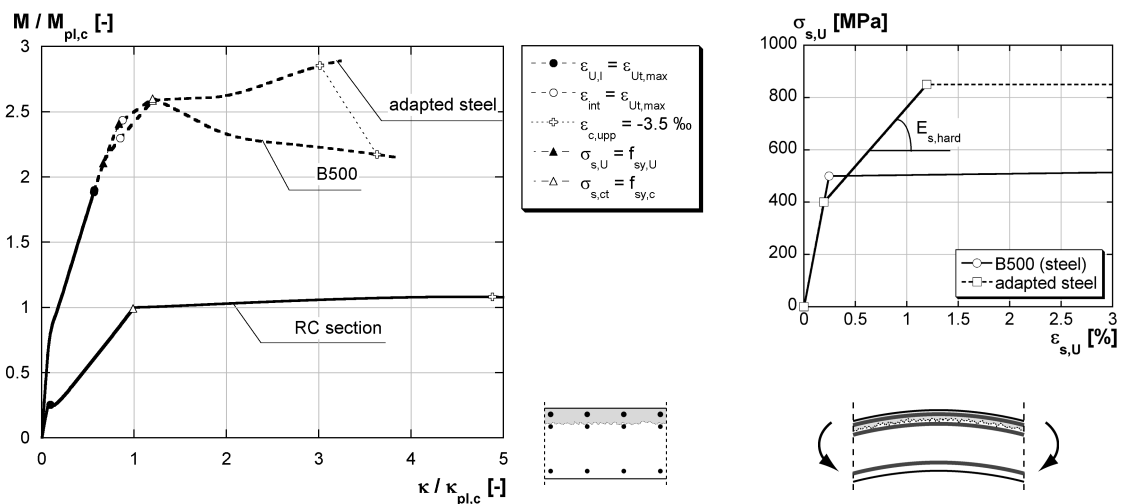


FIGURE 6.27: Adapted tensile behaviour of steel reinforcement

## 6.4 Rules for efficient design of composite “UHPFRC-concrete” elements

In the previous chapters, the time-dependent behaviour and the structural response of composite “UHPFRC-concrete” members have been discussed. In Section 6.1, three configurations have been proposed for composite “UHPFRC-concrete” elements. On the basis of the results of this study, rules for efficient use of structural members are suggested with regard to the selection of materials and element configuration.

### 6.4.1 Design criteria

Composite “UHPFRC-concrete” elements are designed in an efficient way when limit states and durability are verified for the design service life and when concrete and UHPFRC are used according to their material properties: UHPFRC is a relatively expensive material and its use should be limited to parts in the structure subjected to severe environmental conditions and/or when stiffness or resistance of the structural element must be increased without increasing the dead weight or at points of concentrated load introduction (called “increased mechanical loading” in the following). The less exposed and loaded parts of the structure are built of normal strength concrete (NSC).

In case of the composite bending elements discussed in this work, the UHPFRC layer must guarantee the protection function (permeability criterion) and fulfil SLS and ULS verifications as described in Section 6.2.

No localized macrocracks are to appear in the UHPFRC and a minimum thickness must be guaranteed when its *protection function* is required and the ingress of detrimental substances must be prevented.

The *stiffness* is increased under service conditions by increasing the thickness of the UHPFRC layer. Consequently, the thickness of the UHPFRC layer is in function of the SLS requirements on stiffness.

Finally, the *resistance* of the composite element is increased either by increasing the thickness of the UHPFRC layer or by incorporating rebars in the UHPFRC layer. The parametric study in Section 6.3 shows that it is less efficient to increase the resistance by increasing the thickness of the UHPFRC layer, but that it is recommended to incorporate reinforcement in the UHPFRC layer. Consequently, the UHPFRC thickness in efficient composite “UHPFRC-concrete” elements should be as small as possible, if an increase in resistance is required.



## 6.4.2 Selection of materials

The performance of composite “UHPFRC-concrete” members depends largely on the properties of the chosen materials. This section focuses on UHPFRC and reinforcement properties; concrete properties are not discussed, since they cannot be modified in case of conservation projects. For new construction projects, the performance of concrete has to be defined according to the design requirements and in interaction with UHPFRC and reinforcement properties.

The following recommendations are deduced from the results of this study:

### UHPFRC.

- High magnitudes of hardening  $\varepsilon_{U,hard}$  are advantageous: The magnitude of hardening should be superior to 0.2% to ensure that no localized macrocracks form under service conditions due to the time-dependent behaviour of the composite members and to due imposed loads or deformations<sup>12</sup>.
- The magnitude of autogenous shrinkage should be as small as possible. Its 28 days value should not exceed 1000  $\mu\text{m/m}$  in order to avoid debonding and an important exploitation of the magnitude of hardening EMH due to internal UHPFRC deformations.

### Reinforcement.

- Rebars with pronounced hardening behaviour, i.e. with a high modulus of hardening  $E_{s,hard}$ , are favourable, since they lead to hardening behaviour of the composite “UHPFRC-concrete” sections. Theoretically, rebars with a modulus of hardening of  $E_{s,hard} \geq 45 \text{ GPa}$  are necessary to obtain composite “UHPFRC-concrete” members with hardening for the investigated UHPFRC.
- Rebars made of composite materials (e.g. CFRC, GFRC) virtually show linear-elastic behaviour until their fracture at relatively high tensile strengths (1000 to 1500 MPa). Hardening of the composite member is obtained when the modulus of elasticity exceeds a threshold value (in Section 6.3:  $E \geq 45 \text{ GPa}$ ). On the other hand, their low moduli of elasticity reduce the stiffness of the composite “UHPFRC-concrete” member under service conditions.

## 6.4.3 Selection of element configuration

### 6.4.3.1 Conservation projects

In conservation projects, the condition of the existing structure, i.e. its state of deterioration, and the design requirements on the structure determine the selection of the configuration of composite “UHPFRC-concrete” members. The decision process for the choice of the configuration is described by means of the flow chart in Figure 6.28.

In a first step, exposure class and load cases are determined. When the structural member is either exposed to severe exposure classes (XD2, XD3, XS3, XF3, XF4, XC3, XC4 [SIA262]) or to increased mechanical loading, it is recommended to use composite “UHPFRC-concrete” members; when neither of the two criteria is fulfilled, composite members with normal strength concrete may be chosen.

In a second step, the state of the existing structure is evaluated to determine its degree of deterioration, in particular, the loss of cross-section of the rebars and content and distribution of detrimental substances in the existing structure.

On the basis of these studies, the depth of the concrete layer that must be removed for the conservation project is determined, and it is decided whether reinforcement must be treated or replaced: When the reinforcement must be replaced or at least laid open, the composite element is of configuration PR. When the reinforcement is in good condition and no intervention on this level is necessary, the verification of ULS decides between configurations P and R: when the existing concrete member fulfils the

12. According to Section 4.4, a magnitude of 0.05‰ is necessary to avoid localized macrocracks due to internal deformations; after Section 6.3, the magnitude should be at least 2‰ (0.2%).

ULS, element P is recommended; when the resistance of the existing member must be increased, element R is proposed.

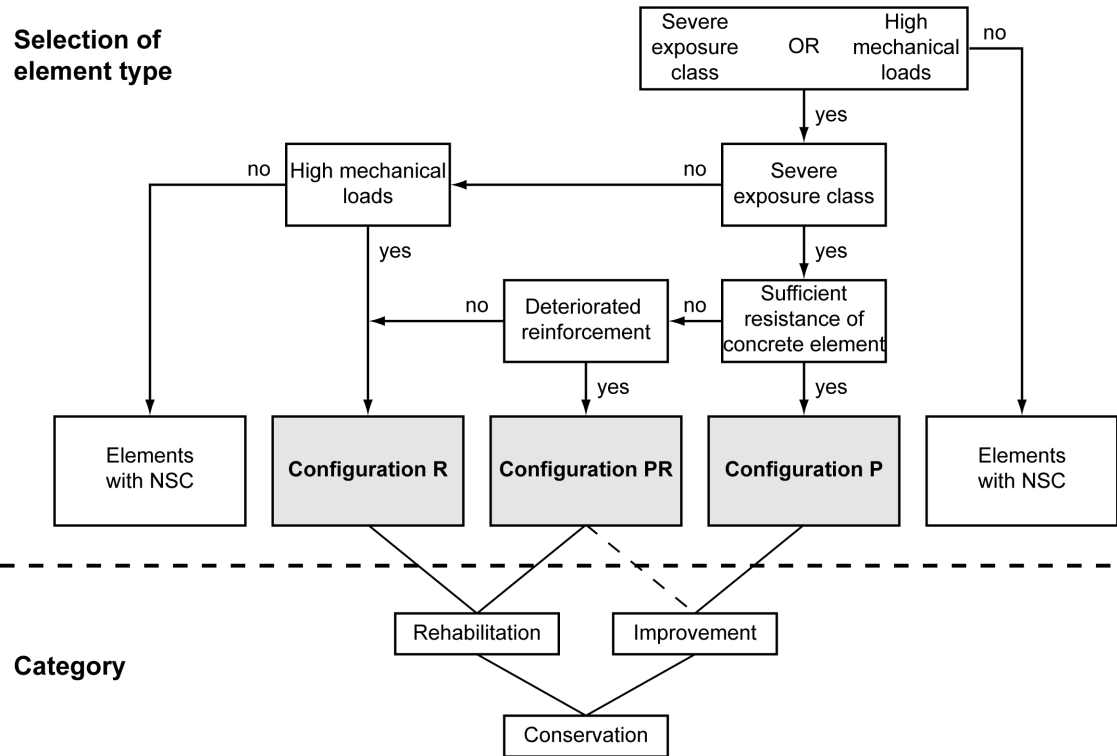


FIGURE 6.28: Selection of the appropriate configuration for conservation projects

6.4.3.2 New construction projects

Composite “UHPFRC-concrete” elements for new constructions are designed according to the requirements on the structure: the structure is planned in a way such that UHPFRC is used in the parts of the structural member where exposure and actions justify the use of high performance materials, while the other parts of the structure consist of normal strength reinforced concrete.

In case of structural members under bending, the UHPFRC is used in parts of the member where the protection function is needed and where high mechanical loads have to be introduced and transferred, as for example in the upper part of a bridge deck slab (Figure 1.3).

Configuration PR is recommended, with the reinforced UHPFRC working as tension chord and compression zone for negative and positive bending moments respectively. Configuration PR has the advantage when compared to configuration P that the reinforcement is integrated in the UHPFRC layer. Thus, the apparent magnitude of hardening of the UHPFRC is larger (see Section 5.2.3) and localized macrocracks form at higher beam deformations. However, configuration P is adapted to structures that require only the protection function of UHPFRC and that are not subjected to increased mechanical loads. In this case, the thickness of the UHPFRC layer and the UHPFRC quantity are minimized. Configuration PR is superior to configuration R because the entire upper reinforcement is placed close to the upper face and the lever arm is optimized for the negative bending moment. Configuration R is clearly designed for conservation projects where the existing structure governs the geometry. It is not appropriate for new construction projects.

New constructions generally leave plenty of freedom for design and also more elaborated configurations such as sandwiches of the form “UHPFRC-concrete-UHPFRC” may be appropriate.

## 6.4.4 Efficient configurations

### 6.4.4.1 Configuration P

Configuration P is used in rehabilitation projects when the resistance of the element is sufficient and the UHPFRC layer must only fulfil the protection function. The permeability of the element must be sufficiently low to guarantee durability.

The *necessary thickness of the UHPFRC cover  $c$*  in function of deformation and crack widths is determined in [Charron04]. In new constructions, the necessary UHPFRC cover is estimated to be 1 cm. In rehabilitation projects, it is dependent on the presence of existing macrocracks: If the concrete substrate exhibits *existing active cracks*, i.e. cracks that open and close under variable actions, the UHPFRC layer must be sufficiently thick ( $\approx 3$  cm) to avoid the formation of a localized macrocrack due to the activity of the existing crack in the concrete (Figure 6.29b). If there are *no existing cracks or only existing inactive cracks*, the necessary UHPFRC thickness is estimated to be 1 cm as for new constructions (Figure 6.29a). The values of 1 and 3 cm are estimated and have to be confirmed by further research. Finally, the thickness of the UHPFRC layer  $h_U$  is defined to be the necessary cover  $c$  and half the depth of the roughness of the contact surface (Figure 6.29).

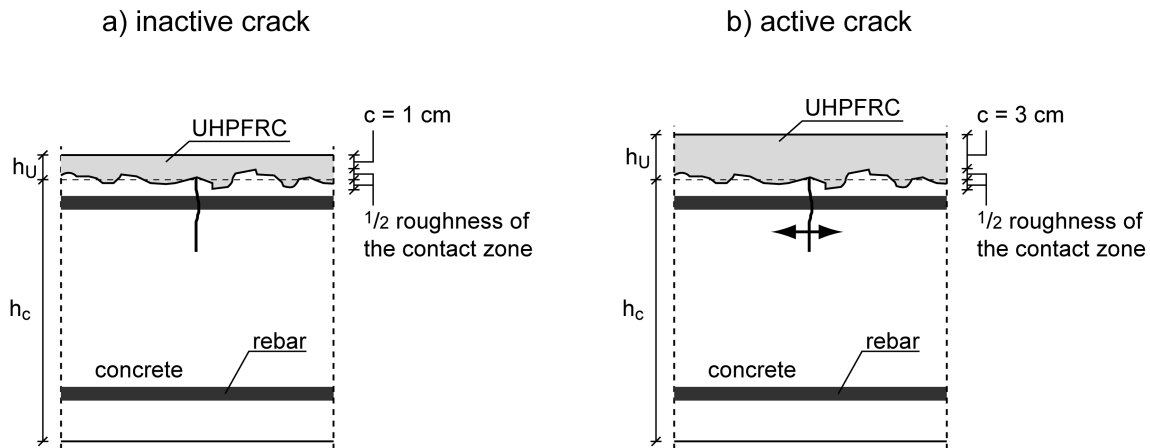


FIGURE 6.29: Recommendation for configuration P in case of a) no existing cracks or existing inactive cracks, b) existing active cracks in the concrete layer

The small thickness of the UHPFRC layer leads to a high degree of restraint. The results of Section 4.4 have shown that the UHPFRC reaches its first cracking strength  $f_{U_t,1st}$  and enters the hardening domain for a thickness of  $h_U \leq 1$  cm in statically determinate systems<sup>13</sup>. However, only  $EMH = 2\%$  of the hardening is exploited for a magnitude of hardening of  $\epsilon_{U,hard} = 1\%$ . It must be verified that there is sufficient deformation capacity of the UHPFRC left to sustain short term loading without exceeding the limit deformation capacity. The limit of deformation of the durability criteria (Section 6.2.3) corresponds to the deformation at the end of the hardening domain  $\epsilon_{U_t,max}$ . UHPFRC with large magnitudes of hardening  $\epsilon_{U,hard}$  are recommended in order to delay the formation of localized macrocracks in the UHPFRC.

### 6.4.4.2 Configuration PR

Configuration PR is appropriate for new constructions and for strongly deteriorated existing structures when the rebars must be laid open and replaced or complemented. The UHPFRC layer fulfils the protection function and contributes significantly to the resistance of the structural member, in particular

13. for the material properties described in Chapter 4

under negative bending moments, i.e. with the combination of reinforcement and UHPFRC acting as tension chord.

The reinforcement ratio in the UHPFRC layer is determined by the ULS verification. The thickness is determined as shown in Figure 6.30:

- The UHPFRC cover  $c$  is the maximum value between the necessary cover to guarantee durability (see Section 6.4.4.1) and the minimum thickness that is necessary to transfer force between rebar and UHPFRC and to avoid splitting cracks.

The thickness of the durability criterion from Section 6.4.4.1 is 1 cm as already determined for configuration P. On the basis of the beam tests ( $c \geq 1.5 \cdot (\text{rebar diameter})$  and no formation of splitting cracks) and the literature review in Section 2.4, it is proposed to define a mechanically necessary UHPFRC cover  $c = 1 \cdot (\text{rebar diameter})$ .

- The distance between rebar and interface roughness is governed by practical limitations for processing and by the force transfer between rebar and UHPFRC. The concrete layer acts as confinement to the rebars. So, the mechanically necessary distance is estimated to be  $\frac{1}{2} \cdot (\text{rebar diameter})$ . The fibre geometry also affects processing and limits the minimum distance: for the tested UHPFRC with a fibre length of 1 cm, it is proposed to keep a distance between rebar and concrete equal to the fibre length, e.g. 1 cm.

In conclusion, the thickness of the UHPFRC layer is approximately 5 cm for a rebars with a diameter 20 mm.

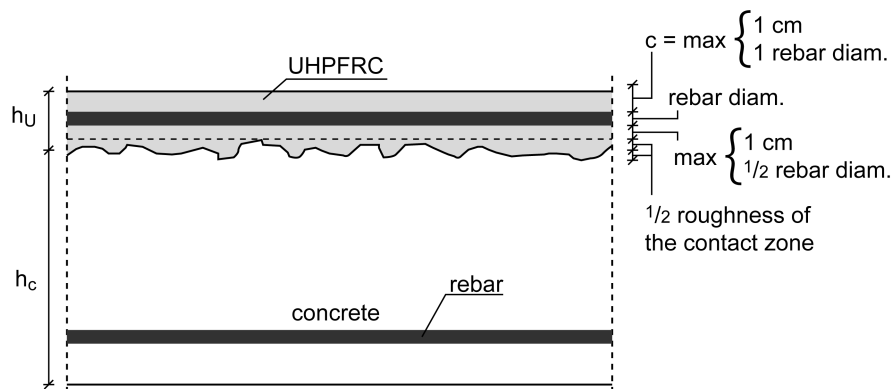


FIGURE 6.30: Recommendation for configuration PR

#### 6.4.4.3 Configuration R

Configuration R is proposed for rehabilitation projects when the resistance of the structural element must be increased and when it is not necessary to lay open the reinforcement in the existing concrete element. The reinforcement ratio in the UHPFRC layer is determined by the ULS verification. The thickness of the UHPFRC layer is identical to the one of configuration PR (see Section 6.4.4.1) and is shown in Figure 6.31.

The increase of resistance by strengthening the tension chord with reinforced UHPFRC is limited, since strengthening of the tension chord implies the reduction of deformation capacity of the “UHPFRC-composite” element. The deformation limit of the compression zone in the normal strength concrete may be reached before the fracture of the rebars leading to a significantly reduced deformation capacity of the composite element. As ductile failure is usually aimed, the composite elements must be designed in a way that the structural element does not fail prematurely in the compression zone, e.g. by strengthening the compression zone of the element with an additional UHPFRC layer. It may not always be possible to exploit the material properties of UHPFRC and normal strength concrete in an optimal way, since the existing structure imposes limits in terms of geometry and dead weight.

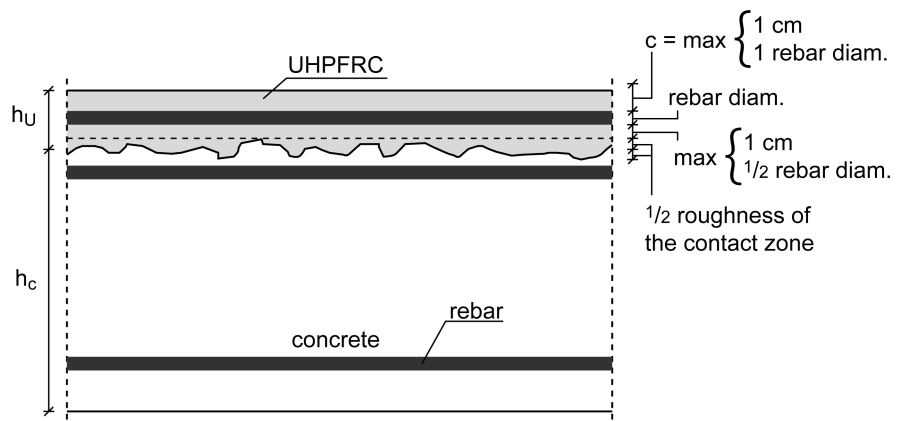


FIGURE 6.31: Recommendation for configuration R



## 7 Conclusions and future work

Chapter 7 focuses on the principal conclusions (Section 7.1) and on recommendations for future work (Section 7.2). The conclusions may be seen as “answers” to the questions raised in Section 1.3, they also refer to the original contributions of this thesis described in Section 1.4.

### 7.1 Conclusions

#### 7.1.1 Composite “UHPFRC-concrete” elements

##### 1. UHPFRC enhance the performance of composite elements.

- The use of UHPFRC in composite “UHPFRC-concrete” elements leads to an *increased stiffness* under service conditions, i.e. the deformations remain smaller for given imposed loads when compared to traditional reinforced concrete elements. Moreover, crack widths and spacing are reduced and the formation of localized macrocracks is delayed. This is attributed to the high tensile strength and strain-hardening of UHPFRC.
- The high strengths of UHPFRC lead to a significant *increase in resistance* of the composite element, in particular when the thickness of the UHPFRC layer and the magnitude of hardening are sufficiently high.
- UHPFRC are successfully used in composite “UHPFRC-concrete” members to prevent the ingress of detrimental substances, i.e. they exert a *protection function* for the structural member. This is explained by their low permeability and by the small crack widths under service conditions ( $< 50 \mu\text{m}$ ).

##### 2. Composite “UHPFRC-concrete” elements show monolithic behaviour.

- No debonding of the UHPFRC layer occurs in composite “UHPFRC-concrete” elements due to internal deformations at early age and in the long-term. The influence of structural parameters such as cross-section geometry and static system on debonding is small. When autogenous shrinkage of UHPFRC is higher than  $1000 \mu\text{m/m}$ , debonding occurs at the free ends of the beams.<sup>14</sup>
- Composite “UHPFRC-concrete” elements behave in a monolithic way under service conditions. Only when localized macrocracks propagate through the UHPFRC layer perpendicular to the interface zone, interface cracks form. In general, this occurs near the maximum force, i.e. for loading far beyond service conditions. The interface cracks may develop into debonding cracks for composite elements without reinforcement in the UHPFRC layer (configuration P, beams NR). In elements with reinforcement in the UHPFRC layer (beams R, configurations PR and R), the interface cracks remain sufficiently small and do not cause debonding of the UHPFRC layer.

##### 3. Early age and long-term deformations in composite “UHPFRC-concrete” elements induce deformations and stresses that may lead to crack formation (of small widths).

Early age and long-term deformations in the composite “UHPFRC-concrete” members are mainly due to autogenous shrinkage and to a lower extent due to heat of hydration of the UHPFRC. The early age and long-term deformations lead to stresses in the composite member, since UHPFRC deformations are restrained by the existing concrete layer and the static system. The stresses are partially relaxed by UHPFRC viscoelasticity (creep). The parameter EMH is introduced to characterize the exploitation of the magnitude of hardening.

---

14. The magnitude of the UHPFRC used in the present study amounts to  $475 \mu\text{m/m}$  (at 28 days); magnitudes of  $1000 \mu\text{m/m}$  are very high and should not occur frequently.

In this study, the first cracking strength ( $f_{U,t,1st}$ ) in the UHPFRC is reached and distributed macrocracks form:

- in statically indeterminate systems (at 7 and 28 days for complete restraint and restraint of moment respectively),
- in statically determinate systems with thin UHPFRC layers ( $h_U \leq 1$  cm, at 26 days),
- for UHPFRCs with high magnitudes of autogenous shrinkage ( $\geq 750$   $\mu\text{m}/\text{m}$ ,  $f_{U,t,1st}$  is reached at less than 26 days, depending on the magnitude of autogenous shrinkage).

However, the maximum strain in the UHPFRC due to early age and long-term deformations is only 0.06%. This deformation is significantly smaller than the magnitude of hardening (i.e. only  $EMH = 5\%$  of the magnitude of hardening are exploited when  $\varepsilon_{U,hard} = 1\%$  and under the hypothesis of an elastic UHPFRC deformation of 0.01%)<sup>15</sup>. This means that no localized macrocracks form in the UHPFRC layer of composite elements due to “internal” deformations.

4. *The incorporation of reinforcement in the UHPFRC layer is an efficient way to increase resistance and enhance the structural response.*

- Stiffness and resistance of composite “UHPFRC-composite” elements are further increased when rebars are incorporated in the UHPFRC layer. The presence of rebars in the UHPFRC layer increases significantly (by three times) its apparent magnitude of hardening.
- Stress is transferred from the UHPFRC to the rebars when the UHPFRC enters the hardening and softening domain. In the softening domain of UHPFRC, this stress transfer leads to an enhanced structural response of the composite element: Less softening or even hardening in the composite element occurs with increasing reinforcement ratio after yielding of the tensile rebars.

5. *Three basic composite “UHPFRC-concrete” configurations are suggested for construction projects as well as for rehabilitation and improvement of existing structures (Figure 7.1).*

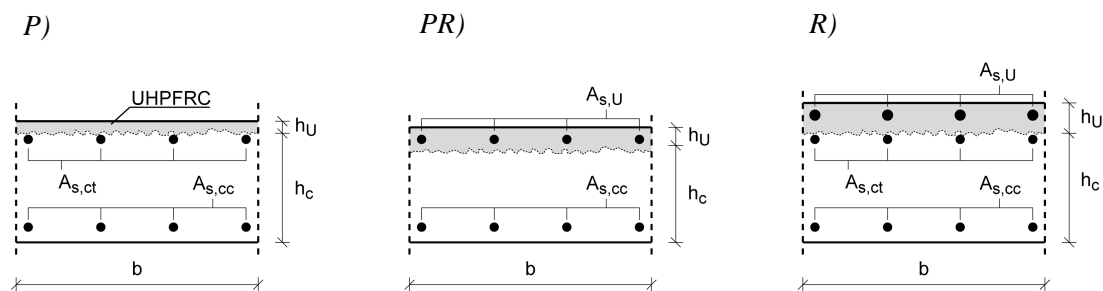


FIGURE 7.1: Basic configurations of composite “UHPFRC-concrete” elements

- *Configuration P* consists of a reinforced concrete substrate and a thin UHPFRC layer ( $h_U = 1$  to 3 cm). This configuration is recommended for rehabilitation and construction projects when only the protection function is required.
- *Configuration PR* is composed of a concrete substrate and a reinforced UHPFRC layer ( $h_U \approx 5$  cm). This configuration allows to obtain the required resistance and the protection function. It is recommended for new constructions and for rehabilitation projects when strongly deteriorated reinforcement in the existing concrete must be replaced.
- *Configuration R* consists of a reinforced concrete substrate and a reinforced UHPFRC layer ( $h_U \approx 5$  cm). This configuration is recommended for rehabilitation projects when the resistance must be increased in addition to the protection function.

15. except for magnitudes of autogenous shrinkage  $\geq 1000$   $\mu\text{m}/\text{m}$  which induce higher damage



6. *The tensile behaviour of UHPFRC and of rebars and their interaction determine the structural response at ultimate limit state.*

In configurations PR and R, minimum softening of the composite element is obtained by combining either an UHPFRC with a high magnitude of hardening with normal strength steel rebars or by using rebars with a pronounced hardening and UHPFRC having a small magnitude of hardening:

- When conventional rebars are chosen (e.g. B500 with  $f_{yk} = 500$  MPa), the best structural response is observed for a magnitude of hardening of the UHPFRC of  $\epsilon_{U,hard} = 1\%$ . The magnitude of hardening should not be smaller than  $\epsilon_{U,hard} = 0.2\%$ .
- When the magnitude of UHPFRC is relatively small (e.g.  $\epsilon_{U,hard} = 0.2\%$ ), tensile reinforcement with a high hardening modulus is advantageous. According to the parametric study, the composite element shows hardening behaviour until failure for a modulus of hardening of 45 GPa. Also the use of rebars made of composite materials (e.g. GFRC, AFRC, CFRC) leads to pronounced hardening behaviour of the structural element. This is explained by their high tensile strength and the relatively low modulus elasticity ( $E \approx 45$  to 120 GPa).

7. *Composite “UHPFRC-concrete” elements are recommended for use in real structures.*

The present study is limited to laboratory tests and to modelling. The results are promising, i.e. UHPFRC enhance the performance of structural elements. Processing of UHPFRC does not differ significantly from the processing of self-compacting concrete. Thus, the ground is prepared for the application of composite “UHPFRC-concrete” elements in real structures.

### 7.1.2 UHPFRC

8. *The tensile behaviour of UHPFRC is outstanding.*

- The tensile strength of the investigated UHPFRC is approximately three times higher than that of normal strength concrete and the magnitude of hardening amounts to 2.8%. These properties are determined in a reliable way by a uniaxial tensile test developed in this study.
- The tensile properties of UHPFRC depend significantly on specimen geometry and on the mode of loading. It is shown that the tensile properties determined with the uniaxial tensile test on notched specimens are higher than the apparent tensile properties of UHPFRC as deduced by inverse analysis from structural members.

9. *Autogenous shrinkage is the predominant part of internal UHPFRC deformations.*

- Autogenous shrinkage is strong during hardening of the UHPFRC, i.e. during the first 48 hours after casting (150  $\mu\text{m}/\text{m}$  at 48 hours). The high autogenous shrinkage (325  $\mu\text{m}/\text{m}$  at 7 days, 475  $\mu\text{m}/\text{m}$  at 28 days) is mainly caused by *high self-desiccation* (relative humidity = 88% at 7 days).
- The autogenous shrinkage of the tested UHPFRC is high, but not detrimental in case of full restraint: the maximum exploitation of the magnitude of hardening is only  $\text{EMH} = 5\%$ . This is also due to the beneficial effect of viscoelasticity. However, autogenous shrinkage may cause significant microcracking in case of high magnitudes ( $\geq 1000$   $\mu\text{m}/\text{m}$ ).

10. *The material properties of UHPFRC remain virtually constant beyond an age of 90 days.*

The determination of mechanical properties such as strengths, modulus of elasticity and shrinkage measurements show that the values do no more evolve beyond 90 days. This seems to indicate that hydration is largely stopped due to water shortage in the UHPFRC which is a consequence of high self-desiccation.

### 7.1.3 Modelling

11. *The existing numerical model [Femmasse04] allows to simulate correctly UHPFRC behaviour.*

Time-dependent behaviour of cementitious material is simulated with a FE-program considering thermo-hygro-chimico-mechanical couplings [Femmasse04]. The results show that almost all phenomena can be correctly simulated:

- UHPFRC viscoelasticity at early age and in the long-term is correctly modelled with the age-dependent generalized Maxwell chain model.
- The overall tensile behaviour is well modelled with the FE-program, however, the results are dependent on the mesh size, and crack localization is not always correctly captured.
- The hygral state in the UHPFRC, e.g. self-desiccation and external drying, is not correctly modelled with the FE-program in its present state. The relation between hydration reaction and relative humidity and the desorption isotherms for UHPFRC have to be determined and modelled properly and implemented in the numerical model.

12. *The time-dependent behaviour of composite “UHPFRC-concrete” elements is realistically simulated with the existing numerical model.*

The simulation of the time-dependent behaviour of composite “UHPFRC-concrete” elements with the numerical model [Femmasse04] is validated by the results of the beam tests. Early age and long-term deformations are simulated with a deviation smaller than 15% using models deduced from material laws. This demonstrates that UHPFRC behaviour can be well modelled when the autogenous shrinkage is considered as internal volumetric deformation, and that moisture exchange between UHPFRC and concrete and with the surrounding environment can be neglected. (It has to be noted that the hygral state of normal strength concrete evolves very slowly and is only virtually stationary beyond a certain concrete age (in this study: > 5 months).)

13. *The structural response of composite “UHPFRC-concrete” elements under bending is predicted with an analytical model.*

The analytical model provides an efficient tool to easily and rapidly determine the structural response of composite “UHPFRC-concrete” elements. It has been validated using results from the fracture tests on the composite beams and the literature. However, the analytical model requires the knowledge of the reference length and the length of plastic hinges which are still research topics for composite “UHPFRC-concrete” members.

## 7.2 Future work

1. *Do variable climatic conditions and loads alter the structural response of composite “UHPFRC-concrete” elements?*

- This study concentrates on the behaviour of composite “UHPFRC-concrete” elements under constant climatic conditions. The structural response due to time-dependent deformations and under loading is investigated separately. However, real structures are subjected simultaneously to climatic changes (mainly temperature, but also hygral changes) and to loading. In consequence, the variable climatic conditions and the interaction of loading and residual stresses should be investigated.
- Furthermore, the composite “UHPFRC-concrete” members may be subjected to fatigue loading, for example when used for bridge decks. Here, it is important to investigate crack propagation in the UHPFRC, the concrete and in the interface zone under high cycle fatigue. The UHPFRC behaviour under fatigue should mainly be studied for UHPFRC with distributed macrocracks or localized macrocracks.

## 2. Which structural composite members are most efficient?

- This study is limited to slender beams and slabs. The behaviour of other composite “UHPFRC-concrete” elements as for example deep beams and walls should be investigated. Furthermore, elements should be designed that have a sufficient resistance under bending on the compression side. This thesis only treats strengthening of the tension chord by UHPFRC which can be detrimental to the deformation capacity, since brittle fracture of the concrete in compression may occur before yielding of the tension chord. Thus, the efficiency of sandwich elements “UHPFRC-concrete-UHPFRC” should be investigated.
- The structural behaviour of composite elements can be improved by combining advanced materials and normal strength concrete. In particular, new elements should be designed in such a way that all materials are exploited with regard to their specific properties. A wide field of structural element types opens to determine the optimal use of concrete, UHPFRC, high performance reinforcement (rebars and prestress) and other materials (such as structural steel).

## 3. How are new composite “UHPFRC-concrete” members best designed and built?

In new constructions, the structural behaviour at early age may be different when compared to rehabilitation projects, since UHPFRC and concrete are both young at construction. The construction process and program should be adapted with respect to internal deformations in such a way that residual stresses and crack formation are minimized in the composite element, in particular at early age. Moreover, the moisture state in the interface zone should be investigated in order to determine the consequences in terms of resistance of the interface zone resulting from the hygral gradient between UHPFRC and concrete (due to the difference in self-desiccation between the two materials).

## 4. When do composite “UHPFRC-concrete” elements have sufficient deformation capacity?

- This study shows that softening occurs in the  $M-\kappa$ -curve when the reinforcement starts to yield. The influence of this softening on the response of the structural element must be investigated further.
- The modelling of the structural response after the formation of localized macrocracks in the UHPFRC depends strongly on the reference length  $L_R$  and on the length of plastic hinges  $L_{hi}$  which cannot be reliably predicted for composite “UHPFRC-concrete” elements at present. Consequently, it is necessary to determine the reference length and to develop a model that predicts the deformation capacity of composite “UHPFRC-concrete” members in a reliable way.

## 5. How are debonding and shear failure reliably predicted?

- Shear stresses are only marginally considered in this study and a verification based on linear elastic material behaviour is proposed. The conclusion that shear failure is not determinant in composite “UHPFRC-concrete” beams and slabs is mainly based on the test results. It is essential to investigate the stress state in composite “UHPFRC-concrete” members and to determine whether a model considering stress fields and stress flow is more adapted for structures containing UHPFRC than a model considering principal and shear stresses.
- The critical part in composite “UHPFRC-concrete” members is the interface zone. A model should be developed to predict the debonding risk in composite elements without localized macrocracks and at crack tips when localized macrocracks penetrate to the interface.

## 6. What are UHPFRC creep mechanisms under high tensile stresses?

- Viscoelasticity relaxes stresses in composite elements. The viscoelasticity is determined for the UHPFRC for a loading age of 0 to 7 and of 28 days and only few test results exist. Thus, it is essential to investigate the viscoelastic behaviour of UHPFRC at early age and in the long-term with regard to thermal and hygral influences and for different load levels. For composite “UHPFRC-concrete” members, it is particularly important to determine the viscoelastic behaviour

under tension at high load levels, i.e. near the first cracking strength and in the hardening domain.

- The mechanisms of UHPFRC viscoelasticity should be determined, in particular the contribution of microcracking, since microcracking may reduce stiffness and increase permeability of the UHPFRC.

*7. How is the hygral state in UHPFRC best modelled?*

The determination of the hygral state in UHPFRC is of fundamental interest, since autogenous shrinkage, which is the main contribution to internal UHPFRC deformations, is primarily caused by self-desiccation. Therefore, the determination of hygral UHPFRC properties constitutes the basis for the modelling of self-desiccation shrinkage. For this, it is necessary to determine UHPFRC desorption isotherms in function of age and to develop a model to predict self-desiccation on the basis of mix design and material parameters.

*8. How are UHPFRC tensile properties correctly predicted?*

- The influence of specimen geometry and test method on UHPFRC tensile properties should be studied further to develop a method which allows to deduce the UHPFRC tensile properties from material tests in a reliable way in order to predict the structural response of composite “UHPFRC-concrete” members.
- A model should be developed that predicts tensile strength and hardening on the basis of UHPFRC matrix properties and steel fibre characteristics.
- Anisotropy and variability in UHPFRC tensile properties should be determined with respect to processing and possible stress states in the structural element.

*9. How does reinforced UHPFRC work?*

Rebars increase the magnitude of hardening of UHPFRC, however, the degree of efficiency of rebars should be expressed on the basis of material properties and the mechanisms of interaction between UHPFRC and rebars should be determined and quantified. It is particularly important to quantify the influence of rebars on the apparent magnitude of hardening of the UHPFRC. Furthermore, tests should be performed in order to determine the bond-slip law between UHPFRC and rebars and the mechanically necessary UHPFRC cover to avoid splitting cracks under bending.

*10. How is it possible to tailor specific UHPFRC?*

Presently, several types of UHPFRC have been developed. However, the different UHPFRC are designed on an empirical basis under consideration of several scientific principles. The aim should be to develop a design method that allows to determine the UHPFRC composition on the basis of the demands on the structure, e.g. the design would be based on a given magnitude of hardening or a limit of permeability. So, it would be possible to tailor UHPFRC for each specific application.

## 8 References

- [Aarup04] Aarup B., *CRC - A Special Fibre Reinforced Reinforced High Performance Concrete*, RILEM Symposium, Advances in Concrete Through Science and Engineering, March 22-24, Evanston, USA, March, 2004, 6 p, CD-ROM.
- [Abrishami97] Abrishami H. H., Mitchell D., *Influence of Steel Fibers on Tension Stiffening*, ACI Structural Journal, Vol. 94, No. 6, November-December, 1997, pp 769-776.
- [Acker01] Acker P., *Micromechanical analysis of creep and shrinkage mechanisms*, Creep, Shrinkage and Durability Mechanics of Concrete and other Quasi-Brittle Materials (Concreep 6), Ed. by F.-J. Ulm, Z. P. Bazant and F. H. Wittmann, Boston, USA, August, 2001, pp 15-25.
- [Acker01a] Acker P., Ulm F. J., *Creep and shrinkage of concrete: physical origins and practical measurements*, Nuclear Engineering and Design, Vol. 203, No. 2, 2001, pp 143-158.
- [AFGC02] Association Française du Génie Civil, *Bétons fibrés à ultra-hautes performances (Ultra high performance fibre-reinforced concretes)*, SETRA - Service d'études techniques des routes et autoroutes, AFGC, France, January, 2002, 152 p.
- [Alaee03] Alaee F. J., Karihaloo B., *Retrofitting of Reinforced Concrete Beams with CARDIFRC*, ASCE Journal of Composites for Construction, Vol. 7, No. 3, August, 2003, pp 174-186.
- [Alford85] Alford N. McN., Birchall J. D., *The properties and potential applications of Macro-Defect-Free Cement*, Symposium on very high strength cement-based materials, Ed. by J. F. Young, Materials Research Society symposia proceedings, Vol. 42, Pittsburgh, USA, 1985, pp 265-276.
- [Alkubaisy75] Al-Kubaisy M.A., Young A.G., *Failure of concrete under sustained tension*, Magazine of Concrete Research, Vol. 27, No. 92, September, 1975, pp. 171-178.
- [Altoubat02] Altoubat S. A., Lange D., *The Pickett effect at early age and experiment separating its mechanisms in tension*, Materials and Structures, Vol. 35, No. 248, May, 2002, pp 211-218.
- [Attiogbe88] Attiogbe E.K., Darwin D., *Strain due to submicrocracking in cement paste and mortar*, ACI Materials Journal, Vol. 85, No. 1, USA, January-February, 1988, pp 3-11.
- [Bache87] Bache H. H., *Introduction to Compact Reinforced Composite*, Nordic concrete research, No. 6, pp 19-33, 1987.
- [Baker61] Baker A. L. L., *Note for discussion at Monaco*, Comité euro-international du béton (CEB), Bulletin d'information No. 30, Lausanne, Switzerland, 1961.
- [Bangham37] Bangham D. H., *The Gibbs adsorption equation and adsorption on solids*, Transactions of the Faraday Society, London, England, Vol. 33, 1937, pp 805-811.
- [Barcelo01] Barcelo L., Boivin S., Acker P., Toupin J., Clavaud B., *Early age shrinkage of concrete: back to physical phenomena*, Concrete Science and Engineering, Vol. 3, No. 10, June, 2001, pp 85-91.
- [Barcelo02] *Chemical shrinkage*, Early Age Cracking in Cementitious Systems, Report of Technical Committee 181-EAS: Early age shrinkage induced stresses and cracking in cementitious systems, Ed. by A. Bentur, RILEM Report 25, France, July, 2002, pp 21-25.
- [Bazant72] Bazant Z., Najjar L. J., *Nonlinear water diffusion in nonsaturated concrete*, Materials and Structures, Vol. 5, No. 25, 1972, pp 3-20.
- [Bazant72a] Bazant Z. P., *Numerical determination of long-range stress history from strain history in concrete*, Materials and Structures, Vol. 5, No. 27, 1972, pp 135-141.
- [Bazant74] Bazant Z., Wu S.T., *Rate-type creep law of aging concrete based on Maxwell chain*, Materials and Structures, Vol. 7, No. 37, 1974, pp 45-60.
- [Bazant83] Bazant Z. P., Oh B., *Crack band theory for fracture of concrete*, Materials and Structures, Vol. 16, No. 93, 1983, pp 155-177.

- [Bazant85] Bazant Z., Chern J.C., *Concrete creep at variable humidity constitutive law and mechanism*, Materials and Construction, Vol. 18, No. 103, 1985, pp 1-20.
- [Bazant87] Bazant Z., Chern J.C., *Stress-Induced Thermal and Shrinkage Strains in Concrete*, ASCE Journal of Engineering Mechanics, Vol. 113, No. 10, 1987, pp 1493-1511.
- [Bazant98] Bazant Z., Planas J., *Fracture and Size Effect in Concrete and Other Quasibrittle Materials*, New Directions in Civil Engineering, CRC Press, Boca Raton, 1998, pp. 616.
- [Behloul03] Behloul M., Kicul C. L., *Ductal<sup>®</sup> Seonyu footbridge*, Structural concrete, Journal of the fib, Vol. 4, No. 4, December, 2003, pp 195-201.
- [Bekaert99] Bekaert A., Behloul M., Dugat J., Adeline R., Lacombe H., *Centrale EDF de Cattenom - Du béton de poudres réactives (BPR) pour le nucléaire*, Travaux, No. 752, April, 2001, pp 69-72 (in French).
- [Bentur02] Bentur, A., *Terminology and definitions*, Early Age Cracking in Cementitious Systems, Report of Technical Committee 181-EAS: Early age shrinkage induced stresses and cracking in cementitious systems, Ed. by A. Bentur, RILEM Report 25, France, July, 2002, pp 13-15.
- [Bernard00] Bernard O., *Comportement à long terme des éléments de structure formés de bétons d'âges différents*, Doctoral Thesis, No. 2283, Swiss Federal Institute of Technology (EPFL), Lausanne, Switzerland, 2000, 190 p. (in French).
- [Bernard00a] Bernard O., *Comportement à long term des éléments de structure formés de bétons d'âges différents*, Test report, EPFL-MCS96.01.01, Swiss Federal Institute of Technology (EPFL), Lausanne, Switzerland, November, 2000, 238 p (in French).
- [Bernard01] Bernard O., Denarié E., Brühwiler E., *Comportement au jeune âge du béton et limitation de la fissuration traversante des structures hybrides*, Report VSS, 1997/064 (82/97), Swiss Federal Roads Authority, Swiss Association of Road and Transportation Experts, Lausanne, Switzerland, October, 2001, 116 p. (in French).
- [Bernard02] Bernard O., Brühwiler E., *Influence of autogenous shrinkage on early age behaviour of structural elements consisting of concretes of different ages*, Materials and Structures, Vol. 35, No. 235, November, 2002, pp 550-556.
- [Bernard03] Bernard O., Brühwiler E., *The effect of reinforcement in the new layer on hygral cracking in hybrid structural elements*, Materials and Structures, Vol. 36, No. 256, March, 2003, pp 118-126.
- [Bissonnette00] Bissonnette B., Pigeon M., *Le comportement viscoélastique du béton en traction et la compatibilité déformationnelle des réparations*, Materials and Structures, Vol. 33, No. 226, March, 2000, pp 108-118 (in French).
- [Bonneau97] Bonneau O., Lachemi M., Dallaire E., Dugat J., Aïtcin P-C., *Mechanical Properties and Durability of Two Industrial Reactive Powder Concretes*, ACI Materials Journal, Vol. 94, No. 4, July-August, 1997, pp 286-290.
- [Boulay03] Boulay C., Arca A., Tailhan J-L., Rossi P., Sananes J., *Comportement mécanique d'un nouveau composite cimentaire à écrouissage positif. II : Caractérisation du comportement en traction uniaxiale*, Bulletin des Laboratoires des Ponts et Chaussées, No. 243, LCPC, France, March-April, 2003, pp 19-30 (in French).
- [Brenni95] Brenni P., *Il comportamento al taglio di una struttura a sezione mista in calcestruzzo a getti successivi*, IBK-Report, No. 211, Swiss Federal Institute of Technology (ETHZ), Zürich, Switzerland, September, 1995, 150 p. (in Italian).
- [Broquet99] Broquet C., *Comportement dynamique des dalles de roulement des ponts en béton sollicités par le trafic routier*, Doctoral thesis, No. 1964, Swiss Federal Institute of Technology (EPFL), Lausanne, Switzerland, 1999, 171 p. (in French).
- [Brühwiler88] Brühwiler E., *Bruchmechanik von Staumauerbeton unter quasi-statischer und erdbebendynamischer Belastung*, Doctoral thesis, No. 739, Swiss Federal Institute of Technology (EPFL), Lausanne, Switzerland, 1988, 169 p. (in German).

- [Brühwiler00] Brühwiler E., Bernard O., Wolf S., *Beton-Beton Verbundbauteil bei der Verbreiterung eines Brückenüberbaus - Massnahmen zur Begrenzung der Rissbildung im neuen Beton*, Beton- und Stahlbetonbau, Vol.95, No. 3, March, 2000, pp 158-166 (in German).
- [Brühwiler04] Brühwiler E., Denarié E., Wälchli T., Maitre M., Conciatori D., *Dauerhafte Kunstbauten bei geringem Unterhalt (Ouvrages d'art durables à entretien minimal)*, final draft, Report VSS, 2000/173 (88/00), Swiss Federal Roads Authority, Swiss Association of Road and Transportation Experts, Lausanne, Switzerland, April, 2004 (in German).
- [Brunauer73] Brunauer S., Yudenfreund M., Odler I., Skalny J., *Hardened Portland Cement Pastes of Low Porosity, VI. Mechanism of the Hydration Process*, Cement and Concrete Research, Vol. 3, No. 2, 1973, pp 129-147.
- [Brunauer73a] Brunauer S., Skalny J., Odler I., Yudenfreund M., *Hardened Portland Cement Pastes of Low Porosity, VII. Further Remarks about Early Hydration. Composition and Surface Area of Tobermorite Gel. Summary*, Cement and Concrete Research, Vol. 3, No. 3, 1973, pp 279-293.
- [Byfors82] Byfors J., *Mechanical properties*, International Conference on Concrete at Early Ages, Vol. 2, Ecole Nationale des Ponts et Chaussées (ENPC), Paris, France, April, 6-8, 1982, pp 13-33.
- [Carino94] Carino N. J., *The Maturity Method: Theory and Application*, Cement, Concrete and Aggregates, Vol. 6, No. 2, 1984, pp 61-73.
- [Casanova94] Casanova P., Le Maou F., Renwez S., Rossi P., *Calcul du béton de fibres métalliques: poutre en flexion simple*, Bulletin de liaison des laboratoires des ponts et chaussées, No. 191, France, May-June, 1994, pp 73-85 (in French).
- [CEB204] CEB, *CEB-FIP Model Code 1990*, Comité euro-international du béton (CEB), Bulletin d'Information 204, Lausanne, Switzerland, July, 1991.
- [CEB242] CEB, *Ductility of reinforced concrete structures - Synthesis Report and Individual Contributions*, Comité euro-international du béton (CEB), Bulletin d'Information 242, Lausanne, Switzerland, May, 1998, 332 p.
- [Charif98] Charif H., Mivelaz P., *Construction de la nouvelle usine GENEX 4 à Genève*, Report 497.023-3.2, ESM Charif & Mivelaz, St Sulpice, Switzerland, 1998 (in French).
- [Charron02] Charron J-P., Marchand J., Bissonnette B., Pigeon M., *Test device for studying the early-age stresses and strains in concrete*, American Concrete Institute Fall Convention, Ed. by O. M. Jensen, D. P. Bentz and P. Lura, Phoenix, USA, 2002, 17 p.
- [Charron03] Charron J-P., *Contribution à l'étude du comportement au jeune âge des matériaux cimentaires en conditions des déformations libre et restreinte*, PhD thesis, CRIB, University Laval, Québec, Québec, Canada, April, 2003, 373 p. (in French).
- [Charron04] Charron J-P., Denarié E., Brühwiler E., *Permeability of UHPFRC under high stresses*, RILEM Symposium, Advances in Concrete Through Science and Engineering, March 22-24, Evanston, USA, 2004, 12 p. CD-ROM.
- [Chausson97] Chausson H., Granju J.-L., *Optimized design of fiber reinforced thin bonded overlays*, 5th International Symposium on Brittle Matrix Composites, Warsaw, Poland, October, 1997, pp 133-142.
- [Cheyrezy95] Cheyrezy M., Maret V., Frouin L., *Microstructural analysis of RPC (Reactive Powder Concrete)*, Cement and Concrete Research, Vol. 25, No. 7, July, 1995, pp 1491-1500.
- [Cheyrezy97] Cheyrezy M., *Structural Applications of RPC*, International Conference - New technologies in structural engineering, Vol. 1, Lisbon, Portugal, July, 1997, pp 5-14.
- [Cheyrezy01] Cheyrezy M., Behloul M., *Creep and Shrinkage of Ultra-High Performance Concrete*, Creep, Shrinkage and Durability Mechanics of Concrete and other Quasi-Brittle Materials (Concreep 6), Ed. by F.-J. Ulm, Z. P. Bazant and F. H. Wittmann, Boston, USA, August, 2001, pp 527-538.
- [Cosenza91] Cosenza E., Greco C., Pecce M., *Nonlinear design of Reinforced Concrete Continuous beams*, Structural Engineering International, Vol. 1 No. 1, February, 1991, pp 19-27.

- [Courard99] Courard L., *Contribution à l'analyse des paramètres influençant la création de l'interface entre un béton et un système de réparation*, University of Liège, Collection des Publications de la Faculté des Sciences Appliquées, No. 192, Liège, Belgium, 1999, 198 p. (in French).
- [DeLarrard94] De Larrard F., Sedran T., *Optimization of Ultra-High-Performance Concrete by the Use of a Packing Model*, Cement and Concrete Research, Vol. 24, No. 6, June, 1994, pp 997-1009.
- [DeLarrard99] De Larrard F., *Concrete mixture Proportioning - A scientific approach*, Modern concrete technology 9, E & FN SPON, London, England, 1999, 421 p.
- [Denarie00] Denarié E., *Etude expérimentale des couplages viscoélasticité-croissance des fissures dans les bétons de ciment*, Doctoral Thesis, No. 2195, Swiss Federal Institute of Technology (EPFL), Lausanne, Switzerland, 2000 207 p. (in French).
- [Denarie01] Denarié E., Brühwiler E., *Comportement d'Eléments de Structure Hybrides formés de béton Traditionnel et de Matériaux Cimentaires Avancés*, Regroupement Francophone pour la Recherche et la Foration sur le Béton ((RF)<sub>2</sub>B), Québec, Canada, August, 2001, 4 p. (in French).
- [Denarie03] Denarié E., Habel K., Brühwiler E., *Structural behavior of hybrid elements with Advanced Cementitious Materials (HPFRCC)*, RILEM Proceedings PRO 30, 4th International Workshop on High Performance Fiber Reinforced Cement Composites (HPFRCC-4), Ed. by A. E. Naaman and H. W. Reinhardt, Ann Arbor, USA, June, 2003, pp 301-312.
- [Denarie04] Denarié E., *personal communication*, Swiss Federal Institute of Technology (EPFL), Lausanne, Switzerland, 2004.
- [DeSchutter96] De Schutter G., Taerwe L., *Degree of hydration-based description of mechanical properties of early age concrete*, Materials and Structures, Vol. 29, No. 190, July, 1996, pp 335-344.
- [DeSchutter00] De Schutter G., *Fictitious degree of hydration method for the basic creep of early age concrete*, Materials and Structures, Vol. 33, No. 230, July, 2000, pp 370-380.
- [DeSchutter02] *Short-term mechanical properties*, Early Age Cracking in Cementitious Systems, Report of Technical Committee 181-EAS: Early age shrinkage induced stresses and cracking in cementitious systems, Ed. by A. Bentur, RILEM Report 25, France, July, 2002, pp 101-109.
- [DeSchutter02a] *Visco-elastic response*, Early Age Cracking in Cementitious Systems, Report of Technical Committee 181-EAS: Early age shrinkage induced stresses and cracking in cementitious systems, Ed. by A. Bentur, RILEM Report 25, France, July, 2002, pp 111-120.
- [Ducret97] Ducret J-M., *Etude du comportement réel des ponts mixtes et modélisation pour le dimensionnement*, Swiss Federal Institute of Technology (EPFL), Doctoral thesis, No. 1738, Lausanne, Switzerland, 1997, 185 p. (in French).
- [Dugat96] Dugat J., Roux N., Bernier G., *Mechanical Properties of Reactive Powder Concretes*, Materials and Structures, Vol. 29, No. 188, May, 1996, pp 233-240.
- [Dupont03] Dupont D., *Modelling and experimental validation of the constitutive law ( $\sigma$ - $\epsilon$ ) and cracking behaviou rof steel fibre reinforced concrete*, Doctoral thesis, Faculty of Applied Science, Catholic University of Leuven, Leuven, Belgium, October, 2003, 256 p.
- [EC01] *Eurocode 1, Draft pr EN 1990 - Eurocode: Basis of Structural Design*, European Committee of Standardization (CEN), Stage 34, Brussels, Belgium, December, 2000, 88 p.
- [Emberson96] Emberson N. K., Mays G. C., *Significance of property mismatch in the patch repair of structural concrete, Part 3: Reinforced concrete members in flexure*, Magazine of Concrete Research, Vol. 48, No. 174, March, 1996, pp 45-57.
- [Emborg89] Emborg M., *Thermal stresses in concrete structures at early ages*, Doctoral thesis, Division of structural engineering, Lulea University of Technology, 189:73 D, Lulea, Sweden, 1989, 285 p.



- [Emmons00] Emmons P. H., Vaysburd A. M., McDonald J. E., Poston R.W., Kesner K., *Selecting Durable Repair Materials: Performance Criteria*, Concrete International, Vol. 22, No. 3, March, 2000, pp 38-45.
- [EN206] EN206, *Beton - Teil 1: Festlegung, Eigenschaften, Herstellung und Konformität*, EN 206-1:2000, SIA, Zürich, Switzerland, 2000, 83 p. (in German).
- [Feldmann68] Feldmann R. F., Sereda P. J., *A model for hydrated Portland cement paste as deduced from sorption-length change and mechanical properties*, Materials and Structures, Vol. 1, Nr. 6, 1968, pp 509-520.
- [Femmasse04] *Finite Element Modules for Materials Science and Structural Engineering*, website, Retrieved: April 20, 2004, from <http://www.femmasse.com>.
- [Ferraris87] Ferraris C.F., Wittmann F.H., *Shrinkage mechanisms of hardened cement paste*, Cement and Concrete Research, Vol. 17, No. 3, 1987, pp. 453-463.
- [fib10] *Bond of reinforcement in concrete: state-of-art report prepared by Task Group Bond models*, Fédération Internationale du Béton (fib), fib Bulletin, No. 10, Lausanne, Switzerland, August, 2000, 427pp.
- [Fischer02] Fischer G., Li V. C., *Influence of Matrix Ductility on Tension-Stiffening Behavior of Steel Reinforced Engineered Cementitious Composites (ECC)*, ACI Structural Journal, Vol. 99, No. 1, January-February, 2002, pp 104-111.
- [Gamble78] Gamble B. R., Parrott L. J., *Creep of Concrete in Compression during Drying and Wetting*, Magazine of Concrete Research, Vol. 30, No. 104, September, 1978, pp 129-138.
- [Gartner89] Gartner E. M., Gaidis J. M., Grace W. R., *Hydration mechanisms I*, Materials Science of Concrete I, Ed. by J. Skalny, American Ceramics Society, Westerville, USA, 1989, pp 95-125.
- [Gibbon98] Gibbon G. J., Ballim Y., *Determination of the thermal conductivity of concrete during the early age stages of hydration*, Magazine of Concrete Research, Vol. 50, No. 3, September, 1998, pp 229-235.
- [Goto71] Goto Y., *Cracks formed in concrete around deformed tension bars*, ACI Journal Proceedings, Vol. 68, No. 4, April, 1971, pp 244-251.
- [Granju01] Granju J.-L., *Debonding of Thin Cement-Based Overlays*, ASCE Journal of Materials in Civil Engineering, Vol. 13, No. 2, March-April, 2001, pp 114-120.
- [Guandalini04] Guandalini S., Muttoni A., *Essais de poinçonnement symétrique des dalles en béton armé sans armature à l'effort tranchant*, Test report, 00.03-R1, Swiss Federal Institute of Technology (EPFL), Lausanne, Switzerland, 2004, to be published (in French).
- [GuenotDelahaie97] Guénot-Delahaie I., *Contribution à l'analyse physique et à la modélisation du fluage propre du béton*, Doctoral thesis, Laboratoire Central des Ponts et Chaussées (LCPC), France, April, 1997, 180 p. (in French).
- [Haardt91] Haardt P., *Zementgebundene und kunststoffvergütete Beschichtungen auf Beton*, Doctoral thesis, Massivbau und Baustofftechnologie, University of Karlsruhe, Karlsruhe, Germany, 1991, 201 p. (in German).
- [Habel00] Habel K., Bernard O., Brühwiler E., *The Numerical Investigation of Delamination in Hybrid Reinforced Concrete Elements*, 3rd International PhD Symposium in Civil Engineering, fib, Ed. K. Bergmeister, Vol. 2, Vienna, Austria, October, 2000, pp 221-228.
- [Habel04] Habel K., *Structural behaviour of "UHPFRC - concrete" elements*, Test report, MCS99.04, Swiss Federal Institute of Technology (EPFL), Lausanne, Switzerland, 2004.
- [Hamza96] Hamza A. M., Naaman A. E., *Bond Characteristics of Deformed Reinforcing Steel Bars Embedded in SIFCON*, ACI Materials Journal, Vol. 93, No. 6, November-December, 1996, pp 578-588.
- [Hansen86] Hansen T. C., *Physical structure of hardened cement paste. A classical approach*, Materials and Structures, Vol. 19, No. 114, 1986, pp 423-436.

- [Hauggaard99] Hauggaard A.B., Damkilde L., Hansen P. F., *Transitional Thermal Creep of Early Age Concrete*, ASCE, Journal of Engineering Mechanics, April, 1999, pp 458-465.
- [Helbling87] Helbling A., Brühwiler E., *Eine neue Halterung für Zugversuche mit Beton-Probekörper*, Material und Technik, No. 4, Switzerland, 1987, pp 103-107 (in German).
- [Hillerborg83] Hillerborg A., *Analysis of a single crack*, Fracture mechanics of concrete Ed. by F.H.Wittmann, Elsevier science Publishers B.V., Amsterdam, Netherlands, 1983, pp 223-249.
- [Holschemacher03] Holschemacher K., Dehn F., *Ultrahochfester Beton (UHFB) - Stand der Technik und Entwicklungsmöglichkeiten*, Ultrahochfester Beton, Innovationen im Bauwesen - Beiträge aus Praxis und Wissenschaft, Ed. by G. König, K. Holschemacher, F. Dehn, Bauwerk, Berlin, Leipzig, Germany, 2003 pp 1-12 (in German).
- [Hua95] Hua C., Acker P., Ehrlacher A., *Analyses and Models of the Autogenous Shrinkage of Hardening Cement Paste, I. Modelling at macroscopic scale*, Cement and Concrete Research, Vol. 25, No. 7, 1995, pp 1457-1468.
- [Jennings00] Jennings H. M., *A model for the microstructure of calcium silicate hydrate in cement paste*, Cement and Concrete Research, Vol. 30, No. 1, 2000, pp 101-116.
- [Jennings04] Jennings H. M., *Colloid model of C-S-H and implications to the problem of creep and shrinkage*, Materials and Structures, Vol. 27, No. 265, January-February, 2004, pp 59-70.
- [Jensen95] Jensen O. M., *Thermodynamic limitation of self-desiccation*, Cement and Concrete Research, Vol. 25, No. 1, January, 1995, pp 157-164.
- [Jensen96] Jensen O. M., Hansen P. F., *Autogenous deformation and change of the relative humidity in silica fume-modified cement paste*, ACI Materials Journal, Vol. 93, No. 6, 1996, pp 539-543.
- [Jensen01] Jensen O. M., Hansen P. F., *Autogenous RH-change and deformation - Exercise*, Behaviour and Performance of Early Age Concrete, Shortcourse organized by D. A. Lange and H. Stang, Technical University of Denmark (DTU), Lyngby, Denmark, July, 2001, 5 p.
- [Jensen01a] Jensen O. M., Hansen P. F., *Autogenous deformation and RH-change in perspective*, Cement and Concrete Research, Vol. 31, No. 12, December, 2001, pp 1859-1865.
- [Jones02] Jones M. R., Zheng L., Newlands M. D., *Comparison of particle packing models for porportioning concrete constituents for minimum voids ratio*, Materials and Structures, Vol. 35, No. 249, June, 2002, pp 301-309.
- [Kada02] Kada H., Lachemi M., Petrov N., Bonneau O., Aïtcin P.-C., *Determination of the coefficient of thermal expansion of high performance concrete from initial setting*, Materials and Structures, Vol. 35, No. 245, January-February, 2002, pp 35-41.
- [Kendall83] Kendall K., Howard A. J., Birchall J. D., *The relation between porosity, microstructure and strength, and the approach to advanced cement-based materials*, Philosophical Transactions of the Royal Society of London, A 310, London, England, 1983, pp 139-153.
- [Kim03] Kim K.-H., Jeon S.-E., Kim J.-K., Yang S., *An experimental study on thermal conductivity of concrete*, Cement and Concrete Research, Vol. 33, No. 3, 2003, pp 363-371.
- [Kosa91] Kosa K., Naaman A. E., Hansen W., *Durability of Fiber Reinforced Mortar*, ACI Materials Journal, Vol. 88, No. 3, May-June, 1991, pp 310-319.
- [Kranz99] Kranz St., *Lokale Schwind- und Temperaturgradienten in bewehrten, oberflächennahen Zonen von Betonstrukturen*, Doctoral thesis, Heft 35, Massivbau und Baustofftechnologie, University of Karlsruhe, Karlsruhe, Germany, 1999, 377 p. (in German).
- [Krstulovic96] Krstulovic-Opara N., Toutanji H., *Infrastructural repair and retrofit with HPFRCCs, High Performance Fiber Reinforced Concrete Composites 2 (HPFRCC 2)*, Ed. by A. E. Naaman and H. W. Reinhardt, RILEM, Proceedings 31 Ann Arbor, USA, June, 1996, pp 423-442,.

- [Krstulovic97] Krstulovic-Opara N., Dogan E., Uang C.-M., Haghayeghi A. R., *Flexural Behavior of Composite R.C.-Slurry Infiltrated Mat Concrete (SIMCON) Members*, ACI Structural Journal, Vol. 94, No. 5, September - October, 1997, pp 502-512.
- [Laplante94] Laplante P., Boulay C., *Evolution du coefficient de dilatation thermique du béton en fonction de sa maturité aux tout premiers âges.*, Materials and Structures, Vol. 27, No. 174, USA, 1994, pp 596-605.
- [Laube90] Laube M., *Werkstoffmodell zur Berechnung von Temperaturspannungen in massigen Betonbauteilen in jungen Alter*, Doctoral thesis, University of Braunschweig, Braunschweig, Germany, May, 1990, 251 p. (in German).
- [Lemberg96] Lemberg M., *Dichtschichten aus hochfestem Faserbeton*, Deutscher Ausschuss für Stahlbeton, (DAfStb), Beuth Verlag GmbH, No. 465, Berlin, Germany, 1996, pp 1-163 (in German).
- [Li00] Li V. C., Horii H., Kabele P., Kanda T., Lim Y. M., *Repair and retrofit with engineered cementitious composites*, Engineering fracture mechanics, Vol. 65, No. 2-3, 2000, pp 317-334.
- [Lim02] Lim Y. M., Kim M. K., Kim J. H. J., Shin S. K., *Is ductility important for repair application?*, Proceedings of the JCI international Workshop on Ductile Fiber Reinforced Cementitious Composites (DFRCC) - Application and Evaluation (DFRCC-02), Takayama, Japan, October, 2002, pp 199-208.
- [Locher76] Locher F. W., Richartz W., Sprung S., *Erstarren von Zement - Teil 1: Reaktion und Gefügeentwicklung (Setting of cement - Part 1: Reaction and development of structure)*, Zement, Kalk, Gips, Vol. 29, No. 10, October, 1976, pp 435-442 (in German).
- [Loukili96] Loukili A., *Etude du retrait et du fluage de Bétons à Ultra-Hautes Performances*, Doctoral thesis, Ecole Centrale Nantes, Nantes, France, November, 1996, 155 p (in French).
- [Martinola01] Martinola G., Sadouki H., Wittmann F. H., *Numerical model for minimizing risk of damage in repair systems*, ASCE Journal of Materials in Civil Engineering, Vol. 13, No. 2, March-April, 2001, pp 121-129.
- [Martinola02] Martinola G., Bäuml M. F., Wittmann F. H., *Modified ECC applied as an effective chloride barrier*, Proceedings of the JCI international Workshop on Ductile Fiber Reinforced Cementitious Composites (DFRCC) - Application and Evaluation (DFRCC-02), Takayama, Japan, October, 2002, pp 171-180.
- [Massicotte03] Massicotte B., *Design of SFRC members in flexure: application to a building floor*, Dimensionato de estruturas de betão reforçado com fibras de aço, Ed. by J. Barros, P. Rossi, B. Massicotte, DEC-UM, Portugal, 2003, p. 4.1-4.17.
- [Mensi88] Mensi R., Acker P., Attolou A., *Séchage du béton: analyse et modélisation*, Materials and Structures, Vol. 21, No. 121, 1988, pp 3-12 (in French).
- [Morin01] Morin V., Cohen Tounedji F., Feylessoufi A., Richard P., *Superplasticizer effects on setting and structuration mechanisms of ultrahigh-performance concrete*, Cement and Concrete Research, Vol. 31, No. 1, 2001, pp 63-71.
- [Morin02] Morin V., Cohen-Tenoudji F., Feylessoufi A., Richard P., *Evolution of the capillary network in a reactive powder concrete during hydration process*, Cement and Concrete Research, Vol. 32, No. 12, 2002, pp 1907-1914.
- [Muttoni97] Muttoni A., Schwartz J., Thürlimann B., *Bemessung von Betontragwerken mit Spannungsfeldern*, Birkhäuser, Basel, Switzerland, 1997, 145 pp (in German).
- [Naaman02] Naaman A. E., *Toughness, ductility, surface energy and deflection-hardening FRC composites*, Proceedings of the JCI international Workshop on Ductile Fiber Reinforced Cementitious Composites (DFRCC) - Application and Evaluation (DFRCC-02), Takayama, Japan, October, 2002, pp 33-57.

- [Neville70] Neville A., *Creep of Concrete: Plain, Reinforced and Prestressed*, North-Holland Publishing Company, Amsterdam, the Netherlands, 1970, 622 p.
- [Neville95] Neville A., *Properties of concrete*, Adison Wesley Longman Limited, 4th edition, Harlow, England, 1995.
- [Odler72] Odler I., Yudenfreund M., Skalny J., Brunauer S., *Hardened Portland Cement Pastes of Low Porosity, III. Degree of Hydration. Expansion of Paste, Total Porosity*, Cement and Concrete Research, Vol. 2, No. 4, 1972, pp 463-480.
- [Odler72a] Odler I., Hagymassy J., Bodor E. E., Yudenfreund M., Brunauer S., *Hardened Portland Cement Pastes of Low Porosity, IV. Surface Area and Pore Structure*, Cement and Concrete Research, Vol. 2, No. 5, 1972, pp 577-589.
- [Orange00] Orange G., Dugat J., Acker P., *DUCTAL: New Ultra High Performance Concretes. Damage, Resistance and Micromechanical Analysis*, Fifth RILEM Symposium on Fiber-Reinforced Concretes (FRC) (BEFIB 2000), Ed. by P. Rossi and G. Chanvillard, Lyon, France, September, 2000, pp 781-790.
- [Parant03] Parant E., *Mécanismes d'endommagement et comportements mécaniques d'un composite cimentaire fibré multi-échelles sous sollicitations sévères: fatigue, choc, corrosion*, Doctoral thesis, Laboratoire Central des Ponts et Chaussées (LCPC), France, December, 2003, 245 p. (in French).
- [Pfyl03] Pfyl Th., *Tragverhalten von Stahlfaserbeton*, Doctoral thesis, IBK-Report, No. 279, Swiss Federal Institute of Technology (ETHZ), Zürich, Switzerland, February, 2003, 140 p. (in German).
- [Pickett42] Pickett G., *The Effect of Change in Moisture-Content on the Creep of Concrete Under a Sustained Load*, Research Laboratory of the Portland Cement Association, Bull. 11, Detroit, USA, March, 1942, 80 p.
- [Pigeon92] Pigeon M. , Saucier F. , *Durability of repaired concrete structures*, International Symposium on Advances in Concrete Technology, Ed. by V. M. Malhotra, Athens, Greece, May, 1992, pp 741-773.
- [Powers48] Powers T. C., Brownyard T. L., *Studies of the Physical Properties of Hardened Portland Cement Paste*, Research Laboratories of the Portland Cement Association, Bull. 22, Detroit, USA, March, 1948, 356 p.
- [Randl00] Randl N., Wicke M., *Schubübertragung zwischen Alt- und Neubeton*, Beton- und Stahlbetonbau, Vol. 95, No. 8, August, 2000, pp 461-473 (in German).
- [Reich97] Reich R., Cervenka J., Saouma V. E., *MERLIN, A Three-Dimensional Finite Element Program Based on a Mixed-Iterative Solution Strategy for Problems in Elasticity, Plasticity, and Linear and Nonlinear Fracture Mechanics*, EPRI Report, Palo Alto, USA, 1997.
- [Richard95] Richard P., Cheyrezy M., *Composition of Reactive Powder Concretes*, Cement and Concrete Research, Vol. 25, No. 7, October, 1995, pp 1501-1511.
- [RILEM02] RILEM TC 181-EAS, *Early Age Cracking in Cementitious Systems*, RILEM report, Technical Committee 181-EAS: Early age shrinkage induced stresses and cracking in cementitious systems, Ed. by A. Bentur, Report 25, France, July, 2002, 337 p.
- [Roelfstra89] Roelfstra P. E., *A numerical approach to investigate the properties of concrete - numerical concrete*, Doctoral Thesis, No. 788, Swiss Federal Institute of Technology (EPFL), Lausanne, Switzerland, 1989.
- [Rossi87] Rossi P., Acker P., Malier Y., *Effect of steel fibres at two different stages: the material and the structure*, Materials and Structures, Vol. 20, No. 120, 1987, pp 436-439.
- [Rossi97] Rossi P., *High Performance Multimodal Fiber Reinforced Cement Composites (HPMFRCC): The LCPC Experience*, ACI Materials Journal, Vol. 94, No. 6, November - December, 1997, pp 478-483.

- [Rossi02] Rossi P., *Development of new cement composite material for construction*, Innovations and Developments in Concrete Materials and Construction, Proceedings of the International Conference, University of Dundee, Ed. by R. K. Dhir, P. C. Hewlett and L. J. Csetenyi, Dundee, Scotland, September, 2002, pp 17-29.
- [Roux96] Roux N., Andrade C., Sanjuan M. A., *Experimental Study of Durability of Reactive Powder Concretes*, ASCE Journal of Materials in Civil Engineering, Vol. 8, No. 1, February, 1996., pp 1-6
- [Roy72] Roy D. M., Gouda G. R., Bobrowsky A., *Very high strength cement pastes prepared by hot pressing and other high pressure techniques*, Cement and Concrete Research, Vol. 2, No. 3, 1972, pp 349-366.
- [Roy73] Roy D. M., Gouda G. R., *High strength generation in cement pastes*, Cement and Concrete Research, Vol. 3, No. 6, 1973, pp 807-820.
- [Rüsch60] Rüsch H., *Researches towards a general flexural theory for structural concrete*, ACI Journal Proceedings, Vol. 57, July, 1960, pp 1-28.
- [Sadouki97] Sadouki H., Van Mier J. G. M., *Simulation of hygral crack growth in concrete repair systems*, Materials and Structures, Vol. 30, no. 203, November, 1997, pp 518-526.
- [Saucier90] Saucier F., *Contribution à l'étude de la durabilité de l'adhérence des réparations en béton*, PhD thesis, University Laval, Québec, Québec, Canada, December, 1990, 144 p. (in French)
- [Schachinger03] Schachinger I., Schmidt K., Heinz D., *Zeitabhängiges Verformungsverhalten von UHFB*, Ultrahochfester Beton, Innovationen im Bauwesen - Beiträge aus Praxis und Wissenschaft, Ed. by G. König, K. Holschemacher, F. Dehn, Bauwerk, Berlin, Leipzig, Germany, 2003, pp 67-77 (in German).
- [Schenkel98] Schenkel M., *Zum Verbundverhalten von Bewehrung bei kleiner Betondeckung*, Doctoral Thesis, IBK-Report, No. 237, Swiss Federal Institute of Technology (ETHZ), Zürich, Switzerland, September, 1998, 162pp. (in German).
- [Schläfli99] Schläfli M., *Ermüdung von Brückenfahrbahnplatten aus Stahlbeton*, Doctoral thesis, No.1998, Swiss Federal Institute of Technology (EPFL), Lausanne, Switzerland, 1999, 113 p. (in German).
- [Schneider92] Schneider B., *Development of SIFCON through applications*, Proceedings of the International Workshop, "High Performance Fiber Reinforced Cement Composites (HPFRCC)", Ed. by H. W. Reinhardt and A. E. Naaman, E & FN Spon, RILEM Proceedings 15, Stuttgart, Germany, June, 1992, pp 177-194.
- [Schrader92] Schrader K. E., *Mistakes, Misconceptions, and Controversial Issues Concerning Concrete and Concrete Repairs, part 1, 2, 3*, Concrete International, Vol. 14, No. 9, 10, 11, September, October, November, 1992, pp 52-56, 48-52, 54-59.
- [Scrivener89] Scrivener K., *The Microstructure of Concrete*, Materials Science of Concrete I, Ed. by J. Skalny, American Ceramics Society, Westerville, USA, 1989, pp 127-161.
- [Sedran94] Sedran T., de Larrard F., Angot D., *Prévision des mélanges granulaires par le modèle de suspension solide, I - Fondements théoriques et étalonnage du modèle*, Bulletin de liaison des laboratoires des ponts et chaussées, No. 194, France, November-December, 1994, pp 59-70 (in French).
- [SIA260] SIA 260, *Grundlagen der Projektierung von Tragwerken (Swisscode 0)*, SIA, Zürich, Switzerland, 2003, 44 p. (in German).
- [SIA261] SIA 161, *Einwirkungen auf Tragwerke (Swisscode 1)*, SIA, Zürich, Switzerland, 2003, 110 p. (in German).
- [SIA262] SIA 262, *Betonbauten (Swisscode 2)*, SIA, Zürich, Switzerland, 2002, 76 p. (in German).
- [SIA469] SIA 469, *Erhaltung von Bauwerken*, SIA, Zürich, Switzerland, 1997, 20 p. (in German).

- [Siebel03] Siebel E., Müller Chr., *Geeignete Zemente für die Herstellung von UHFB*, Ultrahochfester Beton, Innovationen im Bauwesen - Beiträge aus Praxis und Wissenschaft, Ed. by G. König, K. Holschemacher, F. Dehn, Bauwerk, Berlin, Leipzig, Germany, 2003, pp 13-24 (in German).
- [Sigrist95] Sigrist V., *Zum Verformungsvermögen von Stahlbetonträgern*, Doctoral thesis, IBK-Report, No. 210, Swiss Federal Institute of Technology (ETHZ), Zürich, Switzerland, 1995, 160 p. (in German).
- [Silfwerbrand87] Silfwerbrand J., *Effekter av differenskrämpning, krypning och fogytans egenskaper på bärförmågan hos samverkanplattor av gammal och pågjuten betong (Effects of differential shrinkage, creep and properties of the contact surface on the strength of composite concrete slabs of old and new concrete)*, Research Report, No. 147, TRITA-BST-0147, Institutionen för Byggnadsstatik, Royal Institute of Technology, KTH, Stockholm, Sweden, 1987, 131 p. (in Swedish).
- [Silfwerbrand90] Silfwerbrand J., *Improving concrete bond in repaired bridge deck*, Concrete International, Vol. 12, No. 9, September, 1990, pp 61-66.
- [Silfwerbrand97] Silfwerbrand J., *Stresses and Strains in Composite Concrete Beams Subjected to Differential Shrinkage*, ACI Structural Journal, Vol. 94, No. 4, July-August, 1997, pp 347-353.
- [Tazawa98] Tazawa E., *Autogenous shrinkage of concrete*, Proceedings of the International Workshop organized by JCI (Japan Concrete Institute), Hiroshima, Japan, June, E & FN SPON, London, 1998, 411 p.
- [Torrent92] Torrent R., *A two-chamber vacuum cell for measuring the coefficient of permeability to air of the concrete cover on site*, Materials and Structures, Vol. 25, No. 150, 1992, pp 358-365.
- [Tausch01] Tausch J-L., *Verhalten der grenzflächennahen Zone von Instandsetzungs- und Schutzsystemen für Stahlbeton*, Doctoral thesis, Swiss Federal Institute of Technology (ETHZ), Building Material Reports, No. 13, Aedificatio Publishers, Zürich, Switzerland, 2001, 209 p. (in German).
- [VanBreugel92] Van Breugel K., *Numerical Simulation of Hydration and Microstructural Development in Hardening Cement-Based Materials*, Heron, Vol. 37, No. 3, the Netherlands, 1992, 62 p.
- [VanMier97] Van Mier J. G. M., *Fracture Processes of Concrete - Assessment of Material Parameters for Fracture Models*, CRC press, Boca Raton, USA, 1997, 448 p.
- [Vandewalle00] Vandewalle L., *Cracking behaviour of concrete beams reinforced with a combination of ordinary reinforcement and steel fibers*, Materials and Structures, Vol. 33, No. 227, April, 2000, pp 164-170.
- [Vaysburd01] Vaysburd A. M., Sabnis G. M., Emmons P. H., McDonald J. E., *Interfacial bond and surface preparation in concrete repair*, The Indian Concrete Journal (ICJ-journal), January, 2001, pp 27-33.
- [Viviani04] Viviani, M., *personal communication*, Swiss Federal Institute of Technology (EPFL), Lausanne, Switzerland, 2004.
- [Waller00] Waller V., *Relations entre composition des bétons, exothermie en cours de prise et résistance à la compression*, Doctoral thesis, Laboratoire Central des Ponts et Chaussées (LCPC), Nantes, France, May, 2000, 317 p. (in French).
- [Warner98] Warner J., Bhuyan S., Smoak W. G., Hindo K. R., Sprinkel M. M., *Surface preparation for overlays*, Concrete International, Vol. 20, No. 5, May, 1998, pp 43-46.
- [Weimann03] Li V. C., Weimann M. B., *Hygral Behavior of Engineered Cementitious Composites (ECC)*, International Journal for Restoration of Buildings and Monuments, Vol. 9, No. 5, 2003, pp 513-534.
- [Weiss02] Weiss, J., *Experimental determination of the ‘time zero’  $t_0$  (maturity-zero  $M_0$ )*, Early Age Cracking in Cementitious Systems, Report of Technical Committee 181-EAS: Early age

- shrinkage induced stresses and cracking in cementitious systems, Ed. by A. Bentur, RILEM Report 25, France, July, 2002, pp 195-206.
- [Wittmann82] Wittmann F. H., *Creep and shrinkage mechanisms*, Concrete and shrinkage in concrete structures, Ed. by Z. P. Bazant and F. H. Wittmann, John Wiley & Sons, 1982, pp 129-162.
- [Wittmann83] Wittmann F. H., *Structure of concrete with respect to crack formation*, Fracture mechanics of concrete, Ed. by F.H.Wittmann, Developments in Civil Engineering 7, Elsevier science Publishers B.V., Amsterdam, Netherlands, 1983, pp 43-74.
- [Wuest04] Wuest J., *Etude Exploratoire des Propriétés Mécaniques de Bétons de Fibres Ultra Performants de Structures*, Diploma thesis, MCS, Swiss Federal Institute of Technology (EPFL), Lausanne, Switzerland, March, 2004, 137 p. (in French).
- [Yuan94] Yuan Y. , Marosszeky M., *Restrained shrinkage in repaired reinforced concrete elements*, Materials and Structures, Vol. 27, No. 171, 1994, pp 375-382.
- [Yudenfreund72] Yudenfreund M., Odler I., Brunauer S., *Hardened Portland Cement Pastes of Low Porosity, I. Materials and Experimental Methods*, Cement and Concrete Research, Vol. 2, No. 3, May, 1972, pp 313-330.
- [Yudenfreund72a] Yudenfreund M., Skalny J., Mikhail R. S., Brunauer S., *Hardened Portland Cement Pastes of Low Porosity, II. Exploratory Studies. Dimensional Changes*, Cement and Concrete Research, Vol. 2, No. 3, May, 1972, pp 331-348.
- [Yudenfreund72b] Yudenfreund M., Hanna K, M., Skalny J., Odler I., Brunauer S., *Hardened Portland Cement Pastes of Low Porosity, V. Compressive Strength*, Cement and Concrete Research, Vol. 2, No. 6, 1972, pp 731-743.
- [Zhu91] Zhu Y., *Evaluation of bond strength between new and old concrete by means of fracture mechanics method*, Doctoral thesis, Royal Institute of Technology (KTH), Bull. 157, Stockholm, Sweden, May, 1991, 102 p.





## Appendix A: Description of the numerical model (MLS)

The FE-program MLS used to simulate the time-dependent behaviour of the composite “UHPFRC-concrete beams” is described in this appendix. A detailed description of MLS can be found in [Bernard00].

### A.1 Structure of MLS

The detailed structure of MLS is shown in Figure A.1.

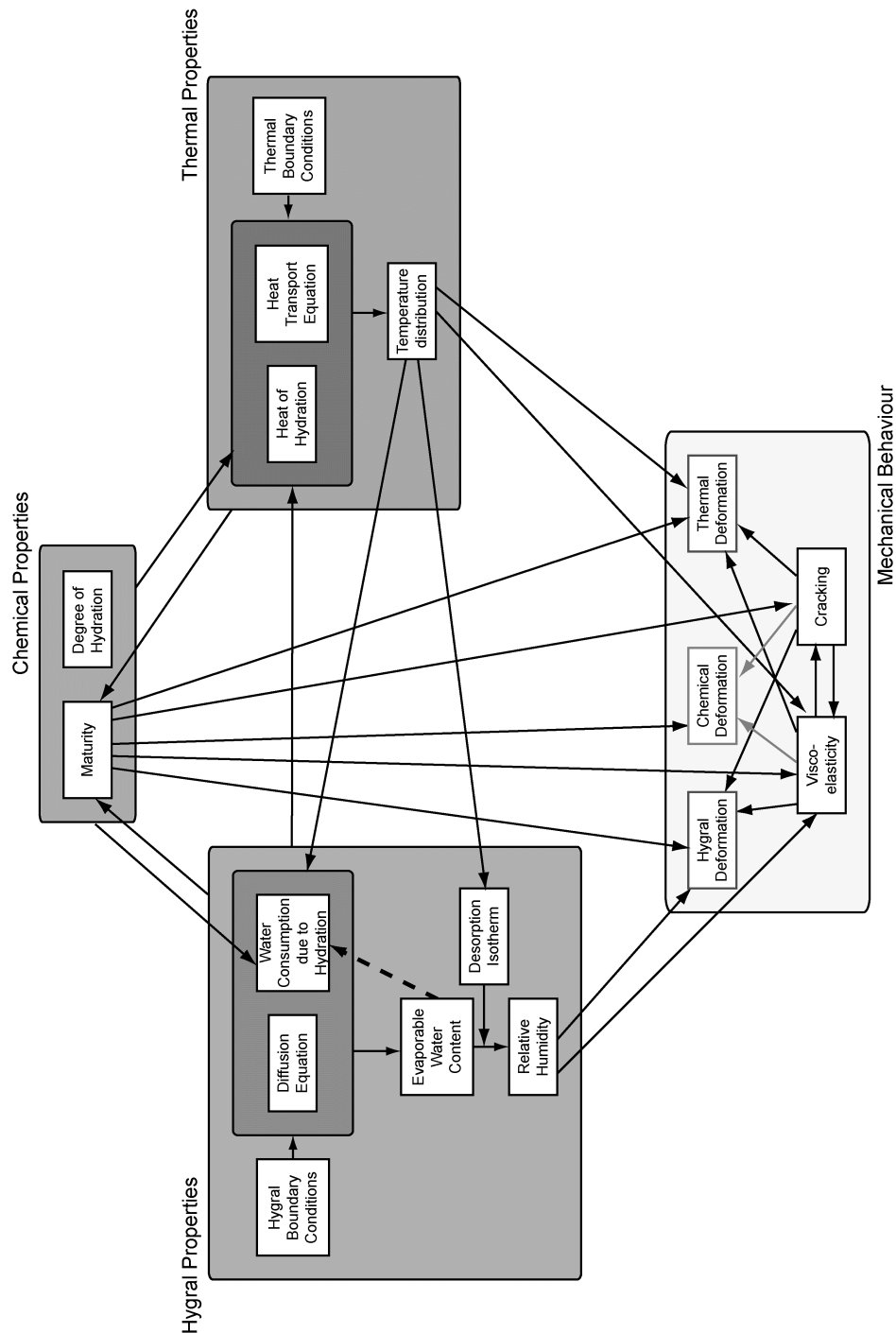


FIGURE A.1: Detailed structure of MLS

## A.2 Material models

### A.2.1 Cementitious materials

The description of the material models is based on the work of [Roelfstra89].

#### Maturity

The maturity of cementitious materials is an equivalent time that considers temperature and moisture (EQ. A.1). The temperature influence is described by an Arrhenius-type law, the dependence on the relative humidity is described by an expression proposed by Bazant and Najjar [Bazant72].

$$M(t) = \int_{t_0}^t e^{\frac{Q}{R} \left( \frac{1}{T_{ref}} - \frac{1}{T(t)+273} \right)} \cdot \frac{1}{1 + (a_c + a_c h)^{b_c}} dt \quad (EQ A.1)$$

with  $t$  [h]: concrete age,  $t_0$  [h]: reference time,  $M$  [h]: maturity,  $Q$  [J/mol]: activation energy,  $R$  [J/(mol K)]: universal gas constant ( $R = 8.3144$  J/(mol K)),  $T_{ref}$  [°C]: reference temperature ( $T_{ref} = 293$  K),  $T$  [°C]: temperature,  $a_c$ ,  $b_c$  [-]: parameters

#### Thermal transport

The thermal transport described by Fick's first law is based on the hypothesis that the rate of heat transfer through an unit area of a section is proportional to the temperature gradient normal to the section (EQ. A.2). Fick's second law describes the heat transfer under transient conditions (EQ. A.3).

$$\vec{q}(t) = -\lambda_T \cdot \vec{\text{grad}} T(t) \quad (EQ A.2)$$

with  $q$  [W/m<sup>2</sup>]: temperature flux,  $\lambda_T$  [W/(m K)]: thermal diffusivity,  $T$  [°C]: temperature.

$$c_T \frac{dT(t)}{dt} + \text{div } \vec{q}(t) - \frac{dH_{hydr}(M(t))}{dt} = 0 \quad (EQ A.3)$$

with  $c_T$  [W/(m K)]: thermal capacity,  $q$  [W/m<sup>2</sup>]: temperature flux,  $H_{hydr}$  [kJ/m<sup>3</sup>]: liberated heat of hydration,  $T$  [°C]: temperature.

Thermal boundary conditions can be given in several ways: either the temperature is prescribed in certain points, lines or areas or heat convection is simulated by EQ. A.4.

$$\vec{q}_B(t) = -\pi_T (T(t) - T_e(t))_B \cdot \vec{n} \quad (EQ A.4)$$

with  $q_B$  [W/m<sup>2</sup>]: temperature flux at boundary  $B$ ,  $\pi_T$  [W/(m<sup>2</sup> K)]: thermal transfer coefficient,  $T_e$  [°C]: external temperature,  $T$  [°C]: temperature in the element.

The heat of hydration can be modelled in three ways: The first way is by the Danish model, developed by the Danish cement industry (EQ. A.5), the second way is by the shrinkage core model (SCM, EQ. A.6) and the third way is by giving the adiabatic temperature rise point by point in function of time.

$$H_{\text{hydr}}(M(t)) = H_T \cdot e^{-\left(\frac{a_d}{M}\right)^{b_d}} \quad (\text{EQ A.5})$$

with  $H_{\text{hydr}}$  [kJ/m<sup>3</sup>]: liberated heat of hydration,  $H_T$  [kJ/m<sup>3</sup>]: total amount of heat of hydration,  $a_d$  [h]: parameter,  $b_d$  [-]: parameter.

$$H_{\text{hydr}}(M(t)) = H_T \cdot \frac{a \cdot (M - d)}{1 + a \cdot (M - d)} \quad (\text{EQ A.6})$$

with  $H_{\text{hydr}}$  [kJ/m<sup>3</sup>]: liberated heat of hydration,  $H_T$  [kJ/m<sup>3</sup>]: total amount of heat of hydration,  $d$  [h]: parameter,  $a$  [-]: parameter.

### Moisture transport

Moisture transport is described on the basis of a model developed by Bazant and Najjar [Bazant72]. The moisture flux is given in EQ. A.7 and the differential equation of the hygral transport in EQ. A.8. The water content  $w$  is transformed into relative humidity by means of desorption isotherms. This isotherms are calculated automatically in MLS and are dependent on concrete mix properties. The diffusion coefficient can be determined by the Bazant model (EQ. A.9) [Bazant72] or by the Mensi model (EQ. A.10) [Mensi88].

$$\overrightarrow{q}(t) = -D(h(t)) \cdot \overrightarrow{\text{grad}} h(t) \quad (\text{EQ A.7})$$

with  $q$  [m/h]: moisture flux,  $D$  [m<sup>2</sup>/h]: diffusion coefficient,  $h$  [-]: relative humidity.

$$\frac{dh(t)}{dt} + \text{div} \overrightarrow{q}(t) - \frac{dh_{\text{hydr}}(M(t))}{dt} = 0 \quad (\text{EQ A.8})$$

with  $h$  [-]: relative humidity,  $q$  [m/h]: moisture flux,  $h_{\text{hydr}}$  [-]: reduction of the relative humidity due to self-desiccation during hydration,  $M$  [h]: maturity.

$$D(h(t)) = D_0 \left[ a_h + \frac{1 - a_h}{1 + \left( \frac{1 - h(t)}{1 - h_c} \right)^4} \right] \quad (\text{EQ A.9})$$

with  $D$  [m<sup>2</sup>/h]: diffusion coefficient,  $D_0$  [m<sup>2</sup>/h]: diffusion coefficient in saturated state ( $h = 1$ ),  $h$  [-]: relative humidity,  $h_c$  [-]: transition point between moisture transport in liquid and gas phase: ( $0.7 < h_c < 0.9$ ),  $a_h$  [-]: parameter.

$$D(h(t)) = a_1 \cdot e^{a_2 \cdot h(t)} \quad (EQ A.10)$$

with  $D$  [ $m^2/h$ ]: diffusion coefficient,  $h$  [-]: relative humidity,  $a_1$  [ $W/m^2$ ]: parameter,  $a_2$  [-]: parameter.

The hygral boundary conditions are convective (EQ. A.11).

$$\overrightarrow{q_B(t)} = -\pi_h(h(t) - h_e(t))_B \cdot \vec{n} \quad (EQ A.11)$$

with  $q_B$  [ $m/h$ ]: hygral flux at boundary  $B$ ,  $\pi_h$  [ $m/h$ ]: hygral transfer coefficient,  $h_e$  [-]: external relative humidity,  $h$  [-]: relative humidity in the element.

### Deformations

Thermal deformations are calculated by EQ. A.12 and hygral deformations by EQ. A.12.

$$\Delta \varepsilon_T = -\alpha_T \{M(t)\} \cdot \Delta T \quad (EQ A.12)$$

with  $\varepsilon_T$  [-]: thermal deformation,  $\alpha_T$  [ $K^{-1}$ ]: thermal dilation coefficient,  $M$  [h]: maturity,  $T$  [ $^{\circ}C$ ]: temperature.

$$\Delta \varepsilon_h = -\alpha_h \{M(t)\} \cdot \Delta h \quad (EQ A.13)$$

with  $\varepsilon_h$  [-]: hygral deformation,  $\alpha_h$  [ $K^{-1}$ ]: hygral dilation coefficient,  $M$  [h]: maturity,  $h$  [-]: relative humidity.

Furthermore, the possibility exists to give a deformation in function of maturity. This option is practical to consider e.g. autogenous shrinkage without calculating self-desiccation or chemical shrinkage.

### Evolution of the mechanical properties

The evolution of mechanical properties such as strengths, secant modulus and Poisson's ratio is given point by point in function of maturity. If only the evolution of the compressive strength is known, the other mechanical properties can be calculated on the basis of the equations proposed in MC90 [CEB204].

### Viscoelasticity

The viscoelasticity is described by a generalized age-dependent Maxwell chain model proposed by Bazant and Wu [Bazant74]. The Maxwell chains approach well rate-type creep laws and are characterized by the viscosity of the dashpots  $\eta$ , defined by the secant modulus  $E$  and the retardation time  $\tau$ , and the stiffness of the resorts, defined by the secant modulus  $E$ . Figure A.2 shows its graphic representation. The Maxwell chain model consists of a number of parallel units. The total strain of all units is always the same, while the subdivision into elastic and viscous strains is generally different. The mathematical formulation is given in EQ. A.14 and EQ. A.15.

$$\sigma_n = \sum_{\mu=1}^m \Delta\sigma_n^\mu + \sum_{\mu=1}^m \sigma_{n-1}^\mu \cdot e^{-\frac{\Delta t}{\tau_\mu}} \quad (EQ A.14)$$

with  $\sigma_n$  [MPa]: stresses at time n,  $\sigma_n^i$  [MPa]: stresses of the i-th Maxwell chain at time  $t_n$ ,  $\sigma_{n-1}^i$  [MPa]: stresses of the i-th Maxwell chain at time  $t_{n-1}$ ,  $\tau_i$  [h]: retardation time of the i-th Maxwell chain, t [h]: time, m [-]: number of Maxwell chains.

$$\sigma_n^i = \left[ \frac{\tau_i}{t} \cdot E_i \left( 1 - e^{-\frac{t}{\tau_i}} \right) \right] \mathbf{A} (\varepsilon - \varepsilon_s) \quad (EQ A.15)$$

with  $\sigma_n^i$  [MPa]: stresses of the i-th Maxwell chain at time  $t_n$ ,  $\tau_i$  [h]: retardation time of the i-th Maxwell chain,  $E_i$  [MPa]: secant modulus of the i-th Maxwell chain at time  $t_{n-1}$ , t [h]: time,  $\mathbf{A}$  [-]: terms linked to the Poisson's ratio  $\nu$ ,  $\varepsilon$  [-]: total deformation,  $\varepsilon_s$  [-]: shrinkage deformation.

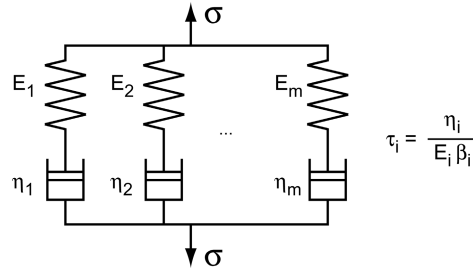


FIGURE A.2: Generalized Maxwell model

The influence of temperature, relative humidity and stress level is taken into account by correcting the time increment used in EQ. A.14. The corrected time is given in EQ. A.16. The first part is an Arrhenius law, the second is taken from work of Bazant and Chern [Bazant85] and the last part is introduced to increase the creep kinetics in relation to the stress level [Bernard00].

$$t_{\text{corr}} = e^{\frac{Q_{\text{cr}}}{R} \cdot \left( \frac{1}{T_{\text{ref}}} - \frac{1}{T + 273} \right)} \cdot (a_t + (1 - a_t)h^2) \cdot \left( \frac{\sinh\left(c_T \frac{\sigma_I}{f_{\text{ct}}}\right)}{c_T \frac{\sigma_I}{f_{\text{ct}}}} \right) t \quad (EQ A.16)$$

with  $t_{\text{corr}}$  [h]: corrected time,  $Q_{\text{cr}}$  [J/mol]: activation energy of creep,  $R$  [J/(mol K)]: universal gas constant ( $R = 8.3144$  J/(mol K)),  $T_{\text{ref}}$ : reference temperature ( $T_{\text{ref}} = 293$  K),  $a_t$  [-]: parameter,  $h$  [-]: relative humidity,  $\sigma_I$  [MPa]: principal tensile stress,  $f_{\text{ct}}$  [MPa]: tensile strength,  $a_T$ ,  $c_T$  [-]: parameters.

Creep deformations are influenced by hygral and thermal changes. Transitional thermal and hygral creep are considered with EQ. A.17 and EQ. A.18.

$$\Delta\varepsilon_{k,h,trans} = r_{\sigma h} \cdot \sigma_I |\Delta h(t)| \quad (EQ A.17)$$

with  $\varepsilon_{k,h,trans}$  [-]: deformation variation due to hygral transitional creep,  $\sigma_I$  [MPa]: principal tensile stress,  $h$  [-]: relative humidity,  $r_{\sigma h}$  [ $m^2/N$ ]: parameter.

$$\Delta\varepsilon_{k,T,trans} = r_{\sigma T} \cdot \sigma_I |\Delta T(t)| \quad (EQ A.18)$$

with  $\varepsilon_{k,T,trans}$  [-]: deformation variation due to thermal transitional creep,  $\sigma_I$  [MPa]: principal tensile stress,  $T$  [ $^{\circ}C$ ]: temperature,  $r_{\sigma T}$  [ $m^2/(N K)$ ]: parameter.

### Tensile and compressive behaviour

The compressive behaviour is linear-elastic, characterized by the secant modulus and the compressive strength. No fracture criterion exists in compression, thus, failure in compression of a structural element cannot be simulated with MLS.

The tensile behaviour of MLS is linear elastic, until the tensile strength  $f_{ct}$  is reached (Figure A.3a). Cracks are modelled by the smeared crack model [Bazant83]. Cracking of the cementitious materials is described either by a bi-linear softening law or a multi-linear law, as shown in Figure A.3b and c respectively. The factor  $\alpha$  defines the relation between the residual crack width and the crack width under load (EQ. A.19). The initial secant modulus  $E_c$  at this point is reduced by the factor  $(1-D)$ , with  $D$  defined as the damage (Figure A.3b). Mesh size independence is obtained by defining a reference length  $L_{ch}$ .

$$\alpha = \frac{w_{res}}{w^*} \quad (EQ A.19)$$

with  $\alpha$  [-]: factor defining the residual crack width,  $w^*$  [mm]: crack width before unloading,  $w_{res}$  [mm]: residual crack width.

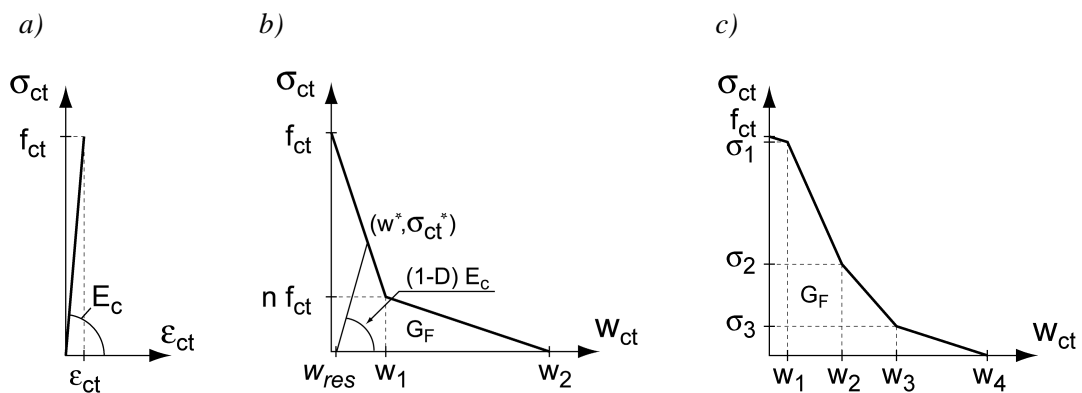


FIGURE A.3: Tensile behaviour in MLS: a) linear-elastic stress rise, b) bi-linear softening law, c) multi-linear law

Hardening behaviour can also be simulated with MLS. However, the multi-linear law is described by the crack width  $w$ , whereas hardening is generally described by the deformation  $\varepsilon$ . Thus, the harden-

ing deformation must be transformed into fictitious crack width by taking into account the FE-mesh size.

The viscoelastic behaviour of concrete in tension is considered by reducing the tensile strength to an apparent tensile strength in function of the load history as described in EQ. A.20 and EQ. A.21 [Bernard00].

$$f_{ct}^x(M(t), \varepsilon_{vis}) = f_{ct}(M(t)) \left[ 1 - (a_{cr}(1 - e^{-b_{cr}\varepsilon_{vis}}))^{c_{cr}} \right] \quad (EQ A.20)$$

with  $f_{ct}^x$  [MPa]: apparent tensile strength,  $\varepsilon_{vis}$  [-]: viscous deformation,  $f_{ct}$  [MPa]: tensile strength,  $M$  [h]: maturity,  $a_{cr}$ ,  $b_{cr}$ ,  $c_{cr}$  [-]: parameters.

$$\varepsilon_{vis} = \varepsilon_I - \frac{\sigma_I}{(1 - D)E_{cc}(M(t))} - \varepsilon_k \quad (EQ A.21)$$

with  $\varepsilon_{vis}$  [-]: total viscous deformation,  $\varepsilon_I$  [-]: deformation in direction of the principal tensile stress,  $\sigma_I$  [MPa]: principal tensile stress,  $D$  [-]: damage coefficient,  $E_{cc}$  [MPa]: secant modulus,  $M$  [h]: maturity,  $\varepsilon_s$  [-]: shrinkage deformation.

## A.2.2 Reinforcement

Rebars are simulated by linear elements, superimposed to the finite element mesh of the cementitious materials. The rebars are defined by a bi-linear stress-strain relationship. The bond stresses between rebar and cementitious material are defined by five points, i.e. four straight lines. Finally, the rebars are defined by their shear stiffness, their dowel stiffness, an unloading factor and the thermal dilation factor  $\alpha_T$ .





# Appendix B: Material input of the numerical model (MLS)

## UHPC

maturity			thermal properties			autogenous shrinkage		cracking		
Q/R	[K]	4000	$\lambda_T$	[W/(mK)]	2.4		[ $\mu\text{m}/\text{m}$ ]		w	$\sigma/f_{U_t,1st}$
$T_{ref}$	[K]	273	$c_T$	[kJ/(m <sup>3</sup> K)]	2800	at 0 hours	0	[mm]	[MPa]	
$a_c$	[-]	0	$H_T$	[kJ/m <sup>3</sup> ]	250'000	30.5 hours	0			
			$\alpha_T$ at 0 hours	[ $\mu\text{m}/\text{m}/\text{K}$ ]	40	32 hours	-10		0.0	1
			31 hours		40	36.5 hours	-128		0.1	1.15
			32 hours		28.7	39.5 hours	-150		2.3	0.38
			33 hours		22.3	44.5 hours	-142		6.1	0
			34 hours		16.7	49 hours	-161	$L_R$	[mm]	10
			35 hours		13.5	70 hours	-218	$\alpha$	[-]	0.8
			35.5 hours		12.5	95 hours	-260			
			36 hours		12	150 hours	-300			
			8760 hours		12	168 hours	-313			
						192 hours	-330			
						336 hours	-395			
						672 hours	-475			
						1008 hours	-520			
						1344 hours	-550			
						2160 hours	-600			
						3000 hours	-620			
						4320 hours	-630			
						8760 hours	-650			

mechanical properties	$f_{U_t,1st}$ [MPa]	$f_{U_c}$ [MPa]	$E_U$ [GPa]	$\nu$ [-]	viscoelasticity retardation times $\tau$ [h]					
					1	10	100	1000	10000	100000
at 0 hours	0.10	0.1	0.1	0.2	0.880	0.120	0.000	0.000	0.000	0.000
31 hours	0.60	1.0	0.5	0.2	0.650	0.350	0.000	0.000	0.000	0.000
33 hours	0.60	17.0	3.5	0.2	0.560	0.340	0.100	0.000	0.000	0.000
36 hours	0.61	53.0	10.0	0.2	0.480	0.330	0.180	0.010	0.000	0.000
42 hours	0.67	92.0	22.0	0.2	0.390	0.310	0.200	0.100	0.000	0.000
48 hours	1.10	104.0	26.7	0.2	0.300	0.280	0.220	0.150	0.050	0.000
54 hours	1.59	112.0	30.0	0.2	0.240	0.250	0.230	0.180	0.100	0.000
60 hours	1.96	118.6	32.8	0.2	0.190	0.230	0.240	0.200	0.115	0.025
72 hours	2.63	127.2	36.6	0.2	0.158	0.205	0.250	0.210	0.137	0.040
84 hours	3.30	136.0	39.8	0.2	0.140	0.190	0.240	0.220	0.150	0.060
96 hours	3.79	139.0	41.8	0.2	0.120	0.175	0.233	0.232	0.160	0.080
120 hours	4.40	143.6	44.2	0.2	0.100	0.160	0.215	0.235	0.175	0.115
144 hours	4.64	147.0	45.1	0.2	0.085	0.150	0.200	0.215	0.191	0.159
168 hours	4.83	149.7	45.7	0.2	0.070	0.140	0.180	0.200	0.210	0.200
192 hours	4.95	152.5	46.0	0.2	0.070	0.140	0.180	0.200	0.210	0.200
336 hours	5.19	160.2	47.8	0.2	0.050	0.135	0.178	0.160	0.152	0.325
672 hours	5.62	168.0	50.0	0.2	0.038	0.130	0.173	0.126	0.035	0.498
1344 hours	6.23	174.0	52.0	0.2	0.035	0.128	0.170	0.126	0.025	0.516
2160 hours	6.60	176.8	53.1	0.2	0.033	0.126	0.168	0.126	0.020	0.527
8760 hours	6.72	177.0	53.2	0.2	0.033	0.126	0.168	0.126	0.020	0.527

**Concrete**

maturity			thermal properties				cracking		
Q/R	[K]	4700	$\lambda_T$	[W/(mK)]	2.4		n	[-]	0.2
$T_{ref}$	[K]	293	$c_T$	[kJ/(m <sup>3</sup> K)]	2200		$w_1$	[mm]	0.03
$a_c$	[-]	0	$H_T$	[kJ/m <sup>3</sup> ]	120'000		$w_2$	[mm]	0.2
			$a_d$	[-]	16		$\alpha$	[-]	0.8
			$b_d$	[-]	1.09				
			$\alpha_T$	[ $\mu$ m/m/K]	12				

mechanical properties	$f_{ct}$	$f_{cc}$	$E_c$	$\nu$	viscoelasticity retardation times $\tau$ [h]					
	[MPa]	[MPa]	[GPa]	[-]	1	10	100	1000	10000	100000
0	0.01	0.1	0.5	0.2	0.250	0.240	0.210	0.160	0.100	0.040
12	0.40	3.7	12.5	0.2	0.200	0.195	0.185	0.170	0.145	0.105
24	0.87	8.4	18.9	0.2	0.130	0.140	0.150	0.165	0.190	0.225
72	1.82	19.7	27.9	0.2	0.080	0.090	0.120	0.160	0.230	0.320
168	2.55	29.4	33.5	0.2	0.080	0.090	0.120	0.160	0.230	0.320
336	3.06	36.7	37.1	0.2	0.060	0.080	0.110	0.160	0.240	0.350
672	3.48	43.0	38.2	0.2	0.060	0.080	0.110	0.160	0.240	0.350
1344	3.80	48.1	-	0.2	-	-	-	-	-	-
2688	4.05	52.0	-	0.2	-	-	-	-	-	-
8760	4.20	54.0	40.0	0.2	0.020	0.040	0.070	0.140	0.270	0.460

non-linear viscoelasticity			transitional viscoelasticity		
Q/R	[K]	4000	$\Gamma_{\sigma T}$	[mm <sup>2</sup> /(N K)]	0.008
$T_{ref}$	[K]	293			
$a_t$	[-]	0.5			
$c_t$	[-]	3.8			

**Concrete in the interface zone**

The concrete in the interface zone has the same material properties as the concrete with the exception that the tensile strength at the interface corresponds to 67% of the tensile strength of the concrete.

**Steel reinforcement**

mechanical properties			bond stress-slip in UHPFRC		bond stress-slip in concrete	
$E_s$	[GPa]	205	slip	stress	slip	stress
$f_{sy}$	[MPa]	500	[mm]	[MPa]	[mm]	[MPa]
$f_{su}$	[MPa]	550	0.0	0.00	0.0	0.00
$\epsilon_{su}$	[%]	10	0.6	4.44	0.1	1.48
shear stiffness	[MPa]	200	3.0	8.45	0.5	2.82
dowel stiffness	[N/mm <sup>3</sup> ]	500	6.6	11.59	1.1	3.86
unloading factor	[-]	0.3	7.2	12.00	1.2	4.00
$\alpha_T$	[ $\mu$ m/m/K]	10				

## Appendix C: Parameters of the generalized age-dependent Maxwell chain model for UHPFRC

TABLE C.1: First adaptation of the Maxwell chain model at early age

maturity [h]	E [MPa]	retardation times [h]					
		0.001	0.01	0.1	1	10	100
0	500	0.01	0.06	0.3	0.51	0.12	0
30	500	0.01	0.06	0.3	0.51	0.12	0
31	5900	0.01	0.06	0.3	0.51	0.12	0
36	12500	0.001	0.05	0.15	0.6	0.199	0
50	41000	0	0.01	0.05	0.13	0.76	0.05
80	41500	0	0.01	0.04	0.1	0.8	0.05
113	41500	0	0	0.01	0.05	0.69	0.25

TABLE C.2: Final adaptation of the Maxwell chain model

maturity [h]	E [MPa]	retardation times [h]					
		1	10	100	1000	10000	100000
0	500	0.880	0.120	0.000	0.000	0.000	0.000
31	500	0.650	0.350	0.000	0.000	0.000	0.000
33	3500	0.560	0.340	0.100	0.000	0.000	0.000
36	10000	0.480	0.330	0.180	0.010	0.000	0.000
42	22000	0.390	0.310	0.200	0.100	0.000	0.000
48	26700	0.300	0.280	0.220	0.150	0.050	0.000
54	30000	0.240	0.250	0.230	0.180	0.100	0.000
60	32800	0.190	0.230	0.240	0.200	0.115	0.025
72	36600	0.158	0.205	0.250	0.210	0.137	0.040
84	39800	0.140	0.190	0.240	0.220	0.150	0.060
96	41800	0.120	0.175	0.233	0.232	0.160	0.080
120	44200	0.100	0.160	0.215	0.235	0.175	0.115
144	45100	0.085	0.150	0.200	0.215	0.191	0.159
168	45700	0.070	0.140	0.180	0.200	0.210	0.200
336	44200	0.050	0.135	0.178	0.160	0.152	0.325
672	45100	0.038	0.130	0.173	0.126	0.035	0.498
1344	45700	0.035	0.128	0.170	0.126	0.025	0.516
2160	45100	0.033	0.126	0.168	0.126	0.020	0.527
4320	45700	0.033	0.126	0.168	0.126	0.020	0.527



## Appendix D: Simulation of the composite beams with the numerical model (MLS)

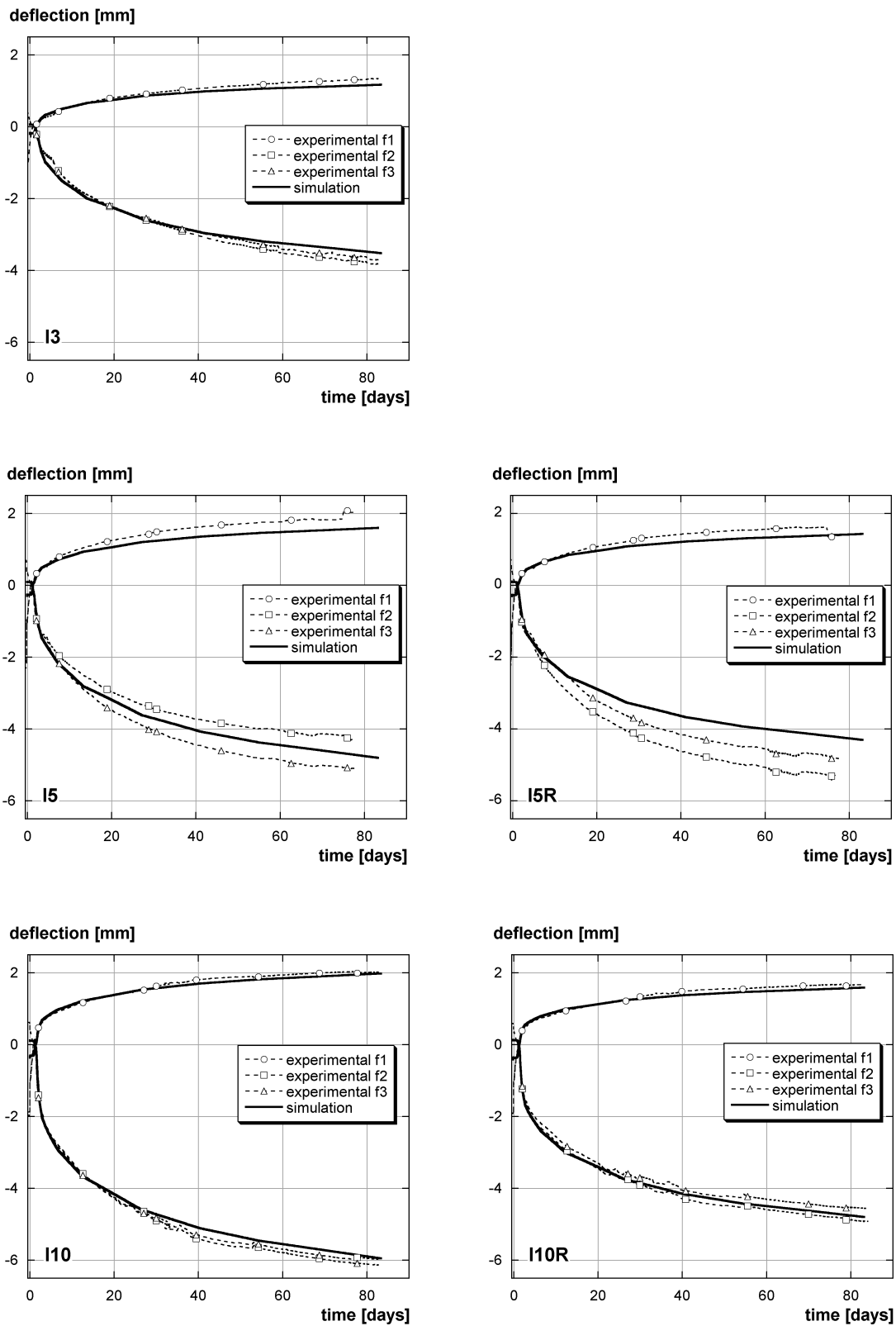


FIGURE D.1: Simulation and experimental results for the statically determinate beams (without loading)

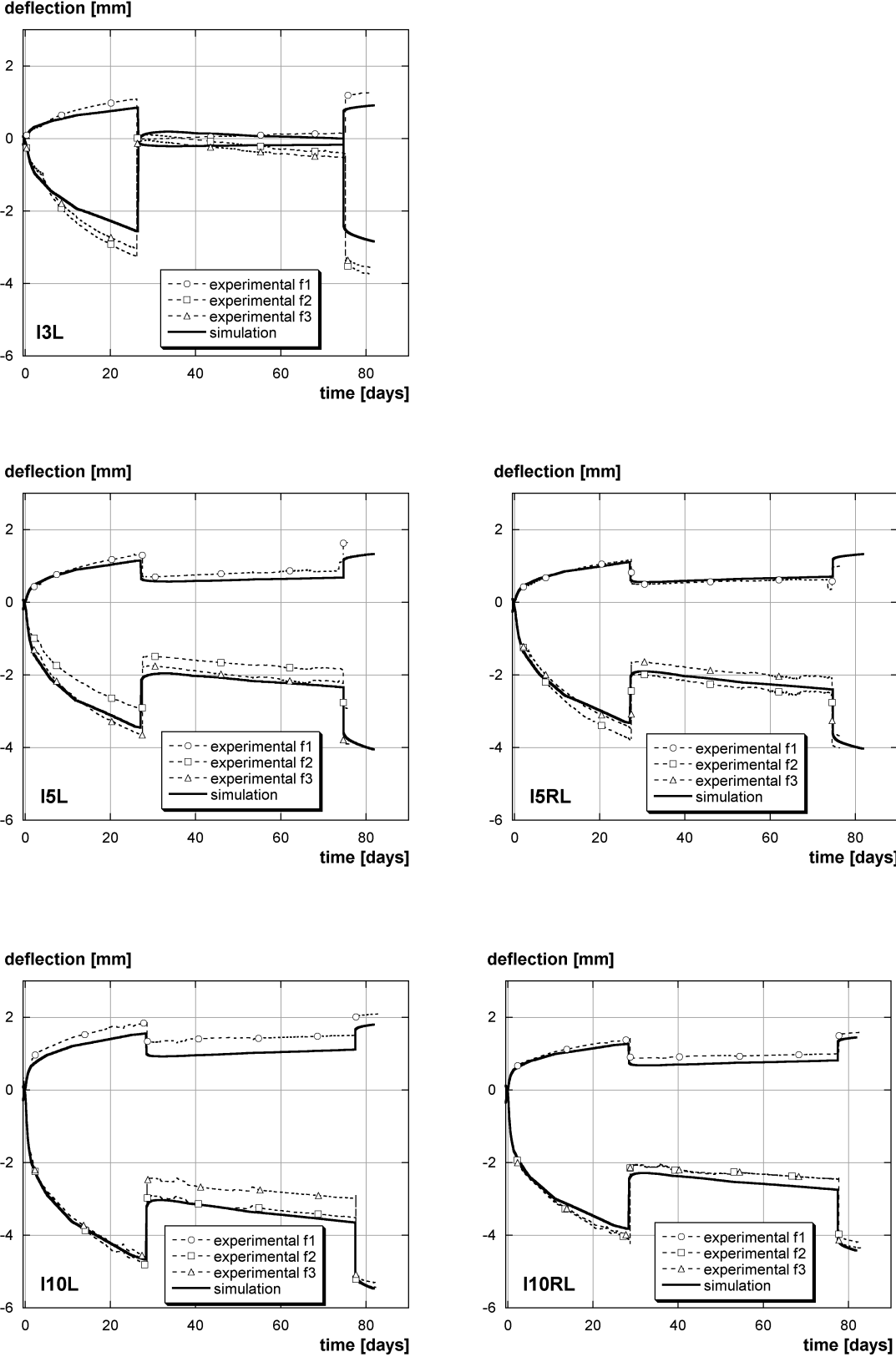


FIGURE D.2: Simulation and experimental results for the statically determinate beams subjected to creep loading

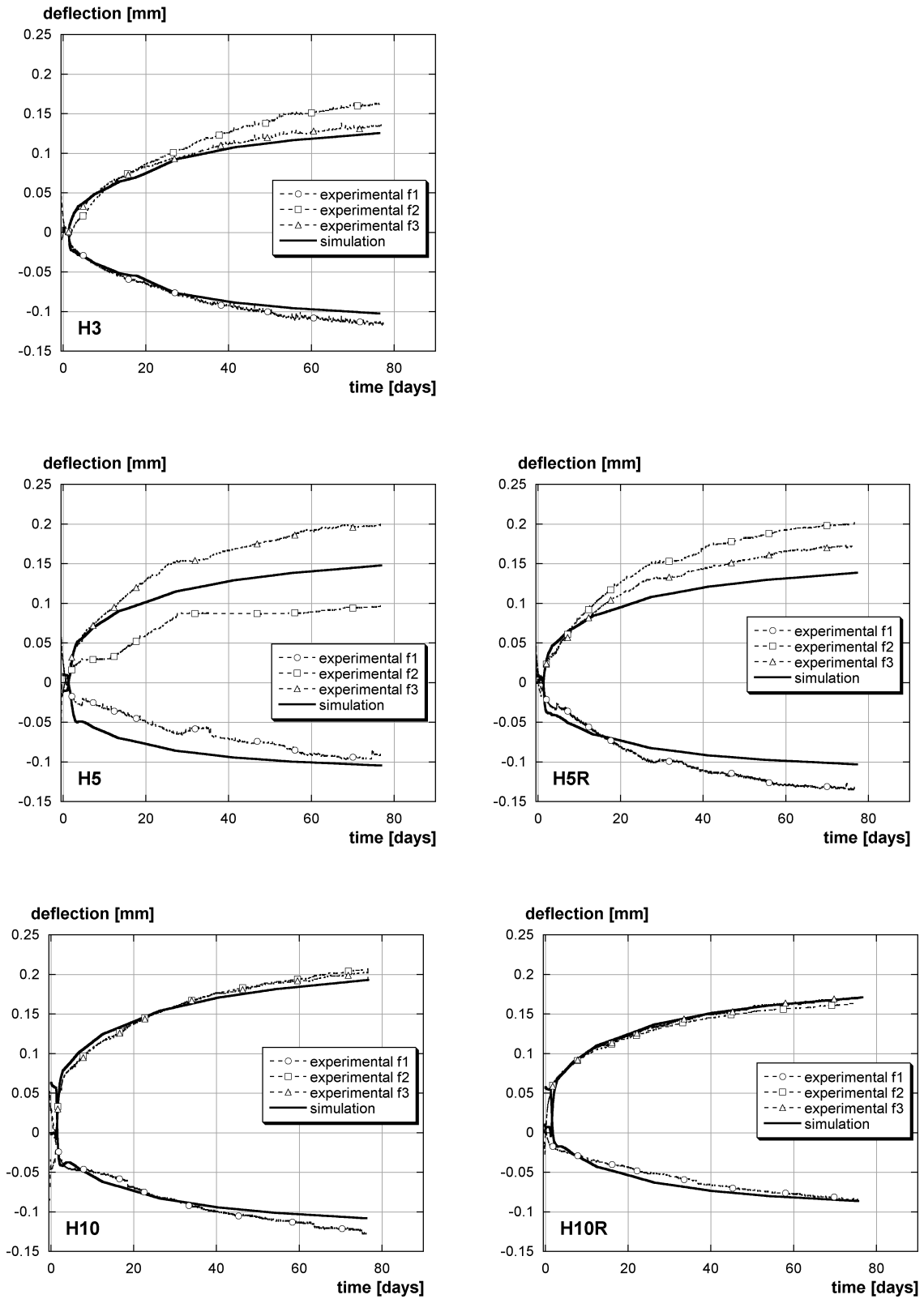


FIGURE D.3: Simulation and experimental results for the statically indeterminate beams

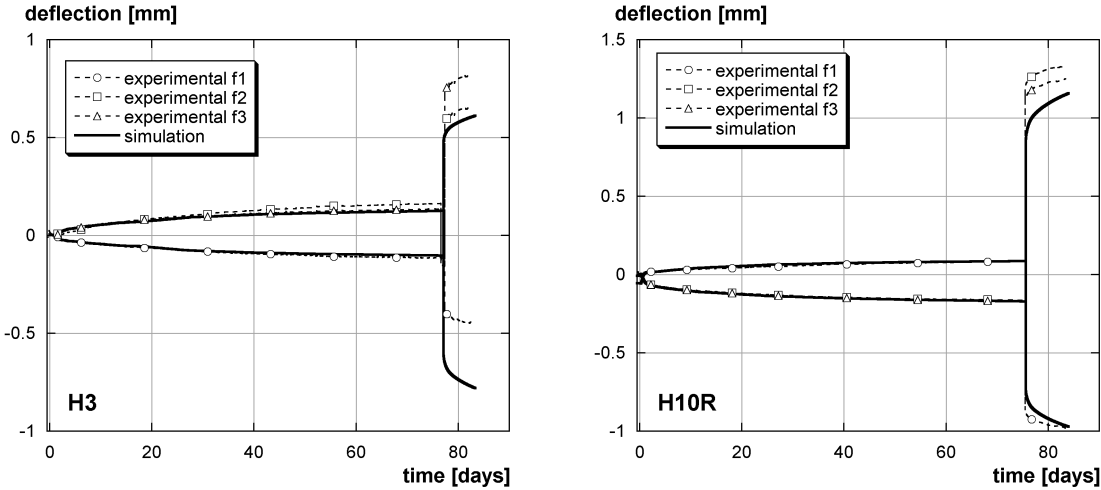


FIGURE D.4: Simulation and experimental results for the statically indeterminate beams with simulation of the removal of the external supports and one horizontal internal support (for H3 and H10R)



## Appendix E: Analytical model for the composite “UHPFRC-concrete” beams

### E.1 Input data

The input data for the cross-section of the composite “UHPFRC-concrete” beams is directly taken from the experimental campaign (Section 3.4):

- geometry of the structural element:
  - width:  $b = 30$  cm,
  - thickness of the UHPFRC layer:  $h_U = 3, 5, 10$  cm,
  - thickness of the concrete layer:  $h_c = 15$  cm,
- the reinforcement ratio:
  - $A_{s,U} = 314$  mm<sup>2</sup> for  $h_U = 5$  cm,  $A_{s,U} = 615$  mm<sup>2</sup> for  $h_U = 10$  cm ( $\rho_{s,U} = 2$  % of  $A_U = b \cdot h_U$ ),
  - $A_{s,ct} = 339$  mm<sup>2</sup> ( $\rho_{s,ct} = 0.83$  % of  $A_c$  with  $A_c = b \cdot d_{s,ct}$ ),
  - $A_{s,cc} = 615$  mm<sup>2</sup> ( $\rho_{s,cc} = 0.9$  % of  $A_c$  with  $A_c = b \cdot d_{s,cc}$ ),
- the position of the reinforcement:
  - $d_{s,cc} = 3.6$  cm,
  - $d_{s,ct} = 13.6$  cm,
  - $c = 2$  cm, ( $d_{s,U} = h_{tot} - c$ ),

The input data of the material models are deduced from the test results of the material characterization conducted in the experimental campaign (Section 3.2) [Habel04].

TABLE E.1: Material input data for the analytical model

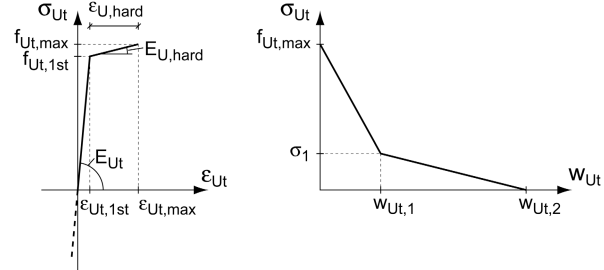
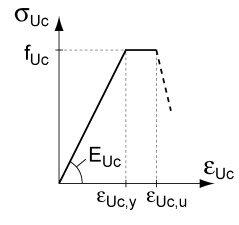
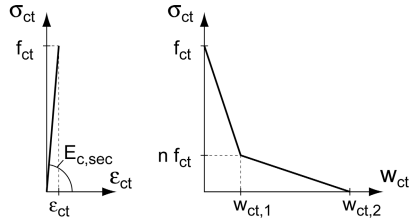
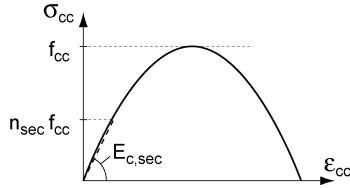
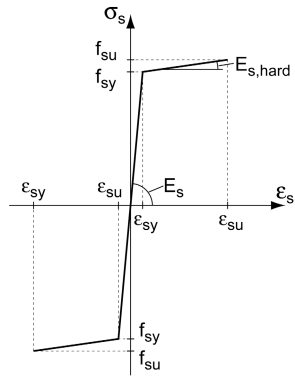
<p>Tensile behaviour of the UHPFRC</p> 	<p><math>E_U =</math> variable,  <math>f_{U,t,1st} =</math> variable,  <math>f_{U,t,max} =</math> variable,  <math>\epsilon_{U,t,max} =</math> variable,  <math>E_{U,hard} =</math> variable  <math>\sigma_1 = 2.5</math> MPa,  <math>w_{U,t,1} = 2.2</math> mm,  <math>w_{U,t,2} = 5</math> mm,  <math>L_R = 400</math> mm,</p>
<p>Compression behaviour of the UHPFRC</p> 	<p><math>E_U = 50</math> GPa,  <math>f_{U,c} = 150</math> MPa,  <math>\epsilon_{Uc,y} = \epsilon_{Uc,u} = 3\text{‰}</math></p>

TABLE E.1: Material input data for the analytical model

<p>Tensile behaviour of the concrete</p> 	<p> <math>f_{ct} = 3.4 \text{ MPa},</math>  <math>E_{c,sec} = 36 \text{ GPa},</math>  <math>n = 0.25,</math>  <math>w_{ct,1} = 0.03 \text{ mm},</math>  <math>w_{ct,2} = 0.2 \text{ mm},</math>                      corresponding to <math>G_F = 120 \text{ J/m}^2</math> </p>
<p>Compression behaviour of the concrete</p> 	<p> <math>E_{c,sec} = 36 \text{ GPa},</math>  <math>f_{cc} = 40 \text{ MPa},</math>  <math>n_{sec} = 0.3</math> </p>
<p>Reinforcement</p> 	<p> <math>E_s = 180 \text{ GPa},</math>  <math>f_{s,y} = 580 \text{ MPa},</math>  <math>f_{s,u} = 600 \text{ MPa},</math>  <math>\epsilon_{s,u} = 0.10,</math>  <math>E_{s,hard} = 140 \text{ MPa}</math>                      (test results from [Guandalini04])                 </p>

## E.2 Results

### E.2.1 UHPFRC tensile data input

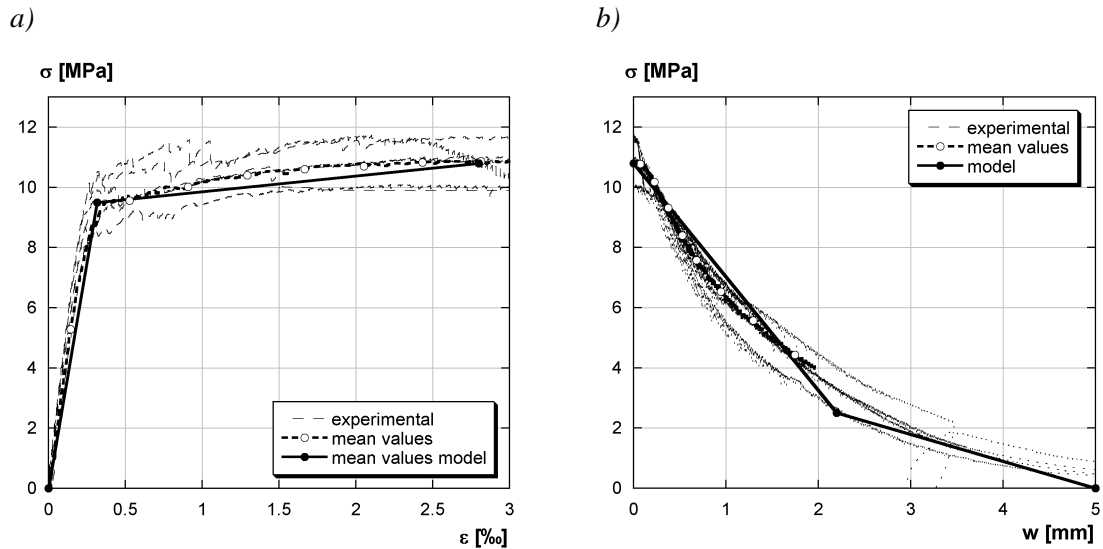


FIGURE E.1: UHPFRC tensile data input - approach I: a) hardening, b) softening

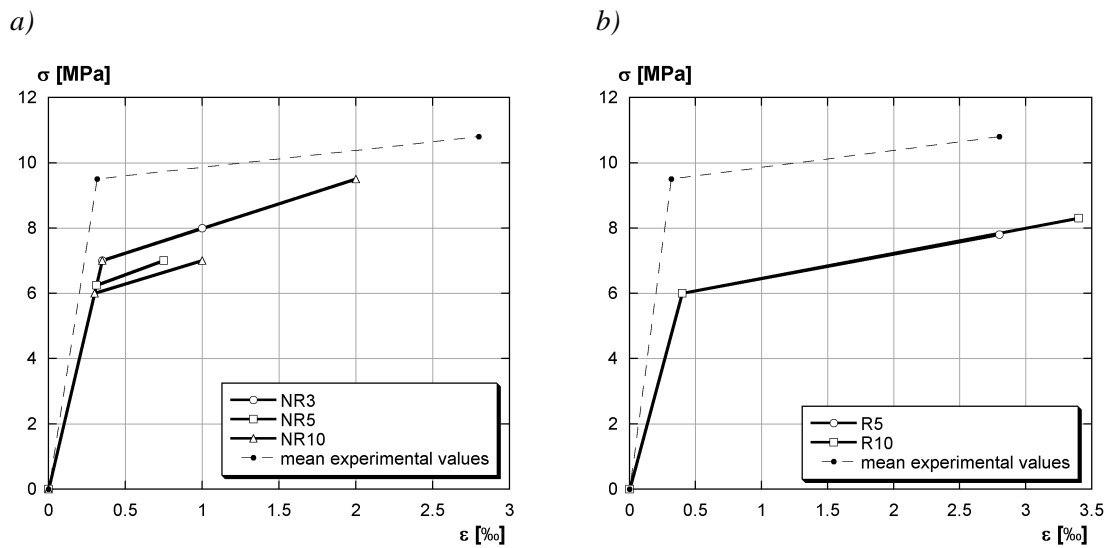


FIGURE E.2: Apparent tensile behaviour - approach II: a) beams NR, b) beams R

TABLE E.2: Reference lengths  $L_R^{\text{hinge}}$  and  $L_R^{\text{beam}}$  (approach II)

Beam	$L_R^{\text{hinge}}$ [mm]	$L_R^{\text{span}}$ [mm]	Beam	$L_R^{\text{hinge}}$ [mm]	$L_R^{\text{span}}$ [mm]
NR3	- <sup>a</sup>	250-500	R5	700-1500	1500
NR5	2000	600	R10	2000-2400	2000
NR10	2000	1500 <sup>b</sup>			

a. not-determinable value

b. estimated value

**E.2.2 Beams without reinforcement in the UHPFRC layer (NR)**

For each beam type, the comparison between experimental results and analytical model is shown. The tensile input data is either derived from test results of the uniaxial tensile test (see Section 3.2.4) or the values determined by inverse analysis of the beam tests. The comparison of crack openings is only possible for beams NR5, NR10, R5 and R10, since insufficient experimental evidence exists for beams NR3.  $\Omega$ -gages-deflection diagrams are established.

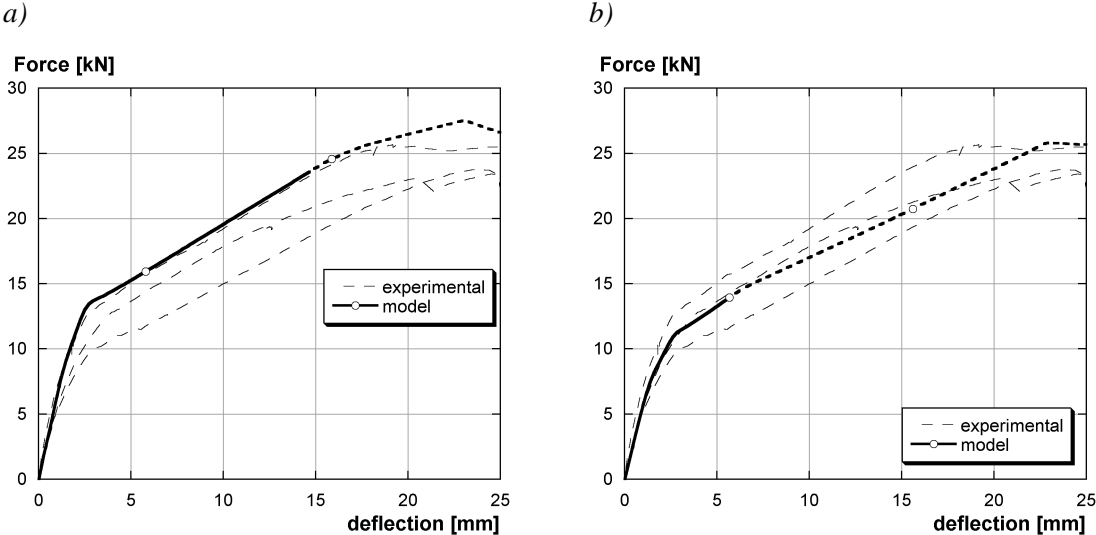


FIGURE E.3: NR3 - comparison between experimental results and analytical model - force-deflection curves: a) approach I, b) approach II

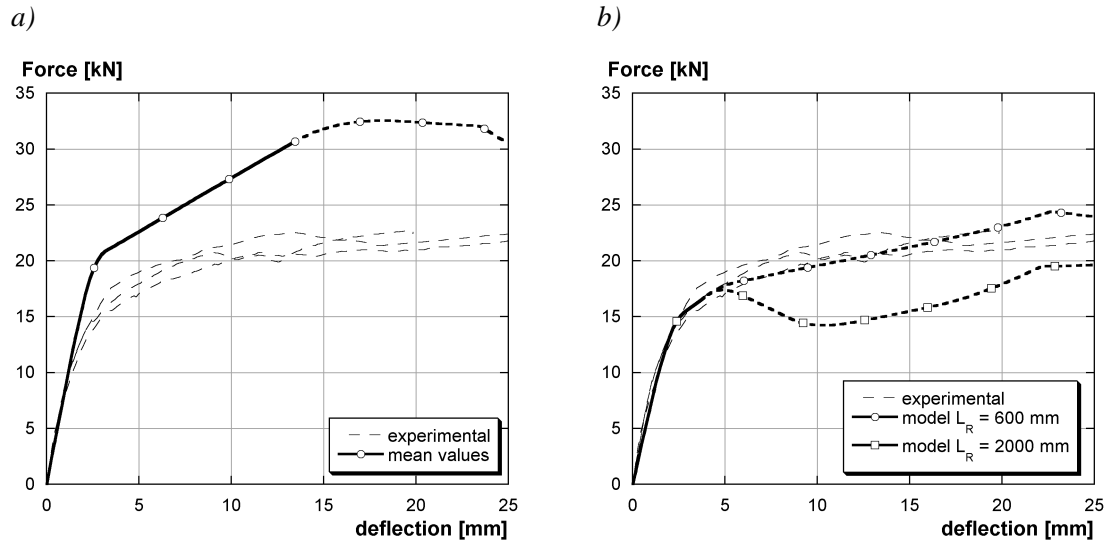


FIGURE E.4: NR5 - comparison between experimental results and analytical model - force-deflection curves: a) approach I, b) approach II

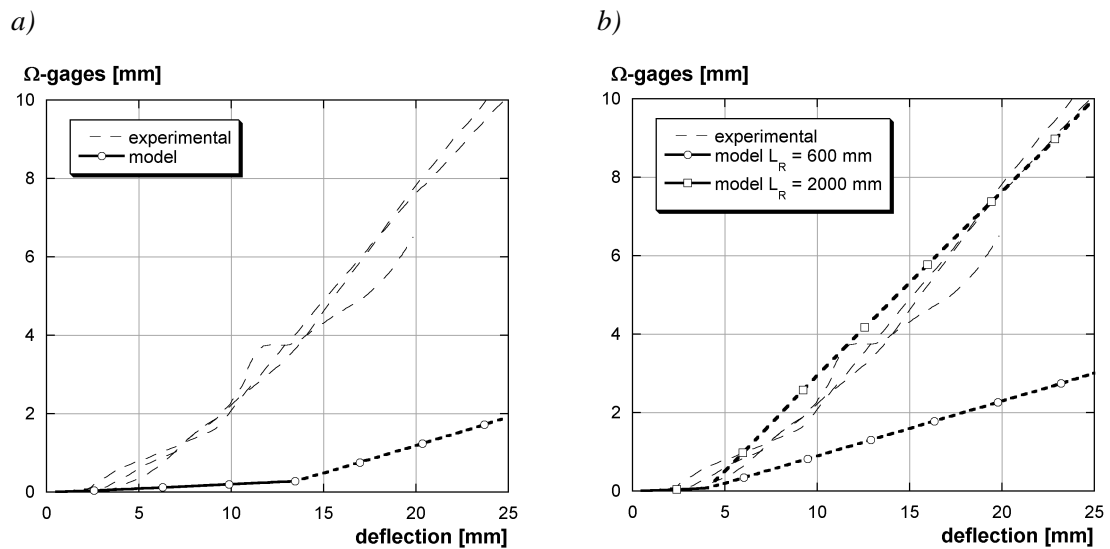


FIGURE E.5: NR5 - comparison between experimental results and analytical model -  $\Omega$ -gages-deflection curves: a) approach I, b) approach II

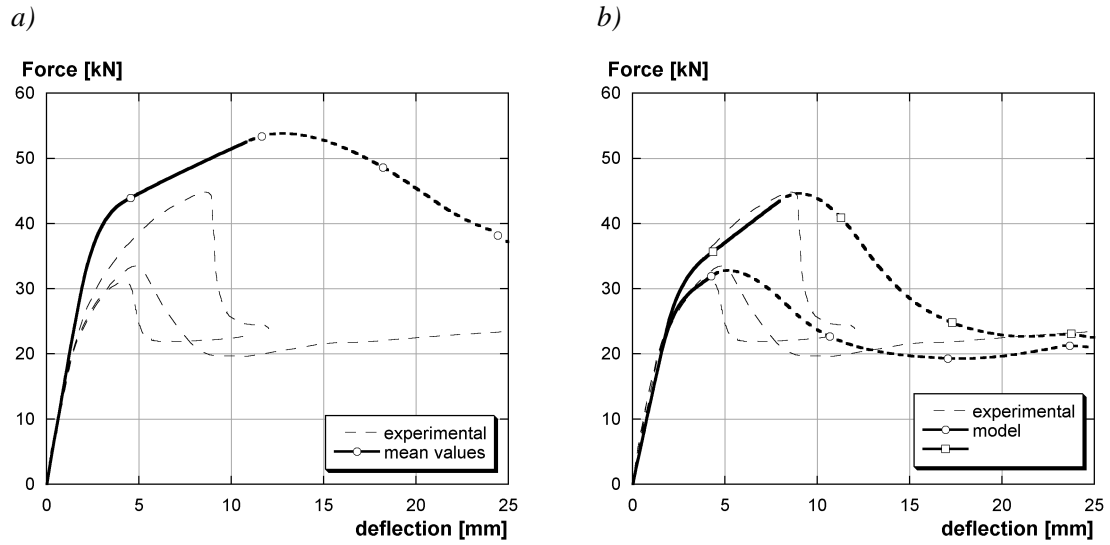


FIGURE E.6: NR10 - comparison between experimental results and analytical model - force-deflection curves: a) approach I, b) approach II

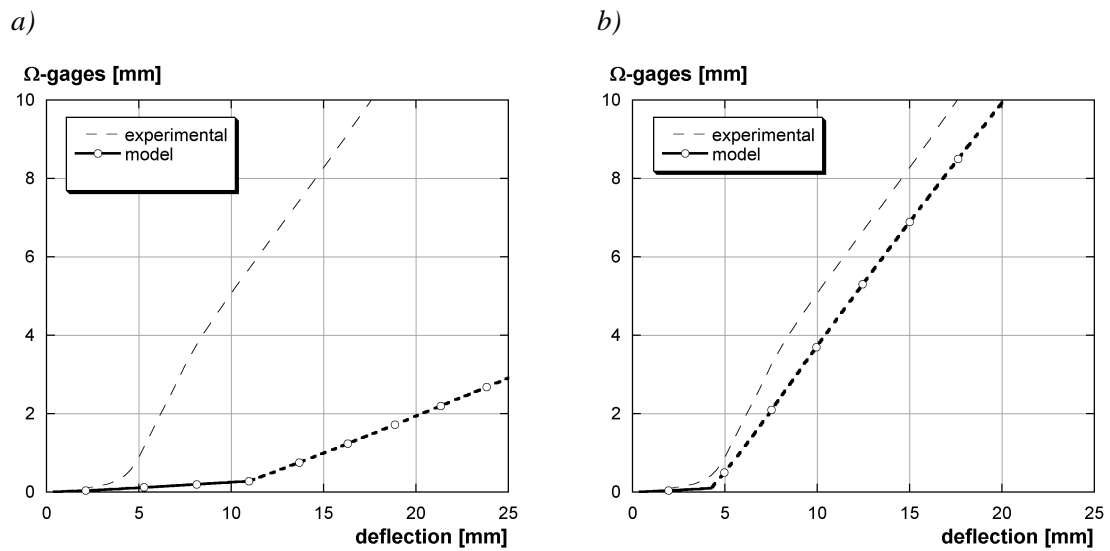


FIGURE E.7: NR10 - comparison between experimental results and analytical model -  $\Omega$ -gages-deflection curves: a) approach I, b) approach II

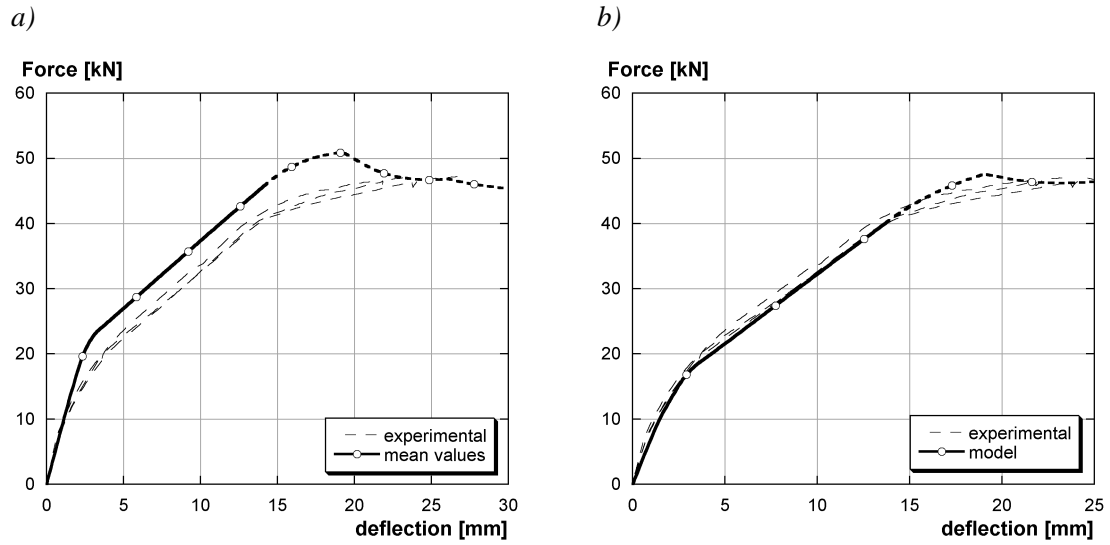


FIGURE E.8: R5 - comparison between experimental results and analytical model - force-deflection curves: a) approach I, b) approach II

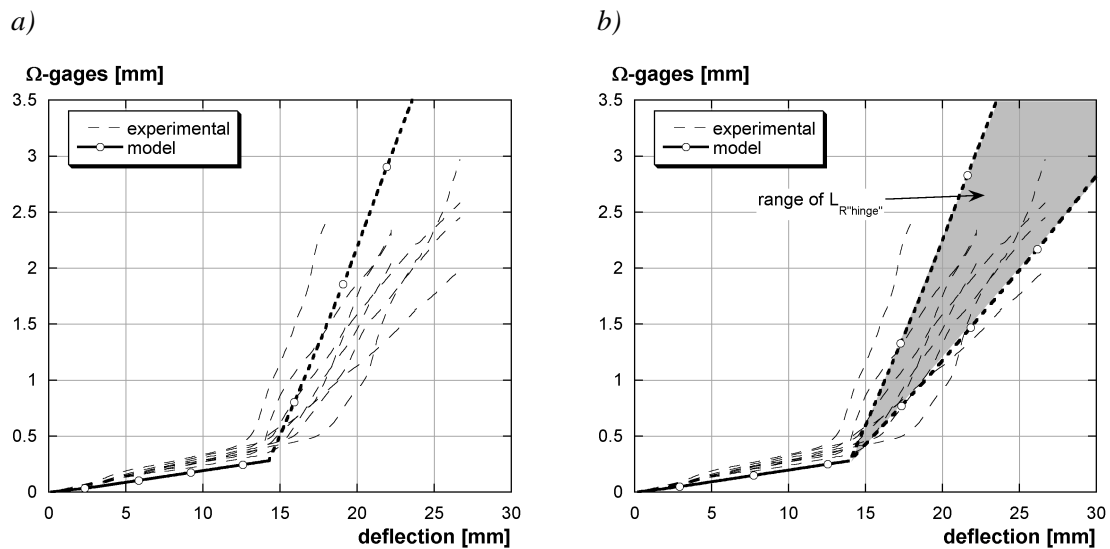


FIGURE E.9: R5 - comparison between experimental results and analytical model -  $\Omega$ -gages-deflection curves: a) approach I, b) approach II

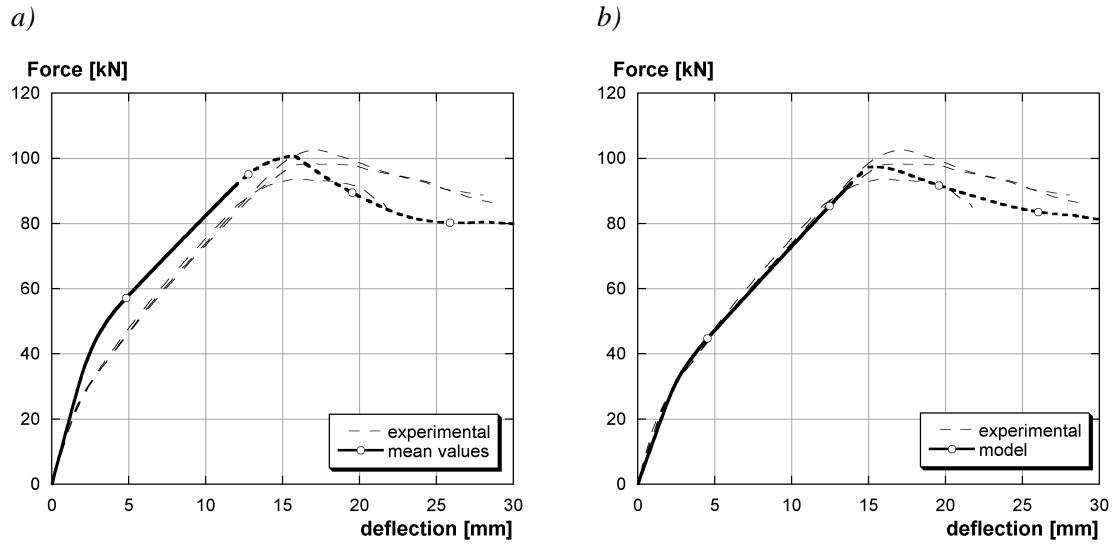


FIGURE E.10: R10- comparison between experimental results and analytical model - force-deflection curves: a) approach I, b) approach II

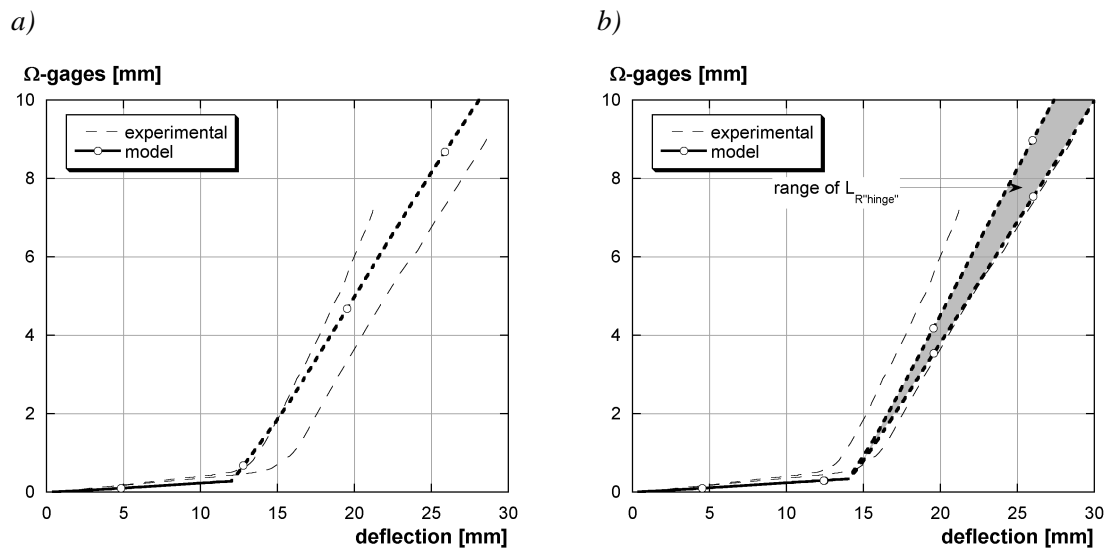


FIGURE E.11: R10 - comparison between experimental results and analytical model -  $\Omega$ -gages-deflection curves: a) approach I, b) approach II



# Curriculum vitae

## Katrin Habel

E-mail: [katrin.habel@alumni.uni-karlsruhe.de](mailto:katrin.habel@alumni.uni-karlsruhe.de)

Nationality: German

Date of birth: May 7th, 1975

## Academic qualifications

2001-2002 Postgraduate course “Risk and Security of Technical Systems” organized by the Swiss Federal Institutes of Technology in Lausanne and Zürich (EPFL, ETHZ) and the university of St. Gallen; Diploma as safety engineer

*Title of the diploma thesis: “Safety evaluation of the structural hall I, IS-ENAC-EPFL”*

1994-1999 M.Sc. in civil engineering at the Technical University of Karlsruhe, Germany (diploma)

*M.Sc. thesis at the EPFL, Lausanne, Switzerland*

*Title of the diploma thesis: “Cracking and debonding of composite structural elements consisting of concretes of different ages”*

## Work experience

since 1999 Research engineer at the EPFL in Civil Engineering at the MCS (Laboratory for Maintenance and Safety of Structures, professor E. Brühwiler)

*Research:- Ultra-high performance fibre-reinforced concretes (UHPRFC),*

- Composite structural elements consisting of two layers of reinforced concrete,*
- Composite structural “UHPRFC-concrete” elements,*
- Time-dependent behaviour of cementitious materials with focus on early age,*
- Fatigue of reinforced concrete.*

*Projects: - Fatigue evaluation of reinforced concrete (Felsenauviadukt, Bern),*

- Limitation of early age cracking of reinforced concrete (Viadotto delle Cantine, Ticino)*

*Teaching: -Assistance in the lectures and exercises “Maintenance of structures”, “Safety and reliability of structures” and “Aesthetics of structures”,*

- Responsibility for diploma projects in the domain of the rehabilitation of structures.*

2001, June Doctoral Course “Behavior and Performance of Early Age Concrete” at the Technical University of Denmark, Lyngby, Denmark, Organized by D. A. Lange (UIUC) and H. Stang (DTU)

1995-1996 Student assistant in applied mechanics at the university of Karlsruhe, Germany

1997-1998 Student exchange at the EPFL, Lausanne, Switzerland

## Languages

German	mother tongue
English, French	very good
Spanish	basic knowledge

